EXPERIMENTAL CHARACTERIZATION OF THERMO-PHYSICAL PROPERTIES OF MOLTEN SALT NANOMATERIALS AND FORCED CONVECTIVE HEAT TRANSFER OF AQUEOUS NANOFLUIDS

A Dissertation

by

ADITYA KUCHIBHOTLA

Submitted to the Office of Graduate and Professional Studies of
Texas A&M University
in partial fulfillment of the requirements for the degree of

DOCTOR OF PHILOSOPHY

Chair of Committee,	Debjyoti Banerjee
Committee Members,	Cynthia M. Hipwell
	Sanjukta Chakraborty
	Michael Pate
	Saurabh Biswas
Head of Department,	Andreas A. Polycarpou

December 2019

Major Subject: Mechanical Engineering

ABSTRACT

Concentrating Solar Power (CSP) plants are progressively gaining commercial success around the world. As of 2016, CSP plants account for a total installed capacity of 4.8GW. A significant cost advantage for CSP plants is enabled by technologies that have afforded cheap Thermal Energy Storage (TES) platforms that have significantly enhanced the reliability of CSP plants for their integration into the power grids. TES platforms provide a means for matching the phase lag between the peaks in energy demand and the diurnal peaks in insolation (solar energy availability and solar power production) thereby balancing the demand and supply of power as well as for mitigating the load fluctuations on the electricity grid.

Typically, molten salt eutectics are employed in commercial CSP plants as both TES medium and as Heat Transfer Fluid (HTF) due to their stability at high temperatures and low vapor pressures (thus obviating the need for costly and bulky pressure vessels, that are typically required for other working fluids, such as steam) as well as for their minimal environmental impact (molten salts are environmentally benign materials). Molten salts however suffer from poor thermo-physical properties (e.g., low specific heat capacity and thermal conductivity values) and are highly corrosive, especially at elevated temperatures.

Stable suspension of nanoparticles in solvents are termed as nanofluids. Literature reports have shown anomalous enhancements in the thermo-physical properties of nanofluids. Hence, doping molten salts with nanoparticles (“molten salt nanofluids”) can

enable significant enhancement in the specific heat capacity and thermal conductivity (over that of the neat solvent). However, the high cost of nanoparticles (~ $1000/ kg) pose a significant barrier to their commercial implementation for molten salts (which cost less than $0.50/kg). Hence, even at 1% mass concentration, nanoparticles can triple the cost of the molten salt nanofluids (i.e., neglecting other issues – such as materials handling costs).

In this study, a one-step synthesis procedure was explored for generation of nanoparticles *in-situ* in the molten salt eutectic (solvent) from cheap additives for realizing a cheap method that is amenable for industrial scale production of molten salt nanofluids.

Additives that were explored in this study include: unstable salts – such as aluminum nitrate nonahydrate (which undergo thermal decomposition when the solid mixture of molten salt and the additive material is heated to form a melt pool) resulting in the *in-situ* formation of ceramic nanoparticles (e.g., alumina). The solvents (molten salts) explored in this study include:

(a) binary nitrate eutectic composed of $NaNO_3$-KNO_3 (60:40 by mass fraction); and

(b) A ternary nitrate eutectic composed of $LiNO_3$-$NaNO_3$-KNO_3 (38:15:47 by molar ratio).

The enhancement in the specific heat capacity and thermal conductivity values of the molten salt nanofluids samples were measured in this study. The specific heat capacity values were measured using a transient Temperature-History (T-History) technique that was adapted and modified in this study for the molten salt samples. The thermal conductivity values were measured using a custom-designed concentric cylinder

experimental apparatus (which enabled the data acquisition of the circumferential distribution of the steady state temperature profiles and the estimation of the corresponding 1-D radial temperature gradients in molten salt samples that were confined in the cylindrical annulus). These measurement strategies were adapted from prior reports in the literature and were modified in the current study - in order to obviate the effects of nanoparticle precipitation on the instrument error and minimize the measurement uncertainties.

Experiments were also performed to study forced convection subcooled boiling heat transfer of de-ionized water (DI Water) and aqueous nanofluids in a circular pipe. Heat removal rates from the heated pipe are measured for various mass concentrations of nanofluids, wall temperatures and coolant flow rates. Anomalous thermal behavior was observed in boiling heat transfer coefficient measurements resulting from the precipitation of the nanoparticle on the heater surface i.e. pipe surface. The precipitation of nanoparticles (resulting in formation of "nanofins" leading to the enhancement of the surface area) resulted in increase in net convective heat transport. Hence, this study highlights the importance of surface morphology in determining the efficacy of nanofluids as coolants. Furthermore, flow visualization was performed to study the flow boiling regimes for various working fluids explored in this study.

DEDICATION

To my family and friends for all the love and support

ACKNOWLEDGEMENTS

I would like to thank my Committee Chair, Dr. Debjyoti Banerjee, as well as my committee members: Dr. Cynthia Hipwell, Dr. Sanjukta Chakraborty, Dr. Michael Pate, and Dr. Saurabh Biswas for their guidance and support throughout the course of my graduate studies.

Special thanks to my friends, colleagues, department faculty and staff for making my time at Texas A&M University a great experience.

Finally, thanks to my mother and father for their encouragement, sister for her love and to Suma for her patience and love.

CONTRIBUTORS AND FUNDING SOURCES

Contributors

This work was supervised by a dissertation committee consisting of Professor Debjyoti Banerjee (advisor), Professor Cynthia Hipwell, Professor Michael Pate of the Department of Mechanical Engineering, Professor Sanjukta Chakraborty of Texas A&M Health Science Center and Professor Saurabh Biswas of the Department of Biomedical Engineering.

Thermal conductivity apparatus for Chapter 2 was designed and manufactured by Professor Donghyun Shin at the University of Texas Arlington.

All other work conducted for the dissertation was completed by the student independently.

Funding Sources

There are no outside funding contributions to acknowledge related to the research and compilation of this document

TABLE OF CONTENTS

Page

LIST OF FIGURES

Page

LIST OF TABLES

Page

1. INTRODUCTION

1.1 Solar energy and Concentrated Solar Power (CSP) plants

1.1.1 Background

For sustained development of all societies, secure and constant delivery of energy services, with low environmental impact, is essential to meet basic human needs such as lighting, cooking, space comfort and mobility. Furthermore, reliable energy sources and conversion technologies are required to be affordable for sustainable social and economic development. In addition, the different technologies meeting the ever-increasing energy needs are required to be environmentally benign with minimal environmental impacts and low greenhouse gas (GHG) emissions. As shown in Figure 1, published by the Intergovernmental Panel on Climate Change (IPCC), in the IPCC Fourth Assessment Report (AR4), which indicates that fossil fuels provided 85% of the global energy needs in 2015 (and was the same value in 2008).

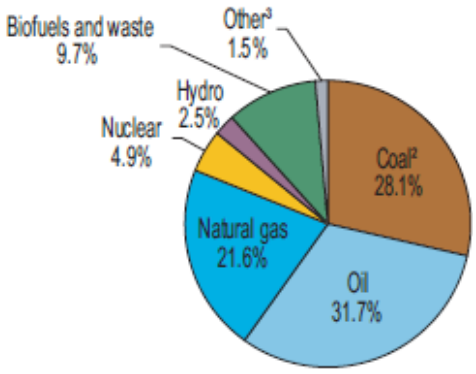

Figure 1. Global energy supply from different energy sources [1].

Continuous increase in global energy requirements demand fast track development of economical, environmentally friendly and socially sustainable energy sources and supply technologies. As reported by International Energy Agency [2] without decisive action greenhouse-gas (GHG) emissions would lead to considerable climate change with an average increase of global temperatures by 6 °C. Energy sources that are replenished by natural processes at a rate that exceeds the rate of use - are termed as renewable energy sources. Renewable energy sources can meet the energy demands in a sustainable manner with minimal environmental impacts. Any form of energy from solar, geothermal heat, hydropower, tidal, wave or biological sources (biomass) are feasible substitutes for conventional fossil fuels. Among renewable energy sources, of particular interest are the direct solar energy conversion technologies. Furthermore, the process of converting primary (renewable) energy sources into electricity involve multi-step processes (with associated energy efficiencies for each step). Electricity generation from thermal conversion processes such as biomass and geothermal undergo net losses of 40 to 90%. On the other hand, direct energy conversion platforms (such as, solar power / photovoltaic (or "PV"), hydro-electric power, ocean thermal energy conversion (OTEC), ocean wave energy conversion (OWEC) and wind energy) are not constrained by the Second Law of Thermodynamics, i.e., do not suffer from thermodynamic exergy losses that are typical of thermodynamic power cycles. However, these technologies do suffer from poor conversion efficiencies for the purpose of generating electricity from these energy sources.

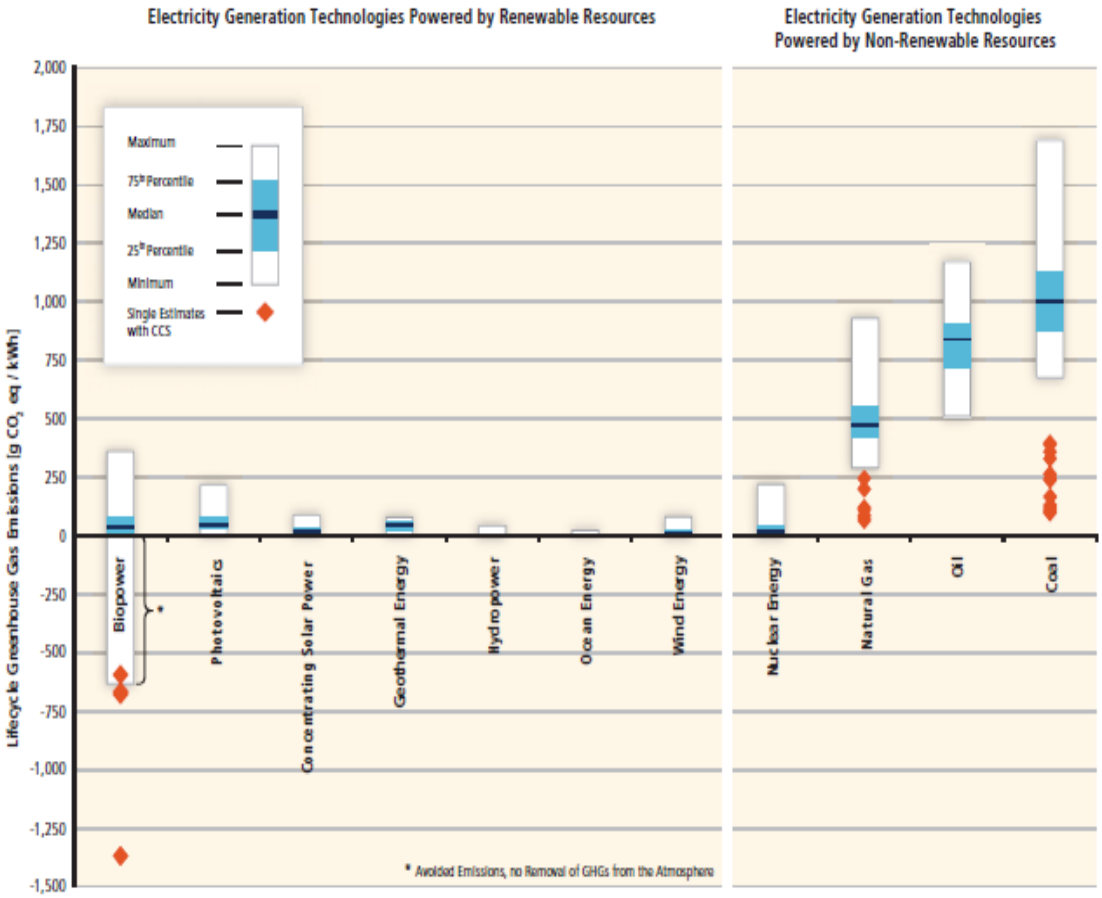

Figure 2. Lifecycle Green House Gas (GHG) emissions (g CO_2 eq. /kWh) for broad categories of fuel sources employed for the purpose of electricity generation technologies [3].

Figure 2 indicates the lifecycle greenhouse gas (GHG) emissions due to power (electricity) generation from various energy sources. As mentioned before, Concentrated Solar Power (CSP) is one of the renewable energy technologies that is highly sustainable as the power production (electricity generation) does not result in greenhouse gas (GHG) emissions. Concentrated Solar Power (CSP), unlike solar photovoltaic (PV) technologies, employs steam turbines thereby providing all the necessary auxiliary services. Furthermore, CSP technologies can leverage thermal energy storage (TES) platforms for electricity

generation that is insensitive to diurnal fluctuations in insolation (i.e., fluctuations in sunlight due to cloud cover or day-night cyles). Integrating a TES platform with a CSP plant can help to ensure several hours of full-capacity electricity generation even after sunset.

1.1.2 Concentrated Solar Power (CSP)

Concentrated Solar Power (CSP) plants typically operate by focusing sunlight (using optical lenses or an array of mirrors - called "heliostats", that can be static (passive actuation or control schemes) or can actively track the sun throughout the day). The sunlight is focused onto a receiver which causes elevated temperatures to be achieved. The receiver is cooled by a Heat Transfer Fluid (HTF), which transfer the thermal energy for electricity generation. The thermal energy collected in the receiver by the flowing HTF is utilized in a heat exchanger to boil working fluids, such as steam (or to heat supercritical fluids), for driving turbines and in turn to generate electricity. Due to the high concentration ratio afforded by CSP technologies, the working fluids reach significantly elevated temperatures – thus enabling higher Carnot efficiencies to be achieved – and therefore accruing cheaper cost of power generation (compared to that of the other renewable technologies). Figure 3 illustrates the four different types of CSP technologies: parabolic troughs (PT), linear Fresnel reflectors (LFR) and parabolic dish type (with a sterling engine at its focal point). The fourth type, known as central receiver systems (CRS), consists of a tower with heliostats focusing the solar energy to the top of the tower. All these CSP

technologies vary with respect to optical design, type of receiver, heat transfer fluid and ability to store heat as well as the operating temperatures.

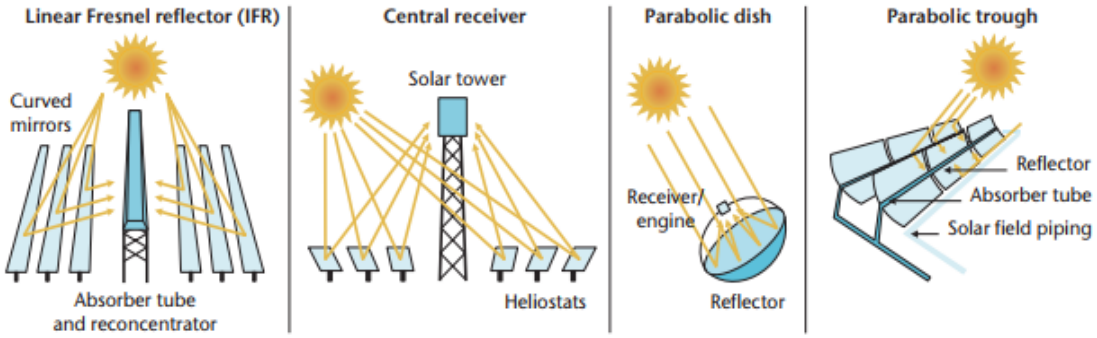

Figure 3. Main types of Concentrated Solar Power (CSP) technologies [2].

Contemporary commercial CSP plants typically imitate the design of the first commercial CSP plants built and commissioned in California in the 1980s. The design comprises of parabolic troughs to track the sun on one axis, concentrate the solar energy onto linear receiver tubes insulated in an evacuated glass envelope, heat the HTF (typically oil) to 390°C, and then transfer this heat to a conventional Rankine cycle.

Spain, on the other hand has a total installed capacity of 14 GWe of Solar Thermal electricity since 2006 and more than half the capacities built have been installed with thermal energy storage comprised of two tanks of molten salts, with 7 hours of nominal capacity (i.e. seven hours at full capacity of power block operation from full thermal storage when the sun does not shine). In the United States, three CSP plants were installed using Parabolic Trough (PT) technology with capacity of 280 MW (gross) – that were built and connected to the grid (in 2013 and early 2014). Of these, two CSP plants are not

integrated with TES: the Genesis and the Mojave projects in California. The third CSP plant is integrated with TES and is rated for six-hours of operation after sunset (or disruption in normal insolation): the Solana generating station in Arizona. As shown below in Figure 4, a typical two-tank Thermal Energy Storage (TES) platform for Concentrated Solar Power (CSP) plant consists of a central tower surrounded by an array of heliostats focusing the direct solar irradiation.

Figure 5 illustrates the variation of Daily Normal Irradiation (DNI) and the thermal flows from solar field to TES and power block for a day. Net electricity generated through the day is also included in the Figure 5. The storage capacity of a TES unit, typically measured in "GWh_{th}", is often expressed in "hours of storage", indicating the hours of operation of the power plant at rated capacity just from TES unit. The major advantage of a CSP with TES unit is its capability to decouple electricity generation from solar irradiation (and thus enhanced reliability for power generation integrated into the electricity grid). The TES unit provides a buffer capacity allowing for uninterrupted electricity production and eliminates short-term variations (which other solar conversion technologies exhibit on cloudy days).

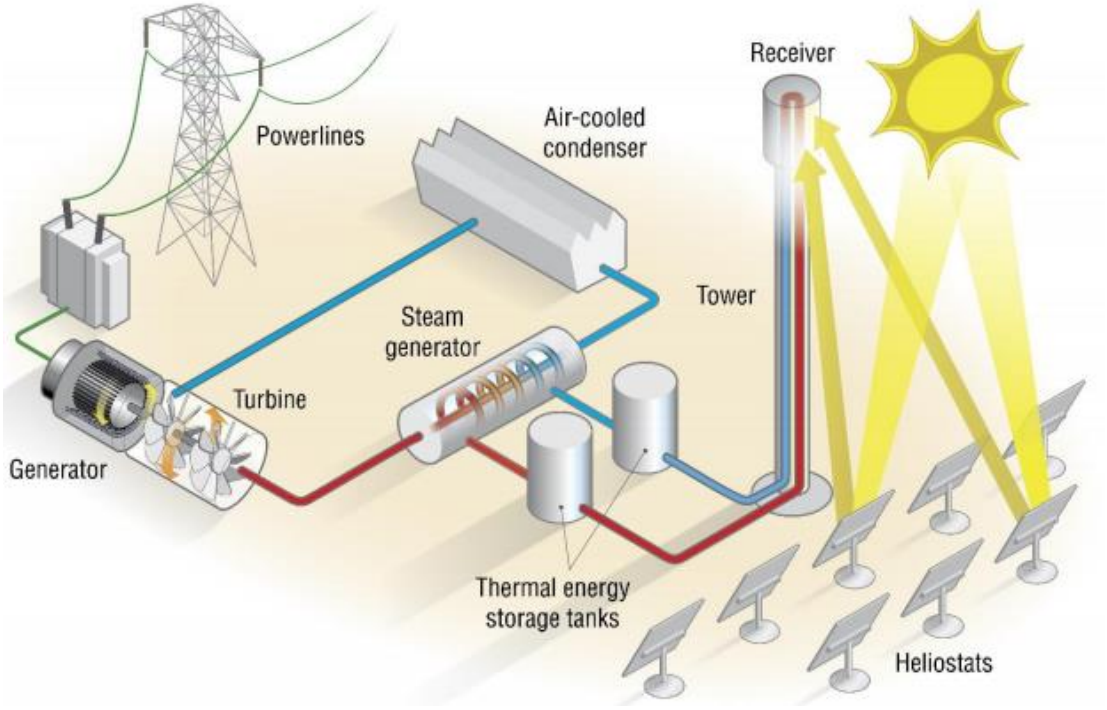

Figure 4. A Central Receiver System type Concentrated Solar Power (CSP) power plant with two tank liquid Thermal Energy Storage (TES) system [4].

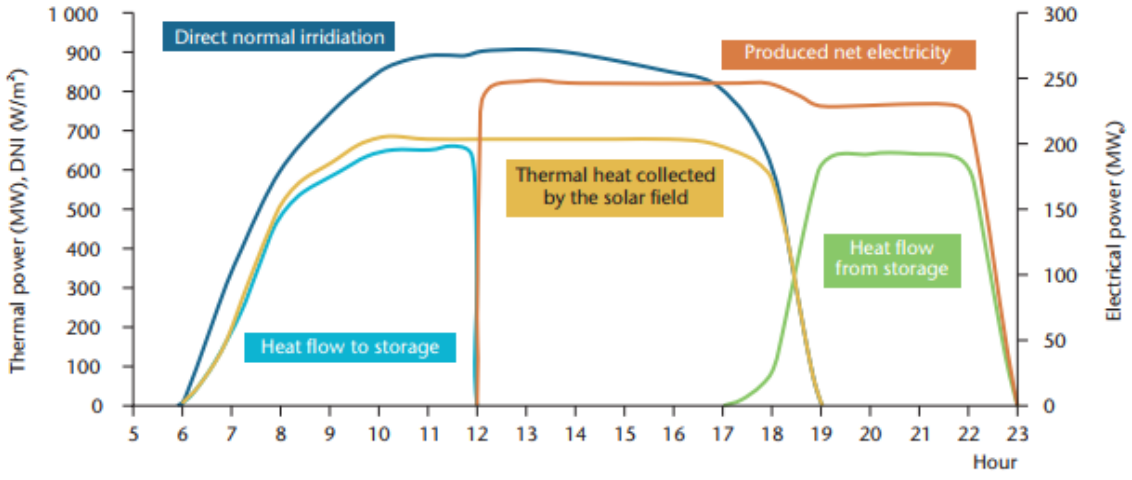

Figure 5. Graph detailing the thermal power (W/m^2) exchange between solar field, storage and power block, and electricity scale generation (250 MW_{net}) for a CSP plant with Thermal Energy Storage (TES) [2].

Table 1 Concentrating Solar Power (CSP) plants – Power Tower systems in development as of 2017.

Name	Location	Size (MWe)	Type, HTFs and Storage Medium	Status
Ashalim Plot B	Israel	121	Tower, Water/Steam, none	Under Construction
Atacama-1	Chile	110	Tower, Molten Salt (2-tank direct, 17.5 hours)	Under Construction
Aurora Solar Energy	Australia	135	Tower, Molten Salt (2-tank direct, 8 hours)	Under development
Copiapó	Chile	260	Tower, Molten Salt (2-tank direct, 14 hours)	Under development
Likana Solar Energy	Chile	390	Tower, Molten Salt (2-tank direct, 13hours)	Under development
NOOR III	Morocco	134	Tower, Molten Salt (2-tank direct, 7 hours)	Under construction
DEWA CSP Tower Project	United Arab Emirates	100	Tower, Molten Salt (2-tank direct, 15 hours)	Under development
Qinghai Gonghe	China	50	Tower, Molten Salt (2-tank direct, 6 hours)	Under development
Redstone Solar Thermal	South Africa	100	Tower, Molten Salt (2-tank indirect, 12 hours)	Under development
Shangyi	China	50	Tower, Molten salt (2-tank indirect, 4 hours)	Under development
SunCan Dunhuang	China	100	Tower, Molten Salt (2-tank direct, 11 hours)	Under Construction
Golden Tower	China	100	Tower, Molten Salt (2-tank direct, 8 hours)	Under development

Table 2 Concentrating Solar Power (CSP) plants – Power Tower systems operational as of 2017.

Name	Location	Size (MWe)	Type, HTFs and Storage Medium	Status
ACME Solar Tower	India	2.5	Tower, Water/Steam, none	Operational
Ivanpah Solar Electric	United States	392	Tower, Water/Steam, none	Operational
Jemalong Solar	Australia	1.1	Tower, Liquid Sodium (2-tank direct, 3 hours)	Operational
Jülich Solar	Germany	1.5	Tower, Air, Ceramic Heat Sink (1.5 hours)	Operational
Khi Solar One	South Africa	50	Tower, Water/Steam, Steam (2 hours)	Operational
Crescent Dunes Solar	United States	110	Tower, Molten Salt (2-tank direct, 10 hours)	Operational
Dahan Power Plant	China	1.0	Tower, Water/Steam, Saturated Steam/Oil	Operational
Planta Solar 10 (PS10)	Spain	11	Tower, Water, none	Operational
Gemasolar Thermosolar Plant	Spain	19.9	Tower, Molten Salt (2-tank direct, 15 hours)	Operational
Sierra SunTower	United States	5	Tower, Water, none	Operational
Sundrop	Australia	1.5	Tower, Water/Steam, none	Operational
Greenway CSP Mersin	Turkey	1	Tower, Molten Salt (3- phase tank natural circulation, 4 hours)	Operational

1.1.3 Technology status

As of 2016, Concentrating Solar Power (CSP) thermal power plants had a total generation capacity of 4815 MW across the globe. Spain alone has a total capacity of 2300 MW installed as of 2017. In United States, 11 CSP power plants were installed totaling a generation capacity of 1740 MW. The largest CSP plant in the world, Ivanpah Solar Power, is located in the Mojave Desert of United States, with a total capacity of 392 MW. In certain regions such as Chile and Australia, CSP plants are economically competitive compared to fossil fuels. Of the installed CSP plants around the globe, parabolic trough is the widely used technology. Tower systems started into commercial applications and Linear Fresnel systems are at transition to commercial application from demonstration phase.

1.2 Thermal Energy Storage (TES)

1.2.1 Background

Thermal Energy Storage (TES) units are like batteries and are employed to store excess thermal energy captured by the working fluid in a Concentrated Solar Power (CSP) plant. TES in CSP plants is achieved through either sensible heat or latent heat. Reduction in the cost of electricity generation in a CSP plant can be achieved by TES installation. The price reduction is however, dependent on storage capacity, technology employed for energy storage and site. Furthermore, energy storage in a CSP plant can provide Transmission and Distribution (T&D) congestion relief by matching energy demand with supply. As shown in Figure 6, the estimated thermal energy storage capacity in United States as of 2011 for utility scale applications is ~1000 MW.

Technology type (application)	Units (MW) in 2011
Ice storage (commercial buildings and district cooling)	1 000
Cold-water storage (district cooling)	355
Electric thermal storage (heating)	1 000

Figure 6. Estimated thermal energy storage capacity in United States as of 2011 [5].

Other advantages of integrating an energy storage system to a CSP plant include:

- Significant reduction in operational costs
- Improved overall efficiency in energy use
- Reduced CO_2 emissions
- Enhanced system reliability and performance

1.2.2 Types of TES systems in CSP plants

In a Concentrated Solar Power (CSP) power plant, the solar energy focused by the field of heliostats is collected in a receiver. The excess thermal energy collected during the day is stored in a Thermal Energy Storage (TES) unit. TES systems can be broadly categorized as active or passive systems.

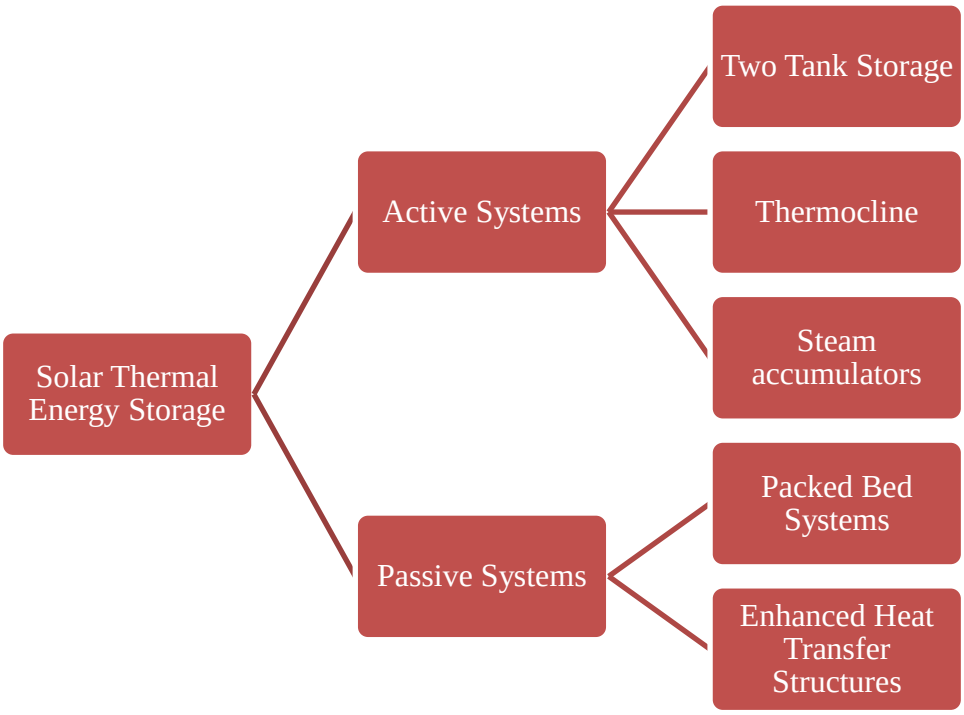

Figure 7 TES systems categorization according to Kuravi [6].

Active TES systems differ from passive systems in that the Heat Transfer Fluid (HTF) serves as the storage medium or transfers heat through forced convection to the storage medium. In passive systems, the HTF passes through the solid TES medium for charging and discharging.

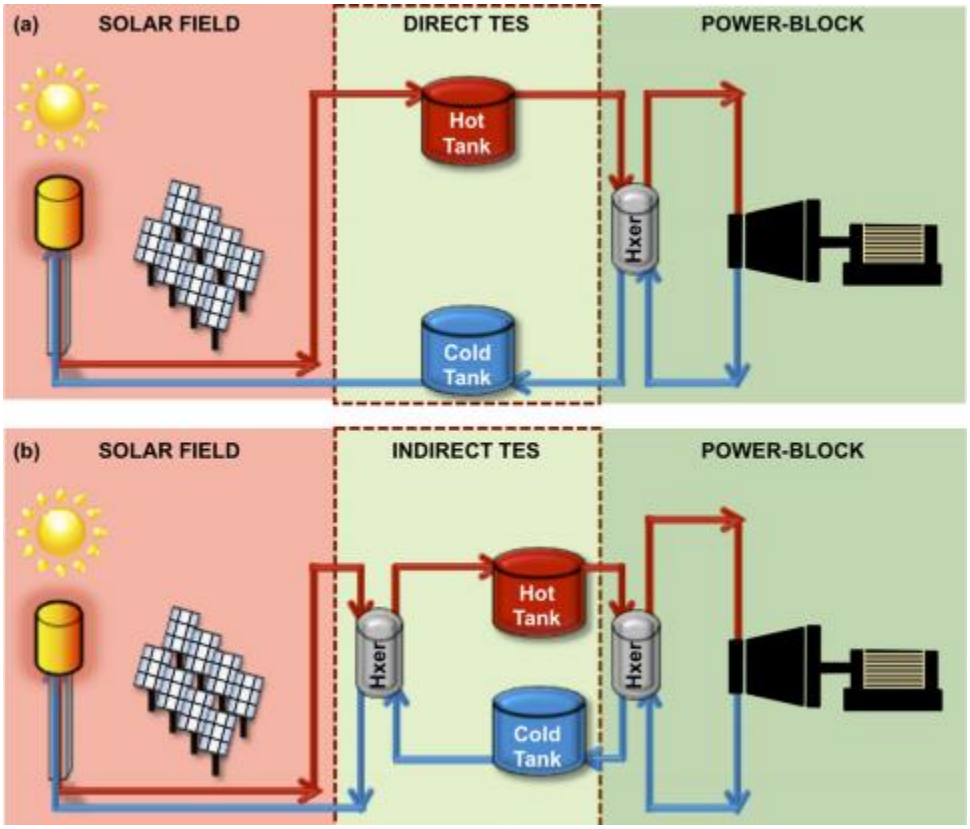

Figure 8. Illustrative view of (a) Two tank direct TES system employing single HTF and TES medium (b) Two tank indirect TES system utilizing different HTF in solar collector and TES medium [7].

An indirect two-tank TES system (Figure 8a) was first commercially installed in a parabolic trough CSP plant in Spain (Andasol I). The storage medium was a Potassium Nitrate/Sodium Nitrate eutectic (40:60 by mass fraction) called solar salt. Thermal Oil was employed as the HTF in the solar collector and an intermediate heat transfer to the storage medium is realized through a heat exchanger. This facility has the capability to store 8 hours of thermal energy for a 1010 MWh power plant.

As shown in Figure 8b, a direct two-tank TES system employs single working fluid as both HTF in the solar collector field and as storage medium in TES unit. This eliminates

the need for an intermediate heat exchanger enhancing operating efficiency and reducing capital cost. ARCHIMEDE CSP plant in Sicily, Italy and SEGS-1, a parabolic trough type CSP plant, in California, USA demonstrated the commercial feasibility of this technology using Thermal Oil and Molten Salts as TES medium, respectively.

Thermocline systems are single tank Thermal Energy Storage (TES) systems utilizing thermal stratification to store energy.

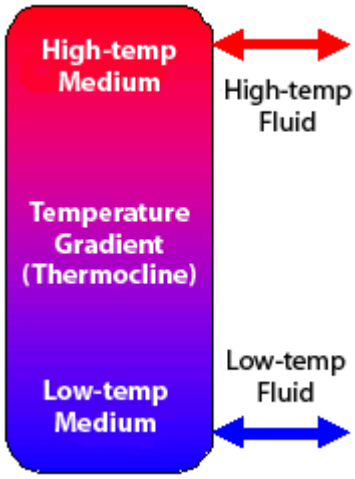

Figure 9 Schematic of a single-tank thermocline energy storage system [8].

As shown in Figure 9, a portion of the medium is at high temperature and a portion of medium is at low temperature separated by a thermocline. The working fluid after collecting solar energy rises in temperature, enters the TES unit at the top of tank and transfers thermal energy to the medium, and exits at the bottom of the tank. The thermocline moves downward as the medium is charged and as the medium discharges to provide energy to generate electricity thermocline moves upward. The advantage of using a single-tank include using a solid storage medium and reduction in capital cost compared to a two-tank system. Solar One power tower, a pilot project in California, USA

demonstrated the technical feasibility of this technology employing Mineral Oil as storage medium and steam as the HTF.

1.2.3 Challenges

For a TES unit to be effective, following design considerations are to accounted for

- TES medium to possess high energy density (high specific heat capacity)
- Maintain high heat transfer between HTF and storage media
- Chemical stability of TES medium and HTF at elevated temperatures
- Corrosion compatibility between HTF or TES medium and storage tanks
- Minimal thermal loss during storage

Most widely implemented TES configuration is two-tank indirect system. However, the obvious drawbacks of this configuration include high capital cost and lower plant performance. The use of single working fluid as both HTF and TES medium increases the temperature drop across turbine improving the power cycle efficiency and increases the operating temperature of HTF in the solar collector field. Molten salts are preferred in a direct two-tank TES system due to their higher operating temperature range enabling lower cost of power production. The cost of production decreases as the maximum operating temperature increases due to improved thermal efficiencies. However, molten salts are corrosive in nature and exhibit poor thermophysical properties. Furthermore, the melting temperatures of pure salts are too high - effectively reducing the operating temperature range of the HTF consequently impeding the operational efficiency of the plant. Hence, salt eutectics (homogenous mixtures of various salts) are ideal candidate as working fluid,

for both TES and HTF, as they possess significantly lower melting point and potentially reduce the cost of electricity production.

1.3 Molten Salt Eutectics

1.3.1 Introduction

Molten salts and their eutectics have been proposed as suitable candidate for HTF and TESF applications (to store thermal energy in the form of sensible heat). Single salt systems melt at higher temperatures and reduce the overall operating efficiency of the plant. Hence, molten salt eutectics, a mixture of salts with super-lattice between different components, confer lower melting temperatures than that of a single salt.

A vast majority of studies in the literature explored the thermo-physical properties of molten salt mixtures. Nitrate/ nitrite salts, carbonate salts and halides (chloride/fluoride) salts have been characterized extensively in the literature. Table 3 summarizes the melting points of various eutectic systems [9]. An ideal candidate as working fluid for HTFs and TES system in a CSP requires low melting point, low cost and minimal occupational hazard. For this reason, $NaNO_3$-KNO_3 eutectics (termed as Solar Salt) are extensively used in commercial CSP plants.

Table 3 Melting points of various salt eutectic systems (all units in Celsius) [9].

	NO_3	NO_2	CO_3	Cl	F
Na-K	220	228	710	685	710
Na-Li	192	150	496	557	649
Li-K	133	98	488	355	492
Na-K-Li	120		397	348	454
Na-K-Ca	133				

Currently, researchers have proposed the use of ternary or quaternary salt eutectic compositions with lower melting points than solar salt (220°C) to be employed in commercial power plants [10].

1.3.2 Convective heat transfer performance of molten salt eutectics

Over the last two decades, research activities involving molten salts have gained popularity as working fluids for high temperature processing applications and thermal-fluidics applications due to their stability at elevated temperatures, as well as their low vapor pressures, wide operating temperature ranges, minimal environmental footprint, ease of materials handling, low materials costs and safe operation. The applications of molten salts as engineering fluids is diverse, which includes solar power generation, advanced nuclear reactors (and in novel fuel cycles), chemical processing, and energy storage. In particular, Concentrating Solar Power (CSP) plants are progressively gaining commercial success around the world. As of 2016, CSP plants account for a total installed capacity of

4.8GW. A significant cost advantage for CSP plants is enabled by technologies that have afforded cheap Thermal Energy Storage (TES) platforms that in turn, have significantly enhanced the reliability of CSP plants for their integration into the power grids. TES platforms provide a means for matching the phase lag between the peaks in energy demand and the diurnal peaks in insolation (i.e., matching the demand peaks with the peaks in solar energy availability and solar power production) thereby balancing the demand and supply of power as well as for mitigating the load fluctuations on the electricity grid [11].

Furthermore, Oak Ridge National lab (ORNL) built the first Molten Salt Reactor (MSR) using a eutectic of fluoride LiF-BeF_2 (termed as FLiBe) with Uranium-233 as the fuel [12]. This experiment was the first demonstration of a new class of nuclear reactor with molten salts as the primary coolant (2LiF-BeF_2) and the fuel (LiF-BeF_2-ZrF_4-UF_4). Hence, detailed information regarding the transport properties and heat transfer behavior of molten salts systems or mixtures is essential for design of a CSP plant or advanced nuclear reactor system. Figure 10 indicates the record of publications over the last decade using a search term online for "molten salt heat transfer" on the ISI web of science publication database [13]. As seen from the plot, there is a general increasing trend in the "moving average" for the number of publications involving molten salt heat transfer as a research topic.

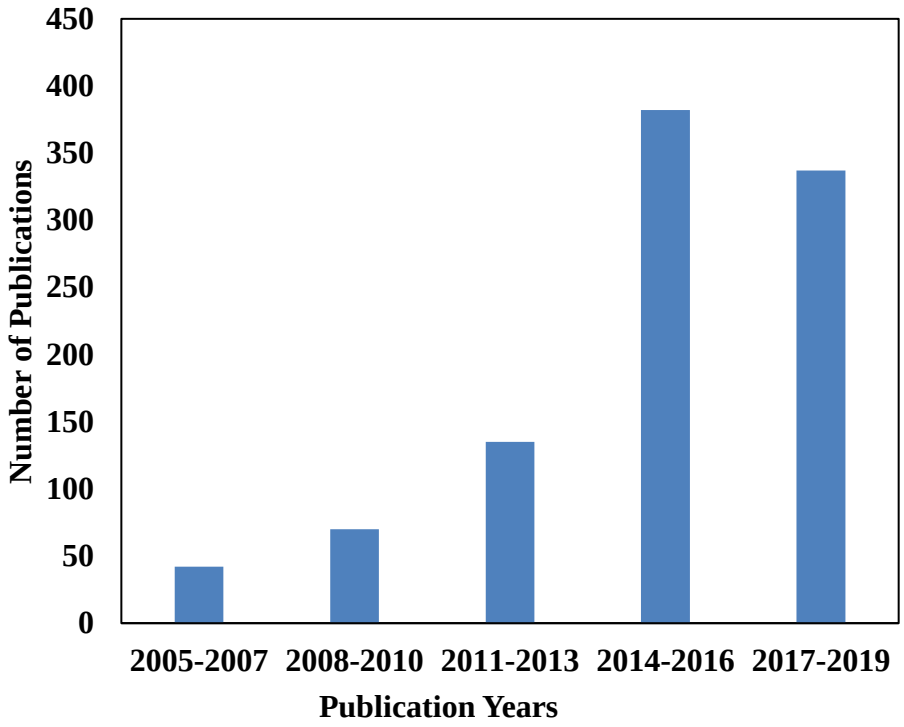

Figure 10 Publications trend on "molten salt heat transfer" since 2005 indexed in the Web of Science on February 2019.

Hoffman et. al. [14, 15] first reported the experimental measurement of heat transfer coefficient for molten salt eutectics flowing in a circular tube. The molten salts used in this study were FLiNaK (LiF-NaF-KF with a mole fraction of 46.5:11.5:42) and Hitec salt (KNO_3-$NaNO_2$-$NaNO_3$ with a mass fraction of 53:7:40). The test section was an Inconel tube with 4.5 mm inner diameter. Heat transfer experiments with FLiNaK as the working fluid were performed for a Reynolds number range of 2,400 – 9,500 in a heated tube with Prandtl number varying from 1.6 to 4. The results indicated that a fouling film formed on the inner surface for tests involving FLiNaK. As a result, the values for the total heat transfer were lower compared to the predictions obtained from Colburn equation [16]

(i.e., due to the additional interfacial resistance - arising from the formation of the fouling film). On the other hand, experimental results obtained from heat transfer experiments using Hitec Salt in a heated Inconel tube (for Reynolds numbers ranging from 4,850 to 24,700 and Prandtl numbers ranging from 4.2 to 9.1) were in good agreement with the predictions from standard correlations such as Dittus-Boelter and Colburn equations [16, 17] which are also listed in Table 4.

Cooke [18] measured the heat transfer coefficient of a fluoride eutectic (LiF-BeF_2-ThF_4-UF_4) flowing through a Hastelloy N circular tube. The flow regimes in these experiments involved laminar flows, transition flows and turbulent flows. The predictions from the standard correlations were in good agreement with the experimental measurements for laminar flow regime. The predictions from the standard correlations were higher than the experimental measurements for the transition and turbulent flow regimes. The authors argued that the effects of formation of a low-conductance interfacial film would be apparent in all flow regimes, but the experimental results show that a low-conductance interfacial film did not exist for laminar flow regimes. Since the laminar flow measurements were consistent with the model predictions, the authors argue that the improper application (or lack of precise material property data) of the molten sat samples, such as viscosity, caused erroneous estimates for the non-dimensional parameters (such as Re and Pr). Hence, the uncertainty in computing the non-dimensional parameters resulted in improper basis for comparisons in the transition and turbulent flow regimes.

Silverman et. al. [19] performed heat transfer measurements for two fluoride eutectics, LiF-BeF_2-ThF_2-UF_4 (with a mole fraction of 72-16-12-0.3) and $NaBF_4$-NaF

(with a mole fraction of 92-8), which are gaining popularity for applications as fuel salt and coolant salt, respectively, for advanced molten salt breeder reactors. The test section was a 12.7 mm outer diameter circular tube made from Hastelloy N. The experimental results from their measurements indicated that the heat transfer performance for both salts could be adequately predicted by Sider-Tate correlation for fully developed turbulent regime and Hausen correlation for transitional regime [20, 21]. Furthermore, the tests reveal extended transition regime for both salts presumably due to high viscosities and a large negative temperature coefficient of viscosity.

Bin et. al. [22] conducted turbulent convective heat transfer experiments using $LiNO_3$ in stainless steel concentric tube. Molten $LiNO_3$ flowing through the inner tube was cooled by flowing mineral oil through the outer tube. The predictions from Dittus-Boelter and Colburn equation, were higher than the experimental data, by as much as 25% and 18%, respectively. This discrepancy was attributed to the large variation of viscosity of the molten salt with temperature. However, both Dittus-Boelter and Colburn correlations do not account for the variation of the thermo-physical properties. On the other hand, the experimental data was in good agreement with Sider-Tate and Hausen correlations [20, 21]. Employing the same experimental apparatus described in [22], Wu et. al. [23] performed heat transfer measurements of $LiNO_3$ in laminar-turbulent transition regime. The authors claimed that the experimental data were within ±15% of the values predicted by both the Hausen and the Gnielinski correlations [20, 24]. The combined results from both studies validate the heat transfer performance of $LiNO_3$ flowing in a Stainless Steel pipe for a broad range of flow regimes, for Reynolds number ranging from 4000 to 45000.

However, the engineering applicability of a single component salt system might be limited, particular for a costly alkali nitrate - such as $LiNO_3$, as a Heat Transfer Fluid (HTF) or as a Thermal Energy Storage (TES) medium. Using the same experimental apparatus and the same circular stainless steel test section, as described in references [22, 23], Wu et. al. [25] performed forced convective heat transfer measurements for Hitec salt in a concentric tube, for both transition and turbulent flow regimes. The authors claimed that the heat transfer data obtained from these experiments are within ±15% of the values predicted by the Sider-Tate correlation and are within ±25% of the values predicted from the Gnielinski correlation [24]. Furthermore, combining their experimental results and the experimental convective heat transfer data for five different kinds of molten salts from [19, 14, 15, 22] the authors propose a general correlation for transition flow and fully turbulent flow, which is also listed in Table 4.

Yang et. al. [26] investigated the heat transfer enhancement accruing from using a spiral tube instead of a smooth tube for receiver tubes in a Concentrated Solar Power (CSP) plant receiver. A ternary nitrate eutectic of KNO_3-$NaNO_2$-$NaNO_3$ (Hitec salt at 53:7:40 by mass fraction) was the working fluid. The authors also used a heated 316L Stainless Steel spiral tube as the test section. The experimental results indicate that the heat transfer performance can be enhanced by as much as 3 times in a spiral tube, in comparison to that of a smooth tube, for Reynolds number ranging from 10,000 to 55,000.

Lu et. al. [27, 28] performed a series of forced convective heat transfer experiments to investigate the efficacy of both spirally grooved and transversely grooved tubes compared to that of smooth tubes. The working fluid was Hitec salt. The test section was

fabricated using stainless steel tubes. In general, both transverse and spiral grooves enhanced heat transfer by as much as ~1.4 times and ~1.5 times, respectively (compared to that of smooth tubes). Furthermore, increase in groove height enhanced heat transfer.

The maximum recommended operating temperature of Hitec salt is 538°C and the salt undergoes a slow decomposition due to conversion of nitrite ions to nitrate - ions for temperatures between 454°C and 538°C [29]. Hence, it is essential to limit the operating temperature to 454 °C for ensuring reliability during operation and obtaining optimal thermal performance. The deterioration of heat transfer performance is reported in [28] when the inlet temperature of the salt was between 487 – 493 °C and the heat transfer performance was reported to worsen rapidly as the wall temperature values were increased from 525 °C to 597 °C, resulting in localized decomposition of the salt samples in the vicinity of the hot walls (or enhanced temperature regions within the flow conduits). However, the authors did not perform measurements for the increase in drag as a result of vortices spawned from within the grooves. Also, the authors did not perform measurements for the increase in pumping power requirements caused by the grooves. Hence, comprehensive investigations are needed for the determination of the efficacy of passive heat transfer enhancement techniques (such as spiral or transverse grooves) based on pumping power consumed per unit heat transfer area.

Chen et. al. [30] rebuilt the experimental apparatus described in [22] by adding differential pressure gauges at the inlet and outlet of the test section and measured the heat transfer performance of Hitec salt flowing in a heated tube with transverse grooves. The experiments were performed for inlet temperatures ranging from 210 °C to 400 °C, with

Reynolds numbers exceeding 10,000 (thus ensuring fully developed turbulent flow conditions were achieved in these tests). The test sections included tubes with three different types of grooves, with transverse pitch of 5 mm, 9 mm and 16 mm. The experimental results indicate that the heat transfer enhancement achieved by the introduction of grooves (compared to that of a smooth pipe) was accompanied by significant increase in drag coefficient. For tested Reynolds number range of 10000 – 24000, on average, increments in the values of the drag coefficient ranged from 8%, 23% and 68%; for a pitch of 16 mm, 9 mm and 5 mm, respectively. The corresponding increase in heat transfer was 9%, 45% and 65% for a pitch of 16 mm, 9 mm and 5 mm, respectively. The authors suggested that the optimal pitch is 9 mm for transverse grooves, taking into account the increase in pumping power requirements resulting from these grooves.

Lu et. al. [31] investigated the heat transfer performance of Hitec salt in a double pipe steam generator with water/steam flowing through the inner tube and molten salt flowing in the annular passage with a cooled wall. The experimental flow conditions ranged from molten salt temperatures of 250 °C – 400 °C and Reynolds number ranging from 4000 – 10000. The authors mentioned that preheated water was pumped through the inlet tube (as a result, a water and steam mixture was used as the cooling medium). However, no details on mass flux, exit vapor fraction or inlet flow conditions were provided. The experimental data for the heat transfer coefficients for the molten salt side were found to be significantly higher than that predicted from the single-phase Gnielinski correlation [24], which is also listed in Table 4.

Chen et. al. [32] investigated the heat transfer performance of Hitec salt in a salt-to-oil concentric tube heat exchanger with hot salt flowing through the inner tube being cooled by oil flowing in the outer tube. The Reynolds number on the molten salt side ranged from 10,000 to 50,000 and the Prandtl number ranged from 11 to 27. The authors provide no additional details regarding the flow conditions on the oil side. The experimental results indicate the measured heat transfer coefficient on the molten salt side were within ± 7% of the values predicted by the Gnielinski correlation and within ±8% from the values predicted by the Sider-Tate correlation in fully turbulent regime [21, 24].

To enhance the heat transfer performance, Chen et. al. [33] modified the experimental apparatus of [32] by replacing the inner tube with a transversely grooved tube. The hot salt flowing through the transversely grooved inner tube was cooled by oil flowing through the outer tube. The Reynolds number on the salt side ranged from 300 to 60,000 and Prandtl number ranged from 11 to 27. The authors reported 60% enhancement in the values of the heat transfer for the grooved tubes compared to that of the smooth tubes. However, measurements were not performed for determining the level of increase in pumping power due to the introduction of the grooves.

Majority of reports in open literature on heat transfer performance of molten salts are concerned with straight or annular tubes. Reports on experimental investigation of heat transfer performance of molten salts in heat exchangers are limited. For example, a molten salt heat exchanger in an advanced Molten Salt Reactor (MSR) is used to take away heat from the primary coolant to secondary coolant circuit. Similarly, in a Concentrated Solar Power (CSP) plant typically a molten salt-based shell and tube heat exchanger is used to

transfer the stored heat to vaporize superheated steam for power generation. Hence, it is crucial to ensure their validity - when the traditional correlations (that are typically used for estimating the heat transfer performance of normal working fluids such as Oil, Water etc., as listed in Table 4.) are used for molten salt systems, especially for modeling tasks performed with the aim of designing and optimizing the overall plant efficiency.

He et. al. [34] performed experiments to investigate the heat transfer performance of Hitec salt in a shell-and-tube heat exchanger without baffles. These experiments were performed by varying the inlet temperatures and flow velocities. The molten salt was pumped in the shell (i.e., external to the tube bundle) with effective Reynolds number ranging from 400 – 2300. Preheated water was pumped through the seven tubes. The measured values of Nusselt number on the molten salt side ranged from 20 - 100 based on the hydraulic diameter of the flow channel (which is computed based on the area of cross-section and the wetted perimeter) [17]. The experimental heat transfer coefficient on the molten salt side was found to be 3 to 5 times of the values predicted from the Sider-Tate correlation [21]. The heat transfer enhancement was attributed to the thin developing boundary layer due to the tube bundle structure in the shell side.

Du et. al. [35] investigated the heat transfer performance of Hitec salt in transitional flow regime in a shell and tube heat exchanger with segmented baffles. The molten salt was pumped through the shell side and around the tube bundles with cooling oil flowing through the tubes. The measured heat transfer coefficient on the molten salt side agreed with traditional Kern correlation [36] with a maximum deviation of 7.1%, which is also listed in Table 4.

Qian et. al. [37] studied the heat transfer performance of Hitec salt in a gas cooled shell and tube heat exchanger (finned tubes) with salt flowing internally through the tubes. The tests ranged from laminar flow to transition flow regimes (Reynolds number ranged from 987 to 12,000) and Prandtl number ranged from 9.8 to 18.9. The experimental data for Nusselt number was found to be within ± 15% of the predicted values that were obtained from the correlation proposed by Wu et. al. in [25], which is also listed in Table 4. One of the concerns for employing segmented baffles in shell side of a molten salt based shell and tube heat exchanger - is the potential for salt solidification in the recirculation "dead" zone. This can compromise the reliability of these devices. Hence, Qiu et. al. [38] investigated the heat transfer performance of Hitec salt in a rod baffled shell and tube heat exchanger, with salt flowing along the tubes rather than across tubes, in a segmented baffle shell and tube heat exchanger. Hot salt flowing through the shell side was cooled by flowing oil through the tube side. Experimental measurements for heat transfer coefficient were performed for a Reynolds number (computed based on hydraulic diameter) range of 2650 to 12,500 on the salt side. The measured heat transfer coefficient on salt side was compared with an existing correlations proposed by Phillips Petroleum Company [39] and Dong et. al. [40] for low temperature working fluids. The results indicate that the measured values of Nusselt number, were on average, within ±15% of the predicted values that were obtained from both correlations.

For successful long-term deployment of molten salts as Heat Transfer Fluid (HTF) or as a Thermal Energy Storage (TES) media it is essential to characterize the heat transfer performance over extended periods of time while monitoring for any degradation in

performance, especially arising from any corrosion and fouling that may occur on the heat exchanger materials, surfaces or pipes and conduits. Yu-Ting Wu et. al. [41] investigated the heat transfer performance of a quaternary nitrate eutectic of KNO_3-$NaNO_3$-$LiNO_3$-$CaNO_3$▪$4H_2O$ (with a mass ratio of 6:1:2:2) with a melting temperature of 86°C in a lab-scale parabolic trough solar collector system. The authors reported an operating period of 1,000 hours. The experimental apparatus consisted of a double pipe salt-to-water heat exchanger. The high temperature salt flowing though the inner tube was cooled by water flowing through the outer tube. The tests were performed for Reynolds number ranging from 10,000 to 21,000 and Prandtl number ranging from 9.5 to 12.2. The experiments indicate that the heat transfer performance of the quaternary salt could be adequately predicted by Sieder-Tate and Gnielinski correlations [24, 21].

Table 4. Summary of experimental studies on the convective heat transfer performance of molten salts.

Authors	Type of Investigation	Test Section	Test Section Dimension	Flow Conditions	Working Fluid	Remarks	Nusselt number (Nu) Range
Hoffman H. W. & Lones J. (1955)	Forced convection heat transfer in a circular tube	Nickel, Inconel and Stainless Steel	3mm (nickel), 4.4mm (Inconel) and 4.5mm (Stainless Steel) ID	Re: 2428 to 9536;Pr: 1.6 to 4	Flinak (LiF-NaF-KF)	Good agreement with Colburn correlation	Nu: 11.5 to 102
Hoffman H. W. & Cohen S. I. (1960)	Forced convection heat transfer in a circular tube	Inconel	4.5 mm ID	Re:4850 to 24710; Pr: 4.2 to 9.1	Hitec Salt (53% KNO_3 + 40% $NaNO_2$ + 7% $NaNO_3$)	Good agreement with Colburn correlation	Nu: 35 to 125
Cooke J.W. & Cox B. (1973)	Forced convection heat transfer in a circular tube	Hastelloy N	4.5mm ID	Re: 400 to 30600; Pr	LiF-BeF_2-ThF_4-UF_4	Good agreement with Sieder-Tate and Hausen correlations	Nu: 6.5 to 138
Silverman et. al. (1976)	Forced convection heat transfer in a circular tube	Hastelloy N	12.7mm ID	LiF-BeF2-ThF4-UF4 (Re: 1542 to 14210; Pr: 6.6 to 14.2) & NaBF4-NaF (Re: 5104 to 44965; Pr: 4.89 to 5.64)	LiF-BeF_2-ThF_4-UF_4 & $NaBF_4$-NaF	Good agreement with Sieder-Tate and Hausen correlations	LiF-BeF_2-ThF_4-UF_4 Nu: 10 to 103 & $NaBF_4$-NaF Nu: 30 to 260

Table 4. Continued

Authors	Type of Investigation	Test Section	Test Section Dimension	Flow Conditions	Working Fluid	Remarks	Nusselt number (Nu) Range
Bin L. et. al. (2009)	Forced convective heat transfer in a concentric circular tube	Stainless Steel	20mm ID	Turbulent regime (Re: 17,000 to 45,000; Pr: 12.7 to 14.7)	$LiNO_3$	Good agreement with Sieder-Tate, Petukhov, and Hausen correlations	Nu: 70 to 140
Yu-Ting W. et. al. (2009)	Forced convective heat transfer in a concentric circular tube	Stainless Steel	20mm ID	Transition regime (Re: 4100 to 9850; Pr: 15 to 18.4)	$LiNO_3$	Good agreement with Gnielinski, and Hausen correlations	Nu: 42 to 83
Yang M. et. al. (2010)	Comparison of forced convective heat transfer coefficient between smooth and spiral tube	Stainless Steel	16mm ID	Turbulent regime (Re: 10,000 to 50,000; Pr: 4 to 5.6)	Hitec Salt (53% KNO_3 + 40% $NaNO_2$ + 7% $NaNO_3$)	Nusselt number for spiral tube was three times that of smooth tube on average	Smooth Tube Nu: 180 to 350; Spiral Tube Nu: 350 to 1150
Yu-Ting W. et. al. (2012)	Forced convective heat transfer in a concentric circular tube	Stainless Steel	20mm ID	Re: 3184 to 34,861; Pr: 8.3 to 23.9	Hitec Salt (53% KNO_3 + 40% $NaNO_2$ + 7% $NaNO_3$)	Good agreement with Gnielinski, Sieder-Tate, and Hausen correlations	Nu: 100 to 350

Table 4. Continued

Authors	Type of Investigation	Test Section	Test Section Dimension	Flow Conditions	Working Fluid	Remarks	Nusselt number (Nu) Range
Jianfeng L. et. al. (2013)	Comparison of forced convective heat transfer coefficient between smooth and spiral tube	Stainless Steel	16mm ID	Re: 5000 to 15000; Pr: 13.5 to 15.2	Hitec Salt (53% KNO_3 + 40% $NaNO_2$ + 7% $NaNO_3$)	Nusselt number for spiral tube was 1.4-1.7 times that of smooth tube on average	Spiral Tube Nu: 130-230
Chen C. et al. (2013)	Comparison of forced convective heat transfer coefficient between smooth and transversally corrugated tube	_	16mm ID	Re: 10000 to 35000; Pr: 4.68 to 16.4	Hitec Salt (53% KNO_3 + 40% $NaNO_2$ + 7% $NaNO_3$)	5% to 68% enhancement in heat transfer	Smooth Tube Nu: 100 to 210;Corrugated Tube: 100 to 240
Jianfeng L. et. al. (2013)	Forced convective heat transfer in an annular passage	_	Outer tube: 57mm; Inner tube: 19mm	Re: 4000 to 10000; Pr: 4.9 to 9.4	Hitec Salt (53% KNO_3 + 40% $NaNO_2$ + 7% $NaNO_3$	Enhanced heat transfer in annular passage compared to smooth tube for same flow conditions	Nu (Hydraulic diameter) 75 to 225

Table 4. Continued

Authors	Type of Investigation	Test Section	Test Section Dimension	Flow Conditions	Working Fluid	Remarks	Nusselt number (Nu) Range
Jianfeng L. et. al. (2013)	Forced convective heat transfer in transversely grooved tube	Stainless Steel	16mm ID	Re: 10000 to 40000; Pr: 4 to 11.8	Hitec Salt (53% KNO_3 + 40% $NaNO_2$ + 7% $NaNO_3$	Enhanced heat transfer for grooved tube (1.2 - 1.65 times) compared to smooth tube.	Smooth tube Nu: 80 to 220; Grooved tube Nu:120 to 360
Jianfeng L. et. al. (2014)	Forced convective heat transfer in a vertical annular duct with cooled wall	_	Outer tube: 57mm; Inner tube: 19mm	Re: 3000 to 16000; Pr: 4.8 to 7.6	Hitec Salt (53% KNO_3 + 40% $NaNO_2$ + 7% $NaNO_3$)	Enhanced heat transfer in annular passage compared to smooth tube for same flow conditions	Nu (Hydraulic diameter) 60 to 300
He S. et. al. (2014)	Forced convective heat transfer outside a tube bundle of heat exchanger	Stainless Steel tube bundle	Shell Diameter: 133mm; Tube Bundle: #7 tubes, 25mm Diameter	Re: 400 to 2300; Pr: 4.6 to 11.8	Hitec Salt (53% KNO_3 + 40% $NaNO_2$ + 7% $NaNO_3$)	Correlation for Nusselt number proposed through experimental data fitting	Nu (Hydraulic diameter) 20 to 100

Table 4. Continued

Authors	Type of Investigation	Test Section	Test Section Dimension	Flow Conditions	Working Fluid	Remarks	Nusselt number (Nu) Range
Xiao P. et. al. (2015)	Forced convective heat transfer in a helical annular duct	_-	Inner Diameter:6mm, Outer Diameter: 19mm	Heat Exchanger-1 Re: 200-20000; Pr: 13.5 to 15.2; Heat Exchanger-2 Re: 500-40000	Hitec Salt (53% KNO3 + 40% NaNO2 + 7% NaNO3)	_-	-
Yu-Ting W. et. al. (2015)	Forced convective heat transfer in a parabolic trough solar collector system	Stainless Steel 304L	Outer tube: 57mm; Inner tube: 32mm	Re: 10000 to 21000; Pr: 9.5 to 12.2	Quaternary nitrate eutectic of KNO_3-$NaNO_3$-$LiNO_3$-$CaNO_3$▪$4H_2O$	Measured heat transfer coefficient within ±10% of predictions from Sieder-Tate correlation	Nu: 110 to 196
Chen Y. S. et. al. (2016)	Forced convective heat transfer in a concentric circular tube	_-	Outer tube: 39mm; Inner tube: 20mm	Re: 10000 to 50000; Pr: 11 to 27	Hitec Salt (53% KNO_3 + 40% $NaNO_2$ + 7% $NaNO_3$)	Good agreement with traditional correlations	Nu: 130 to 300

Table 4. Continued

Authors	Type of Investigation	Test Section	Test Section Dimension	Flow Conditions	Working Fluid	Remarks	Nusselt number (Nu) Range
Du B-C. et. al. (2017)	Convective heat transfer performance in a shell-and-tube heat exchanger with segmental baffles	–	Shell Outer Diameter: 108mm, Inner Diameter: 100mm; 18 segmental baffles. Length of HX 1.95m	Re: 6142 to 9125; Pr: 19 to 22	Hitec Salt (53% KNO_3 + 40% $NaNO_2$ + 7% $NaNO_3$)	Maximum enhancement of 26% in heat transfer performance with segmental baffles in shell side	Nu (Hydraulic diameter) 111 to 143
Qian J. et. al. (2017)	Convective heat transfer performance in a finned tube shell-and-tube heat exchanger	Stainless Steel	Tube inner diameter 13.75mm, Outer diameter 10.45mm	Re: 2500 to10000; Pr: 9.8 to 18.9	Hitec Salt (53% KNO_3 + 40% $NaNO_2$ + 7% $NaNO_3$)	Experimental values ± 15% of the computed values from the correlation proposed in [25]	Nu: 100 to 190
Satoh T. et. al. (2017)	Convective heat transfer performance in a sphere packed pipe	Stainless Steel 304	Inner Diameter 19mm	Re: 3500 to 12000; Pr: 9.5 to 12.2	Hitec Salt (53% KNO_3 + 40% $NaNO_2$ + 7% $NaNO_3$)	Measured Nu with 25% of modified Petukhov equation	–

Table 4. Continued

Authors	Type of Investigation	Test Section	Test Section Dimension	Flow Conditions	Working Fluid	Remarks	Nusselt number (Nu) Range
Qiu Y. et. al. (2018)	Convective heat transfer performance in a rod baffled shell-and-tube heat exchanger	Stainless Steel 316	Shell side inner diameter 100mm, Length	Re: 2697 to 12517; Pr: 14.2 to 23.3	Hitec Salt (53% KNO_3 + 40% $NaNO_2$ + 7% $NaNO_3$)	Good match of experimental data with existing correlations	Nu (Hydraulic diameter) 60 to 200
Chen Y. S. et. al. (2018)	Forced convective heat transfer in a concentric circular tube with transverse grooves	Inconel 600	Outer tube: 39mm; Inner tube: 20mm	Re: 300 to 60000; Pr: 11 to 27	Hitec Salt (53% KNO_3 + 40% $NaNO_2$ + 7% $NaNO_3$)	Average enhancement of 1.6-1.8 compared to smooth tube	Nu: 70 to 1000

1.3.3 Applications beyond solar energy

In the last decade, there has been a rapid increase in interest for high temperature (300°C to 1000°C) liquid coolants for nuclear, hydrogen production systems, enhanced oil recovery and shale oil processing industries. Such high temperature liquid coolants enable operation of high-temperature reactors for efficient electricity production than conventional steam cycles (this also obviates nuclear proliferation issues). Recent advances in gas-turbine technology have enabled the conversion of heat efficiently to electricity (currently steam cycles are limited to ~550°C) - paving the way for high-temperature reactors. Molten Salt Reactors (MSR) with fuel dissolved in the liquid molten salt has received attention due to improved economics of such MSR reactors compared to current helium or sodium cooled high-temperature systems [8]. Liquid salt coolant systems operate at atmospheric pressure, whereas helium cooled high-temperature reactors operate at high pressures. Potential economic advantages from scaling down the size of piping, valves and heat exchangers from shifting to liquid salt coolant systems are reported in [42]. In general, typical requirements for molten salts used in MSR as heat transfer medium and coolants (HTF) are:

- Excellent thermal stability and chemical compatibility
- Low vapor pressure and corrosivity
- Good heat transfer and fluid flow characteristics
- Acceptable accident or spill performance

For this reason, fluorides are ideal candidates for nuclear applications compared to nitrates, nitrites, and carbonates. Another major advantage of fluorides is their capability to hold high concentrations of uranium and thorium. However, an enormous amount of work is necessary in addressing the chemistry of nuclide decay chains and behavior of each species in molten salt media.

1.3.3.1 Molten Salt Reactor (MSR)

Currently, a total of 375GWe is generated from nuclear power over 31 countries with about 435 nuclear power plants in operation [65]. Furthermore, nuclear power contributes about 11% of total global electricity generation [65]. Light Water Reactors (LWR) are the most common configuration of reactor type employed commercially. The current design of the nuclear reactor's did not change much from the 70's owing to high costs associated with research and development, cost of building and regulation. Generation IV International Forum, a coalition formed by 13 countries decided to develop six reactor designs as shown in Figure 11 [77].

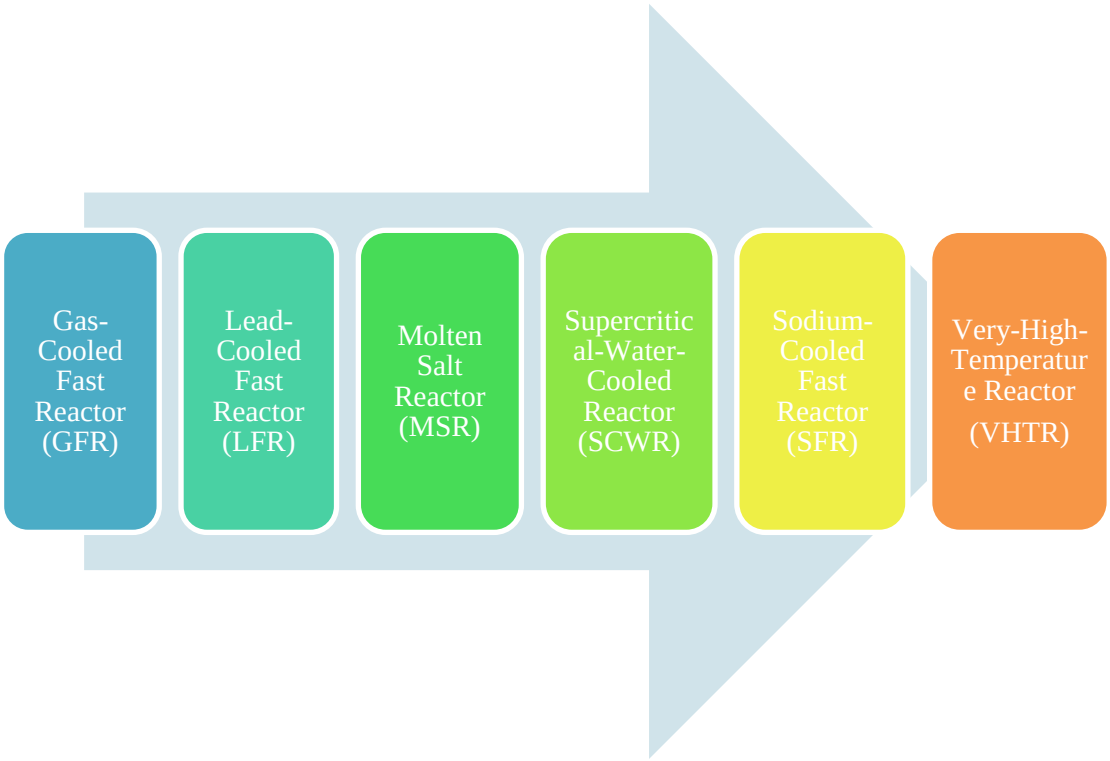

Figure 11. Generation IV advanced nuclear designs under development in Gen IV International Forum [77]

As shown in Figure 11, six reactor designs were chosen from evaluated 130 reactor concepts for further development. Of the six reactor designs, Molten Salt Reactors (MSR) uses a molten fluoride salt with dissolved fuel in its core. Although, the reactor design was explored 50 years ago, the current interest lies developing a fast reactor as an alternative for solid-fueled fast neutron reactors. Key areas of research include safety, advance salt redox potential measurement and control tools in order to limit corrosion rate of structures.

1.3.3.2 Enhanced Oil Recovery

The petroleum industry is increasingly moving towards heavier fossil feedstock's such as heavy oils and shale oil as the light crude oil reserves shrink. In most cases, the use of fossil fuels to power the conversion process produces exponentially more greenhouse gases. In certain cases, the energy requirement for liquefaction is twice compared to the energy value of liquid fuel produced.

Typically, combustion of oil or natural gas generates on-site steam. Researchers explored the idea of integrating nuclear power with oil processing plants for years. Although, proposed configurations had merits, they could not achieve the required conditions at the steam outlet. Molten Salt Reactors (MSR) as discussed earlier are generation IV fission nuclear reactors and can be used for safe, economical and viable heat generation. Integration of an MSR for oil development would drop significantly the greenhouse gas production during the refinement process and would be able to assist in the production of hydrogen through bitumen upgrading. The key hindrance for deployment of such a hybrid oil processing plant is lack of regulatory support for MSRs as of 2018.

The official estimate of recoverable oil in Eagle ford formation in Texas and Bakken shale formation in North Dakota are 3.35 billion and 2 to 4 billion, respectively [96]. The term “shale oil” is improperly referred to oil in “tight formations”. The oil in tight reserves, such as Eagle Ford and Bakken Shale, is extracted from shale reserves and the advances in fracking made it possible to recover oil form these formations economically. On the other hand, reserves such as Green River consists of oil shale like rock. Unlike the hydrocarbons in tight oil formations such as Eagle Ford or Bakken the hydrocarbons in Green River resemble coal than oil. To convert this into liquid fuel, significant amount of heat addition is required to the oil shale.

An economical conversion technique of this oil shale to liquid fuel is to use high temperature molten salts to provide direct heat. Concentrated Solar Power (CSP) or Molten Salt Reactor (MSR) can be coupled with the oil field to achieve the desired temperatures within the oil shale. Moreover, steam based thermal recovery processes involves steam injection into heavy oil formations to make the oil less viscous and easy to recover.

1.3.4 Challenges

As detailed in TES analysis, two tank-direct TES systems are widely used configurations due to potential capital savings eliminating intermediate heat exchanger. Furthermore, commercially used molten salt in CSP plants is Solar Salt (eutectic mixture of Sodium nitrate and Potassium nitrate, 60:40 by mass fraction) and has high freezing temperature of 220°C. This in turn increases the operational cost, as special care needs to be taken in the form of freeze protection (heat tracing) and maintenance to prevent freezing of salt in pipes during night.

Furthermore, engineering analysis performed by Kearney *et al.* [43] suggested that use of molten salts as HTF in a trough solar field is economically viable only with a coupled Thermal Energy Storage (TES) system. One potential solution is to enhance the specific heat capacity of the molten salt used as TES medium. The temperature drop across the turbine dictates the minimum heat capacity of the TES medium. Increasing the temperature drop across the turbine increases the overall plant efficiency significantly and reduces the cost of electricity production. Hence, given the potential savings and benefits of enhancing the specific heat capacity, several studies attempted to enhance the energy storage density by doping the TES medium with tiny fractions of nanoparticles. However, for this technology to be potentially commercialized, significant progress needs to be made for economically viable synthesis of molten salt nanomaterials.

1.4 Nanofluids

Stable homogeneous suspensions of nanoparticles in liquid solvents are called nanofluids. Various nanofluids were explored by Choi [44] in early 1990s, as heat exchanging fluids for several industrial applications. Nanofluids with enhanced thermal transport properties have been envisioned for applications as efficient coolants in solar collectors, electronics cooling systems, nuclear reactors, industrial process heating and cooling systems. Hence, numerous researchers investigated the heat transfer performance and flow characteristics of nanofluids by doping commonly used heat transfer working fluids such as water and ethylene glycol with different types of nanoparticles (metallic and non-metallic). Although literature is awash with controversial and contradictory studies about the thermo-physical properties of nanofluids, many researchers concur

that minor variation in synthesis protocol can significantly affect the enhancement of material properties. Hence, the various synthesis protocols are discussed next.

1.4.1 Synthesis

Nanofluid synthesis techniques are broadly classified as one-step or two-step methods. In a typical two-step method, nanoparticles procured directly from commercial vendors are dispersed into base fluid. Due to its simplicity, two-step method is extensively used. Adjusting the synthesis conditions (such as pH, temperature, Ultra sonication time etc.) can result in desired particle size distribution in the solvent. The high surface energy of nanoparticles results in particle agglomeration (caused by Brownian motion). Hence, nanofluids synthesized through two-step method suffer from stability issues. Techniques such as ultra-sonication, control of pH through additives and use of surfactants are employed to minimize particle agglomeration in the solvent. Ultra sonication is effective only for a limited time, as particles tend to agglomerate under gravity. Other techniques such as pH control and surfactants alter the chemical composition of the solvent. To conclude, nanofluids prepared through two-step methods are relatively unstable.

On the other hand, one-step method includes the *in-situ* generation and dispersion of nanoparticles in the solvent phase. Physical or chemical techniques are employed to generate and disperse nanoparticles in a single step. Physical techniques include vapor condensation of target metal in base solvent, submerged arc spray synthesis and laser ablation. The particle size distribution and size is precisely controlled by controlling the vapor condensation rates. However, these methods are not suitable for mass production. To the contrary, chemical approach involves precursor addition to the base solvent and reaction initiation through microwaves or thermal energy

to yield nanoparticles. Control of size and shape of nanoparticles is validated with this technique as well.

1.4.2 Thermal Conductivity

The idea of enhancing the thermal conductivity of conventional fluids by doping with millimeter or micrometer-sized metallic particles was first proposed by Maxwell [45] in 1873. However, issues such as erosion, sedimentation and significantly high-pressure drop barred the use of micro-particle slurries as heat transfer fluids. To the contrary, nanoparticle doped suspensions (nanofluids) are stable and exhibit enhanced thermal properties compared to micrometer slurries.

As shown in Figure 12, a brief review of literature reveals the parameters affecting thermal conductivity of nanofluids. Of the various factors, particle concentration and size are investigated extensively. Thermal conductivity enhancement increases with the volumetric loading of the nanoparticles in the suspension. Majority of the researchers found the relation to be linear between nanoparticle concentration and enhancement. Similarly, nanoparticle size also greatly influences the thermal conductivity enhancement in nanofluids. Several reports [46] [47] [48] in the literature note that the effective thermal conductivity of nanofluids increases with decrease in nanoparticle size. Xie *et al*. [49] investigated the effect the nanoparticle shape on the effective thermal conductivity of nanofluids. The authors observed that cylindrical-shaped nanoparticles presented greater enhancement than spherically shaped nanoparticles for same base fluid, and other studies [50, 51, 52, 53, 54] later reported similar relation between nanoparticle shape and enhancement. Pak and Cho [55] recommend the use of high thermal conductivity nanoparticles to obtain greater

thermal conductivity enhancement of the base fluid. Several other reports [56, 57, 58, 47] exist in the literature corroborating the recommendation. With regard to base fluid, numerous studies [49, 47, 53, 59, 60] in the literature report that the level of enhancement observed in thermal conductivity is inversely proportional to the thermal conductivity of the base solvent. Among the listed parameters influencing the effective thermal conductivity of nanofluids, synthesis protocol is the most neglected parameter in majority of these studies. Nanoparticle dispersion technique, stability of the nanofluid suspension and the particle size distribution in the suspension considerably influence the effective thermal conductivity.

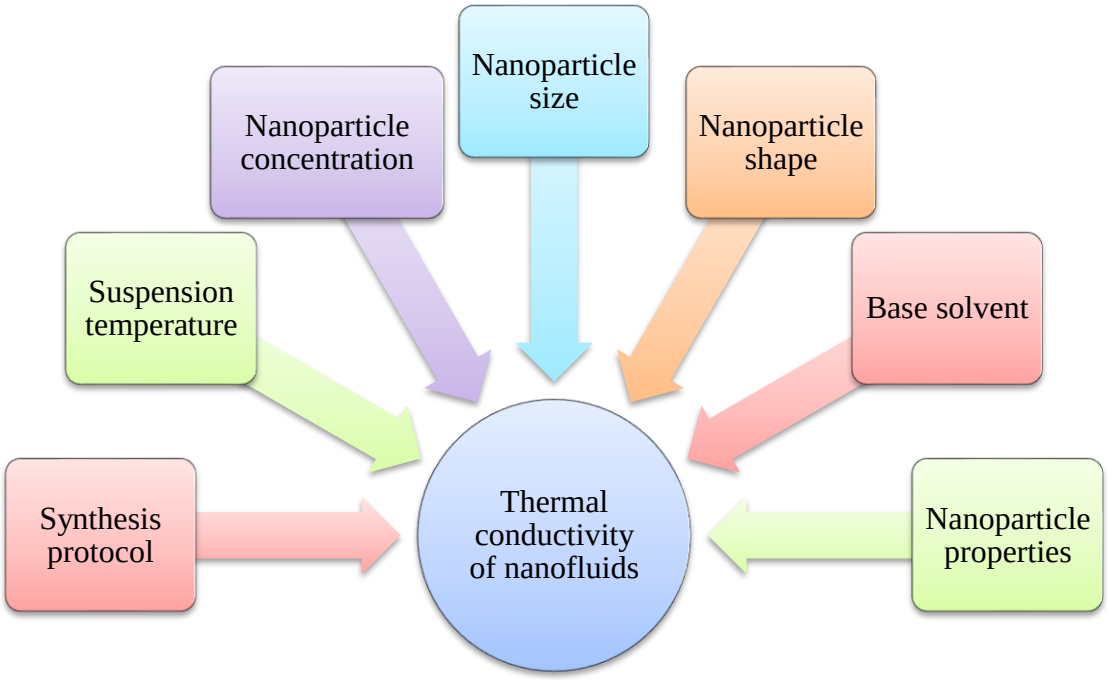

Figure 12. Parameters influencing effective thermal conductivity of nanofluids.

Table 5. Summary of experimental reports for thermal conductivity enhancement of nanofluids.

Author	Particle type	Base fluid	Particle volume fraction (%)	Particle size (nm)	Maximum enhancement (%)
Masuda et al. (1993)	Al_2O_3	Water	1.30-4.30	13	32.4
	SiO_2		1.10-2.40	12	1.1
	TiO_2		3.10-4.30	27	10.8
Lee et al. (1999)	Al_2O_3	Water/EG	1.00-5.00	38.4	18
	CuO		1.00-4.00	23.6	23
Das et al. (2003)	Al_2O_3	Water	1.00-4.00	38.4	24
	CuO		1.00-4.00	28.6	36
Sadegh A et al. (2016)	AG	HTO	0.6	10	36.3
Khedkar et al. (2016)	TiO_2	EG	7	5	19.52
Aberoumand S. et al.(2016)	AG	HTO	0.17	20	41
Agarwal R. et al. (2016)	CuO	Water	2	55-66	24
		EG	2		21
		EO	2		14
Li H. (2016)	ZnO	EG	2.4	50	13
Li X. (2016)	SiC	DO	0.8	30	7.36
Hemmat E. M.(2015)	MgO	EG-Water (40:60 wt. %)	3	40	34.43
Karimi A et al. (2015)	$NiFe_2O_4$	DI	2	8	17.2
Parametthanuwat T. (2015)	AG	DI	0.5	NA	16

Table 6. Summary of experimental reports for thermal conductivity enhancement of nanofluids.

Author	Particle type	Base fluid	Particle volume fraction (%)	Particle size (nm)	Maximum enhancement (%)
Usri N. A. (2015)	Al_2O_3	EG-Water (60:40 wt. %)	2	13	8.4
		EG-Water (50-50 wt. %)	2		12.6
		EG-Water (40:60 wt. %)	2		16.2
Hemmat E. M. (2015)	DWCNT + ZnO	EG-Water (60:40 wt. %)	1	10-30	33
Buonomo B.(2015)	Al_2O_3	Water	4	40	14.4
Cingarapu S.(2014)	Sn-SiO_2	TH66	5	50-100	13
Angayarkanni S. (2014)	γ-Al_2O_3	Water	6	13	14.5
	SiO_2		6	15	10.8
	TiO_2		4	13.5	15.1
Sundar L. S. (2013)	Al_2O_3	EG-Water (50:50 wt. %)	8	36.5	17.89
	CuO		8	27	24.56
Sun C. et al. (2013)	SiO_2	Water	1.2	10-60	13
Pakdaman M. (2012)	MWCNT	HTO	2	5-20	15
Khedkar R. (2012)	CuO	Water	7.5	25	32.3
		MEG	7.5		21.3
Harish S. (2012)	SWCNT	EG	0.21	100-600	15.5

1.4.3 Specific Heat Capacity

Compared to the vast amount of studies on nanofluid thermal conductivity, the research reports on the specific heat capacity is rather limited. Nevertheless, it has also been shown that the addition of small amount of nanoparticles can greatly enhance the specific heat capacity of non-aqueous fluids (despite the fact that the bulk material properties of these particles generally show a lower value of the specific heat capacity than the base fluid). Nelson et al. [61] provided the first report in the literature, based on experimental measurements, for conclusively demonstrating the enhancement of the specific heat capacity for oil based nanofluids. Different mechanisms were proposed to explain such drastic changes including higher surface energy, solid-fluid interaction energy and the semi-solid nanolayer adsorbed on the surface of the nanoparticle. For water-based nanofluids however, experiments have shown that addition of nanoparticles would decrease the overall specific heat capacity. This is mostly likely caused by the lower specific heat capacity of the adsorbed "ice" like layer than that of the liquid water.

The study of molten salt nanofluids is a relatively new field of research. Major research efforts thus far have been focused on experimental techniques. Shin and Banerjee [62] were the first researchers to report anomalous enhancement of specific heat capacity of molten salt upon addition of minute concentrations of nanoparticles. As shown in Figure 13, the authors also propose three possible mechanisms for the enhancement and are based on molecular level interaction between nanoparticles and base solvent. According to the authors, the specific heat capacity anomalous enhancement can be due to

- Mode I: Higher specific heat capacity of nanoparticles than the bulk material
- Mode II: Solid-fluid interaction energy
- Mode III: “Layering” of liquid molecules at the nanoparticle surface

Theoretical [63] and experimental [64] evidence exists supporting the hypothesis proposed in Mode I that the specific heat of nanoparticles is significantly higher (~25%) compared to the bulk material due to high surface energy. In Mode II, the authors propose that the high interfacial thermal resistance between nanoparticles and ions of the base solvent can contribute to the increased thermal energy storage capacity of the nanofluid. In Mode III, they suggest that based on the surface energy of the nanoparticle, a “semi-solid” liquid layer forms and possess superior thermal properties compared to the bulk base solvent. Oh *et al.* [65] report existence of such secondary structures through Transmission Electron Microscopy (TEM). Khanafer *et al.* [66] considers the models listed by Shin and Banerjee, provide in depth discussion on the adsorption of molecules. The authors also experimentally demonstrate the strong influence of nanoparticle size on the specific heat capacity of molten salt nanofluid.

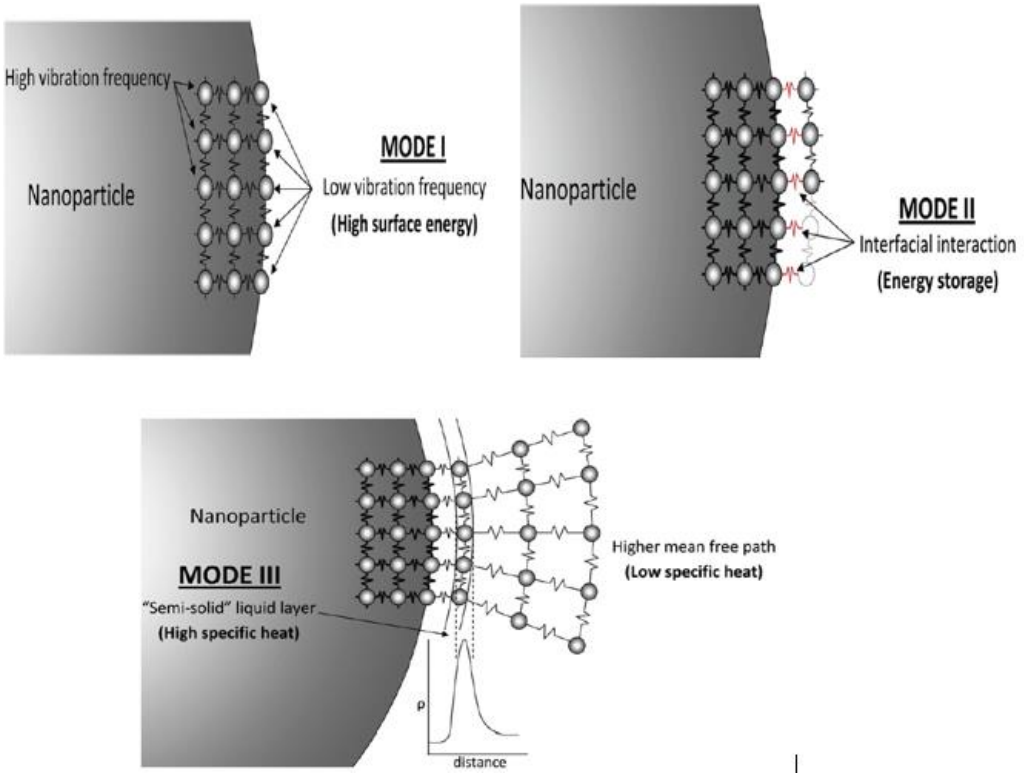

Figure 13. Models proposed by Shin and Banerjee [62] for anomalous enhancement of specific heat capacity of molten salt nanofluids.

Table 7 summarizes the experimental studies on specific heat capacity enhancement reported in the literature pertaining to molten salt-based nanofluids. The experimental results and the factors effecting the specific heat capacity of nanofluids is still a contested topic among researchers for various reasons. The potential solutions for creating a concrete knowledge base for researchers include:

- **Initial characterization of materials**

  The characterization of nanoparticles or the additives (precursor for nanoparticles formed *in-situ*) is of great importance, since specific properties such

as actual particle size and shape greatly influence the final properties of nanofluid and need to be characterized.

- **Synthesis Protocol**

  Currently, synthesis protocols employed by researchers require aqueous solvents and are not scalable for mass production. For nanofluids to be employed in practical applications, novel synthesis techniques (such as thermal decomposition, microwave assisted protocols) need to be developed for industrial scale synthesis and reproducibility.

- **Stability of nanoparticles in the solution**

  Agglomeration of nanoparticles in the solution is a major hindrance for the advancement of the field of nanofluids. The use of techniques such as ultrasonication or mechanical stirring for preventing particle agglomeration is not a viable solution.

- **Standardized measurement techniques**

  The thermo-physical property (such as thermal conductivity, viscosity and specific heat capacity) characterization techniques for molten salt based nanofluids needs to be standardized. Currently, various research groups employ different measurement techniques developed in-house with limitations in accuracy and repeatability.

- **Liquid state thermo-physical property characterization**

  At this time, no characterization method exists to identify the actual particle size distribution of nanoparticles in a molten salt nanofluid in liquid state. Same problem arises to measure the thermal conductivity of molten salt nanofluids. At this time, the size of the nanoparticles in the suspension is measured using either SEM or DLS.

- **Corrosion of storage tanks and piping**

  The corrosive effect of the molten salt nanofluids on the storage tanks or on piping is an important aspect that needs to be addressed before industrial deployment. The possibility of physical erosion of pipes or tanks with nanofluid is yet to be explored thoroughly.

- **Economic Analysis**

  The prospect of implementing molten salt nanofluids is ultimately dependent on the potential cost savings. To the best of the author's knowledge, no economic analysis on system level exists in the literature taking into account the enhanced thermo-physical properties and the synthesis costs (material costs etc.). Traditional two-step synthesis methods for synthesizing nanofluids suffers from high material cost and offsets the benefits of enhanced thermo-physical properties.

Table 7. Summary of experimental reports on molten salt based nanofluids on specific heat capacity enhancement.

Author	Base Solvent	Nanoparticle	% Mass Fraction	% Maximum Enhancement
Chieruzzi, M. et al (2017)	Solar Salt*	SiO_2/Al_2O_3 (86:14 by mass fraction)	1%	14%
Hu, Y. et al. (2017)	Solar Salt*	Al_2O_3	2%	8.30%
Chen, X. et al. (2018)	$Ca(NO_3)_2$-KNO_3-$NaNO_3$-$LiNO_3$ (2:6:1:2 in mass ratio),	SiO_2	1%	16.40%
Shin, D. & Banerjee D (2011)	Quaternary Eutectic of $BaCl_2$, NaCl, $CaCl_2$ & LiCl	SiO_2	1%	14.50%
Jo, B. & Banerjee, D. (2014)	Li_2CO_3-K_2CO_3	Graphite	0.10%	56.80%
Ho, M. X. & Pan, C.(2014)	Hitec Salt*	Al_2O_3	0.01%	19.90%
Chieruzzi, M. et al. (2015)	KNO_3	Al_2O_3	1.00%	10%
		SiO_2	1.00%	
		SiO_2/Al2O3 (86:14 by mass fraction)	1.00%	
Tiznobaik, H. & Shin, D. (2013)	Li_2CO_3-K_2CO_3	SiO_2	1.00%	25%
Schuller, M. et al. (2015)	Solar Salt*	Al_2O_3	0.78%	30.60%
Dudda, B. & Shin, D. (2013)	Solar Salt*	SiO_2	1.00%	27%

1.4.4 nanoFin Effect ("nFE")

The compressed phase has also been attributed to cause peculiar phenomena – which are modeled by the "*nanoFin Effect*" ("*nFE*") [67]. One manifestation of nFE occurs when nanoparticle coatings (e.g., due to precipitation of nanoparticles on heater surfaces from nanofluids) formed by nanoparticles cause "anomalous" thermal performance. For example, nanofins formed using nanoparticles with lower thermal conductivity values can cause higher levels of enhancement in heat flux values (compared to that of nanoparticles with higher values of thermal conductivity), especially during phase-change (such as boiling on nanostructured heaters) [68, 69, 70, 71, 72]. A transport model that resolves the conundrum associated with these anomalous heat transfer phenomena (i.e., due to the formation of the compressed phase that envelopes these nanoparticles) was therefore termed as the "*nanoFin Effect*" ("*nFE*") [67].

Prior experimental reports involving pool boiling on nanostructured heater surfaces indicated greater degree of critical heat flux (CHF) enhancement for heater surfaces coated with lower thermal conductivity nanofins compared to that of surfaces coated with higher thermal conductivity nanofins. For instance, silicon heater surfaces with etched silicon nanofins exhibited a CHF enhancement of 120% (compared to 60% enhancement in CHF observed in silicon substrates coated with carbon nanotubes / "CNT") [68, 69, 70, 71, 72]. The reason for these peculiar experimental observations is attributed to the interfacial thermal resistance (also called "Kapitza resistance" [73, 74, 75] between nanofin surface and surrounding solvent molecules; resulting from impedance mismatch of the thermo-

mechanical vibrations between nanofin surface and solvent molecules) [76, 77, 78, 79]. Figure 14 illustrates the resistance analogy of a single nanofin in a solvent including the Kapitza resistance at the solid-liquid interface (i.e., on the surface of the nanofin). Hence, the higher levels of enhancement for heat transfer involving silicon nanofins is a result of their lower interfacial resistance (compared to that of the CNT coated heaters) by three orders of magnitude [80, 81, 82]. Hence, the lower values of the total thermal resistance of the silicon nanofins compared to that of the CNT (when including the Kapitza resistance) leads to the higher levels of enhancement in heat flux values for silicon nanofins. Therefore, the Kapitza resistance is the dominant component of the total thermal resistance in the thermal impedance network of these nanofins [83, 84, 85].

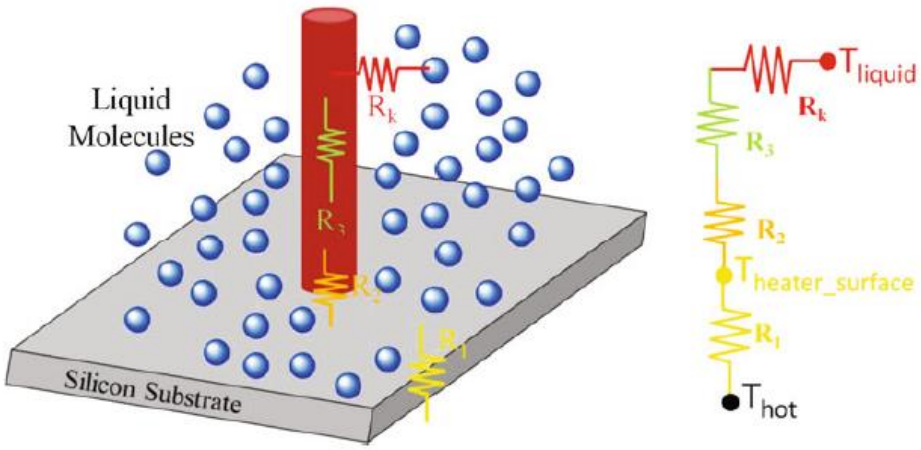

Figure 14. Illustration of interfacial surface resistance (or "Kapitza resistance") for a solid-liquid interface of a nanofin on a silicon substrate with a resistance model analogy [86]

Furthermore, by employing molecular dynamics (MD) simulations, Jo [83] investigated the effects accruing from the formation of the "compressed phase" of solvent molecules around various nanoparticles (e.g., SWNT, graphite sheets, and C_{60} Fullerene) in a high temperature salt eutectic. Simulation results indicated that the thickness of the compressed layer around the nanoparticle was weakly sensitive (or almost insensitive) to the size or shape of the nanoparticle, for a given combination of solid and fluid (solvent) materials. In addition, the spatial variation of concentration (e.g., due to Van Der Waals forces and ionic force interactions within the solvent and in the vicinity of nanofins) was shown to affect the thermo-physical properties of the nanoparticle mixture. Figure 15 and Figure 16 shows that the oscillations in the profiles for density and ionic concentrations that were induced in the solvent phase (due to the presence of a graphite nanoparticle) would cause severe variations in species concentration gradients at different distances away from the surface of a nanoparticle. These estimates were obtained from MD simulations using classical force field models [83]. The plots - for the spatial distribution (in the radial direction) of the density and species concentration profiles - demonstrate the existence of the compressed phase where a region in the solvent phase has higher magnitudes of density (and concentration of component species) in the immediate vicinity of the nanoparticle surface. The MD simulations show that the thickness of this compressed phase is in the range of 1-2 nm [83]**.** These plots also show that there is a "void space" between the solvent molecules and the nanoparticle surface. The thickness of the void space on the nanoparticle surface (where no solvent molecules exist) is

approximately ~ 5Å (~ 0.5 nm). This void space corresponds to the equilibrium spacing (average intermolecular spacing) between the solvent molecules and the atoms on the surface of the nanoparticle.

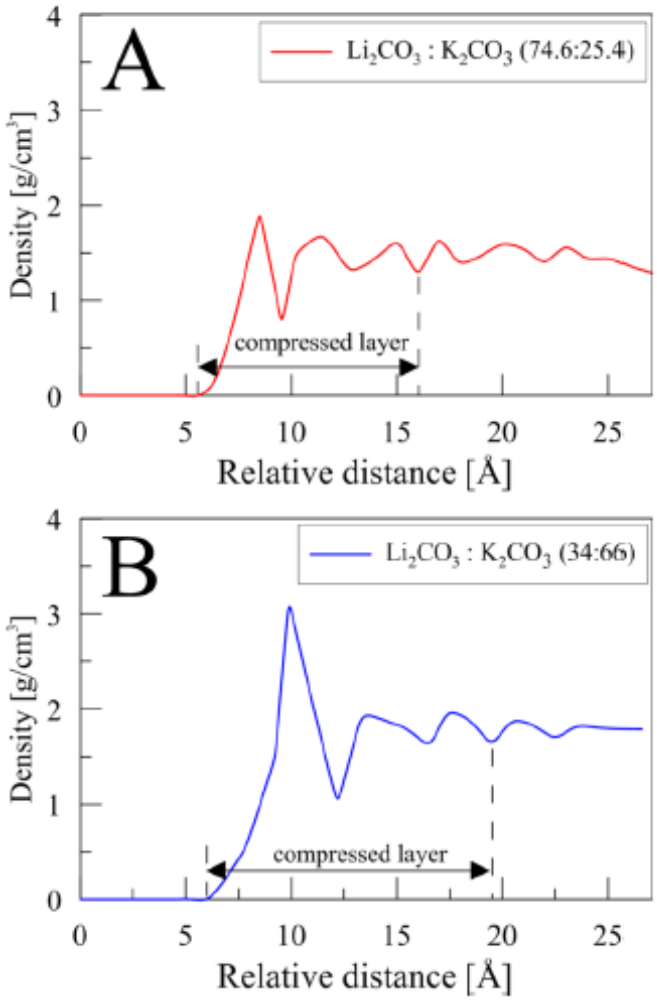

Figure 15. Spatial distribution of density values for different carbonate salt eutectics around a graphite nanoparticle obtained from MD simulations [83]. (A) For a carbonate eutectic of Li_2CO_3: K_2CO_3 (74.6:25.4) (B) For a carbonate eutectic of Li_2CO_3: K_2CO_3 (34:66)

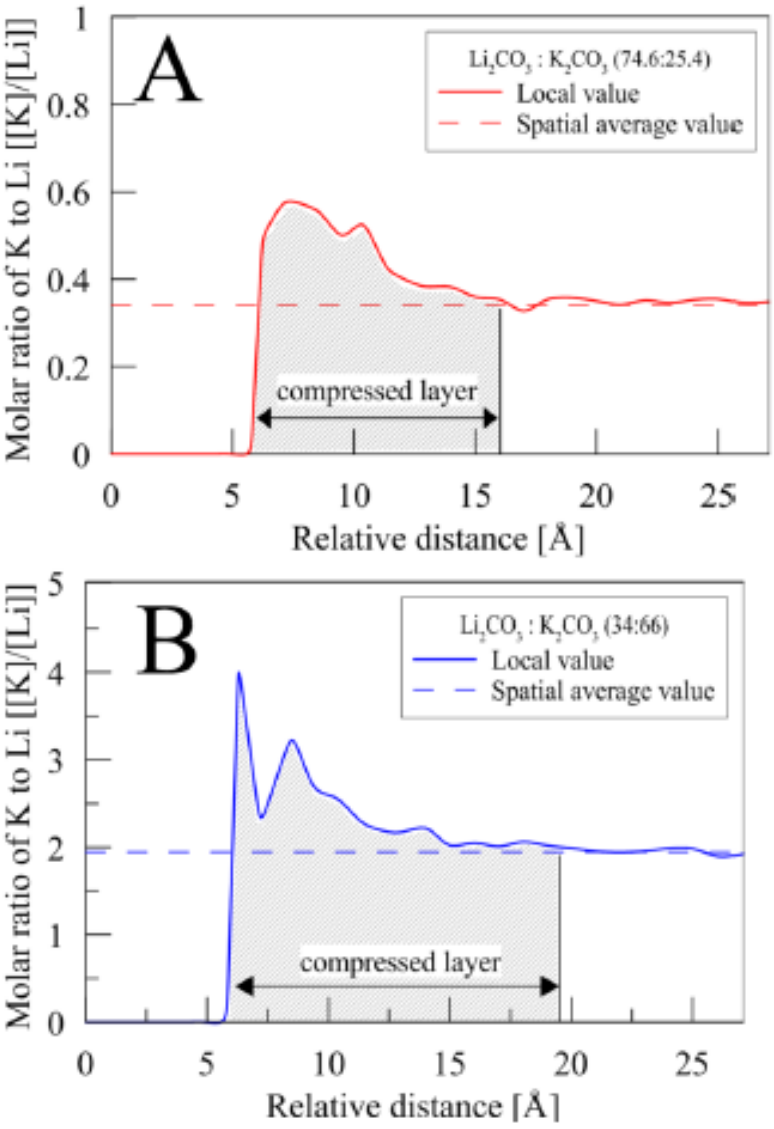

Figure 16. Spatial distribution of species concertation for different carbonate salt eutectics around a graphite nanoparticle obtained from MD simulation results [83]. (A) For a carbonate eutectic of Li_2CO_3: K_2CO_3 (74.6:25.4) (B) For a carbonate eutectic of Li_2CO_3: K_2CO_3 (34:66)

Yang [87] investigated the implications of the compressed layer (i.e., density and concentration gradients) on the transient heat transfer in nanoparticle suspensions as well as for heaters with nanostructured surfaces (i.e., nanofins). The local variations in the thermal characteristics resulting from the different values of the thermal properties of the bulk phase and the compressed phase can be attributed to the surface adsorption of the fluid molecules on the solid surfaces. Figure 17 shows the density profile observed near a SiO_2 nanoparticle immersed in a refrigerant (PF5060, which was the working fluid for the pool boiling experiments in this study [87]). Consistent with prior literature reports [88, 89, 90], Yang [87] observed that the compressed layer thickness was ~1 nm and the peak density of the compressed phase was predicted to be that of solid phase density of solvent (i.e., approximately twice as much as the bulk phase values). Furthermore, the formation of a compressed phase of the solvent molecules around the nanoparticles or nanofins was the dominant mechanism responsible for enhancing the effective specific heat capacity of the nanocomposites (e.g., nanoparticles suspended in a solvent) [91, 92, 93, 94, 95]. In other words, the formation of the compressed phase, due to the surface adsorption and the resulting re-ordering of the solvent molecules on the nanoparticle (or nanofin) - can provide a supplementary receptacle for additional thermal energy storage.

While the density fluctuations near the solid-liquid interface of a nanofin or a nanoparticle, can have direct implications on the thermo-physical properties (e.g., thermal conductivity and specific heat capacity), *nFE* implies that severe concentration gradient values caused by the concomitant oscillations in species concentration also has a

significant impact on the transport mechanisms. The formation of a concentration gradient of the solvent molecules on the nanoparticle (or nanofin) surface results in a bias that modulates the heat flux depending on the directionality of the temperature difference (or "diode" like behavior for material and thermal transport), i.e., according to the predictions afforded by the *nFE* model, it causes the formation of a thermal diode [87]. The mass transfer (or diffusion) resulting from the chemical concentration gradient drives this thermal diode like behavior where higher heat flux is achieved for a hot nanoparticle to colder solvent phase (where the thermal gradient and species concentration gradients are covariant, i.e., they decay in the same direction), than that of the configuration involving a cold nanoparticle in a hot solvent phase (where the thermal gradient and species concentration gradients are contravariant, as they decay in the opposite directions). Hence, for the same temperature difference between two nanoparticles and the liquid phase, a hot nanoparticle (or nanofin) is expected to yield 2~ 10 % higher heat flux than that of a cold nanoparticle (depending on the material combination chosen for these experiments).

To summarize, the addition of nanoparticles into a neat solvent (or surface modification through formation of nanostructures or nanofins on heater surfaces) often result in anomalous enhancement in specific heat capacity as well as thermal conductivity while also causing deviant enhancement of heat flux values; as observed from the varying levels of enhancement of phase-change heat transfer (such as boiling) and is termed as the "*nano-Fin Effect*" ("*nFE*)" [86]. This phenomenon (*nFE*) arises due to non-linear coupling of the transport mechanisms involving temperature gradients and mass concentration

gradients (as well as species concentration gradients). The authors [86] proposed a combination of transport mechanisms, as shown in Figure 18, which are primarily dominated by three distinct transport mechanisms, itemized as follows:

1. Surface adsorption of solvent molecules around the nanoparticle resulting in the formation of a compressed phase ("nanolayer" with a typical thickness of 1 ~ 2 nm on the solid surface) with different effective mass density and specific heat capacity than that of the bulk solvent phase (thus contributing to the thermal resistance and thermal capacitance of the mixture);

2. Interfacial thermal resistance between the nanoparticle and solvent molecule (termed as "Kapitza resistance") resulting from the vibration impedance mismatch (for the molecular and atomic scale vibrations arising from the thermal transport) between the solvent molecules and atoms on the surface of the nanoparticles;

3. Mass diffusion driven by the concentration gradients resulting from the preferential adsorption of different species of the solvent on the surface of the nanoparticles, i.e., adhesion of the solvent species on the surface of the nanoparticle (this in turn causes gradients in the mass concentration and gradients in the ionic concentration of the different species in the solvent phase, this contributing to the formation of a "thermal diode").

It is interesting to note that *nFE* is most pronounced for the following situations or combination of situations [67]: (i) for nanoparticle diameters less than 10 nm (and particularly acute for nanoparticle diameters less than 6 nm), (ii) for nanoparticle

density values less than 1 g/cc; (iii) for solvents with solid phase density higher than that of the liquid phase; (iv) for solvents with liquid phase density less than 1 g/ cc; (v) for solvents with solid phase density greater than 1 g/cc; (vi) for solvents where the ratio of liquid phase density to that of the solid phase density is less than 1; and (vii) for the material combinations (i.e., the combination of nanoparticle and solvent) where the thickness of the compressed phase is maximized, such as through control of pH or Zeta potential (for ionic fluids) or surfactant concentration(for polar fluids). This shows that the consequences of nFE are very hard to detect (to almost non-existent) for aqueous nanofluids and more pronounced for non-aqueous solvents (e.g., oleo-nanofluids, molten salt nanofluids, etc.).

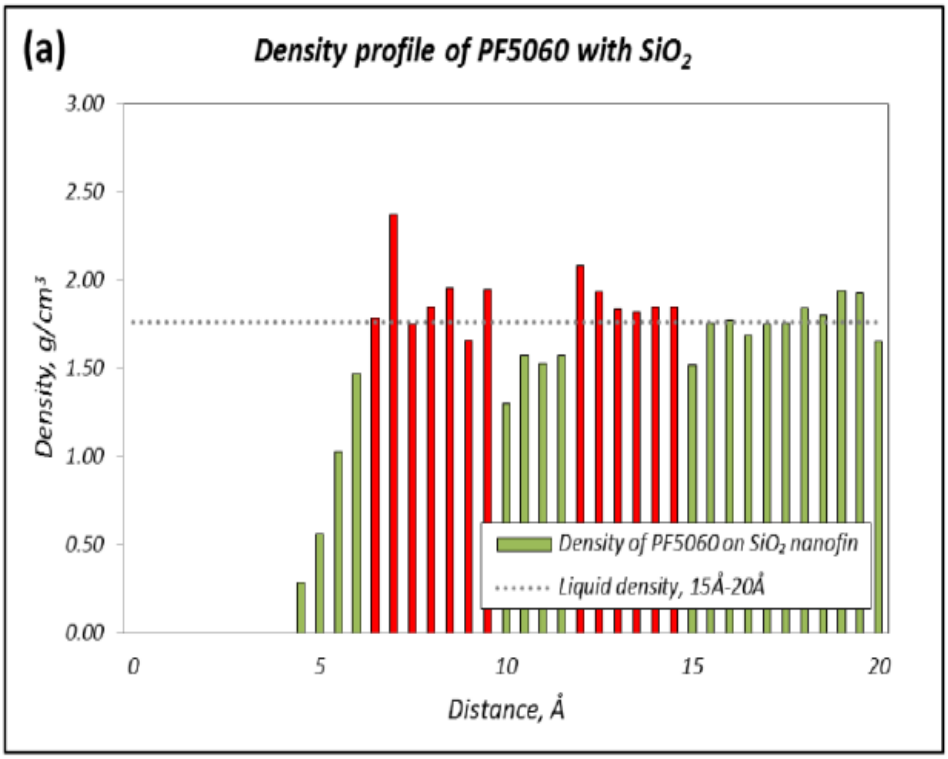

Figure 17. Density profile of fluid phase (PF-5060 solvent) in contact with SiO_2 nanoparticle (or nanofin) surface. These results were obtained from MD simulations. The dashed line indicate the average liquid density and red color bars indicate the compressed phase with density values higher than bulk value. [87]

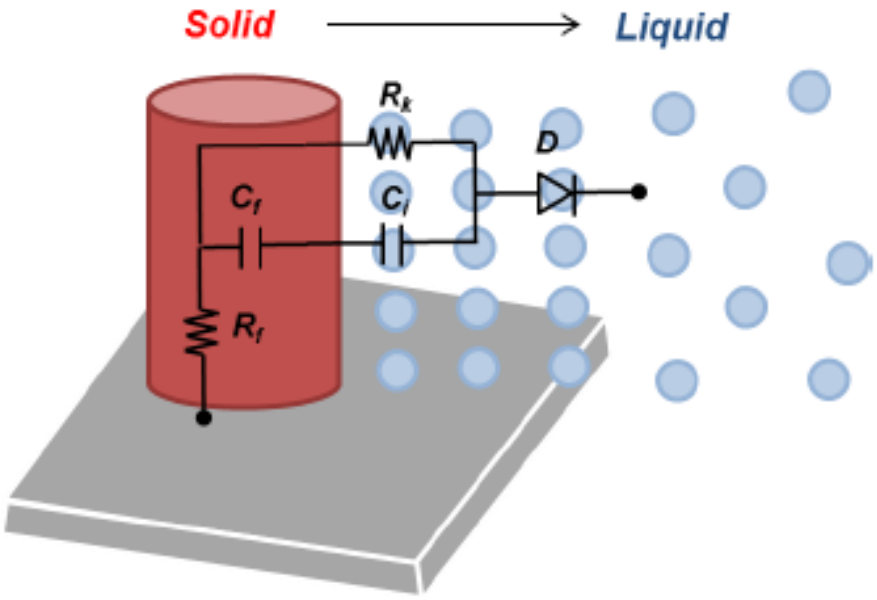

Figure 18. The phenomena of "nanoFin Effect" ("nFE") is schematically represented as a thermal impedance network and is modeled to consist of three constituents: (a) a thermal resistance, and (b) a thermal capacitance, in parallel; which are in series with: (c) a thermal diode. [87]

Compared to the numerous literature reports on thermal conductivity of nanofluids (and to a lesser extent, the literature reports on the specific heat capacity of nanofluids), surprisingly, only a few reports [96, 97, 98] were detected, from our literature review, that have consciously attempted to perform experimental measurements for the values of the density of nanofluids (compared to that of the neat solvent), albeit erroneously. Of these experimental measurements reported in the literature, only six [96, 98, 99, 97, 100, 101] have pursued consciously (or hypothesized that) the underlying causes for deviations in density enhancement were a result of the formation of compressed layer (sometimes

referred to in these literature reports as the "nanolayer"). Interestingly, there was one study [96] that assumed that the simple mixing rule was valid and proceeded to suggest a correction factor, even though the surplus density exceeded 8% in some of the nanofluids samples used in their experimental measurements. Several implications and applications involving densification of solvents using nanoparticles will be explored later in this paper.

In majority of the studies reported in the literature, classical or simple mixing model for density (i.e., linear approach for estimating density values and volume fractions, based on thermodynamic equilibrium) was used for the nanofluids. As mentioned before, only a few of these studies consciously accounted for the contribution of the enhanced density of the compressed phase in the nanofluid (compared to that of the neat solvent) in modulating the net density of the mixture [101, 100], but suffered from severe deficiencies, itemized below:

(a) Measurement uncertainty was not reported or measurement uncertainty analyses were faulty and completely erroneous. For example, one study erroneously claimed that measurement uncertainty for density measurement was 0.012% ~ 0.016% [101], which clearly shows that the authors misunderstood the procedure for estimating measurement uncertainty (as repeatability of the experiments was not demonstrated and the statistical uncertainty values for the measurements were not obtained).

(b) Many studies reported increase in deviant density component with increasing mass fraction of the nanoparticles (however, the theoretical underpinning were not explored or validated) [96].

(c) In all studies, except one [98], the diameter of the nanoparticles were more than 10 nm, often in the range of 40-60 nm. As will be shown later in this study, that the deviant density component is expected to be below the measurement uncertainty values for nanoparticle diameter less than 10 nm. Only one study [98] reported density measurement in aqueous nanofluid, with alumina nanoparticle diameter less than 10 nm and deviant density of 6 mg/cc or 0.6% where the precision in the measurement apparatus was reported to be 0.1 mg/cc (which makes the claim dubious since the measurement uncertainty was not reported and the statistical component of the measurement uncertainty is unclear as the authors did not show repeatability of their experiments).

(d) In all studies, the density of the nanoparticles was more than 1 g/cc, and often the density of the nanoparticles was in the range of 2 - 6 g/cc [99, 96]. As will be shown later in this study, that the deviant density component is expected to be conclusively above the measurement uncertainty values (with statistical significance greater than 68%) for nanoparticle density less than 1 g/cc.

(e) Some of the studies involved nanoparticle mass fractions greater than 5%. These results are circumspect as agglomeration kinetics dominate and compromise the stability of the nanoparticles for higher mass fractions and often it is desirable to

perform the experiments for nanoparticle mass fractions to be less than 2% (and ideally 1% or less). [100, 96]

(f) Two sets of measurement instruments were used for the same measurement but only one set of measurements for density were reported [99]. Therefore, it is not clear if there were discrepancies between the two sets of measurements.

(g) One study showed deviant density component caused the specific heat capacity of the aqueous nanofluid to be conspicuously lower than that of the solvent [99], and violated the simple mixing rule (as can be expected from the theoretical analyses we are presenting in our study). However, the authors were completely oblivious to this discrepancy.

(h) A void space exists (with a thickness of ~5 Å, which is in the same order of magnitude as the equilibrium inter-molecular spacing values) between the surface of the nanoparticle and the solvent molecules in the compressed phase [102, 103]. However, the volume of the void space between the nanoparticle and the compressed phase was neglected in one of the studies [101]. The authors erroneously claimed that the void space increases with nanoparticle size (and to be as high as 1.3 nm, which is higher than the equilibrium intermolecular spacing values). The correlation developed in this study implies that as the particle size increases the size of the compressed phase increases, which contradicts the idea of nanoparticles enhancing density by bigger margin than micron-scale particles. The plots for the comparison of the experimental data are also inconclusive as they

occupy the region between predictions from the mixing rule and the predictions from the erroneous model developed by the authors.

(i) One study accounted for the effects of agglomeration (where the secondary nanostructures are expected to play a dominant role and would permeate the whole volume intervening the nanoparticle clusters) [100]. However, the authors did not consider previous reports in the literature, where electron microscopy images distinctively demonstrated the compressed layer occupying the intervening volume between clusters of closely spaced nanoparticles. Further, the authors also erroneously assumed that the compressed phase (or nanolayer) existed on the outskirts of the cluster and not within the cluster. This would cause the effect of the clusters to be underestimated by orders of magnitude. For density values exceeding 1100 kg/ m3, the authors report predicted values of density to the fourth place of decimal (which shows that they did not account for measurement uncertainties or the precision of the measuring instruments in the experimental validation of the theoretical predictions). As a result, the conclusions presented by the authors are circumspect and in need of additional verification.

1.5 Convective heat transfer of nanofluids

1.5.1 Single phase heat transfer

The heat transfer properties and flow characteristics of nanofluids are to be characterized before employing them in industrial applications as heat transfer fluids (HTF). For this purpose, several research groups investigated the forced heat transfer performance of a variety of colloidal suspensions with metallic and oxide nanoparticles in commonly used heat transfer fluids such as water, propylene glycol, ethylene glycol etc. However, the results from different studies are contradictory and controversial and are therefore subject of much debate, due to multiple omissions and inconsistencies that are typical of these studies. As stated earlier, one of the reason for this sparsity of data in literature is due to different approaches or models followed by scholars in deriving thermo-physical property calculations. Most nanofluid heat-transfer studies in literature make use of correlations available in literature based on effective medium theory for determining thermal conductivity. The effect of nanoparticle size, concentration and temperature of suspension on thermal conductivity is reported by several publications and needs to be considered while investigating heat transfer performance of nanofluids. Heyhat et al. [104] experimentally investigated the laminar convection heat transfer behavior of water-based Al_2O_3 nanofluid in a horizontal tube with volume concentrations of 0.1-2 %. The heat transfer coefficient of nanofluid at 2 % was approximately 32% greater than that of pure water and the enhancement was greater than thermal conductivity enhancement observed in this study. Conventional correlations failed to predict the

enhancement of heat transfer coefficient and the pressure drop of nanofluids – that were higher than that of water.

Yu et al. [105] measured the convection heat transfer coefficient of water-based nanofluid with SiC nanoparticles at 3.7% volume. The results showed that the heat transfer coefficient was enhanced by 50-60% at same Reynolds number and decreased by 7% when compared at same mass average velocity (compared to that of water).

He et al. [106] carried out convection heat transfer tests using nanofluids formed by suspending TiO_2 nanoparticles of different sizes in water. The flow loop consisted of a vertical pipe. The enhancement in heat transfer coefficient was observed to be 12% and 40% in laminar and turbulent regimes respectively, at the same Reynolds number compared to that of the base fluid.

Utomo et al. [107] investigated the effect of addition of Al_2O_3, TiO_2 and CNT nanoparticles to water for laminar heat transfer coefficient in horizontal pipe with constant heat flux boundary condition (independently at two universities). Only 10% enhancement in heat transfer coefficient is observed and results are in good agreement between two universities. Classical laminar convection correlations were able to predict the observed heat transfer coefficients. The average heat transfer coefficient of nanofluids was compared to that of base fluid for several parameters such as mass flow rate, average velocity, pumping power and Reynolds number. They concluded that the heat transfer enhancement obtained using nanofluids is offset by the increase in pressure drop.

Hwang et al. [108] studied laminar convection heat transfer and pressure drop of Al_2O_3 doped water based nanofluid flowing in a circular pipe with constant heat flux. The results showed that the heat transfer coefficient enhancement was greater than the thermal conductivity enhancement. They performed numerical analysis and suggested that the flattening of velocity profile induced due to large gradients in bulk properties such as thermal conductivity, viscosity and nanoparticle concentration to be the dominating mechanism for this incongruous heat transfer coefficient enhancement.

Haghighi et al. [109] investigated convection heat transfer characteristics of Al_2O_3, ZrO_2, TiO_2 water-based nanofluids in both laminar and turbulent flow regimes. Thermal conductivity and viscosity were measured at 20 ºC. The results indicate that classical correlations such as Shah and Gnielinski for laminar and turbulent flow respectively were able to predict the measured heat transfer coefficient. The average enhancement in heat transfer coefficient with base fluids was 51%, 41% and 13% for Al_2O_3, ZrO_2, TiO_2 nanofluids respectively in turbulent regime at equal Reynolds number and decreased by 63%, 52% and 17% at equal pumping power for Al_2O_3, ZrO_2, TiO_2 nanofluids respectively.

Ferrouillat et al. [110] studied heat transfer performance of SiO_2-water nanofluids, with 5-34% of SiO_2 nanoparticles, in a horizontal pipe with constant surface temperature at different inlet temperatures (20 ºC, 50 ºC and 70 ºC). Thermal conductivity and viscosity are measured at same temperature as the testing conditions and results indicated that the heat transfer coefficient was enhanced by 10 – 60% at equal Reynolds number with water. A Performance Evaluation Criterion (PEC), defined as ratio of heat transferred to required

pumping power, indicated that the studied nanofluid is not efficient for use in industrial application.

Chen et al. [111] measured thermal conductivity and viscosity of TiO_2 nanotube water-based nanofluids and investigated the heat transfer performance of these aqueous suspensions. They observed that the suspensions exhibited non-Newtonian behavior (shear thinning at low shear rates) and the convection heat transfer coefficient enhancement is greater than thermal conductivity enhancement due to nanotubes. They speculated particle re-arrangement under shear, enhanced wettability and shape effect to be the possible mechanisms responsible for this anomaly.

The heat transfer performance of ZnO/ethylene glycol-water based nanofluids for pipe flow in transition regime was experimentally investigated by Li et al. [112]. They report a maximum of 30% enhancement in heat transfer coefficient at 2.5 % compared to base fluid and the enhancement decreased with increasing particle mass concentration.

Huang et al. [113] experimentally investigated the pressure drop and convection heat transfer performance of Al_2O_3 water-based nanofluids and MWCNT water-based nanofluids in a chevron plate heat exchanger. At equal Reynolds number, the heat transfer coefficient of nanofluids was greater than that of water and deterioration at equal average velocity comparison. In addition, the viscosity increase for MWCNT nanofluids is higher compared to Al_2O_3 nanofluids resulting in greater decrease in heat transfer coefficient at constant average velocity compared to base water.

Agarwal et al. [114] studied turbulent heat transfer behavior of Kerosene-Al_2O_3 nanofluid in circular test section and the effect of particle size and volume fraction on heat transfer performance was investigated. They observed that the heat transfer enhancement for larger particle size is greater compared to nanofluid with smaller particle size. This observation is in contrast with thermal conductivity enhancement.

Yarmand et al. [115] investigated thermal conductivity, viscosity and heat transfer performance of functionalized graphene nanoparticles under turbulent flow in a square pipe with constant heat flux thermal boundary condition. They observed strong dependence of weight concentration and temperature on thermal conductivity and heat transfer coefficient enhancement. The highest enhancement observed in heat transfer coefficient was 19% with 9% increase in friction factor.

Nelson et al. [61] investigated thermal-hydraulic performance of exfoliated graphite nanoparticle based polyalphaolefin nanofluid. They observed more than 4 times enhancement in thermal diffusivity with less than 10% enhancement in convective heat transfer. Yu and Banerjee [116] in 2012 reported results from microchannel flow experiments using SiO_2-DIW nanofluid in which they observed a competing effects between thermal properties of nanofluids and the "nanofin effect" that could lead to an anomalous enhancement in forced convective heat flux.

Gupta made a comprehensive review in 2014 on experimental investigations of forced convective heat transfer characteristics for various nanofluids. It was concluded that most of the experimental studies demonstrated improved heat transfer coefficient for

nanofluid and it increases with increasing nanoparticle concentration as well as Reynolds number. However, no general correlation or equations have been developed for accurately predicting convective heat transfer coefficient for nanofluids.

Most experimental investigations on forced heat transfer of nanofluids remain inconclusive today due to different experimental conditions across research groups and no consensus is reached on the mechanisms responsible for forced heat transfer enhancement. A brief literature review indicates the research direction in nanofluids application and the following information can be obtained

- Nanofluids behave like single-phase fluids conditionally, depending largely on the base fluid, nanoparticle materials, concentration and size. More experimental evidence is needed to evaluate the applicability of traditional convective heat transfer correlations available in the literature for single-phase flows to estimate the nanofluids forced heat transfer performance.
- Under forced convective flow condition, either in the laminator turbulent regime, the shear stress and temperature gradient in the boundary layer may lead to distribution of nanoparticles, resulting in a non-uniform thermal conductivity and viscosity distribution, changing the thermal resistance of boundary layer.
- Using numerical simulation to estimate the migration on movement of nanoparticles due to Brownian motion or thermophoresis to check for two-phase flow behavior of nanofluids. Slip velocity between particle and base fluid might play crucial role in heat transfer performance.

- Forced heat transfer enhancement is not observed for all nanofluids with enhanced thermal properties but is observed only under suitable conditions such as appropriate particle size and material, correct distribution, and appropriate synthesis protocol.
- For development of nanofluids for a wide spectrum of heat transfer applications it is essential to understand the fundamentals of heat transfer and wall friction. More feasible models are to be developed and validated with experimental evidence.
- Enhanced thermal conductivity is not only the factor influencing forced heat transfer performance of nanofluids. Several underlying mechanisms such as nanoparticle behavior in the boundary layer can also be possible reasons. Numerical simulations such as Boltzmann dynamic simulations might provide clear insight into the nanoparticles motion and distribution in the boundary layer of the nanofluids

1.5.2 Two-phase heat transfer

Numerous reports exist in the literature on nanofluid two-phase flow. However, due to the complicated physical phenomena, the fundamentals of two-phase flow and boiling heat transfer with nanofluids are not well characterized. No accepted physical phenomena or prediction models for two-phase flow, boiling heat transfer, and two-phase pressure drop exist for nanofluids. As an interdisciplinary research subject, there are still challenges in understanding the physical mechanisms associated with nanofluid two-phase flow and boiling heat transfer. Table 8 summarizes few reported flow boiling heat transfer of nanofluids in macroscale channels.

The overall thermal resistance of a closed two-phase thermosiphon was investigated by Khandekar et al., [117] using aqueous nanofluids (Al_2O_3, CuO, and laponite clay) as the working fluids. The experimental results indicate heat transfer performance deteriorated compared to water. Henderson et al. [118] studied flow boiling of R134a-based nanofluid in a horizontal pipe and have found flow boiling heat transfer performance enhanced through nanofluids. However, Xue et al. [119] investigated the thermal performance of a CNTs– water nanofluid in a closed two-phase thermosiphon and found that the nanofluid deteriorated the heat transfer performance.

Park et al. [120] investigated flow boiling heat transfer performance of nanofluids in a horizontal plain tube having an inside diameter of 8 mm. They report a decrease in heat transfer performance and attribute the deterioration to particle deposition on the tube surface. Akhavan-Behabadi et al. [121] studied the effect of efficacy of R600a-Polyester mixture (99/1)-CuO based nanofluid on flow boiling heat transfer in a horizontal smooth tube with an inner diameter of 8.2 mm. The nanoparticle concentrations varied from 0.5 – 1.5 wt.% and the experimental results indicate that a maximum enhancement of up to 63% was achieved at 1.5 wt%. Setoodeh et al. [122] performed subcooled flow boiling heat transfer experiments with aqueous Al_2O_3 nanofluid at 0.25 vol.% in a horizontal channel with a hot spot. The experimental results indicated that the heat transfer performance enhanced with increasing surface roughness and mass flux. Flow-boiling experiments with CuO/water nanofluids in an upward conventional heat exchanger were performed by Nikkhah et al. [123]. Surface images taken with the digital microscopic imaging system

revealed the thickness of deposited layer of nanoparticles and roughness of surface increased with time, potentially affecting the wettability of surfaces and the contact angle. The measured deposition increased with increase in nanoparticle concentration and mass flux. However, the particle deposition on the surface reduced with increase in wall temperature at higher values of heat flux as the heat transfer changed from the convection dominated regime to nucleate boiling dominated heat transfer regime.

Sarafraz et al. [124] investigated subcooled flow boiling in an upward annular channel with CuO/water nanofluids at 0.1-0.3% mass fractions. The experimental results indicate that the heat transfer coefficient decreased with increase in nanoparticle mass fraction. Flow visualization revealed that with decreasing mass flux or increasing heat flux resulted in increase in bubble sizes. Experimental investigation of aqueous nanofluids with Multi Walled Carbon Nanotubes (MWCNT), CuO, and Al_2O_3 nanoparticles in an upward annulus. Their results indicate that the MWCNT nanofluid has higher boiling heat transfer coefficient compared to Al_2O_3 and CuO nanofluids. Table 8 summarizes the nanofluid flow boiling studies in the literature.

Table 8. Summary of selected studies on flow boiling heat transfer of nanofluids.

Author	Nanofluid	Flow Configuration	Enhancement/Deterioration
Khandekar et al. [117]	Al_2O_3, CuO - water	Flow boiling in closed two-phase thermosyphon	Heat Transfer Deterioration
Henderson et al. [118]	R134a based nanofluid	Flow boiling in horizontal tube	Heat Transfer Enhancement
Xue et al. [119]	CNT-water	Flow boiling in closed two-phase thermosyphon	Heat Transfer Deterioration
Liu et al. [50]	Cu-water	Flow boiling in a miniature syphon	Heat Transfer Enhancement
Ma et al. [125]	Diamond-water	Flow boiling in an oscillating heat pipe	Heat Transfer Enhancement
Liu et al. [126]	CuO-water	Flow boiling in a flat heat pipe evaporator	Heat Transfer Enhancement
Liu and Qiu [127]	CuO-water	Boling heat transfer of jet impingement	Heat Transfer Enhancement
Park et al. [128]	Refrigerant based nanofluid	Flow boiling in horizontal tube	Heat Transfer Deterioration
Behabadi et al. [121]	CuO-R600a-Polyester	Flow boiling in horizontal tube	Heat Transfer Enhancement
Setoodeh et al. [122]	Al_2O_3-water	Flow boiling in horizontal tube	Heat Transfer Enhancement
Nikkhah et al. [123]	CuO-water	Flow boiling in upward conventional heat exchanger	Heat Transfer Deterioration
Sarafraz et al. [124]	CuO-water	Flow boiling in an upward annular channel	Heat Transfer Deterioration
Paul et al. [129]	Al_2O_3-water	Flow boiling in vertical tube	Heat Transfer Enhancement
Sarafraz and Hormozi [124]	MWCNT-water,CuO-water, and Al_2O_3-water	Flow boiling in upward annulus heat exchnager	Heat Transfer Deterioration
Wang and Su [130]	Al_2O_3-water	Flow boiling in vertical tube	Heat Transfer Enhancement

A short review of literature of flow boiling heat transfer of nanofluids in macro channels indicate that the following mechanisms are attributed to the enhancement in heat transfer

- Nanoparticle deposition on the heater surface
- Increase in thermo-physical properties such as thermal conductivity or specific heat capacity
- Enhanced heat transfer due to improved bubble dynamics caused by nanoparticle suspension

Nonetheless, the physical mechanisms responsible for heat transfer enhancement in flow boiling needs further investigation owing to the incongruous results from different researchers. Of particular contention is the modification in surface wettability resulting from nanoparticle deposition on the heater surface. Several reports in literature attribute the enhancement in heat transfer to the modification of surface characteristics while on the other hand several other reports attribute the heat transfer deterioration to the surface modification resulting from nanoparticle precipitation.

1.6 Motivation of this study

A vast majority of studies in the literature report on enhanced thermo-physical properties of molten salt nanomaterials for application in Concentrated Solar Power (CSP) applications. However, issues such as actual flow behavior of such nanofluids, ease of synthesis, economic feasibility and long-term stability need to be addressed for actual application in a CSP plant. For a significant number of reports in the literature, the actual

cost of the nanoparticle employed in the synthesis of molten salt nanomaterial offsets the benefits from enhanced thermo-physical properties. Furthermore, to the best of the knowledge of the author, no experimental data exists on the heat transfer characteristics of molten salt nanomaterials in a forced convective flow loop. Hence, a novel and cost-effective synthesis protocol for generating stable molten salt nanomaterials, thermo-physical property characterization, material characterization, and heat transfer characteristics of prepared nanofluids are investigated in this study.

1.7 Objective of this study

The goal of this study is to characterize the thermal-hydraulic performance of molten salts and molten salt nanomaterials in a closed loop flow system, identify suitable precursor candidates for the realization of molten salts nanomaterials (e.g., nanofluids) and characterize their effect on the thermo-physical properties such as thermal conductivity and specific heat capacity.

In addition, this study aims to measure the forced subcooled flow boiling heat transfer coefficient for various novel coolants (DI water and aqueous nanofluids) in straight circular pipe. The objective of this study is to investigate and contribute to the understanding of the thermo-fluidic behavior of various nanofluid coolants. To that effect, the thermal efficacy of nanofluid coolants with that of the pure solvent (De-Ionized Water or “DIW”) in macro channel flow were compared.

1.8 Significance

This study will strengthen and contribute new knowledge to the field of Thermal Energy Storage (TES) in Concentrated Solar Power (CSP) plants by developing and characterizing advanced working fluids. Furthermore, this study will to contribute to the fundamental understanding of transport phenomena at nano-scale. This will be achieved by fulfilling the following objectives:

- Novel and convenient synthesis approach for molten salts nanomaterial
- Characterization and analysis of thermo-physical properties (e.g., specific heat capacity, thermal conductivity etc.)
- Microscopic material characterization of molten salts nanomaterial (e.g., crystal structure, nanoparticle size, distribution, etc.)
- Heat transfer and fluid flow characteristics of aqueous nanofluids

The results from this study are also applicable to many other energy related technologies as discussed in section 0 such as nuclear power and oil recovery where nanofluids with enhanced thermo-physical properties and heat transfer characteristics could enable better industrial performance.

1.9 Summary

This study aims to provide a pathway for implementation of advanced materials such as molten salt nanomaterials as Thermal Energy Storage (TES) medium and Heat Transfer Fluid (HTF) in Concentrated Solar Power (CSP). Experimental studies in this effect to synthesize and characterize the molten salt nanomaterials for thermo-physical properties, heat transfer and pressure drop performance were performed.

Section 2 provides a detailed overview of the experimental techniques developed and standardized in this study thus far including synthesis technique and protocol for molten salt nanomaterials, material and microscopic characterization, thermal stability and colloidal stability tests and a detailed overview of the assembly components of a forced convection flow loop apparatus for heat transfer and pressure drop performance testing. Section 3 provides experimental results for thermo-physical property measurements, material characterization and validation tests (water as working fluid) performed for flow loop apparatus.

Section 4 summarizes the results obtained for this study and key conclusions of the work, discusses the challenges of the work and provides a direction for future research in the field of molten salt nanomaterials and advanced working fluids such as aqueous nanofluids.

2. EXPERIMENTAL METHODS

The experimental work performed in this study can be categorized as shown in Figure 19.

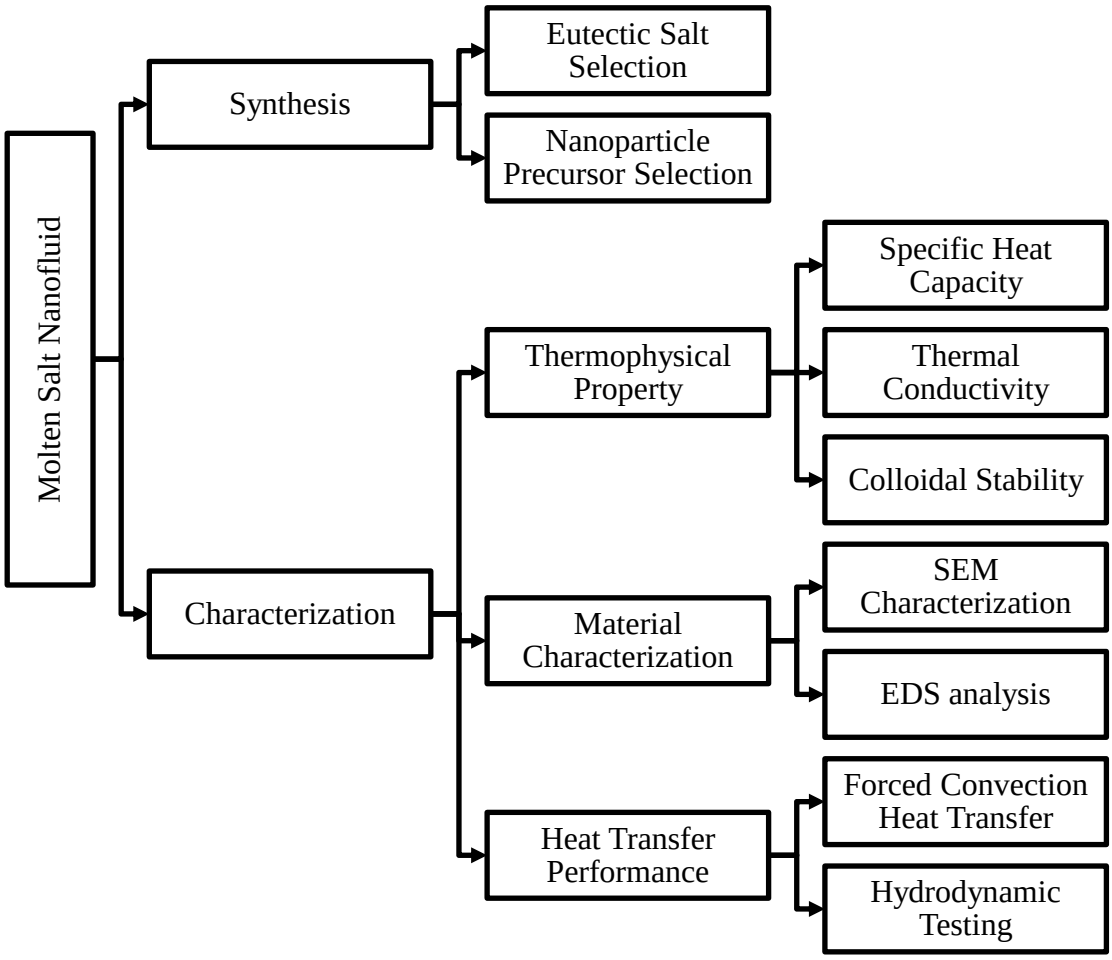

Figure 19. Overview of the experimental work performed in this study.

2.1 Material Synthesis

In this study, the $NaNO_3$-KNO_3 binary nitrate salt (solar salt) and $NaNO_3$-KNO_3-$LiNO_3$ ternary eutectic-based nanofluids were prepared using innovative one-step synthesis protocols. 50g sample is synthesized each time for comprehensive thermo-physical property test. Each nitrate salt component is purchased directly from Sigma-Aldrich (with a reagent grade ~ 99% purity) and are used directly without further purification to mimic the condition in actual CSP operations.

2.1.1 Overview: Conventional two-step method for nanofluid synthesis

The conventional synthesis protocol for nanofluid involves a two-step procedure, namely: synthesis or procurement of nanoparticle and dispersion of nanoparticles in the base solvent. The advantage of such synthesis protocol include simplicity, and control of nanoparticle size and shape. Nanofluids prepared through two-step techniques suffer from compromised colloidal stability, as nanoparticles tend to agglomerate and precipitate over time. Ultrasonic nanoparticle fracturing is the widely used technique for nanofluid stabilization that uses sound waves to break particle agglomerates into fine particles. Another powerful technique employed for stabilizing nanofluids is by forcing nanofluid through narrow passage under high pressures. Although, this technique of rupturing agglomerates into fine particles under high shear termed as High-Pressure Homogenizing (HPH) is not explored thoroughly, few nanofluids prepared through HPH exhibited smaller particle size distribution. Several other stabilization techniques include addition of dispersant (or surfactant), pH control to alter the zeta potential or through addition of

functional groups for surface modification of nanoparticles to reduce the surface energy of nanoparticles. Hence, the synthesis of nanofluid via two-step method is not mere addition of nanoparticles but rather a complex process of stabilizing the nanofluid. As a result, nanofluid researchers started exploring alternate synthesis techniques such as one-step method that combines synthesis and dispersion of nanoparticles into a single step. Such synthesis protocols are classified as physical or chemical techniques based on the nature of approach. In this study, a thermal decomposition technique [131] is adapted for its advantages such as low cost instrumental needs, ease of scalability to industrial applications.

2.1.2 Direct one-step method (dry mixing)

In the one-step synthesis technique, employed in this study, all the salt components including the nanoparticle precursor are premixed in dry powder form in a beaker. The premixed mixture of salt components is subsequently heated in a furnace to a predetermined temperature to yield nanoparticles. Thermogravimetric Analysis (TGA) of the nanoparticle precursor determines the temperature for the synthesis protocol. The ideal range temperature range of decomposition for nanoparticle precursor lies within the melting point and decomposition temperature of the base solvent. During the heating process the furnace is set to a temperature above the decomposition temperature of the nanoparticle precursor to ensure nanoparticle generation. During the decomposition reaction of precursor - the solvent is in liquid phase - thus yielding molten salt nanofluids.

The procedure is illustrated in Figure 20. The change in morphology before and after the heating and baking process is shown in

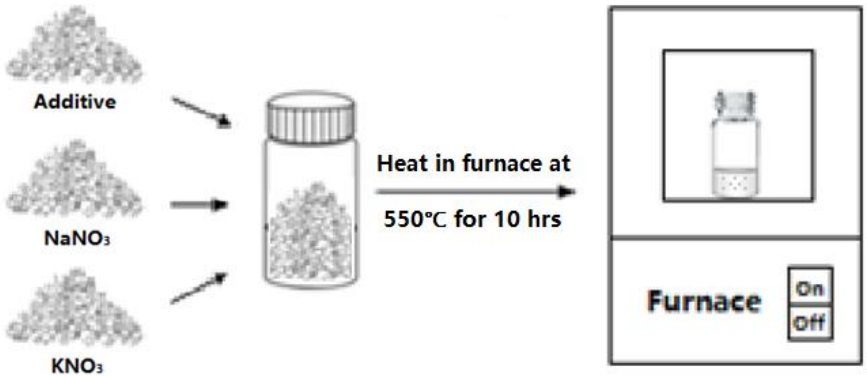

Figure 20 Schematic diagram of direct one-step synthesis procedure (dry mixing) [131].

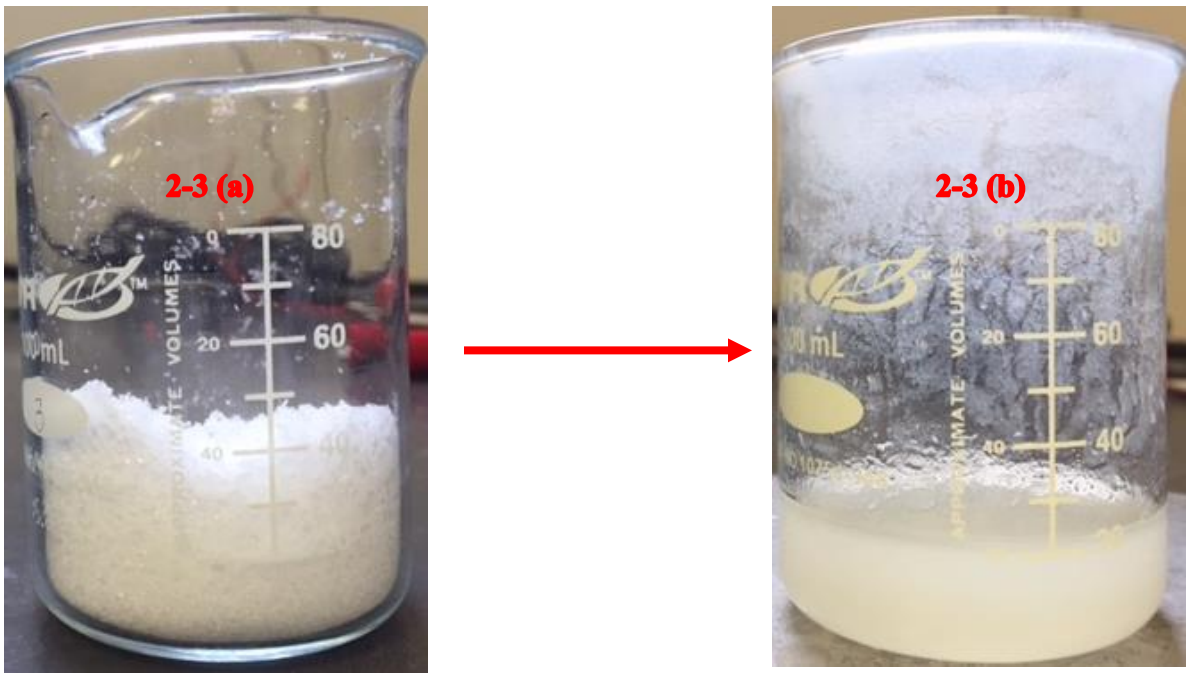

Figure 21 Samples images of Ternary Nitrate Salt nanofluid samples. a.) Nitrate salt additive mixture with nanoparticle precursor b.) Molten salt nanofluid after melting and baking the mixture in muffle furnace.

2.2 Material Characterization

2.2.1 SEM Imaging

Material characterization of the prepared nanofluid samples is realized using Scanning electron microscopy (SEM) coupled with Energy Dispersive X-Ray Spectroscopy (EDS). The microstructure of the samples was analyzed with FEI QUANTA 600 FE-SEM. A comparison of images between pure molten salt samples and the nanofluid samples reveals the morphology of the generated nanoparticles. The meticulous procedure adapted for SEM sample preparation after nanofluid synthesis is as follows:

- Heat the substrate (silicon wafer or a DSC Aluminum pan) on a hot plate with temperature set to above the melting point of the sample
- Stir manually the beaker with nanofluid in liquid state by holding the beaker with tongs to ensure uniform dispersion of nanoparticles
- Transfer roughly (~5mg to 10mg) of sample from the beaker to the substrate
- Leave substrate with the sample on it for 5 minutes for complete melting of the sample
- Transfer the sample into a vacuum chamber to prevent any moisture absorption
- Based on the base solvent composition coat the samples with 80:20 Pt/Pd layer to enhance the thermal conductivity of the sample for better imaging
- For SEM parameters, the accelerating voltage is limited to 10KV and the working distance around 10mm. was employed for better resolution of images.

Energy Dispersive X-ray Spectroscopy (EDS) was performed to analytically determine the chemical composition of the samples. The interaction of a source of high-energy particles such as electrons or protons and the sample emits characteristic X-rays unique to the specimen. An energy-dispersive spectrometer measures the number and energy of emitted X-rays. As a result, elemental mapping was realized by performing regional EDS on a sample. Furthermore, the nanoparticles and the resulting microstructure chemical composition in the nanofluid samples was determined by point-shoot EDS analysis.

2.2.2 Dynamic Light Scattering for Nanoparticle Size

The particle size distribution in the molten salt nanomaterials was determined by means of Dynamic Light Scattering (DLS). The size distribution of nanoparticles in a liquid medium are determined non-invasively through DLS. Brownian motion is random fluctuation of particles suspended in a liquid medium due to bombardment of surrounding molecules. The particle motion is dependent on particle size, viscosity and suspension temperature. Interaction of light with particles results in light scattering. Hence, in a DLS, the light scattering because of particle illumination with a laser is measured and particle size is determined.

However, the diameter measured in a DLS is the hydrodynamic diameter of the particles i.e. an equivalent diameter corresponding to the diameter of a sphere with identical diffusion coefficient as that of the particle being measured. As a result, the DLS measurement result for non-spherical particles is often not interpreted appropriately. A

typical DLS measurement result includes intensity distribution of a particle size distribution in the liquid suspension. Furthermore, using Mie Theory [132]volume and number distribution can be determined from intensity distribution. The four assumptions that needs to be satisfied for this transformation:

- Particles are spherical
- All particles are homogenous in both composition and crystalline structure
- The optical properties of the particles are known i.e. refractive index
- Intensity distribution is error free

Hence, volume and number distributions derived from intensity distributions are never to be taken as absolute and should be used for comparative purposes only. In this study, Beckman Coulter Delsa Nano series was used to characterize the nanoparticle size distribution. The analysis was performed in room temperature for the molten salt nanomaterials. The synthesized salt samples are dissolved in de-ionized water just before the experimental measurement to avoid nanoparticle sedimentation. As shown in Table 9, the concentration of sample in the liquid solution is determined from the recommendations in [133].

Table 9. Nanoparticle concentration in the liquid solution for DLS measurement based on expected size [132].

Particle Size, nm	***Minimum Concentration***	***Maximum Concentration***
<10	0.5 mg/mL	Only limited by particle aggregation
10-100	0.1 mg/mL	5% mass
100-1000	0.01 mg/mL	1% mass

2.3 Stability Testing

2.3.1 Thermal Stability Test

Thermogravimetric analysis (TGA) and Differential Scanning Calorimetry (DSC) are the most widely employed instruments for thermal stability measurement of molten salts. The advantages of TGA and DSC include fast measurement result and accuracy but suffer from short reaction times during measurement and chemical equilibria are not reached. Hence, the mass loss data measurement result from TGA and DSC does not provide a realistic estimate of chemical stability of pure molten salts or molten salt nanomaterials. Therefore, pure nitrate salts and molten salt nanomaterials synthesized in this study are tested for mass loss at elevated temperatures (565°C). Erlenmeyer flasks contained about 27.5g of molten salt were thermo-cycled in a furnace and the total mass change was recorded before and after each testing cycle. Flasks with stopper prevented evaporative loss of the nitrate salt at elevated temperatures. The detailed procedure followed is as follows:

Process I: Synthesis of molten salt nanofluid

- The following amount of salt components and precursor are weighed carefully

Salt system	**$NaNO_3$**	**KNO_3**	**$LiNO_3$**	**Precursor**
Ternary nitrate salt	4.05g	15.11g	8.33g	NA
Ternary nitrate salt - Al_2O_3 nanofluid				2.04g $Al(NO_3)_3.9H_2O$

- The salt and precursor are transferred to a glass beaker and stirred for five minutes manually to attain uniform mixing
- Bake the powder form contents of the salt mixtures in a muffle furnace for 3 hours at 550°C.

Process II: Stability test protocol

- Weigh Erlenmeyer flask and the stopper carefully on a precision microbalance
- Transfer 27.5g of molten salt sample into the flask and place the stopper on top of the flask
- Reweigh the total mass of beaker (M_0) with molten salt sample (pure salt or nanofluid sample) along with stopper
- Soak the sample in a muffle furnace for 72 hours at 550°C
- After the predetermined soaking time, measure the mass (M_1) of the testing beaker on a precision microbalance immediately
- Remove the stopper carefully and reweigh the mass of the testing flask (M_2) with molten salt sample

- Heat the molten salt flask without the stopper on a hot plate at 250°C for 1 hour
- Measure the mass of the testing sample (M_3) on a precision microbalance after heating on a hot plate
- Repeat the thermal cycling steps for two more cycles

2.3.2 Colloidal Stability Test

The long term colloidal stability of molten salt based nanofluids is crucial for efficient implementation in an engineering application. In low temperature nanofluids based on water or Heat Transfer Fluids (HTF) surfactants can enhance the stability of the suspension. Such stabilization techniques are impractical to molten salt based nanofluids owing to extreme operating temperatures. Nanoparticles in a solvent collide and agglomerate and finally precipitate. Hence, characterization of colloidal stability of the nanofluids is crucial for design evaluations. Currently, there is no standard technique or method for characterizing the colloidal stability of molten salt nanofluids. Visual observation under quiescent conditions is the commonly employed measurement technique by researchers to estimate the colloidal stability. In this study, colloidal stability of the ternary nitrate salt nanofluids is estimated through a similar visual observation technique. As shown in Table 10, the molten salt nanofluid samples were obtained by adding $Al(NO_3)_3 \cdot 9H_2O$ at different mass fraction (as nanoparticle precursor) to pure ternary nitrate salt eutectic for different target mass fractions of resulting Al_2O_3 nanoparticles obtained by thermal decomposition (one-step synthesis protocol).

Table 10. The compositions of various salt for different target concentrations of nanoparticles after thermal decomposition in ternary nitrate salt eutectic system

Ternary nitrate eutectic nanofluid	Initial synthesis mass (g)				Target mass (g) after decomposition reaction			
	KNO_3	$NaNO_3$	$LiNO_3$	$Al(NO_3)_3.9H_2O$	KNO_3	$NaNO_3$	$LiNO_3$	Al_2O_3
0.5% Al_2O_3 by mass fraction (target)	19.13	5.13	10.55	1.29	19.13	5.13	10.55	0.17
1.0% Al_2O_3 by mass fraction (target)	19.04	5.10	10.49	2.60	19.04	5.10	10.49	0.35
1.5% Al_2O_3 by mass fraction (target)	18.94	5.08	10.44	3.92	18.94	5.08	10.44	0.53

Synthesized nanofluids are transferred into a standard glass vial and are left in a muffled furnace at 300°C undisturbed. Periodic photographs of the suspension were obtained using a digital camera. The photographs were recorded 1 hour, 2 hours, 3 hours, 24 hours (1 day), 48 hours (2 day) up to 14 days after synthesis of the fresh samples

2.4 Thermo-physical Properties Measurement

2.4.1 Specific Heat Capacity

The specific heat capacity of the different samples was measured using a lumped capacitance (T-History) method. The measurement technique put into effect also influences the specific heat capacity enhancement observed. Modulated Differential Scanning Calorimetry (MDSC) is an established technique of specific heat capacity characterization. The typical sample size in a MDSC is ~15mg. Nanofluids inherently are non-homogeneous colloidal mixtures; as a result, property measurements performed for very small quantities (~15mg, typical MDSC sample size) differ from bulk property value. Although, specific heat capacity is an intensive property i.e. independent of sample mass, for nanofluids an experimental method capable of measuring specific heat capacity of larger sample quantities (~30g) is required given the non-homogenous nature of suspensions. Hence, T-History measurement technique is preferred over DSC in this study to characterize the molten salt nanomaterials on a scale (~30g) representative of actual engineering applications. The source of measurement error in T-History technique is variation of environment temperature (by ~10°C within the testing furnace) and thermocouple measurement uncertainty. The experimental details and analysis of the T-History method employed in this study are discussed below.

2.4.1.1 Lumped capacitance method (T-History method)

Figure 22 and Figure 23 indicates the experimental schematic for lumped capacitance (T-History test). At the center of furnace, two identical vials with different samples undergo consecutive heating and cooling. One test vial contains pure ternary salt eutectic (reference sample ~30g) and an identical vial consists of nanofluid sample (test sample~30g). Mass of individual vials was recorded carefully before and after sample filling using a precision analytical balance (Ohaus Scout 220). Both vials, reference sample and nanofluid sample, are preheated to 150°C in a muffle furnace. Thermocouples are inserted into both the samples to monitor the temperature and ambient air temperature around the samples. The furnace is allowed to reach steady state conditions. T-History measurements start with ramping up the furnace temperature from 150°C to 550°C. The temperature change of both the samples is recorded in the heating ramp to upper limit of 550°C. Once both the samples reach 550°C, the temperature ramp is cut off and furnace temperature is set back to 150°C. This cycle is repeated for three times consecutively. The specific heat capacity ratio between the samples is computed from the temperature history curve obtained for both reference and testing sample (nanofluid).

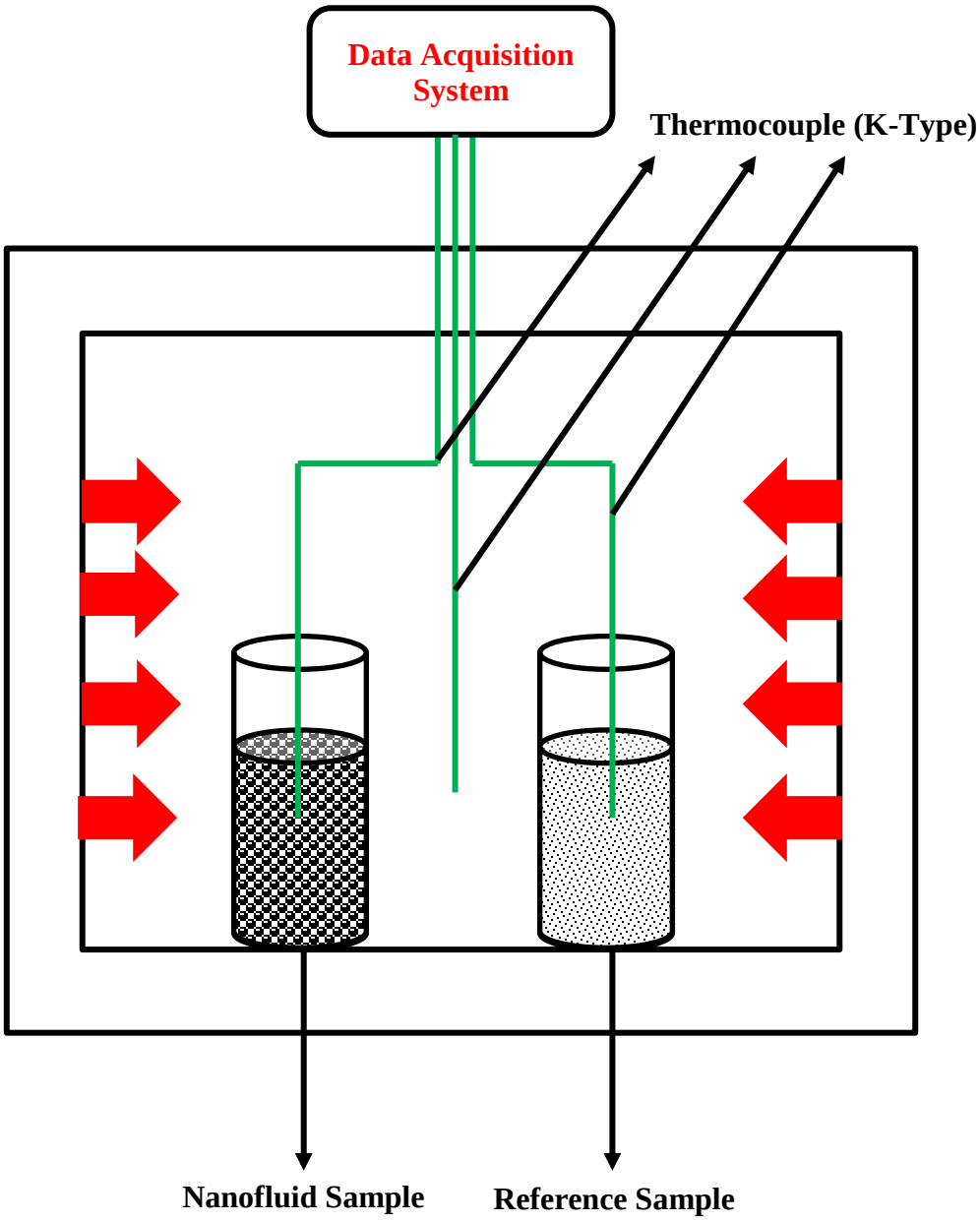

Figure 22. Schematic of the experimental setup for specific heat capacity measurement using transient T-History method.

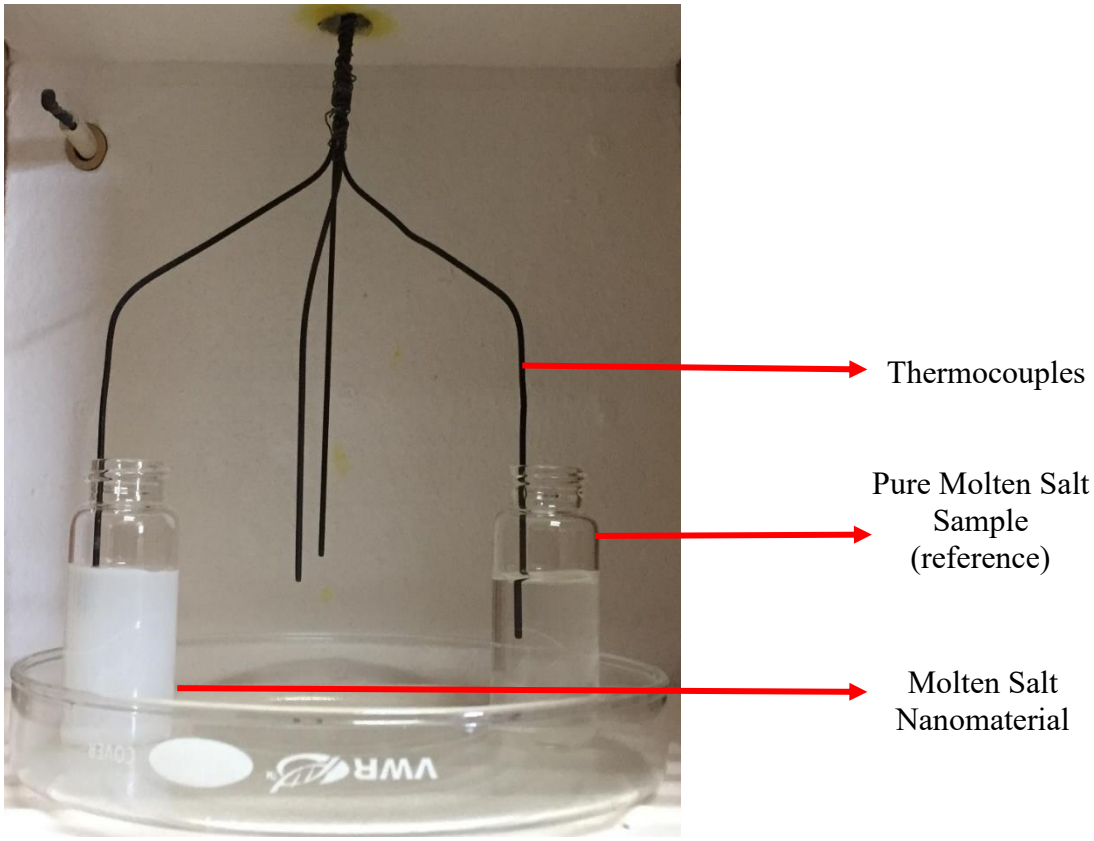

Figure 23. Actual experimental transient T-History setup for specific heat capacity measurement of molten salt nanofluid in a muffle furnace.

To validate the testing protocol it is essential to check for Biot number < 0.1 to satisfy the lumped capacitance assumption. The Biot number for the reference sample is computed from:

$$Bi = \frac{h_{air} L_c}{k} = \frac{h_{air} V_{sample}}{A_{surface} k} \quad (1)$$

Where, h_{air} is the natural convection coefficient, L_c is the characteristic length for the sample computed from V_{sample} (volume of the sample) and $A_{surface}$ (surface area of the vial) and k is the thermal conductivity of the sample.

The testing vial used in this study is 1.0 inch in diameter and has a nominal height of 1.25 inch. The characteristic length computed is L_c **= Volume/Area = 4.5 mm.** The thermal conductivity of the pure ternary eutectic is estimated to be 0.5 W/mK and the natural convection heat transfer coefficient is assumed to 5 W/m^{2}K. The Biot number computed from Equation (1) is found to be 0.045 validating the lumped capacitance system assumption. This enables to treat the temperature within the sample to be uniform for the period of testing. The rate at which temperature of the sample change is given by

$$T'_{sample} = \frac{dT_{sample}}{dt} = \frac{h_{air} A_{surface} \left(T_{air} - T_{sample}\right)}{m_s C_{p,sample}} \tag{2}$$

Where, T_{air} and T_{sample} are instantaneous temperature of the air and the sample, m_s and C_p are the mass and specific heat capacity of the testing sample.

The surface area of both the vials is equal considering equal mass of samples inside. The variation of natural convective heat transfer coefficient between the samples is negligible. As a result, the ratio of specific heat capacity between the samples at any instant can be expressed by:

$$\frac{C_{p,sample}}{C_{p,ref}} = \frac{m_{ref}}{m_{sample}} \frac{\left(dT/dt\right)_{ref}}{\left(dT/dt\right)_{sample}} \frac{\left(T_{air} - T_{sample}\right)_{nano}}{\left(T_{air} - T_{ref}\right)_{ref}} \tag{3}$$

In this study, 8th order polynomial curve fit is employed to fit the temperature history of both reference and nanofluid samples with respect to time. The order of the curve fit enabled smooth profile compared to that of two-point finite difference method.

2.4.1.2 Uncertainty Analysis

Uncertainty of the experimental measurement is estimated by Kline-McClintock method [134]. Temperature measurement of both nanofluid and reference samples was accomplished using K-Type probe thermocouples. All thermocouples are calibrated in-house using a standard NIST thermometer. Uncertainty associated with $\boldsymbol{T_{air}}$, $\boldsymbol{T_{sample}}$ and $\boldsymbol{T_{ref}}$ were approximately 0.1% after calibration.

$$\frac{C_{p,nano}}{C_{p,pure}} = \frac{m_p}{m_n}\frac{(dT/dt)_p}{(dT/dt)_n}\frac{(T_{air}-T_n)}{(T_{air}-T_p)} \tag{4}$$

$$\text{Uncertainty in } C_p \text{ ratio is : } \left[\left(\frac{\partial y}{\partial(T_{air}-T_n)}\right)^2 \in_1{}^2 + \left(\frac{\partial y}{\partial(T_{air}-T_p)}\right)^2 \in_2{}^2\right]^{1/2} \tag{5}$$

where, $\boldsymbol{y}$ is the specific heat capacity ratio between nanofluid sample and reference sample, $\boldsymbol{\varepsilon_1}$ and $\boldsymbol{\varepsilon_2}$ are the uncertainties associated with temperature difference between air and nanofluid, air and reference sample, respectively.

2.4.2 Thermal conductivity

A customized concentric cylindrical chamber was employed for the thermal conductivity measurement for pure molten salts and molten salt nanomaterials synthesized in this study. The design and construction of the experimental apparatus was performed after careful review of existing thermal conductivity measurement techniques for nanofluids. The apparatus used in this study is a concentric cylindrical steady state device. The principle of measurement is to obtain a 1-D steady state heat conduction in the radial direction of a concentric cylinder across a thin molten salt film as shown in Figure 24. The apparatus was placed in a muffle furnace to attain steady state condition for a constant ambient temperature.

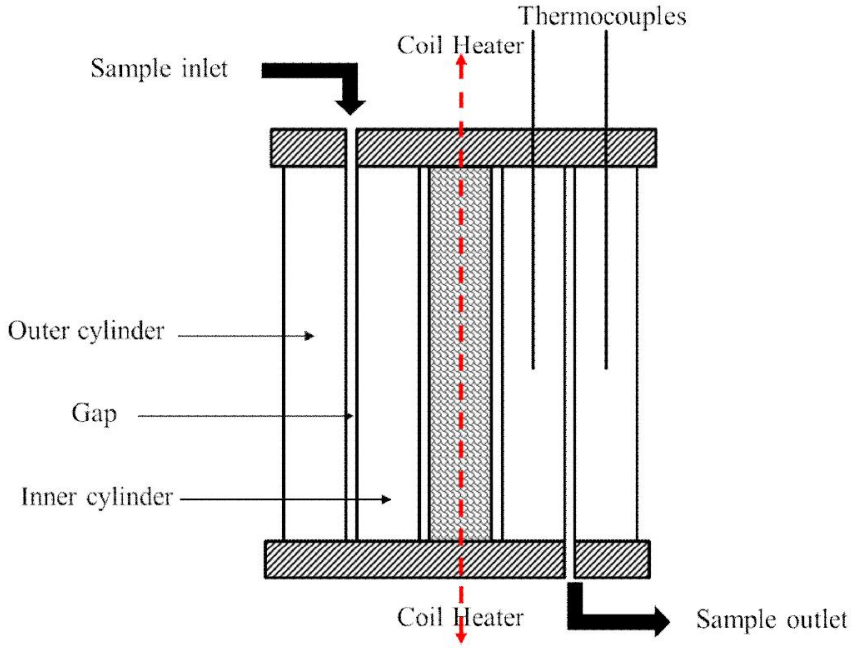

Figure 24. Design of thermal conductivity testing chamber [131].

2.4.2.1 Concentric cylindrical testing chamber

Accounting for the interior space of the furnace the dimensions of the chamber are finalized and are listed in Figure 26. The apparatus consists of an inner cylinder and an outer cylinder shown in Figure 25 & Figure 26. A heater source in the form of a cartridge heater is placed into the inner cylinder to provide constant heat flux and the entire assembly is inserted into the outer cylinder. The outer cylinder is filled with testing sample before inserting the inner cylinder assembly. Eight thermocouples are placed in pairs along the radial direction in the holes shown in Figure 28 and the temperature drop across the molten salt film is measured. From steady state 1-D radial heat conduction the thermal conductivity of the molten salt sample is given by

$$\mathrm{k} = \frac{\dot{q} \cdot \ln(r_2/r_1)}{2\pi L \Delta T} \qquad (6)$$

where, $\dot{q}$ is the applied power, L is the height of the testing chamber, r_1 and r_2 are the inner and outer radius of the concentric cylinder, respectively.

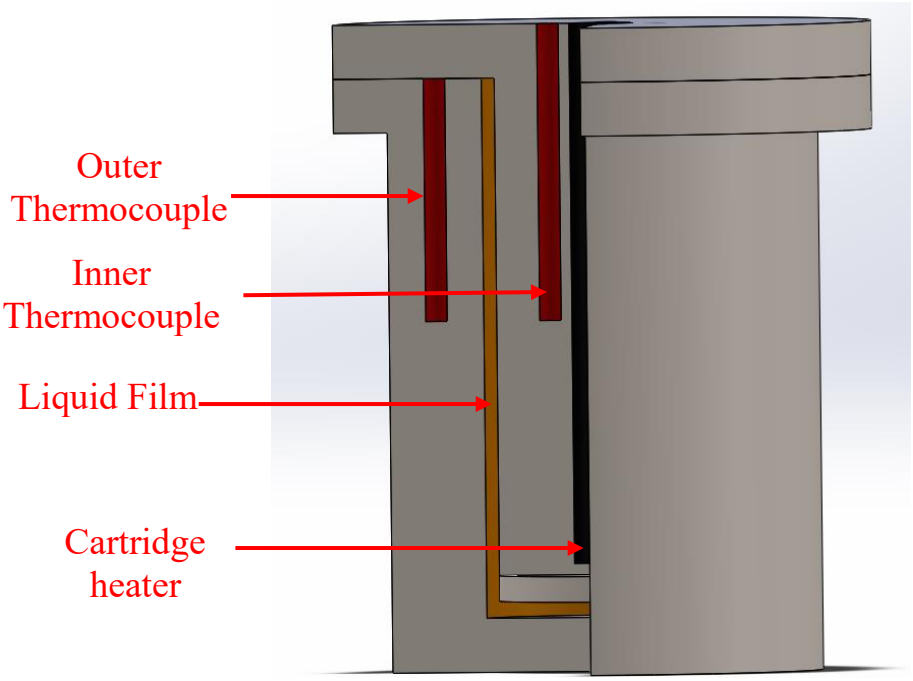

Figure 25. Schematic of cross section of the experimental apparatus for thermal conductivity measurement.

The thermal conductivity of the testing samples could be measured at different temperatures by adjusting the furniture temperature. Figure 25 illustrates the position of thermocouples and the liquid film.

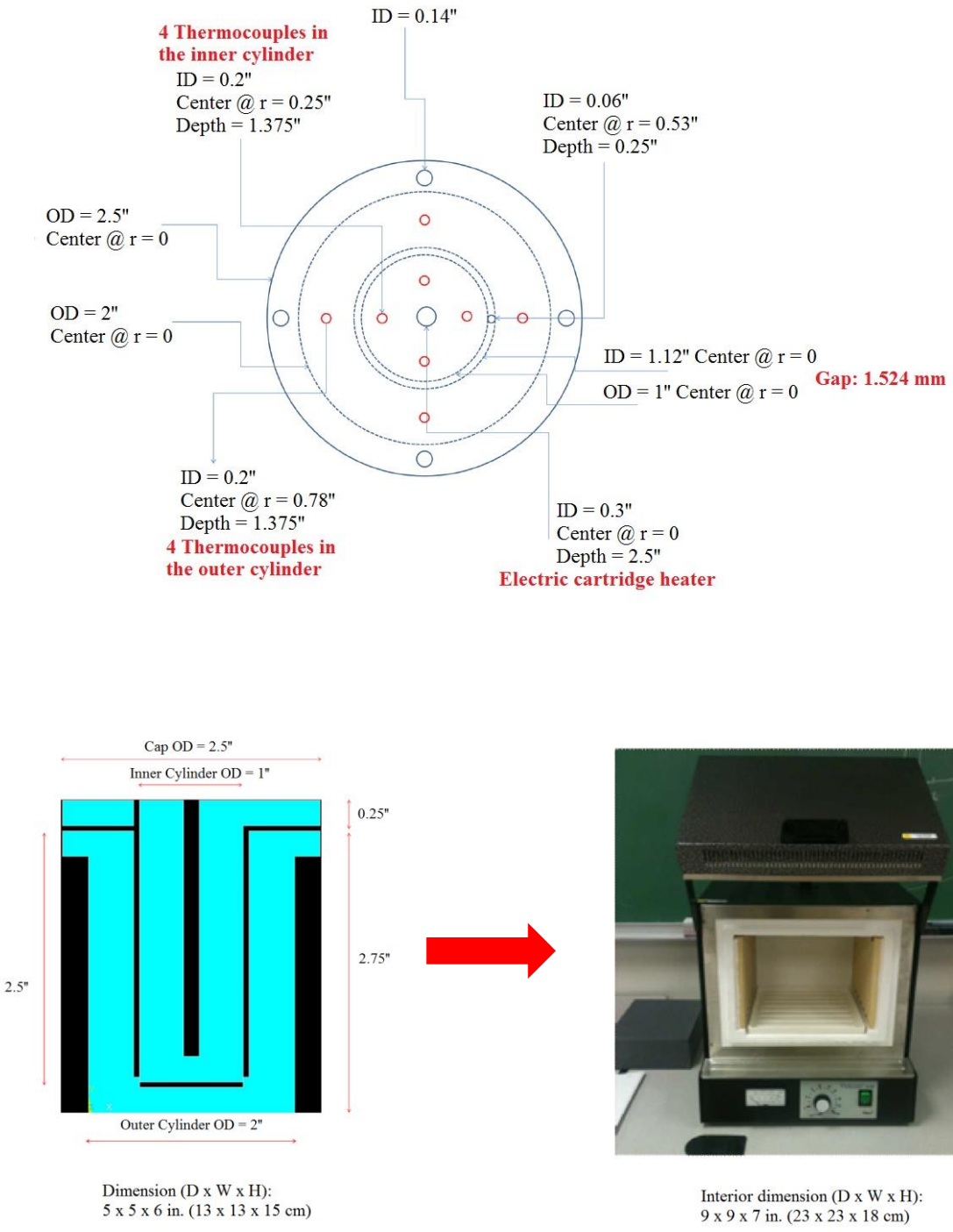

Figure 26. Design and dimensions of the concentric cylinder test apparatus for measuring thermal conductivity [131].

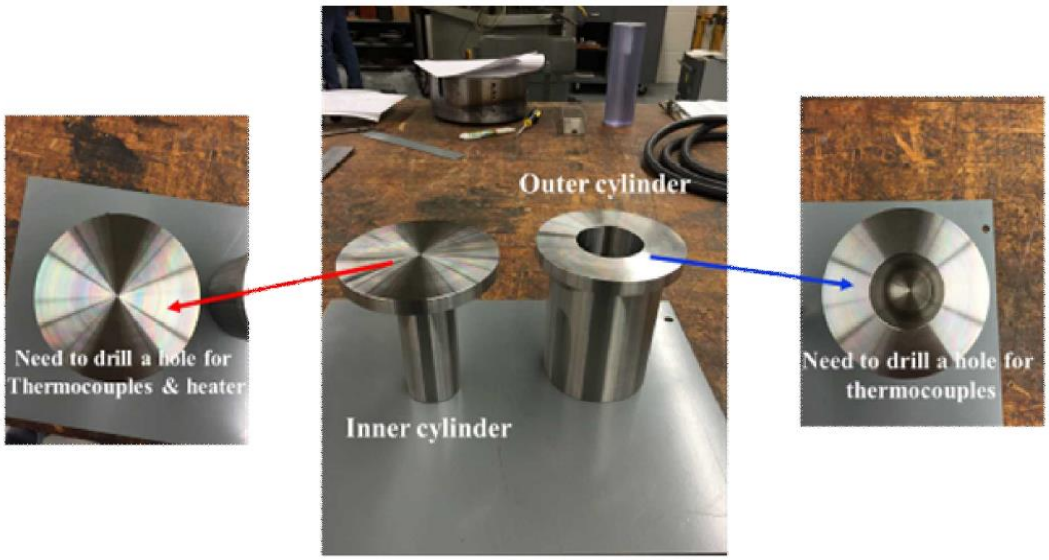

Figure 27. Design and assembly of the concentric cylinder test apparatus for measuring thermal conductivity.

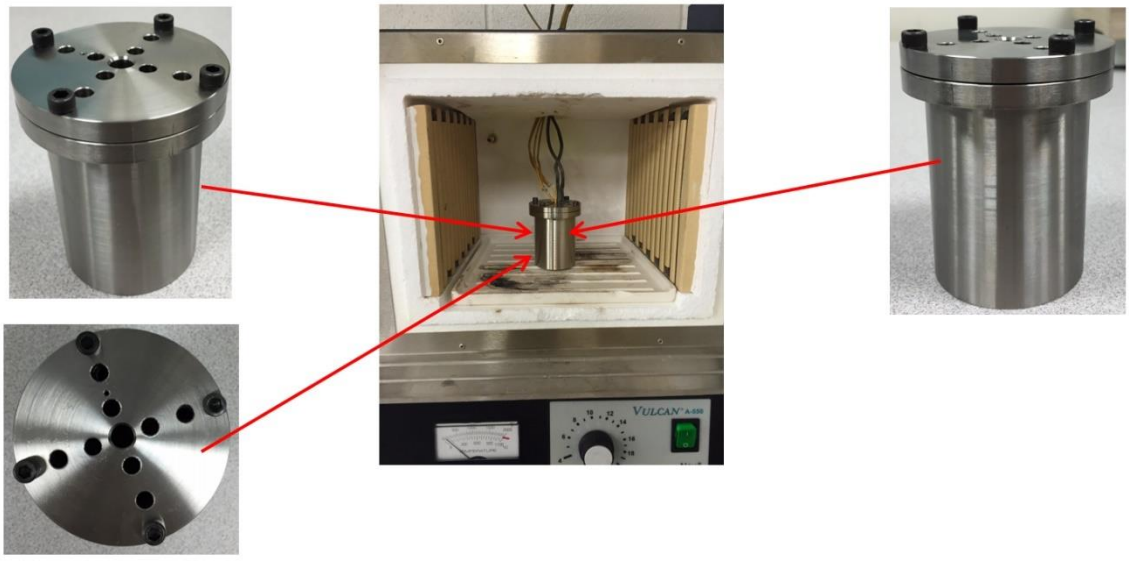

Figure 28. Assembly and implementation of the concentric cylinder test apparatus for measuring thermal conductivity [131]**.**

2.4.3 Density

As discussed earlier in section 1.4.4 , review of experimental results in the literature clearly demonstrate the deficiencies of the simple mixing rule for accurately predicting the density of nanofluids. In this context, a simple analytical model to predict the effective density of nanofluids accounting for the interfacial phenomena (at the solid-liquid interface) has been proposed in this study. The model proposed in the present study depicting the deviant densification of neat solvents is of practical relevance for the applications of nanofluids as coolants and for thermal energy storage (TES), including phase change materials (PCM) such as molten salt nanofluids and industrial grade solvents.

A simple mathematical model accounting for the interfacial phenomena at the solid-liquid interface was implemented in this study. The model developed in this study is based on a simple schematic and was formulated by considering an ensemble of spherical nanoparticles suspended and dispersed uniformly (or homogeneously) in a liquid phase (solvent). As shown in Figure 29, a compressed phase of the solvent molecules of a certain thickness (δ) was assumed to envelope each nanoparticle. An intervening "void space" (ε, which is the same order of magnitude as the equilibrium spacing for the molecules due to inter-molecular interactions, such as due to Van Der Waals forces and ionic repulsion interactions) was assumed to exist between the surface of the spherical nanoparticle and the compressed phase of solvent molecules engulfing each nanoparticle. Hence, a compressed layer (with a nominal thickness, δ, of 1 ~ 2 nm) of solvent molecules is considered to be the dominant player that modulates the effective density of the nanofluids

(along with an intervening void space with a thickness, ε, of ~0.5 nm, that is modeled to exist between the compressed phase and the surface of the nanoparticle).

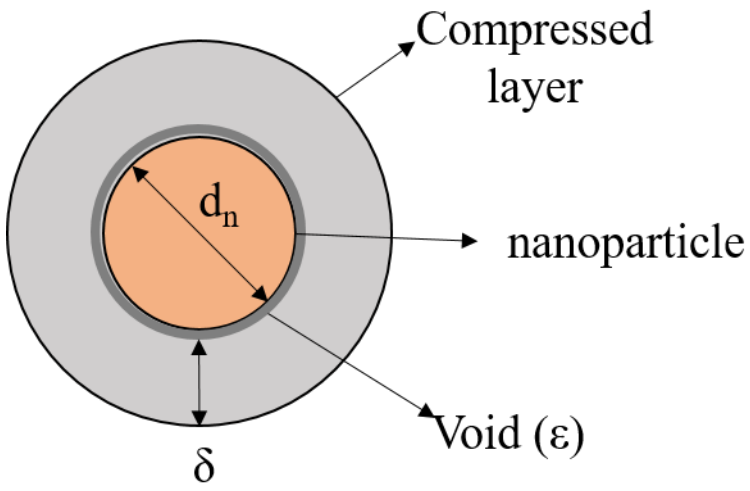

Figure 29. Graphical representation of a nanoparticle in a base fluid and surrounding interfacial layer for a spherical nanoparticle

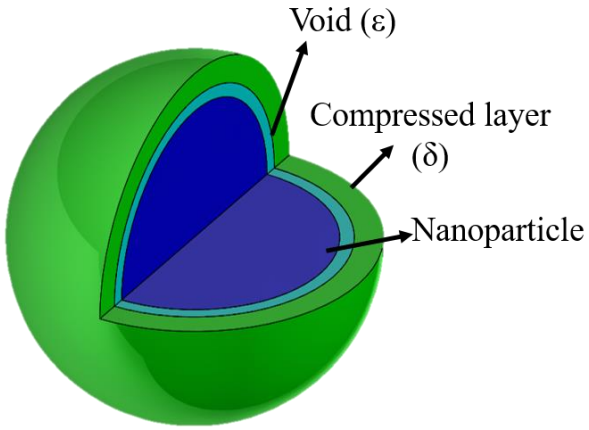

Figure 30. A 3D graphical representation of a nanoparticle in a base fluid and surrounding interfacial layer for a spherical nanoparticle

For a spherical nanoparticle, the analytical model (termed as compressed phase model), accounts for the contribution of the elevated density of the compressed phase (ρ_c) and the density of the bulk solvent phase (ρ_f) (which also the density of the neat solvent), as well as the density of the nanoparticle (ρ_n) to the total density of the nanofluid (ρ_{T2}). The total density of the mixture (ρ_{T2}) is calculated based on the mass fractions of the three individual components (nanoparticle, bulk solvent phase and compressed phase). The size and mass fraction of the compressed phase is varied parametrically (and this is based on information gleaned from the experimental measurements reported in the literature [135] for the thickness of the compressed phase and the numerical predictions reported in the literature [136, 83] for the density of the compressed phase estimated using Molecular Dynamics simulations). Based on this analytical model, the effective values of density for the nanofluid samples can be computed as:

$$\frac{1}{\rho_{T2}} = \frac{x}{\rho_n} + \frac{y}{\rho_c} + \frac{(1-x-y)}{\rho_f}; v_{T2} = xv_n + yv_c + (1-x-y) \qquad (7)$$

where, $\boldsymbol{\rho_{T2}}$ is the total (or effective) density (i.e., accounting for the compressed phase), $\boldsymbol{x}$ is the mass fraction of the nanoparticles, $\boldsymbol{y}$ is the mass fraction of the compressed phase, $\boldsymbol{\rho_c}$ is the density of compressed phase, $\boldsymbol{\rho_n}$ is the density of a nanoparticle, and $\boldsymbol{\rho_f}$ is the density of the bulk phase of the solvent (i.e., the density of the neat solvent), $\boldsymbol{v_{T2}}$ is the total (or effective) specific volume (i.e., accounting for the compressed phase), $\boldsymbol{v_c}$ is the

specific volume of compressed phase, $\boldsymbol{v_n}$ is the specific volume of a nanoparticle, and $\boldsymbol{v_f}$ is the density of the bulk phase of the solvent (i.e., the density of the neat solvent).

In contrast, using the simple mixing rule - the prediction from the conventional theory (which does not account for the formation of the compressed phase) can be used to predict the total (or effective) value of density of the nanofluid, ρ_{T1}, (or specific volume, v_{T1}) using a simple mixing rule and is expressed as follows:

$$\frac{1}{\rho_{T1}} = \frac{x}{\rho_n} + \frac{(1-x)}{\rho_f};\ v_{T1} = xv_n + (1-x)v_f \tag{2}$$

Rearranging the terms in Equation (2), we have

$$\rho_{T1} = \frac{\rho_f}{x\left(\frac{\rho_f}{\rho_n}\right) + (1-x)} \tag{8}$$

Defining,

$$F_1 = x\left(\frac{\rho_f}{\rho_n}\right) + (1-x) = 1 - x\left[1 - \left(\frac{\rho_f}{\rho_n}\right)\right] \tag{9}$$

the density, ρ_{T1}, (or specific volume, v_{T1}) predicted by simple mixing rule can be expressed as:

$$\rho_{T1} = \frac{\rho_f}{F_1};\ v_{T1} = v_f F_1 \tag{5}$$

Similarly, rearranging the terms for Equation (3), i.e., by accounting for the contribution of the compressed phase, the total density can be expressed as follows:

$$\left(\frac{\rho_f}{\rho_{T2}}\right) = x\left(\frac{\rho_f}{\rho_n}\right) + y\left(\frac{\rho_f}{\rho_c}\right) + (1 - x - y); \qquad v_{T2} = xv_n + yv_c + (1 - x - y)v_f \tag{6}$$

From purely geometric considerations - for a spherical nanoparticle, the ratio of the mass fractions for the nanoparticle (x) and the bulk of the solvent phase (y) can be expressed as:

$$\left(\frac{y}{x}\right) = \frac{V_c}{V_n}\frac{\rho_c}{\rho_n} \tag{7}$$

where, V_n is the volume of a nanoparticle and V_c is the net volume of the compressed phase (also, considering that there is zero mass in the void space). Accounting for the thickness of the compressed layer (δ) and the thickness of the void region (ε) between the compressed phase and surface of the nanoparticle (which is also the average equilibrium spacing between the first layer of the solvent molecules and the surface of the nanoparticles), the relationship between r_c (radial location of the outer extent of the compressed phase) and r_n (radius of the spherical nanoparticle) can be expressed as:

$$r_c = r_n + \varepsilon + \delta \tag{8}$$

From Equation (8), Equation (6) is expressed as:

$$\left(\frac{y}{x}\right) = \left(\frac{V_c}{V_n}\right)\left(\frac{\rho_c}{\rho_n}\right) = \left[\left(\frac{r_c}{r_n}\right)^3 - \left(1 + \frac{\varepsilon}{r_n}\right)^3\right]\left(\frac{\rho_c}{\rho_n}\right) \tag{9}$$

Introducing the mass fraction of compressed phase from equation (9) in equation (6) results in

$$\rho_{T2} = \frac{\rho_f}{F_1 + \left(\frac{\rho_f}{\rho_n}\right) y - y} \tag{10}$$

Defining,

$$F_2 = F_1 - y\left[1 - \left(\frac{\rho_f}{\rho_c}\right)\right] = F_1 - x\left(\frac{\rho_c}{\rho_n}\right)\left[1 - \left(\frac{\rho_f}{\rho_c}\right)\right]\left(\frac{V_c}{V_n}\right) \tag{11}$$

the density predicted by the modified mixing rule (accounting for the contribution to the total density from the compressed phase) can be expressed as:

$$\rho_{T2} = \frac{\rho_f}{F_2}; v_{T2} = v_f F_2 \tag{12}$$

Hence the surplus contribution to density (ρ_{T21}), or specific volume (v_{T21}), that is above and beyond the predicted values for density that is obtained from the simple mixing rule, can be expressed as:

$$\rho_{T21} = \rho_{T2} - \rho_{T1} = \frac{\rho_f}{F_2} - \frac{\rho_f}{F_1};\ v_{T21} = v_{T2} - v_{T1} = v_f(F_2 - F_1) \tag{13}$$

Hence, the percentage value of the surplus contribution to specific volume (Δ_{v21}), that is above and beyond the predicted values for density obtained from the simple mixing rule, can be expressed as:

$$\Delta_{v21} = \frac{(v_{T2} - v_{T1})}{v_{T1}} = \frac{(F_2 - F_1)}{F_1} \tag{14}$$

Substituting for the values of F_2 and F_1, the following expression is obtained:

$$\Delta_{v21} = -\frac{x\left(\frac{\rho_c}{\rho_n}\right)\left[1-\left(\frac{\rho_f}{\rho_c}\right)\right]\left(\frac{V_c}{V_n}\right)}{1-x\left[1-\left(\frac{\rho_f}{\rho_n}\right)\right]};\ \left(\frac{\Delta_{v21}}{x}\right) = -\frac{\left(\frac{\rho_c}{\rho_n}\right)\left[1-\left(\frac{\rho_f}{\rho_c}\right)\right]\left(\frac{V_c}{V_n}\right)}{1-x\left[1-\left(\frac{\rho_f}{\rho_n}\right)\right]} \quad (15)$$

Equation (15) shows that the absolute value of Δ_{v21} is maximized (i.e., surplus density term or the "deviant" density term is enhanced) when the numerator is maximized and the denominator is minimized. Hence, the value of Δ_{v21} is maximized, when:

1. the value of ρ_n is minimized (i.e., nanoparticles should have low density: preferably, the specific gravity of the nanoparticles should be less than 1);
2. the value of ρ_c is maximized (i.e., the compressed layer should have a high value of density, preferably, the specific gravity of the neat solvent should be more than 1; as a result aqueous nanofluids are ruled out since, as the compressed phase formed by water molecules on nanoparticle surface are expected to possess properties similar to that of ice; and ice typically has a specific gravity less than 1);
3. the value of ρ_f is minimized (i.e., the neat solvent should have a low density: preferably, the specific gravity of the neat solvent should be less than 1);
4. the ratio of $\left(\frac{\rho_f}{\rho_c}\right)$ should be less than 1 (i.e., the solid phase of the solvent should have a higher density than the liquid phase of the solvent; as a result - aqueous nanofluids are ruled out - as the compressed phase formed by water molecules on nanoparticle surface are expected to possess properties similar to that of ice; and since ice typically has a specific gravity less than 1);

5. the volume of the compressed phase is maximized (i.e., the volume of the compressed phase should be as high as possible);
6. the volume (or size) of the nanoparticle should be minimized (i.e., the volume or size of the nanoparticle should be as low as possible).

This theoretical analysis (for Δ_{v21} and ρ_{T21}) shows that careful design of experiments is needed to be able to conclusively discern the deviant enhancement in density arising from the contribution of the compressed phase while every effort should be made for minimizing measurement uncertainty.

2.4.3.1 Selection of Solvent Candidates:

The results from the MD simulations [83] show that the density of the compressed phase is typically 25 ~ 100% higher (i.e., almost double) than that of the neat of solvent (especially for non-aqueous solvents, such as for organic solvents, particularly for oil-based solvents and molten salt eutectics). Considering this behavioral pattern reported in the literature involving MD simulations, in this study, oil based solvents were chosen for the experiments. A paraffin-based oil, which is typically used commercially as phase change material (PCM), was procured for this study (from PureTemp, with commercial brand name: PureTemp-15X). Hence, assuming that for oil based solvents, approximately, $\left[\left(\frac{\rho_c}{\rho_f}\right) = 2\right]$; we get:

$$\Delta_{v21} = -\frac{x\left(\frac{\rho_c}{\rho_n}\right)\left(\frac{V_c}{V_n}\right)A}{1 - x\left[1 - \left(\frac{\rho_f}{\rho_n}\right)\right]} \quad (16)$$

where, the correction factor, A, is approximately 0.5 for oils. In contrast, for water, approximately, $\left[\left(\frac{\rho_c}{\rho_f}\right) \approx 0.9\right]$; since ice has a specific gravity of 0.9. As a result, we get, a positive value of Δ_{v21}, as shown below:

$$\Delta_{v21} = \frac{x\left(\frac{\rho_c}{\rho_n}\right)\left(\frac{V_c}{V_n}\right)B}{1 - x\left[1 - \left(\frac{\rho_f}{\rho_n}\right)\right]} \quad (17)$$

where, the correction factor, B, is approximately 0.1.

This theoretical analyses shows that the detection of the deviant density (or surplus density) caused by the compressed layer is virtually undetectable in experiments involving aqueous nanofluids and the density of the aqueous nanofluids are more likely to conform to the simple mixing rule (even for nanoparticles less than 6 nm diameter). Hence, aqueous nanoparticles may have a miniscule deviation in density (i.e., miniscule decrease in density) than that of the values predicted by simple mixing rule. This deviant density reduction for aqueous nanofluids is so tiny (estimated to be less than ~ 0.5%) that it is virtually undetectable by most of the conventional measurement techniques or commercial instruments that are typically used for measuring density (e.g., using densitometers). However, this analyses has significant implications for the specific heat capacity of aqueous nanofluids as well. This also implies, that the detection of the deviant values of

specific heat capacity (or surplus values of specific heat capacity) caused by the compressed layer is virtually undetectable in experiments involving aqueous nanofluids and the specific heat capacity of the aqueous nanofluids are more likely to conform to the simple mixing rule and there may be a miniscule degradation (less than 2%) in the values of specific heat capacity of aqueous nanofluids (even for nanoparticles less than 6 nm diameter), that are very difficult to detect since the typical measurement uncertainty for measurement of specific heat capacity (e.g., using Differential Scanning Calorimetry/ DSC) is approximately 5% or more. As mentioned before, it is interesting to note that studies in the literature (e.g., [99]) showed degradation in the specific heat capacity of aqueous nanofluid samples and were consistently below the predictions afforded by the various flavors of the simple mixing rule.

2.4.3.2 Selection of Nanoparticle Candidates:

Apriori, it is not known, what the density or thickness of the compressed phase will be for a given nanofluid (e.g., only indirect estimates can be obtained for these parameters from MD simulations), since these parameters are also very sensitive to even minute variations in the synthesis conditions (e.g., pH, surfactant concentration, synthesis temperature, etc.). Hence, to begin with, the density of the nanoparticles should be minimized (as the primary control variable in these experiments).

However, this creates a conundrum, since the conventional nanoparticles that are typically used for nanofluids experiments in the literature (such as metallic, ceramic or

carbon based nanoparticles) have specific gravity values typically exceeding 2 [137]. Typically, ceramic nanoparticles (such as silica, alumina, etc.) have a specific gravity of 2 (approximately). Metallic nanoparticles (such as tungsten, gold, silver, etc.) possess even higher values of specific gravity, often exceeding 2. Carbon based nanoparticles also possess specific gravity typically exceeding 2 (e.g., 2.2 for graphene, 3.5 for exfoliated graphite, 1.4 for carbon nanotubes, 3.4 for diamond nanoparticles, etc.). Carbon nanotubes have the lowest specific gravity but are also very difficult to disperse in typical solvents with the goal of obtaining stable nanofluids, i.e., for either aqueous-nanofluids or oleo-nanofluids (oil based nanofluids).

A brief literature search reveals that organic nanoparticles (such as proteins, lipids/ vesicles, etc.) have specific gravity less than 1 (typically, the values range from 0.4-0.9) [138]. However, commercial procurement of these nanoparticles tend to be very expensive and the material (or chemical) stability is very unreliable as proteins (as well as lipids/ vesicles) tend to denature promptly when subjected to thermal shock or mechanical stresses / shear forces or chemical gradients.

Interestingly, the proteins obtained from dehydrated non-fat skimmed milk (which is primarily composed of the protein, casein) are stable (even for severe thermal shock) and are easy to dissolve in water or oil. The Stokes-diameter of casein (as typical of various proteins and peptides) is expected to range from 2 nm ~ 6 nm. The specific gravity of these class of proteins (e.g., casein) obtained from dehydrated non-fat skimmed milk varies from

0.45 ~ 0.5 [138]. Hence, protein suspensions created using casein, were targeted in this study (i.e., sourced from dehydrated non-fat skimmed milk).

Based on the predictions from the analytical model, the experimental validation performed in this study was targeted for protein suspensions in oil, i.e., oleo-nanofluids (since aqueous nanofluids are unsuitable due to the marginal deviations in the density compared to that of the predictions afforded by the simple mixing rule and these deviations are virtually undetectable owing to the deviations being less than the typical values of measurement uncertainty). In contrast oleo-nanofluids with low density proteins (such as low density lipo-proteins/ LDL) is expected to provide sufficient resolution for discerning the "deviant" component of the density enhancement such that the experimental results can be used to conclusively differentiate the magnitude of the surplus density that is higher than the values of the measurement uncertainty in these experiments.

The neat solvent chosen for this study was an oil (PureTemp-15X). Casein, a milk protein (sourced from dehydrated non-fat skimmed milk), was chosen as the ideal low-density nanoparticle candidate (since it has specific gravity less than 1) for ensuring the success of the experimental measurements performed in this study. As mentioned before, the Stokes-diameter of the protein used in this study is expected to range from 2 nm ~ 6 nm [138] (depending on the size of the complexes formed between surfactants and proteins along with differing levels of hydration for the hydrated-protein molecules). The synthesis protocol, experimental apparatus and procedure as well as the results (both analytical predictions and experimental validation) are discussed next.

2.4.3.3 Synthesis protocol

The oleo-nanofluid samples explored in this study are obtained by mixing the protein nanoparticles (casein) in a paraffin based oil (procured under the commercial name PureTemp-15X). The following synthesis protocol, based on prior reports in the literature [139, 140, 141], was established for the preparation of the protein based oleo-nanofluid samples:

Step 1: Add surfactant (Sodium Dodecyl Sulfate or "SDS") to water (for example at mass concentration of 0.5%).

Step 2: Dissolve milk powder in small batches in a cold aqueous solution of surfactant by manual stirring.

Step 3: Add surfactant (SDS) to oil (neat solvent) and stir gently.

Step 4: Mix the aqueous solution of milk (from Step 2) and the oil solution (from Step 3) while stirring manually.

Step 5: Fill the Ultra-sonicator with ice cubes and water alongside salt to maintain sub-zero temperature in the bath.

Step 6: Ultra-sonicate the whole mixture for about 30 minutes

Step 7: Use a pipette to extract the oleo-nanofluid samples and measure density.

The detailed specification for the mass of the ingredients used in this synthesis protocol are listed in Table 11.

Table 11. Mass of ingredients used for the synthesis of samples of oleo-nanofluid

Beaker	Component	Mass
Water Solution	Water	10 g
	SDS	0.05 g
	NaOH	0.1 g
Oil Solution	Oil (PCM)	10 g
	SDS	0.05 g
	Milk Powder	0.1 g

It should be noted that the specific gravity of SDS is typically ~ 1.01 [142] while the Stokes-diameter of SDS is typically ~1 nm [143]. In addition, as mentioned before, the Stokes-diameter of the hydrated-protein-SDS complex is expected to range from 2 ~ 6 nm [138].

2.4.3.4 Experimental Apparatus

The apparatus for measuring the density of the nanofluid samples in this study was based on the Archimedean principle of buoyancy of immersed bodies along with an unequal-arm balance. A wire attached to one end of the balance arm (lever) was used to suspend a "sinker" of a known standard mass. In this technique, the density of an unknown liquid was calculated from the buoyancy force exerted by the liquid on the immersed "sinker" (calibrated value of the standard mass). This experimental apparatus enables the measurement of the buoyancy force by measuring the difference in weight for the sinker immersed in the test fluid (i.e., nanofluid with unknown density) compared to that of the

baseline state (i.e., the mass of the sinker in air). All measurements were performed under ambient conditions (i.e., at a room temperature of 24 °C).

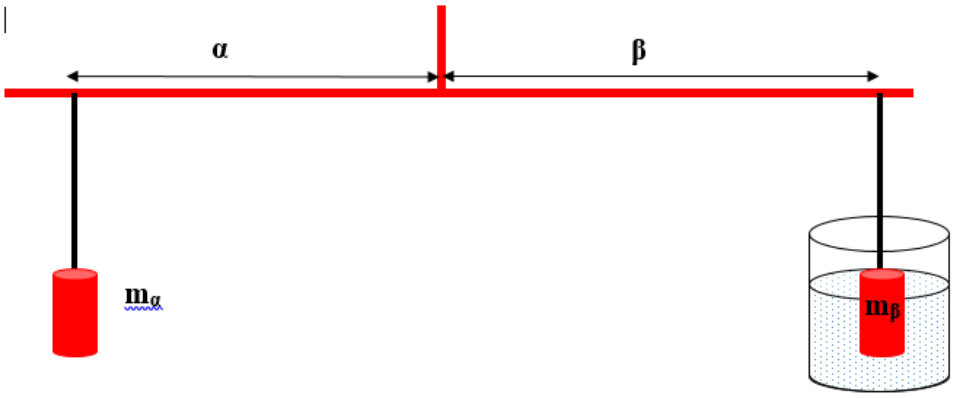

Figure 2-31. Experimental apparatus for measuring the density of nanofluids

$$m_{\beta}^{liquid} = \frac{m_{\alpha} \cdot \alpha}{\beta} \tag{18}$$

$$\rho_{liquid} = \frac{\rho_{SS,mass} * (m_{\beta}^{air} - m_{\beta}^{liquid})}{m_{\beta}^{air}} \tag{19}$$

where, $\boldsymbol{m_{air}}$ is the mass of the body immersed in air, $\boldsymbol{m_{liquid}}$ is the mass of the body in liquid (reduced due to buoyancy), $\boldsymbol{\rho_{liquid}}$ is the density of the test liquid, $\boldsymbol{\rho_{SS,\,mass}}$ is the density of the sinker (which is the same as the density of stainless steel).

2.4.3.5 Uncertainty Analysis

Uncertainty values of the experimental measurements were quantified using the Kline-McClintock method [11]. The measurement uncertainty associated with the technique developed in this study is described below.

- Let $\Delta\alpha$ and $\Delta\beta$ be the uncertainties in the length measurement (of α and β, respectively). The least count of the scale is 0.125 in. The uncertainty in the measurement is 50% of least count. Therefore, $\Delta\alpha = \Delta\beta = 0.0625$ in.
- The counter masses used in the experiment are standard mass (NIST calibrated) and the uncertainty in the measurement can be neglected (since the differential change in the measurement of mass is required in these experiments).
- The density of stainless steel is obtained from the NIST data base [144].

Hence the uncertainty in the density measurement is

$$\pm\rho_{liquid} = \pm m_{\beta}^{liquid} = \left\{\left(\frac{\partial m_{\beta}^{liquid}}{\partial \alpha}\right)^2 (\Delta\alpha)^2 + \left(\frac{\partial m_{\beta}^{liquid}}{\partial \beta}\right)^2 (\Delta\beta)^2\right\}^{1/2} \quad (20)$$

$$\pm\rho_{liquid} = \pm m_{\beta}^{liquid} = \frac{\Delta\alpha . m_{\alpha}}{\beta}\left\{\frac{\alpha^2}{\beta^2} + 1\right\}^{1/2} \quad (21)$$

2.5 Flow loop apparatus: Construction and Validation

2.5.1 Description of the flow loop

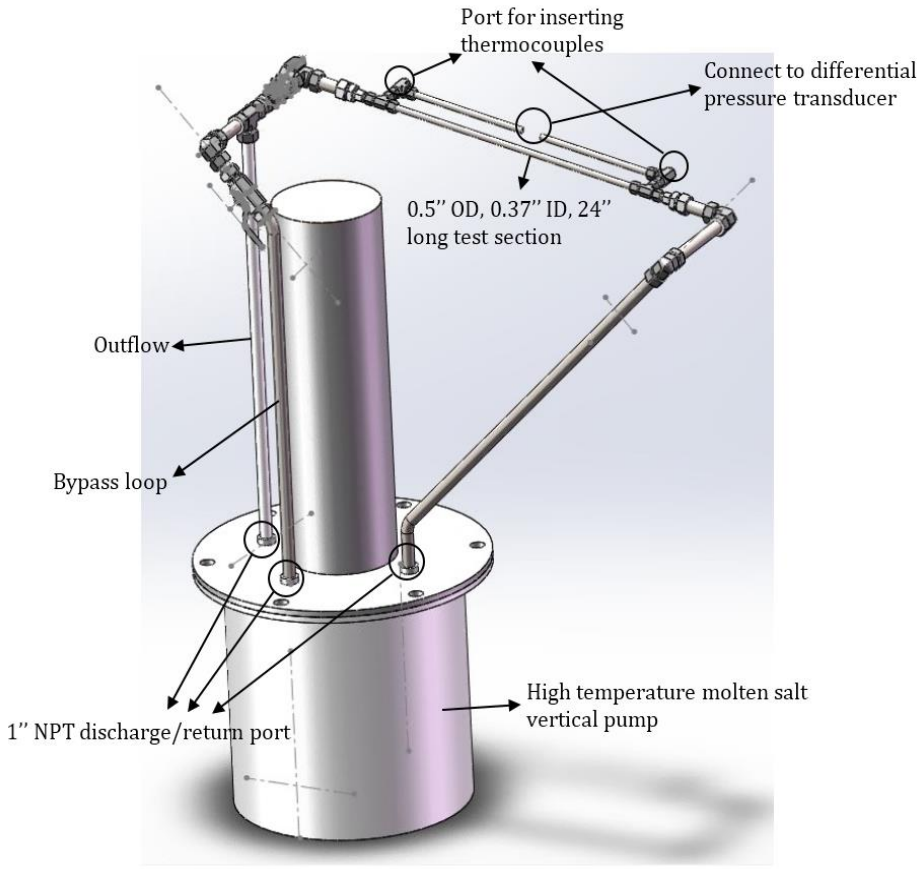

Figure 32. CAD model of the high temperature flow loop.

The CAD model shown in Figure 32 indicates the direction of flow in clockwise direction from the reservoir tank. Figure 33 illustrates the main components of a high temperature flow loop and its main components after assembly. SS316 tubing was used for construction of the flow loop. Pressure ports and thermocouple ports are custom built

for measuring pressure drop across the test section and bulk fluid temperatures, respectively. The test section is a SS316 tubing (0.5in. OD, 0.36in. ID, 30 in. length) wrapped with a heater tape to provide constant heat flux. K-type bead thermocouples measured the wall temperatures along the length of the test section. A turbine type flow meter measured the volumetric flow rate of the liquid. Before performing any flow-loop heat transfer experiments all the components were calibrated in-house. Thermal-hydraulic performance evaluation of molten salts and molten salt nanomaterials is the goal of the design and construction of the experimental rig. Furthermore, Overhang supports from roof support the entire piping of the experimental apparatus to sustain any fatigue due to high temperature working fluid (~500 °C). The detailed experimental set-up for each component is discussed in the following sections.

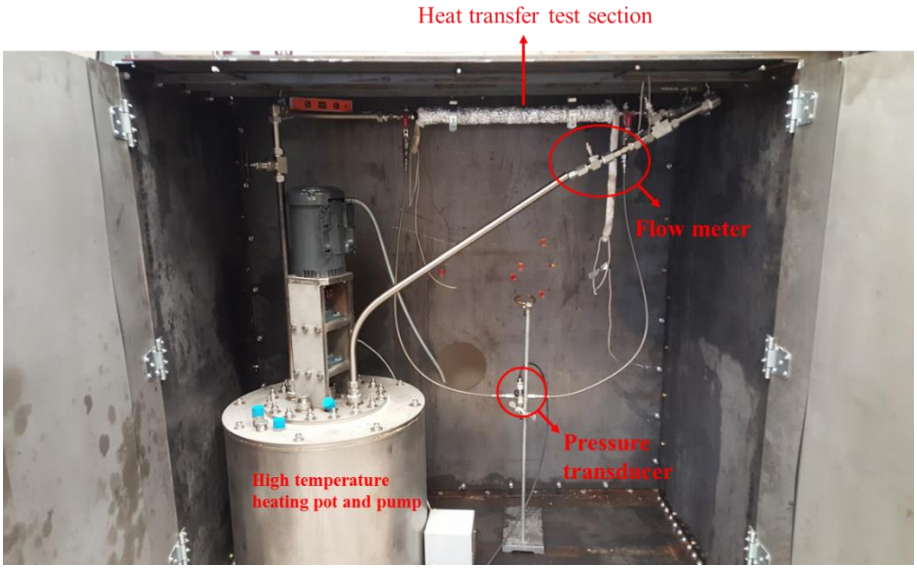

Figure 33. High temperature liquid salt loop and its main components.

2.5.2 Test section

The material selection of the test section involved a careful review of available literature [145] for molten salt heat transfer characterization. For its excellent corrosion resistance properties in both reducing and oxidizing environments up to 900 °C, 316 SS seamless tubing was the ideal candidate. The heat transfer test section is also a seamless 316 SS tube with 0.5" O.D (outer diameter), 0.065" wall thickness and 30" long.

SS316 compression tube fittings alongside reducers are used for assembly of test section to the rest of the flow apparatus. The advantages of compression fitting include superior resistance to corrosive fluids, pressure and temperature – resistant. Furthermore, the use of pipe compression fittings eliminates additional assembly processes. The effect of extreme temperatures, say molten salts at 500°C, may cause unwanted thermal expansion and cause a leak. A high temperature sealant is then recommended for high temperature molten salt testing [131].

2.5.3 Pump and tank

The commercial options for a pump capable of handling high temperature corrosive molten salts and the desired flow ranges are limited. Wenesco Inc. supplied high temperature industrial scale molten salt melting pot integrated with vertical pump. The specifications of the pump and tank system are tabulated in Table 12. A variable-frequency drive (VFD) controls the flow rate discharge from the pump.

Table 12. Specification of the high temperature molten salt pot and pump system.

High temperature Pot & Pump	Operating temperature	up to 700°C
	Motor	2 HP
	Minimum Flow Rate	0.1 gal/min
	Operating Pressure	~atmospheric
	Impeller (Material of Construction)	Stainless Steel
	Tank Volume	120 lb. salt

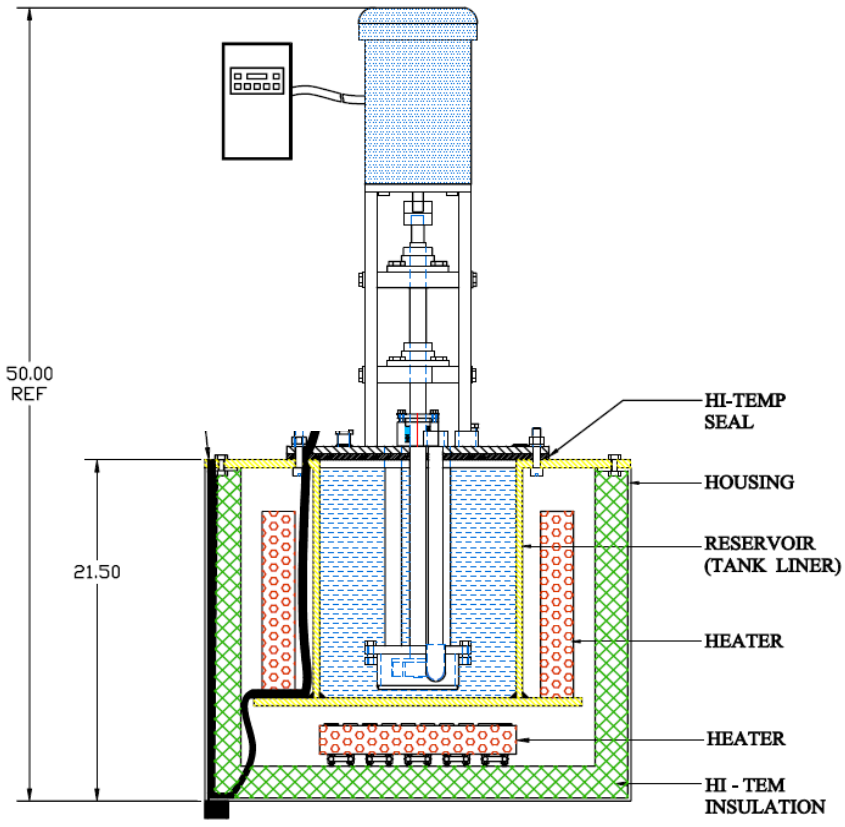

Figure 34. Deatiled schematic of the melting pot and pump assembly.

2.5.4 Heating elements (Heat Trace)

As shown in Figure 34, the main heater for molten salts is integrated as a single unit along with the pump and is capable of working up to 600 °C. For molten salt flow experiments, it is essential to prevent thermal shock and unwanted freezing of molten salts in the piping. Hence, a heat trace from Omega Inc., is proposed to be wrapped on the piping to preheat the molten salt to desired inlet temperature. As shown in Figure 35, infrared image of the heating tape reveals uniform heating of the tape.

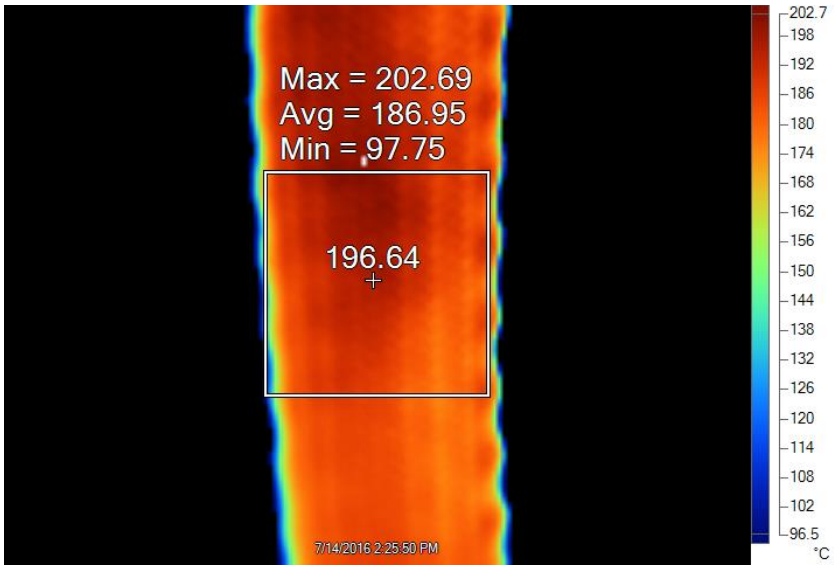

Figure 35. Infrared Image of the high temperature heating tape for a heat electrical input of 500W.

2.5.5 Pressure measurement

To obtain differential pressure drop across the length of the test section, a wet/wet differential pressure transmitter (PX409-150DWUV) was procured. A measurement port (cross union device) as shown in Figure 36 was assembled for measuring the bulk fluid properties, both pressure and temperature, before and after the test section. A four way cross union with a K-type probe thermocouple for bulk temperature measurement is on one side of the device and a compression fitting for differential pressure transducer is on the opposite end. The insertion length of the bulk-temperature (fluid-in and fluid-out) thermocouple is adjusted to ensure the tip of the probe is in the center of the fluid flow.

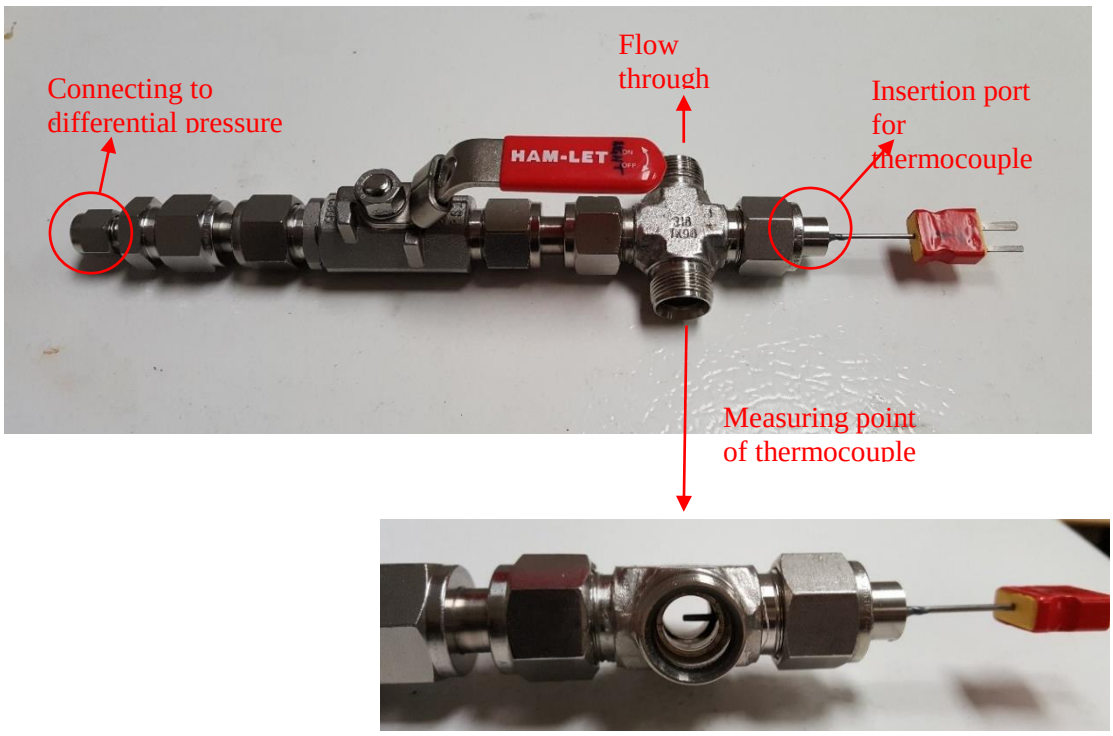

Figure 36. Measurement port (cross union) for differential pressure and bulk- fluid temperature measurement.

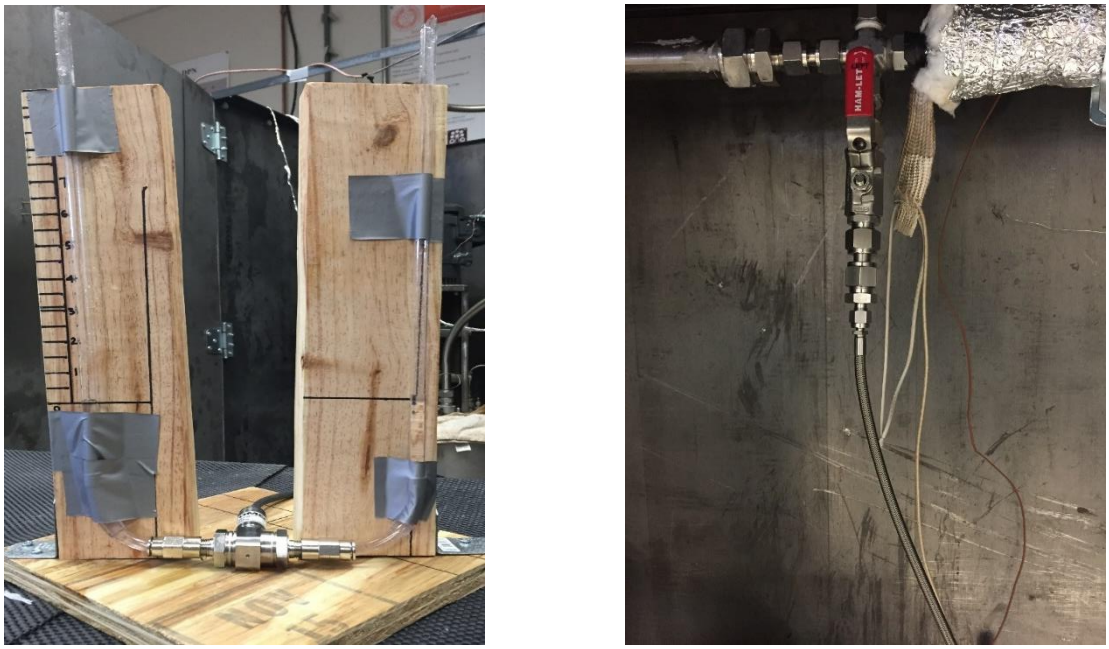

Figure 37. U-tube device used for calibration the pressure transducer before flow experiments (LEFT). The measurement port (Cross union) fixed in the flow apparatus along with connection tubing to Differential Pressure Transducer (DPT) (RIGHT).

The two-way valve (Swagelok SS-12NBS16) shown in Figure 36 was fitted to prevent hydraulic shock to the transducer during start-up. The size of the connecting tube from the test section (measurement port) to the pressure transducer effect the dynamic characteristics of the fluid oscillator; liquid in the connection tube. This in turn effects the pressure drop measurement and its magnitude. The damping characteristic of the fluid oscillator is enhanced for slender tubes (small diameter and long tube) compared to stubby tube (large diameter and short tube) as the natural frequency of oscillation for slender tubes is greater compared to stubby tubes.

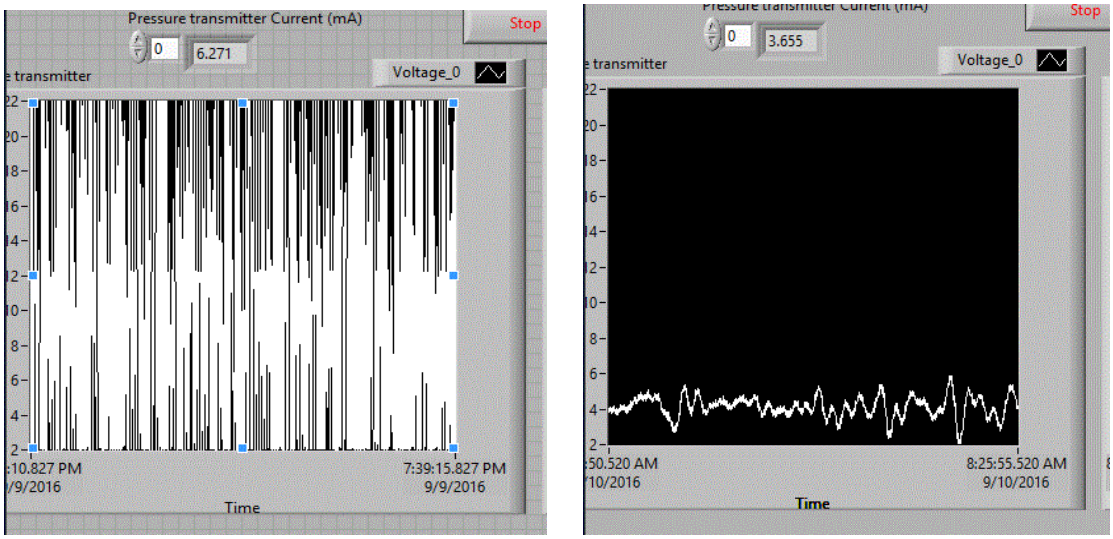

Figure 38. Comparison of LabVIEW widget for differential pressure measurement across the test section for identical flow conditions: (LEFT) 0.25'' ID connection tube; (RIGHT) 0.14'' ID connection tube.

Figure 38 illustrates this phenomenon for a flow experiment (water as working fluid). The fluctuation in the signal of the differential pressure is severe with a 0.25" ID (internal diameter) tubing whereas the pressure measurement improved significantly with the change of the tubing diameter to 0.14" ID.

2.5.6 Flow rate measurement

For initial validation tests with water a turbine-type flow meter from Omega Inc., (FTB 1411-HT) was procured. The flow meter is capable of measuring the volumetric flow rate of liquids up to 232°C to a maximum pressure rating of 5000 psi. For molten salt thermal-hydraulic performance characterization, no commercial flow meter matched the flow requirements. Non-intrusive Doppler flow meters also designated ultrasonic flow

meters are capable of measuring flow of highly corrosive high temperature liquids are potential candidates for molten salts and molten salt nanomaterial experiments.

2.5.7 Wall temperature measurement

The wall temperature of the test section is measured along the length at three equidistant different locations. A slot was milled into the test section along the length to insert the thermocouple junction tip for better estimation of inner wall temperature of the test section. The measurement of surface temperature of a stainless steel pipe is a critical task as the heat transfer measurement is directly dependent to the wall temperature measurement. After careful consideration of available options for types of thermocouples to measure wall temperature of the test section, K-type bare wire bead thermocouples were finalized.

The isolation of the thermocouple tip both electrically and thermally from the heater tapes is needed for accurate measurement of temperature of the test section. As shown in Figure 39, three different adhesion techniques were tried initially to mount the thermocouples. Merely fixing the thermocouple junction to the bare surface of the pipe results in electrical grounding of the junction and results in erroneous measurement. As a result, high temperature epoxies capable of electrically isolating the junction from the bare metal surface with high thermal conductivity are explored. Epoxy based Omegatherm 201 alongside a high conductive thermal paste, and magnesium based ceramic adhesive Ceramabond 501 were investigated for efficacy. Ceramabond 571 is finalized as the suitable adhesive for this study given its superior thermal and adhesion properties. Figure

40 demonstrates the finalized technique employed for fixing the thermocouples for surface temperature measurement of the test section.

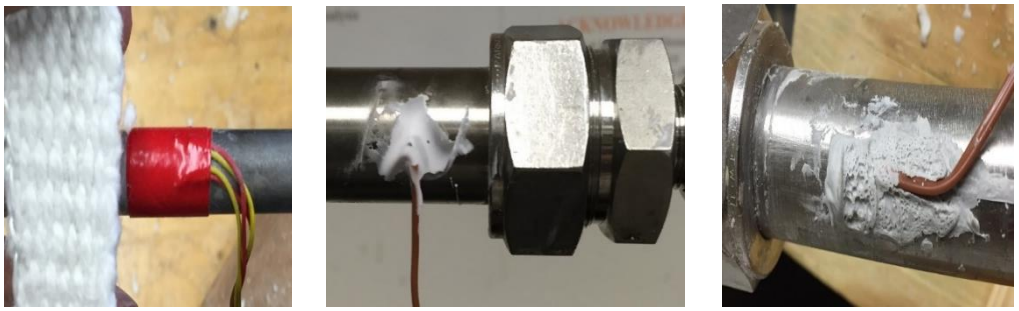

Figure 39. Schematic of techniques employed for mounting K-type bead thermocouple. A.) Using a high temperature electrical tape to fix the thermocouple on the pipe surface and ceramic tape to insulate from heating tape. B.) Use of Omegatherm 201 high conductive epoxy. C.) High temperature magnesium adhesive Ceramabond 571.

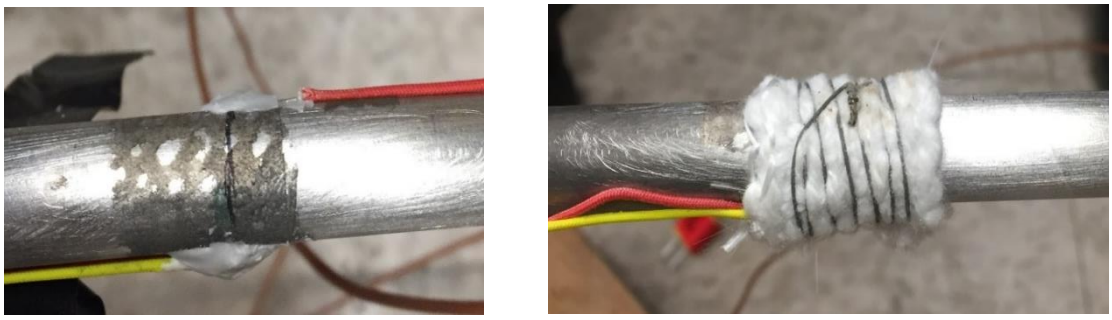

Figure 40. Schematic of the final thermocouple assembly for surface temperature measurement with a high temperature ceramic tape.

2.5.8 Preliminary test procedure and data analysis

The validation of the experimental apparatus was achieved with heat transfer experiments with water as working fluid. The experimental procedure is as follows:

- Ensure enough water level in the tank and start the pump. After 15 minutes of flow stabilization, turn on the power to the heater tape around the test section.
- Set the Variable Frequency Drive (VFD) to maximum possible value, in this case 42Hz, i.e. start with the maximum flow rate of water
- Turn on the power to the electrical heating tape and set the voltage to desired power
- Monitor the inlet water temperature to the test section for quasi-steady state condition. (Temperature change within 2°C for a 15 minute period)
- Record the output from all thermocouples, differential pressure transducer and flow meter.
- After data recording, decrease the VFD frequency to a lower value i.e. decrease the volume flow rate of the water.
- Repeat from step – 4 to step – 6 for desired number of data points. In this study, for a given heat input data collection was performed for six different flow rates.
- After reaching the minimum flow rate point desired, increase the VFD frequency and repeat steps – 4 to 6 until the maximum flow rate is reached.

- The system shut down protocol includes turning off the electrical heater tape power first and then cutting off the flow to pressure transducer to avoid hydraulic shock
- After ensuring both heater tape and pressure transducer are secure, turn off the pump

The analysis of the heat transfer behavior is made by the evaluation of local heat transfer coefficient along the test section defined as follows:

$$h(x) = \frac{\dot{q}}{T_{wall,i}(x) - T_{fluid}(x)} \tag{10}$$

where, $\dot{q}$ is the heat flux input to the test section, $T_{wall,i}(x)$ is the local temperature of the inner wall of the test section and $T_{fluid}(x)$ is the interpolated local bulk fluid temperature.

The wall temperature measured by the thermocouples is the outer surface temperature and one-dimensional steady state Fourier's law gives the temperature of the inner surface of the pipe as

$$T_{wall,i}(x) = T_{wall,o}(x) - \frac{\dot{q}A}{2\pi L K_{304SS}} \ln\left(\frac{r_{outer}}{r_{inner}}\right) \tag{11}$$

where, $\dot{q}$ is the heat flux input to the test section, $T_{wall,i}(x)$ and $T_{wall,o}(x)$ are the temperatures of the inner and outer surface of the test section respectively. L is the length of the test section, K_{304SS} is the thermal conductivity of 304 Stainless Steel, and r_{outer} and r_{inner} are the outer and inner radius of the test section, respectively. A is the outer surface area.

The heat flux input to the test section is computed from

$$\dot{q} = \frac{\rho \dot{V} C_p (T_{fluid,out} - T_{fluid,in})}{A} \tag{12}$$

where $\boldsymbol{\rho}$ and $\boldsymbol{V}$ are the density and volume flow rate of the liquid respectively. $\boldsymbol{T_{fluid,out}}$ and $\boldsymbol{T_{fluid,in}}$ are the bulk fluid temperatures at outlet and inlet of the test section, $\boldsymbol{C_p}$ is the specific heat capacity of the working fluid and $\boldsymbol{A}$ is the outer surface area of the test section. The bulk fluid temperature along the test section is linearly interpolated from the fluid inlet and outlet temperatures by

$$T_{fluid}(x) = \left(\frac{x}{L}\right) T_{fluid,out} + \left(1 - \frac{x}{L}\right) T_{fluid,in} \tag{13}$$

where $\boldsymbol{x}$ is the location along the test section and $\boldsymbol{L}$ is the total length of the test section, $\boldsymbol{T_{fluid,out}}$ and $\boldsymbol{T_{fluid,in}}$ are the bulk fluid temperatures at outlet and inlet of the test section.

The nusselt number for the flow conditions tested is best estimated by Gnielinski correlation as

$$Nu_D = \frac{\left({}^{f}/_{8}\right)(Re_D - 1000)Pr}{1 + 12.7\left({}^{f}/_{8}\right)^{0.5}\left(Pr^{2/3} - 1\right)} \tag{14}$$

where $\boldsymbol{f}$ is the friction coefficient, $\boldsymbol{Re}$ is the Reynolds number and $\boldsymbol{Pr}$ is the Prandtl number. The friction coefficient is computed from the pressure drop measured by differential pressure transducer as

$$f = \frac{2DP}{\rho L v^2} \tag{15}$$

Where ***P*** is the pressure drop, ***D*** is the diameter, ***ρ*** is the density of the working fluid, ***L*** is the length of the test section and ***v*** is the velocity of the liquid.

The Reynolds number and Prandtl number are computed as follows

$$Re = \frac{\rho v D}{\mu} \tag{16}$$

$$Pr = \frac{\mu C_p}{k} \tag{17}$$

Where ***ρ*** is the density of the working fluid, ***v*** is the velocity of the liquid, ***D*** is the diameter of the pipe, ***μ*** is the absolute viscosity and ***k*** is the thermal conductivity of the liquid.

2.5.9 Uncertainty analysis

The quantification of the uncertainty associated with each measured and derived property was done using Kline-McClintok method. The uncertainties associated with each thermocouple is 0.3°C after calibration and the absolute uncertainty for temperature of fluid is

$$\pm T_{fluid}(x) = \left[\left(1 - \frac{x}{L}\right)^2 \varepsilon_{T,in}^2 + \left(\frac{x}{L}\right)^2 \varepsilon_{T,out}^2\right]^{1/2} \tag{18}$$

Where $\boldsymbol{\varepsilon_{T,in}}$ and $\boldsymbol{\varepsilon_{T,out}}$ are the thermocouple uncertainty associated with bulk fluid temperature measurement.

Similarly the uncertainty of the friction coefficient and heat transfer coefficient are estimated.

2.6 Summary

In this chapter, experimental methods developed for characterizing molten salts and novel molten salt nanomaterials for thermo-physical properties such as thermal conductivity and specific heat capacity are discussed. Furthermore, construction details of a high temperature forced convection heat transfer loop for evaluating the heat transfer performance of molten salts in presented. A custom made 1D cylindrical apparatus was employed for measuring the thermal conductivity and a transient temperature history (T-History) technique was developed for estimating the specific heat capacity enhancement of molten salt nanomaterials. The thermal stability of the molten salts and molten salt nanomaterials is estimated through mass loss of a sample baked in a muffled furnace at 550°C. Material characterization of the molten salts and molten salt nanomaterials was performed through Scanning Electron Microscopy (SEM).

3. EXPERIMENTAL RESULTS

3.1 Flow Loop Set up Validation: Water testing

3.1.1 Differential Pressure Transducer Calibration

A U-Tube Manometer was employed for the calibration of the pressure transducer (PX409-150DWUV). Representative plot for the calibration data is shown in Figure 41. The calibration data indicates that the DPT display excellent linearity in response with a bias error that slightly under predicted pressure drop. The pressure drop of water, in inches, across the ports is measured by means of electrical amperes through a Data Acquisition System (DAQ). Equation (19) indicates the linear regression relation fit for measured output current and imposed pressure drop in inch of water. As Table 13 indicates in spite of the slight deviation, the performance of the DPT is quite accurate, as validated by the high value of R^2 and good match with the NIST reported coefficients. Thus it can be concluded that measured pressure drops using the DPT after calibration are reliable to within 1.5%.

$$\text{Pressure difference, in. H2O} = \text{A} * (\text{LabVIEW reading, mA}) - \text{B} \qquad (19)$$

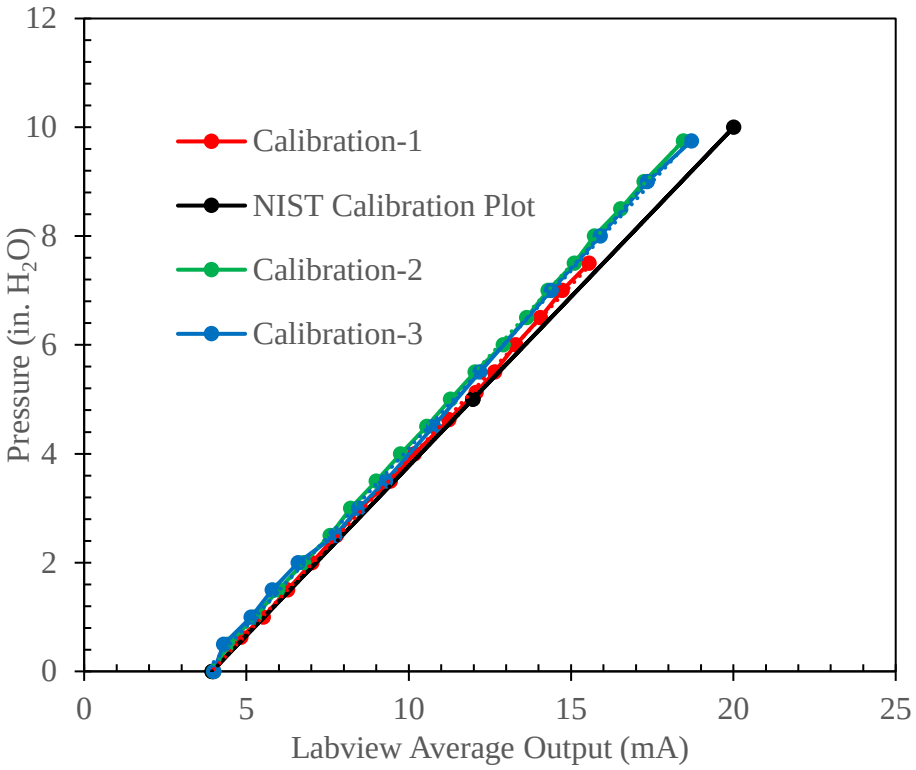

Figure 41. Calibration curve for the DIfferential Pressure Transducer (DPT) compared with the NIST calibration plot.

Table 13. The regression coefficients for the calibration curve for Differential Pressure Transducer (DPT) for the three repeated cycles and NIST provided values.

Data	A	B
Run-1	0.64	2.52
Run-2	0.67	2.51
Run-3	0.65	2.44
Average	**0.65**	**2.49**
St. Dvt.	**1.5%**	**1.5%**
NIST	**0.62**	**2.45**

3.1.2 Turbine flow meter calibration

The volumetric flow rate of the fluid through the test section is crucial to accurate determination of friction coefficient and heat transfer coefficient. Of the commercially available types of flow meters, a turbine type flow meter is selected for its wide flow range and durability. Turbine flow meters measure the volumetric flow rate by means of a "turbine" or a "pinwheel" in the flow stream. The mechanical energy of the fluid rotates the pinwheel converting flow energy to rotational energy. The speed of the rotor is proportional to the volumetric flow rate. The rotation is detected magnetically by means of a embedded metal piece generating a pulse. The frequency is later processed by a Fast Fourier Transform (FFT) to determine the volumetric flow rate of the fluid.

$$Flow\ rate, \dot{V}\left({}^{mL}/_{s}\right) = A * \left(Frequency, (Hz)\right) + B \tag{20}$$

Equation (20) indicates the linear regression fit for actual volumetric flow rate and measured frequency. Table 14 indicates the calibration coefficients for both NIST provided calibration data and the calibration test. Figure 42, indicates in spite of the slight deviation, the performance of the turbine flow meter is quite accurate, as validated by the high value of R^2 and good match with the NIST reported coefficients. Thus it can be concluded that measured pressure drops using the DPT after calibration are reliable to within 1.5%.

Table 14. Comaprison of calibration coefficients for turbine flow meter.

	A	B	R^2
NIST	0.2265	-0.117	1
Calibration	0.238	-0.61914	0.997

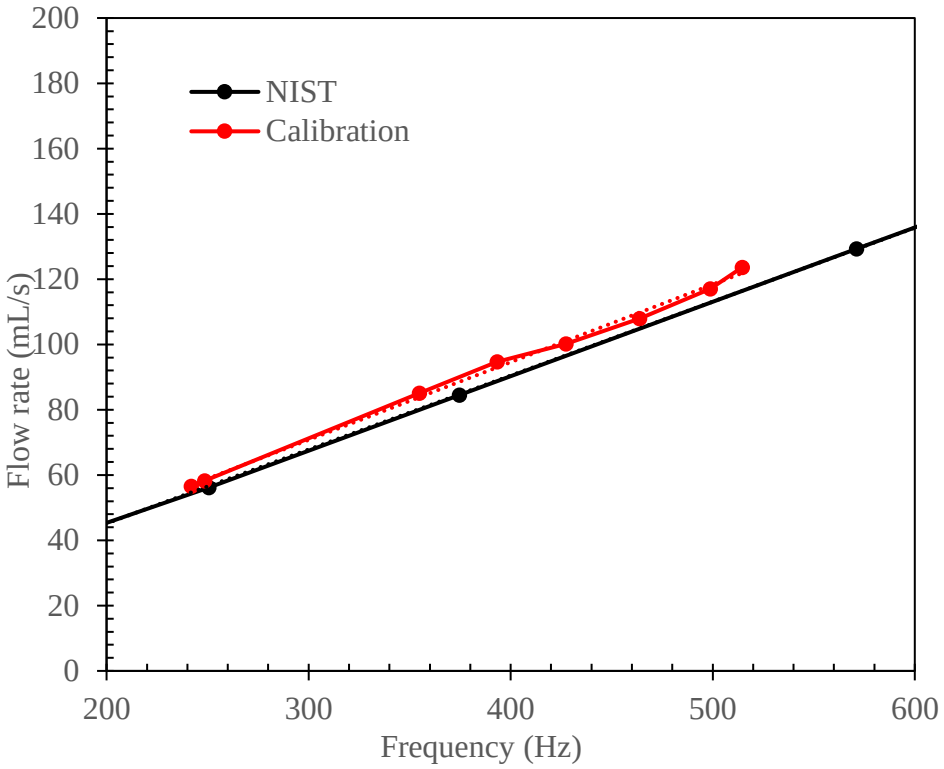

Figure 42. Calibration curve for the turbine flow meter compared with the NIST calibration plot.

3.1.3 Hydrodynamic performance

To validate and establish the functionality of the flow loop apparatus constructed, hydrodynamic performance experiments were performed initially using water in the flow loop. Without any heat input to the test section, water as the working fluid, pressure drop across the test section is measured for different flow rates. The test fluid is initially heated to 90°C through the radiative heaters in the storage tank. Once the PID control establishes the steady state bulk temperature of water in the tank, test fluid is circulated and experiments are performed as outlined in section 2.5.8. Pressure drop measured across the test section plotted as a function of volume flow rate through the loop is plotted as shown in Figure 44. As shown in Figure 43, experimental friction factor computed from equation (15) and plotted against Reynolds number. Theoretical friction factor for the test section is computed from Haaland equation, an explicit approximation for Colebrook equation as shown in equation(21).

$$\frac{1}{\sqrt{f}} \cong -1.8log\left[\frac{6.9}{Re} + \left(\frac{\varepsilon/_D}{3.7}\right)^{1.11}\right] \tag{21}$$

where, $\boldsymbol{f}$ is Darcy friction factor, $\boldsymbol{Re}$ is the Reynolds Number, $\boldsymbol{\varepsilon}$ is the pipe roughness, $\boldsymbol{D}$ is the diameter of pipe.

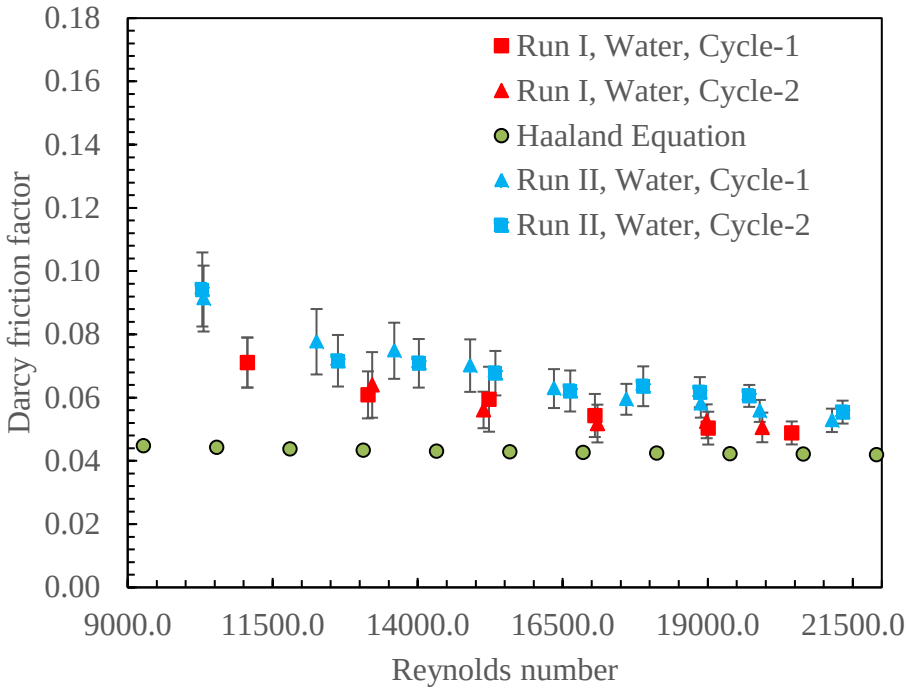

Figure 43. Experimental friction factor computed from measured pressure drop across the test section plotted as a function of Reynolds number compared with theoretical friction factor computed from Haaland equation.

As shown in Figure 43, good match for friction factor exist between different experiments demonstrating the validity of the experimental setup. The experimental uncertainty for measured friction factor ranged between 7% - 18% for the range of flow rates tested. Furthermore, the experimental values are greater than theoretical values at lower flow rates. This deviation can be attributed to the difficulty in estimating the pipe roughness factor theoretically in Haaland equation. Hence, the experiments performed validated the reliability of the instrumentation for evaluating hydrodynamic performance.

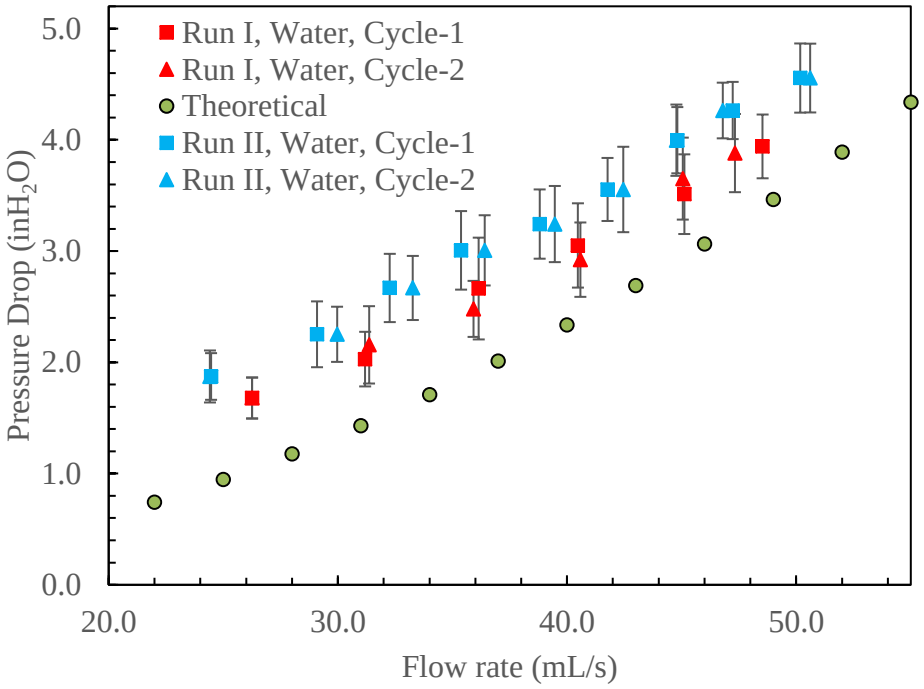

Figure 44. Experimental pressure drop across the tes section plotted as a function of volumetric flow rate compared with theoretical pressure drop.

Figure 44 indicates the measured pressure drop as a function of flow rate. As illustrated, the pressure drop increases as the flow rate increased. Furthermore, the experimental data between different experiments matches with reasonable accuracy. The theoretical pressure drop is computed from equation (15) with friction factor from Haaland equation as shown in equation(21). The theoretical predictions are under predicted as expected due to under prediction of friction factor.

3.1.4 Heat transfer performance

Heat transfer experiments were performed on turbulent and transition regime of water in a circular tube test section at various flow rates (30 ml/s – 60 ml/s) and temperatures (50°C – 100°C). The temperatures, flow rates of water and the pressure drop across the test section were measured and the local heat transfer coefficients were obtained. Experimental data of convective heat transfer were compared to general correlations in order to verify the experimental setup. Heat Transfer tests were performed at four different heater inputs to the test section (240W, 320W, 405W and 475W). The heat transfer test section is also a seamless 316 SS tube with 0.5" O.D (outer diameter), 0.065" wall thickness and 30" long. Detailed experimental procedure and apparatus are provided in section 2.4.3. Section 2.5.8 details the data reduction process of the experimental data collected and uncertainty analysis.

Figure 45 illustrates the measured temperature rise of water at different flow rates for a fixed heater power of 240W. As the results indicate, good agreement can be seen between the present experimental data and predicted curve from energy balance. The heating tape being a two-sided tape has a fraction of heat input lost to ambient. As a result, the true heat input to the test section is best estimated by the change in temperature of water through the test section rather than the power applied to the heating tape.

3.1.4.1 240W Heat Input

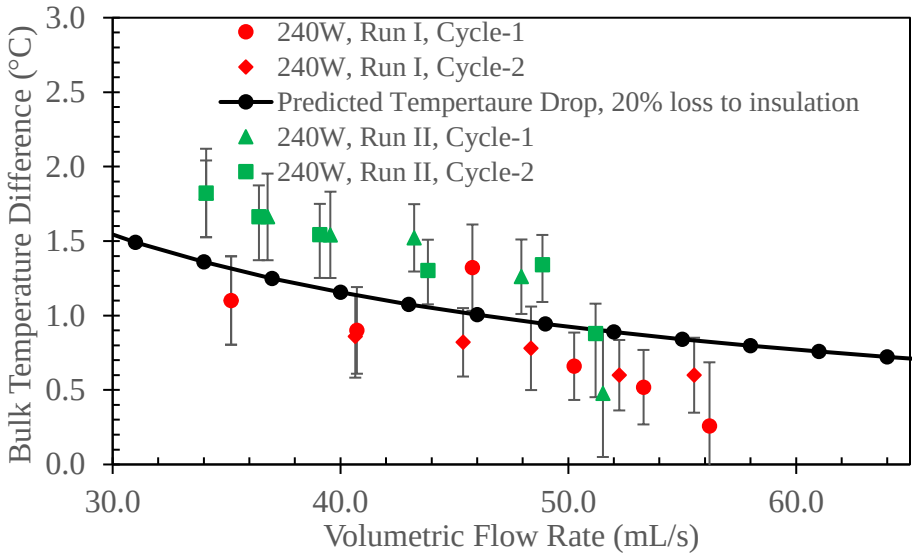

Figure 45. Fluid bulk temperature drop across the test section as a function of flow rate for 240W heat input.

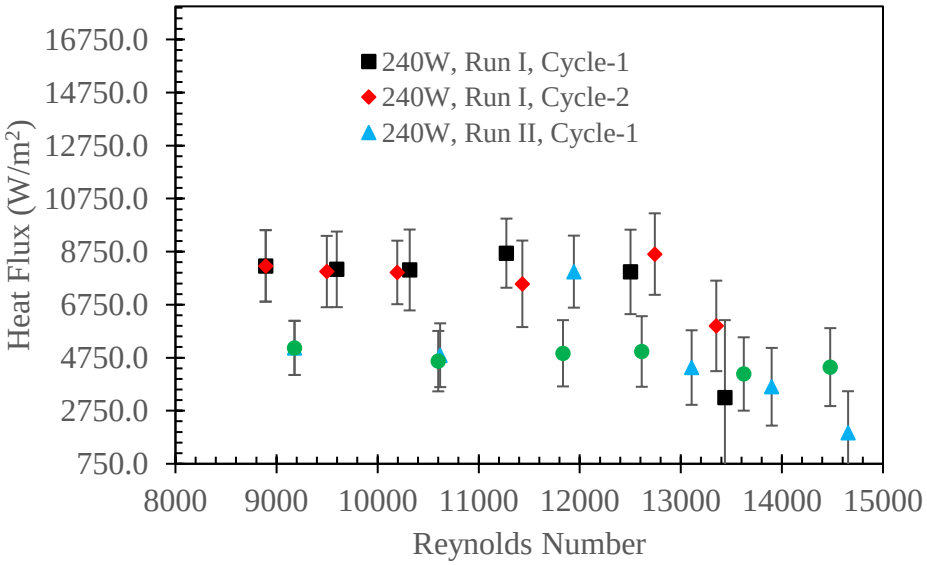

Figure 46. Applied heat flux computed from the energy balance across the test section for heater input setting of 240W.

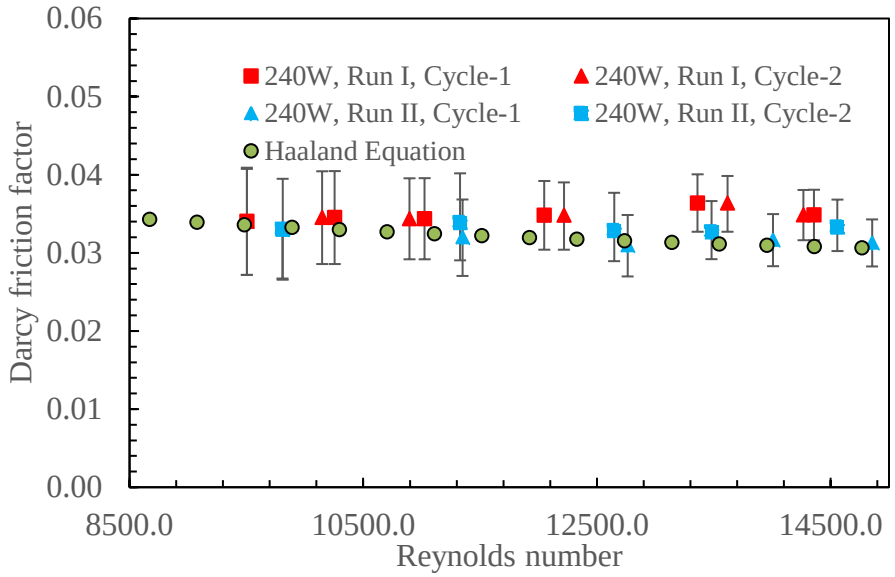

Figure 47. Experimental friction factor computed from measured pressure drop across the test section plotted as a function of Reynolds number compared with theoretical friction factor computed from Haaland equation for 240W heat transfer test.

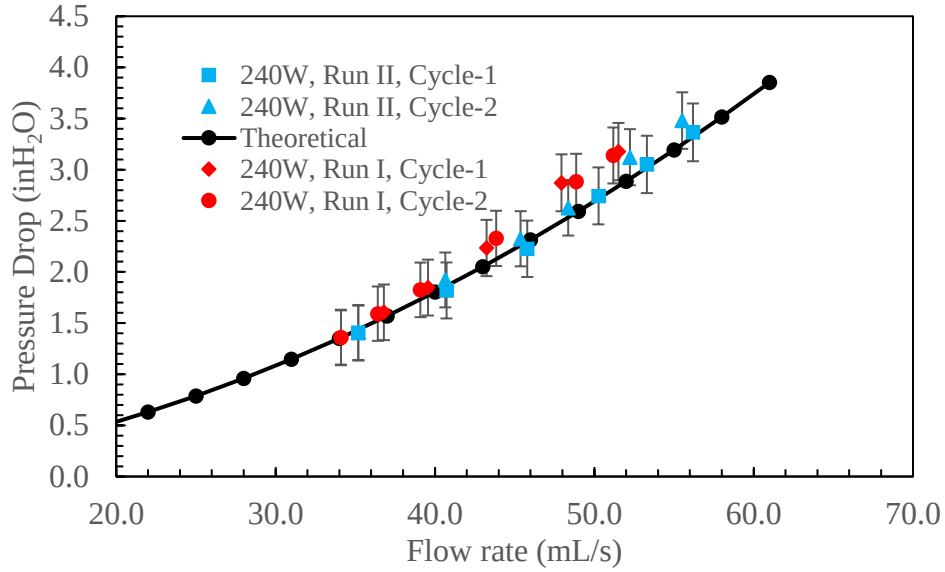

Figure 48. Experimental pressure drop across the test section plotted as a function of volumetric flow rate compared with theoretical pressure drop for heat input of 240W to the stainless steel circular test section.

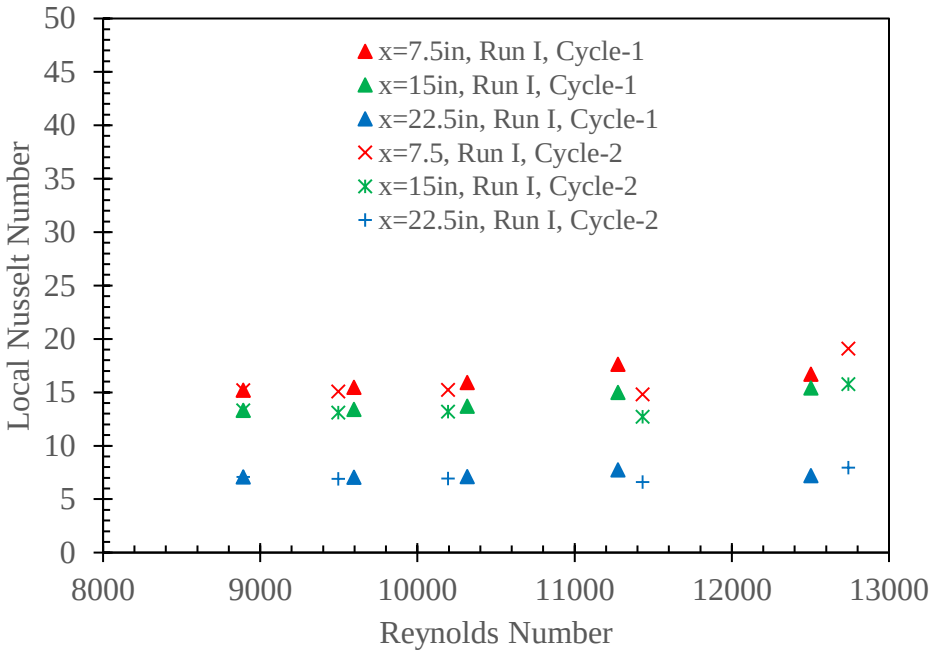

Figure 49 Local Nusselt number (axial distance) as a function of Reynolds number for a circular test section for a heater input of 240W.

Figure 47 and Figure 48 illustrate the measured friction factor and experimental pressure drop across the test section for the range of flow conditions. As the plots indicate good match between the experimental data and theoretical predictions and are within measurement uncertainty. Figure 49 illustrates the local Nusselt number computed, at three different axial locations along the test section, plotted as a function of Reynolds number. The Nusselt number increased as the mass flow increased due to enhanced heat transfer and was within 20% of the predicted value from widely accepted Gnielinski correlation. The deviation from the correlation was expected to be due to uncertainty in measurement of surface wall temperature measurement of the test section. The use of an ungrounded bare wire thermocouple for measuring the surface temperature of a metal

resulted in a ground loop formation in the data measurement system, resulting in higher fluctuation in the measured temperature. To eliminate such error, a high temperature magnesium based ceramic adhesive to electrically isolate the thermocouple from the test section was employed. Appendix A summarizes the forced convection heat transfer measurement results for various test conditions.

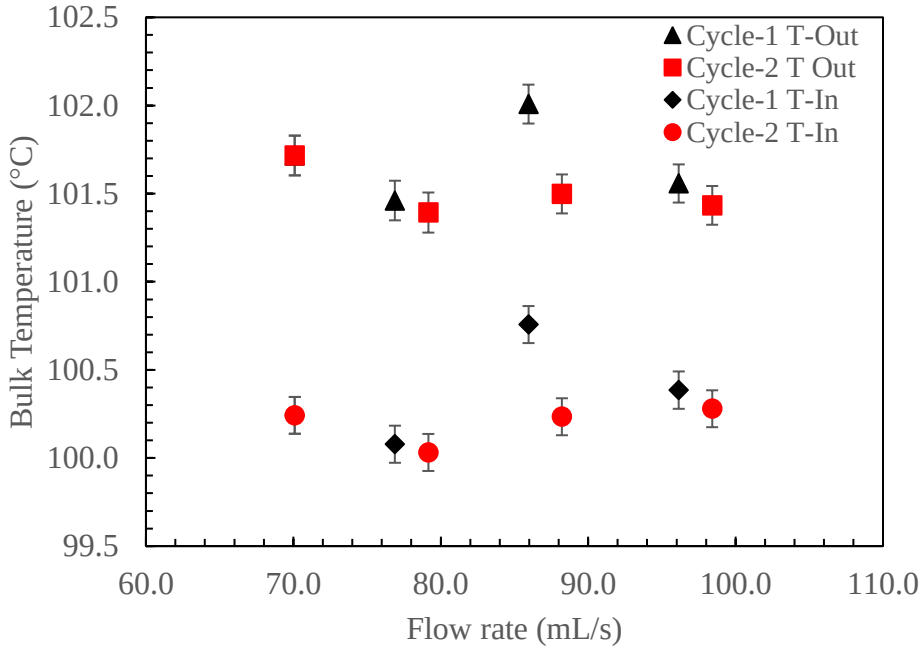

Figure 50. Plot of inlet and outlet fluid temperatures as a function of flow rate for improved flow loop experimental system.

Figure 50, Figure 51, Figure 52 indicate the experimental results for a high temperature forced convection heat transfer test performed with water as the working fluid after improving the surface wall temperature measurement technique. As the results indicate, the measured local Nusselt number matched with decent accuracy with the predicted value from Gnielinski correlation

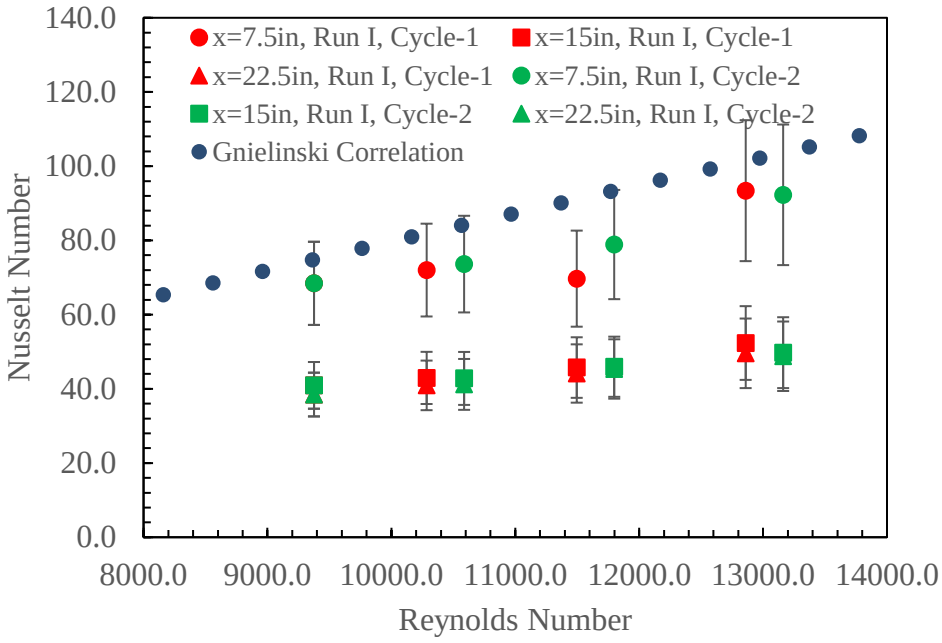

Figure 51. Local Nusselt number (axial distance) as a function of Reynolds number for a circular test section for a heater input of 475W.

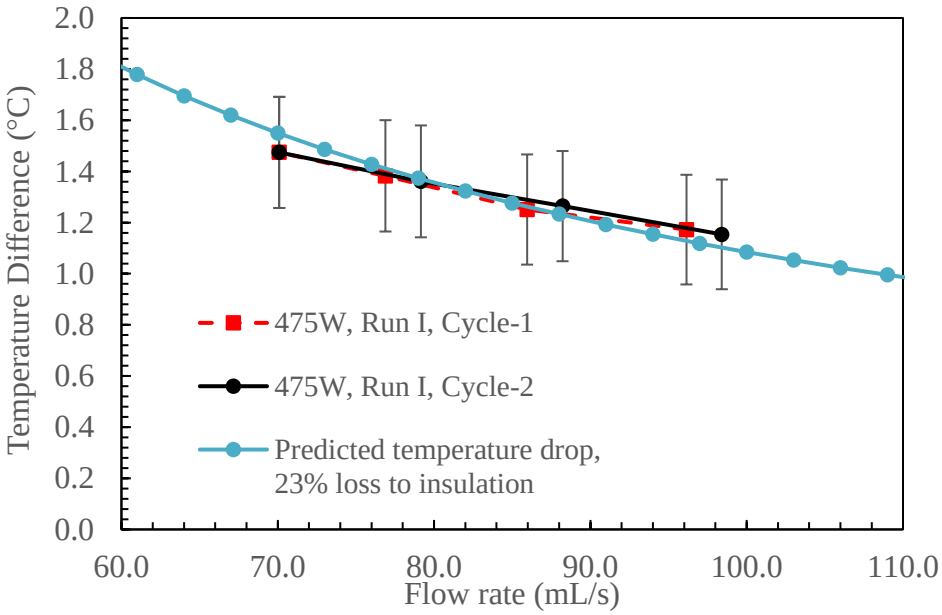

Figure 52. Fluid bulk temperature drop across the test section as a function of flow rate for 240W heat input.

3.2 Specific heat Capacity

3.2.1 Validation Test

The minimum distance required between the two testing vials needs to be determined before specific heat capacity testing. The distance between the two vials needs to greater than the thermal boundary to avoid measurement errors. The cylindrical vial is estimated to be an isothermal vertical plate in a quiescent medium. The thermal boundary layer thickness at the edge of the vial is computed for the geometry and is tabulated in Table 15. The critical Rayleigh number for vertical plates is 10^9 for laminar flow and at all testing temperatures in this study the flow is laminar. The fluid properties are evaluated at mean film temperature. The thickness of the film at the edge of the vial ranges from 44mm to 27mm. Hence, during testing both the samples are placed at least 8 cm. apart from each other to avoid thermal boundary layer interactions.

Table 15. Boundary layer thickness for the sample vial estimated from isothermal vertical surface in a quiescent medium.

Vial (°C)	Air (°C)	Properties of air film				Rayleigh Number	Laminar Flow	Thickness (mm)
		T (K)	ν (m^2/s)	Pr	β (1/K)			
550	603.7	850	0.0000938	0.716	0.0011765	6611.85	TRUE	43.97
500	553.7	800	0.0000849	0.709	0.0012500	8485.32	TRUE	41.21
400	453.7	700	0.0000681	0.695	0.0014286	14785.19	TRUE	35.69
300	353.7	600	0.0000527	0.685	0.0016667	28399.94	TRUE	30.21
250	303.7	550	0.0000456	0.683	0.0018182	41298.51	TRUE	27.49

Before characterizing nanofluid samples for specific heat capacity enhancement, a validation test was performed to check for the accuracy of the technique in capturing the difference in specific heat capacity between samples. For this purpose, two identical pure solar salt vials were tested in the T-history apparatus as described in section 2.4.1.1. Figure 53 illustrates the temperature response of both the samples and the furnace air temperature plotted for one cycle.

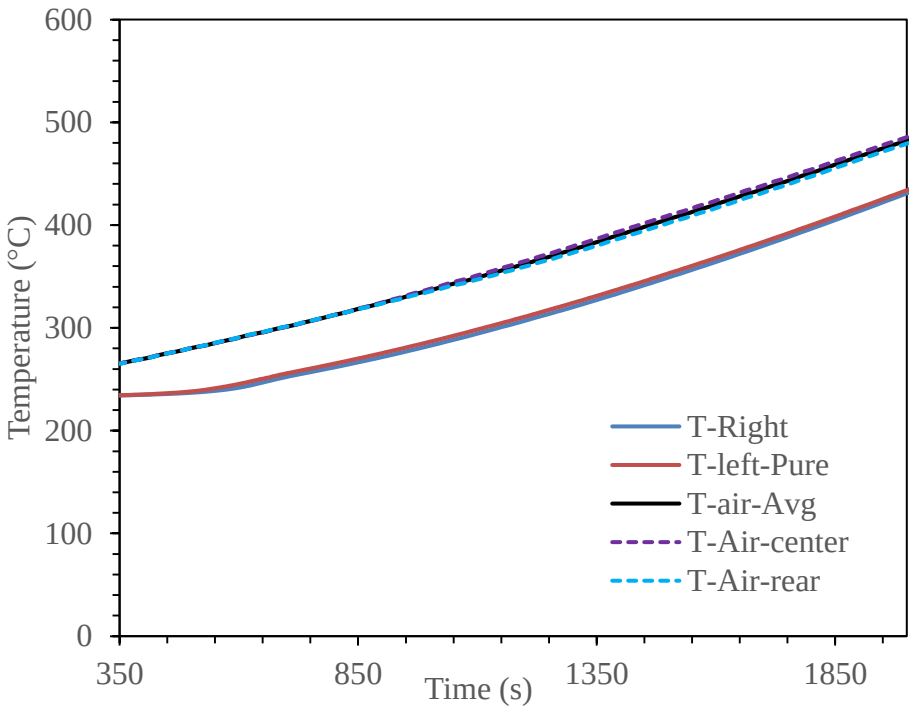

Figure 53. Plot of temperature response obtained from T-History experiments for pure solar salt samples and air temperature in the furnace.

Figure 54 illustrates the specific heat capacity ratio calculated from the temperature response for one cycle of T-History experiments for both pure solar samples. The samples were heated from 270°C to 550°C and the data analysis was performed according to equation(3). Figure 53 illustrates that the temperature of both the samples increased at the same rate. At any given instant of time, the temperature of both the samples is identical implying both the samples have same specific heat capacity. Figure 54 illustrates that the ratio of specific heat capacity between the samples is ~1 for the entire temperature range tested. Hence, this technique is validated for its accuracy in determining the ratio of specific heat capacity for large sample quantities over a range of temperatures.

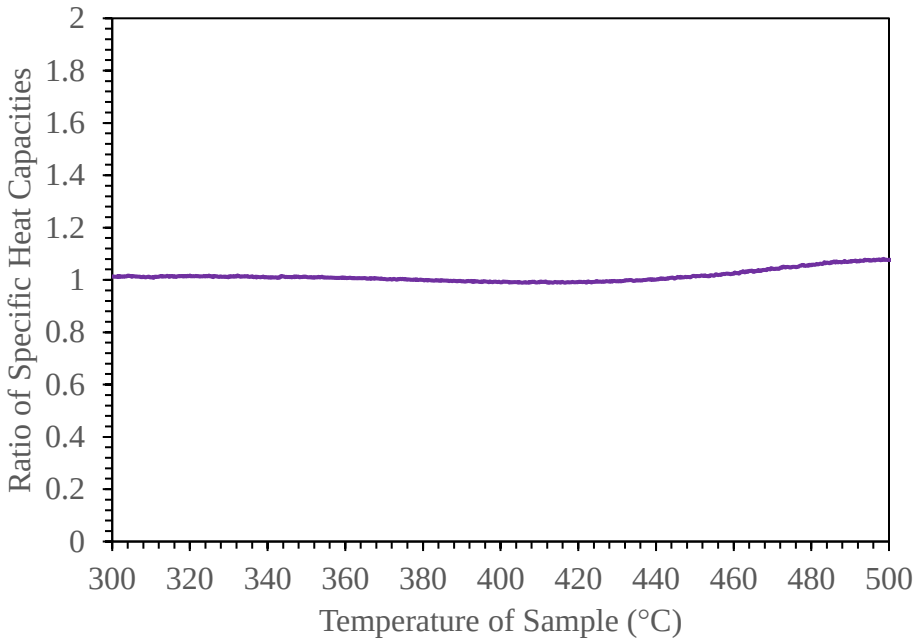

Figure 54. Plot of specific heat capacity as a function of temperature for pure solar salt samples for validation tests.

3.2.2 Solar salt nanofluid (One-step synthesis)

The specific heat capacity of solar salt nanomaterials synthesized through one-step synthesis technique described in section 2.1.2. The precursor candidate for Alumina (Al_2O_3) nanoparticles in the nitrate salt eutectic system was Aluminum Nitrate Nonahydrate [$Al(NO_3)_3.9H_2O$]. The compositions of each component for different target nanoparticle concentrations are tabulated in Table 16.

Table 16. The compositions of various salt components for different target concentrations of nanoparticles after thermal decojmposition in solar salt eutectic system.

Solar Salt Nanofluid	Initial synthesis mass (g)			Target mass (g) after decomposition reaction		
	KNO_3	$NaNO_3$	$Al(NO_3)_3.9H_2O$	KNO_3	$NaNO_3$	Al_2O_3
0.5% Al_2O_3 by mass fraction (target)	13.93	20.89	1.294	13.93	20.89	0.17
1.0% Al_2O_3 by mass fraction (target)	13.86	20.79	2.575	13.86	20.79	0.35
1.5% Al_2O_3 by mass fraction (target)	13.79	20.68	3.921	13.79	20.68	0.53

The specific heat capacity enhancement for solar salt with addition of Al_2O_3 nanoparticles synthesized through [$Al(NO_3)_3.9H_2O$] are reported earlier in [131]. Hence, in this study only solar salt nanomaterial with 6.9% mass fraction of precursor for a target 1.0% of Al_2O_3 nanoparticles was synthesized for a comparative study.

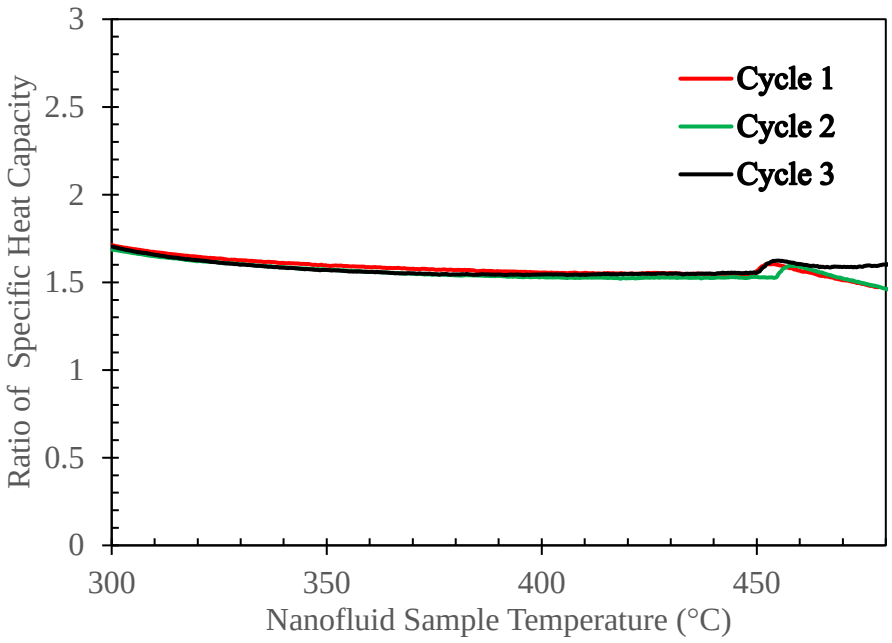

Figure 55. Plot of specific heat capacity ratio of nanofluid to the pure solar salt sample as a function of temperature obtained from T-History experiment. The molten salt samples are prepared by a one-step thermal decomposition technique by addition of 6.9% of [$Al(NO_3)_3.9H_2O$] for a target concentration of 1.0% by mass fraction of Al_2O_3 nanoparticles.

Table 17. Specific heat capacity ratio of nanofluid to the pure solar salt sample as a function of temperature obtained from T-History experiment. The molten salt samples are prepared by a one-step thermal decomposition technique by addition 6.9% of [$Al(NO_3)_3.9H_2O$] for a target concentration of 1.0% by mass fraction of Al_2O_3 nanoparticles.

	300°C	400°C	500°C
Cycle-1	70.2%	55.5%	47.1%
Cycle-2	68.6%	53.1%	43.5%
Cycle-3	60.6%	62.7%	42.3%
Average	66.4%	57.1%	44.3%
STDEV error	6.3%	7.1%	4.6%

3.2.3 Ternary nitrate eutectic nanofluid (One-step synthesis)

The effect of the nanoparticle concentration on the specific heat capacity of the molten salt nanomaterial was examined for a ternary nitrate salt eutectic. The eutectic is $LiNO_3$-$NaNO_3$-KNO_3 (38:15:47 by molar ratio) and has a melting point of 120°C. The lower melting point is favorable in a CSP plant as the need for freeze protection in the form of auxiliary heaters is eliminated. Current commercially used binary eutectic, solar salt, melts at 220°C and needs special care in the form of freeze protection lowering the exegetic efficiency and increasing the cost of electricity. Hence, the ternary nitrate salt eutectic and its nanomaterials for different concentration of nanoparticles are investigated. The synthesis protocol for nanofluid preparation is detailed in section 2.1.2. Table 18 summarizes the components of each salt component along with the additive mass needed for 0.5%, 1.0% and 1.5% by mass fraction of Alumina (Al_2O_3) after complete thermal decomposition of the precursor. All the molten salt nanomaterials were tested for specific heat capacity enhancement through transient T-history analysis as detailed in section 2.4.1.1.

Table 18. The compositions of various salt components for different target concentrations of nanoparticles after thermal decomposition in ternary nitrate salt eutectic system.

Ternary nitrate eutectic nanofluid	Initial synthesis mass (g)				Target mass (g) after decomposition reaction			
	KNO_3	$NaNO_3$	$LiNO_3$	$Al(NO_3)_3.9H_2O$	KNO_3	$NaNO_3$	$LiNO_3$	Al_2O_3
0.5% Al_2O_3 by mass fraction (target)	19.13	5.13	10.55	1.29	19.13	5.13	10.55	0.17
1.0% Al_2O_3 by mass fraction (target)	19.04	5.10	10.49	2.60	19.04	5.10	10.49	0.35
1.5% Al_2O_3 by mass fraction (target)	18.94	5.08	10.44	3.92	18.94	5.08	10.44	0.53

3.2.4 Specific Heat Capacity

Figure 56 shows the results for all the tests performed for samples synthesized for three different target concentrations of alumina. The samples were synthesized for three different concentrations of the $Al_2(NO_3)_3 \cdot 9H_2O$ additive (3.5%, 6.9% and 10.1%) with target mass fraction of the alumina nanoparticles of 0.5%, 1% and 1.5%. The T-History experiments were performed for exactly the same condition as discussed in Section 2.4.1.1 (i.e., all of the samples were heated from 150ºC to 550ºC for 3 consecutive cycles and the temperature response of the thermocouples were recorded for further analyses).

The measurement results from T-History method tabulated in Figure 57. Table 19 and Table 20 indicate that the specific heat capacity of nanofluid samples for a target mass fraction of alumina nanoparticles of 1.0% is the highest of the three mass concentration (for the three temperature values of 300°C, 400°C and 500°C) that were targeted in this study. Table 19 and Table 20 indicate the calculated enhancement values of specific heat capacity for three different target mass concentrations for nanoparticles for the ternary nitrate salt nanofluid samples explored in this study. The detailed calculation procedure is listed in section 2.4.1.1. The results indicate that the level of enhancement decreases as the temperature increases. In addition, the level of enhancement observed decreased as the nanoparticle concentration increased from 1.0%. For the nanofluid sample with 1.5% target mass concentration of alumina nanoparticles, the average enhancement is only 19.5%. It is inferred from these results that the ideal concentration for maximizing the specific heat capacity enhancement for the ternary nitrate salt nanofluids is in excess of 0.5% and less than or equal to 1%.

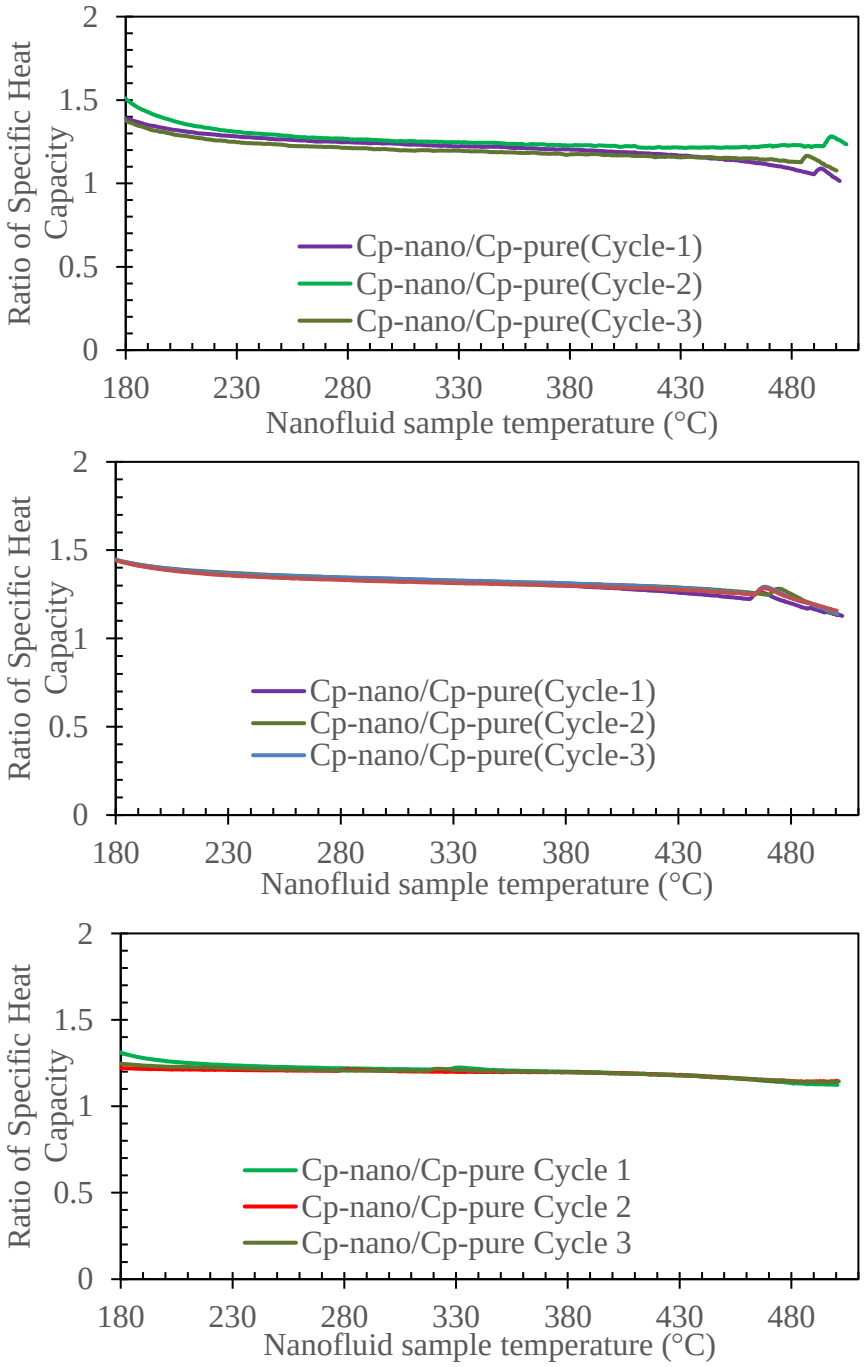

Figure 56. Specific heat capacity ratio of nanofluid samples with respect to pure ternary nitrate salt. The mass fraction of precursor used and target mass fraction alumina nanoparticles, are: (TOP) 3.5% and 0.5%; (MIDDLE) 6.9% and 1.0%; & (BOTTOM) 10.1% and 1.5%, respectively.

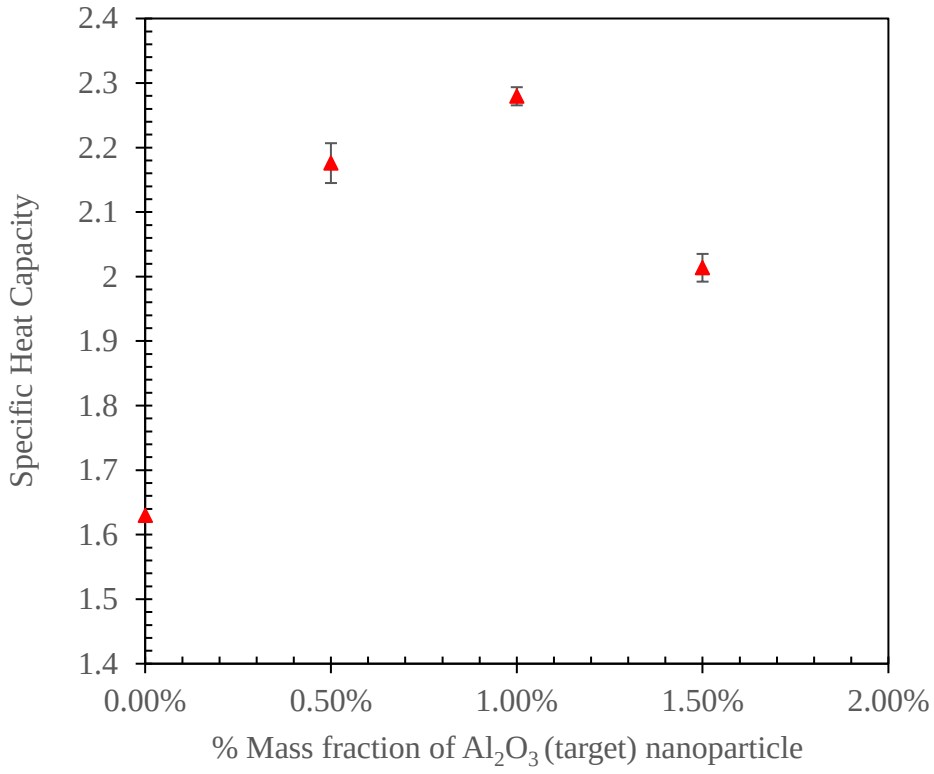

Figure 57. The effect of concentration of alumina nanoparticles synthesized through one-step synthesis thermal decomposition of $Al_2(NO_3)_3 \cdot 9H_2O$ precursor on the ratio of specific heat capacity enhancement of ternary nitrate salt eutectic.

Table 19. Specific heat capacity enhancement of nanofluid samples with respect to pure ternary salt eutectic. The mass fraction of precursor used and the target mass fraction of alumina nanoparticles, are: (TOP TABLE) 3.5 % and 0.5%; (BOTTOM TABLE) 6.9% and 1%.

Cycle No.	200°C		300°C		400°C		500°C	
	Ratio	Uncertainty	Ratio	Uncertainty	Ratio	Uncertainty	Ratio	Uncertainty
1	1.32	1.0%	1.24	1.0%	1.19	1.4%	1.03	2.6%
2	1.38	1.0%	1.25	1.0%	1.23	1.4%	1.27	2.6%
3	1.30	1.0%	1.20	1.0%	1.17	1.4%	1.08	2.4%
Average C_p Enhancement	33%	3.1%	23%	2.5%	19%	3.1%	12%	10.2%

Cycle No.	200°C		300°C		400°C		500°C	
	Ratio	Uncertainty	Ratio	Uncertainty	Ratio	Uncertainty	Ratio	Uncertainty
1	1.39	0.8%	1.33	0.9%	1.29	1.2%	1.14	1.9%
2	1.40	0.8%	1.34	0.9%	1.30	1.2%	1.14	1.9%
3	1.39	0.8%	1.32	0.9%	1.29	1.2%	1.16	1.9%
Average C_p Enhancement	39.8%	1.4%	33.6%	1.6%	29.7%	2.2%	13.9%	3.3%

Table 20. Specific heat capacity enhancement of nanofluid samples with respect to pure ternary salt eutectic. The mass fraction of precursor used and the target mass fraction of alumina nanoparticles are 10.1 % and 1.5%.

Cycle No.	200°C		300°C		400°C		500°C	
	Ratio	**Uncertainty**	**Ratio**	**Uncertainty**	**Ratio**	**Uncertainty**	**Ratio**	**Uncertainty**
1	1.26	0.9%	1.21	0.9%	1.19	1.2%	1.12	1.9%
2	1.21	0.7%	1.20	0.9%	1.19	1.2%	1.14	1.9%
3	1.23	0.8%	1.21	0.9%	1.19	1.2%	1.14	1.9%
Average C_p Enhancement	24%	2.1%	21%	1.6%	19%	2.1%	14%	3.4%

3.3 Thermal Conductivity

3.3.1 Validation Test: Pure Molten Salt

Theoretical validations for buoyancy effects (in the thermal conductivity apparatus described in section 2.4.2.1) were performed. The annulus between the concentric cylinders is treated as liquid between a vertical channel with different sidewall temperatures. Rayleigh number calculated, as shown in equation (17), was used to estimate the effect of buoyancy-driven flow in the cavity.

$$Ra_L = \frac{g\beta(T_1 - T_2)L^3}{\alpha\nu} \tag{22}$$

The critical Rayleigh flow for such configuration is 1000, below which the buoyancy forces cannot overcome the viscous forces and the heat transfer in the fluid medium is purely through conduction [36]. Estimation of Rayleigh number for the apparatus with fluid properties at different temperatures for Solar Salt (60:40 $NaNO_3$:KNO_3 by mass fraction) was performed and tabulated in Table 21. As shown the Rayleigh number estimated for a temperature difference of 20 K, at all temperatures, is significantly lower than the critical value 1000. Hence, on a first approximation it is reasonable to assume that the heat transfer through the liquid film is purely through conduction.

Table 21. Rayleigh number estimation for Solar Salt in a vertical cavity with different sidewall temperatures.

Property	Temperature		
	300°C	**400°C**	**500°C**
μ [Pa-s]	0.00364	0.00228	0.00195
ρ [Kg/m^3]	1899.10	1835.50	1771.90
k [W/(m.K)]	0.43	0.5	0.57
C_p [J/(kg.K)]	1494.62	1511.82	1529.02
g [m/s^2]	9.8	9.8	9.8
β	0.00006	0.00006	0.00006
ΔT, [K]	20	20	20
Spacing, [m]	0.00152	0.00152	0.00152
Pr	12.67	6.89	5.25
α [m^2/s]	0.00000015	0.00000018	0.00000021
ν [m^2/s]	0.00000192	0.00000124	0.00000111
Ra	143.11	185.91	179.05

The thermal conductivity of the pure solar salt was measured at three different temperatures (300°C, 400°C and 500°C). The furnace temperature was adjusted and the chamber along with the molten salt sample is soaked for 12 hours to ensure steady state conditions. After the system reached steady state, temperature drop across the four pair of thermocouples in radial direction is recorded for data analysis. Figure 58 illustrates the temperature measurement plots obtained at three different temperatures for pure solar salt sample as a function of temperature. The heater is located as described in section 2.4.2.1 at the center of the inner cylinder and as a result, the heat transfer occurs radially outward. This is evident as shown is Figure 58, the thermocouples in the inner cylinder are at a higher temperature compared to the thermocouples in outer cylinder.

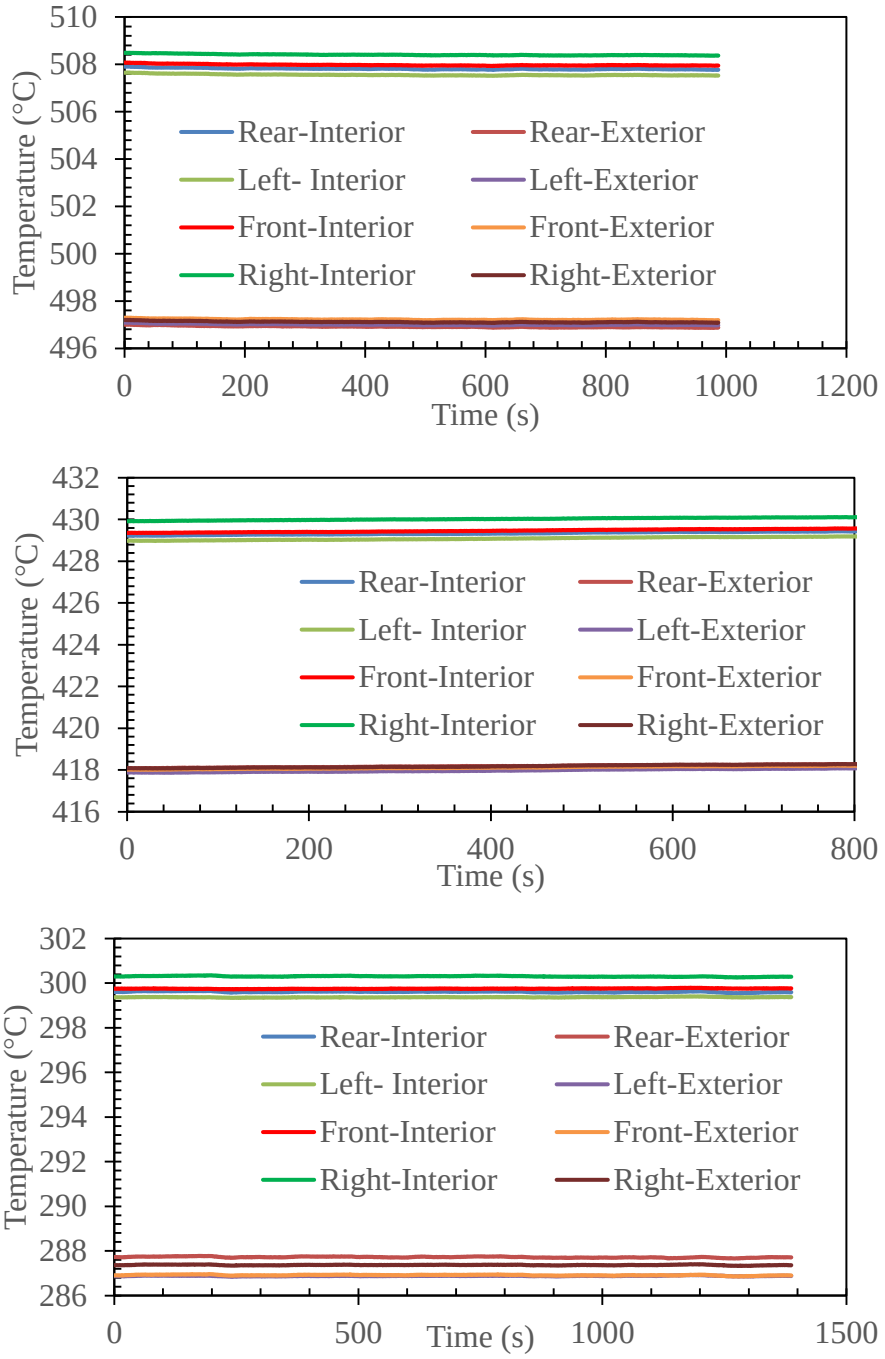

Figure 58. Measurement of temperature across the molten salt film at different temperatures for thermal conductivity tests.

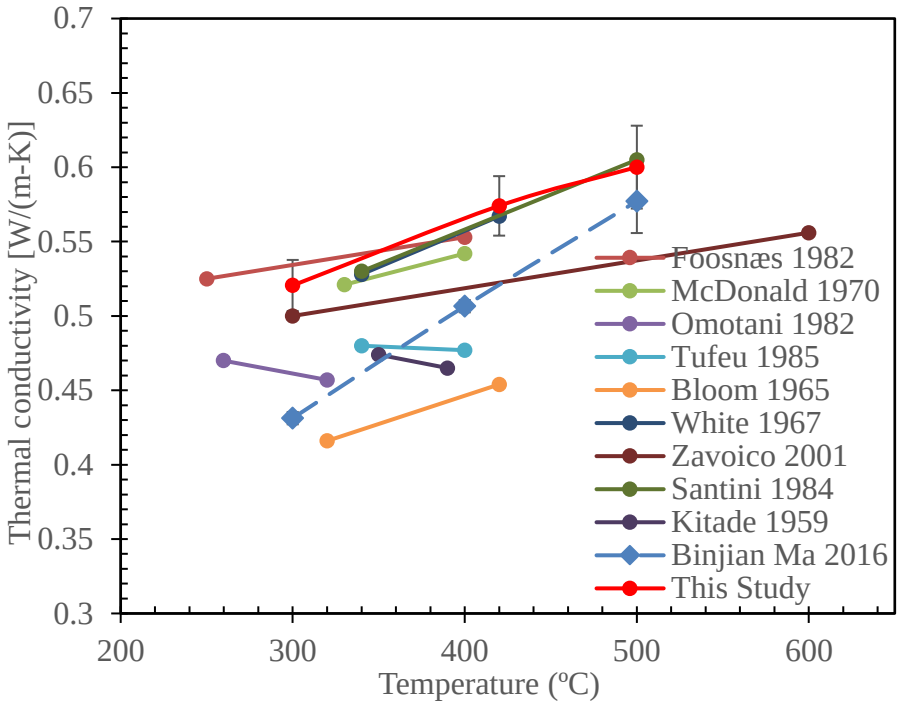

Figure 59. Comparison of the measured thermal conductivity of solar salt with that of the literature.

Table 22. Thermal conductivity measurement values for Solar Salt at three different temperatures measured in this study.

Temperature (°C)	Thermal Conductivity [W/(m.K)]	% Uncertainty
300	0.52	3.3
420	0.57	3.4
500	0.60	4.6

Data analysis was performed according to 1-D steady state heat conduction analysis as detailed in section 2.4.2.1. The measured thermal conductivity of the solar salt samples is compared to existing literature reports as illustrated in Figure 12. The measured thermal conductivity in this study closely matches with the existing literature reports and thus validates the technique for its accuracy. Table 22 summarizes the measurement values at three different temperatures along with the measurement uncertainty.

3.3.2 Solar salt based nanofluid (One-step synthesis)

Molten salt nanomaterials investigated in this study were synthesized through a one-step chemical decomposition technique as discussed in section 2.1.2. The ideal precursor candidate for nanoparticle generation for this synthesis technique are chemically compatible to the base solvent. Hence, in this study Aluminum Nitrate Nonahydrate [$Al(NO_3)_3.9H_2O$] was chosen as a precursor for Alumina Al_2O_3 nanoparticles. The required amount of precursor for a target concentration of Alumina nanoparticles based on the chemical decomposition are tabulated below in Table 23.

Table 23. Mass (g) of components required for a target mass of 35g of solar salt nanofluid.

Solar Salt Nanofluid (target 1.0% Al_2O_3 by mass fraction)	Initial synthesis mass (g)			Target mass (g) after decomposition reaction		
	KNO_3	$NaNO_3$	$Al(NO_3)_3.9H_2O$	KNO_3	$NaNO_3$	Al_2O_3
	13.86	20.79	2.575	13.86	20.79	0.35

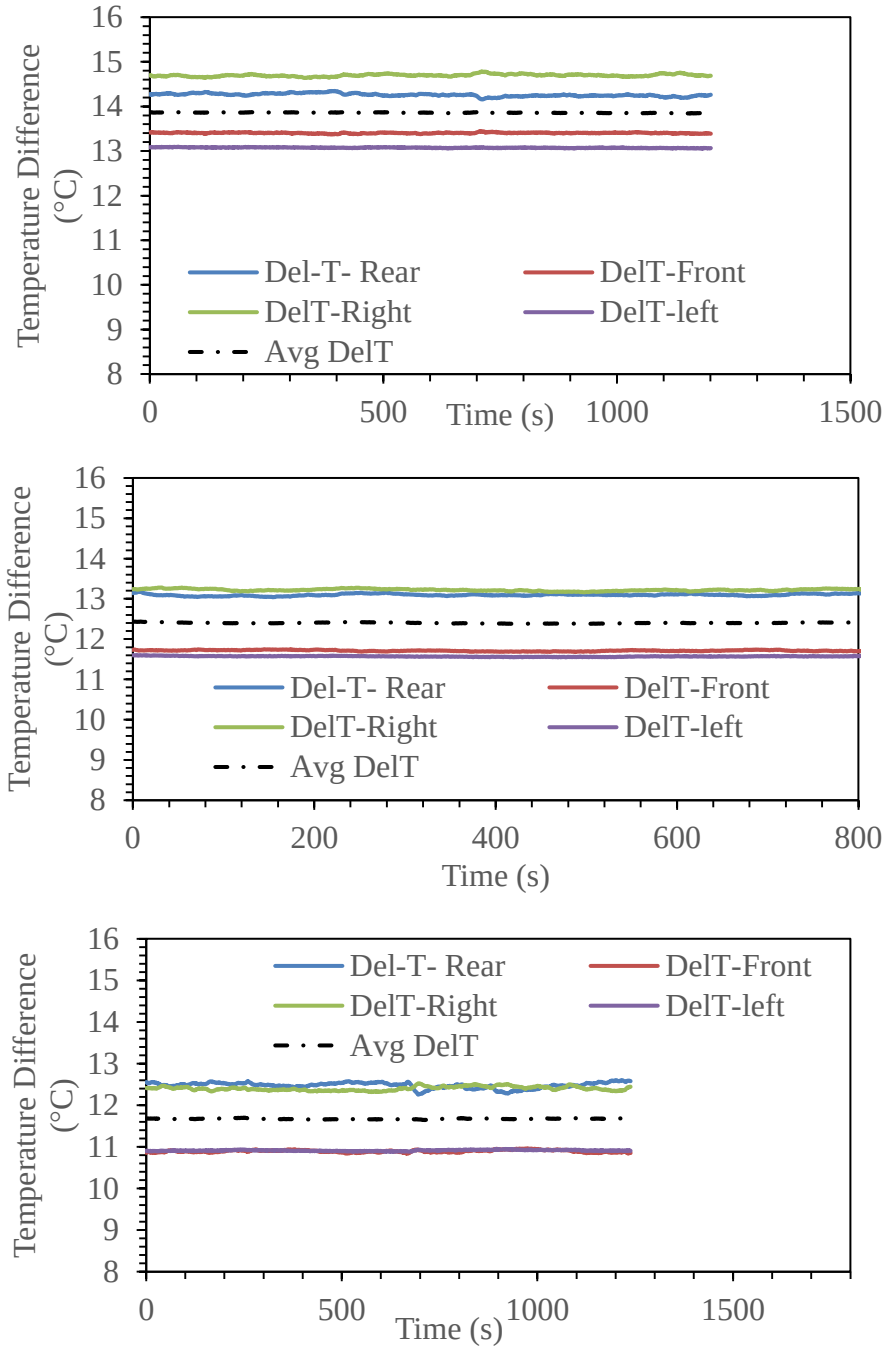

Figure 60. Temperature difference between inner and outer thermocouples pairs for solar salt based alumina nanofluid synthesized through one-step synthesis protocol.

Table 24. Thermal conductivity as a function of temperature for Solar Salt nanofluid samples prepared through one-step synthesis protocol from 6.9% by mass fraction of $Al(NO_3)_3.9H_2O$ (targeting 1.0% Al_2O_3 nanoparticles).

Temperature °C	*SS Al NF[1] [W/(m.K)]*	*Pure Solar Salt [W/(m.K)]*	*% Enhancement*	*% Uncertainty*
300	0.59	0.52	13.46%	4.71%
400	0.66	0.57	15.79%	5.55%
500	0.71	0.6	18.33%	5.00%

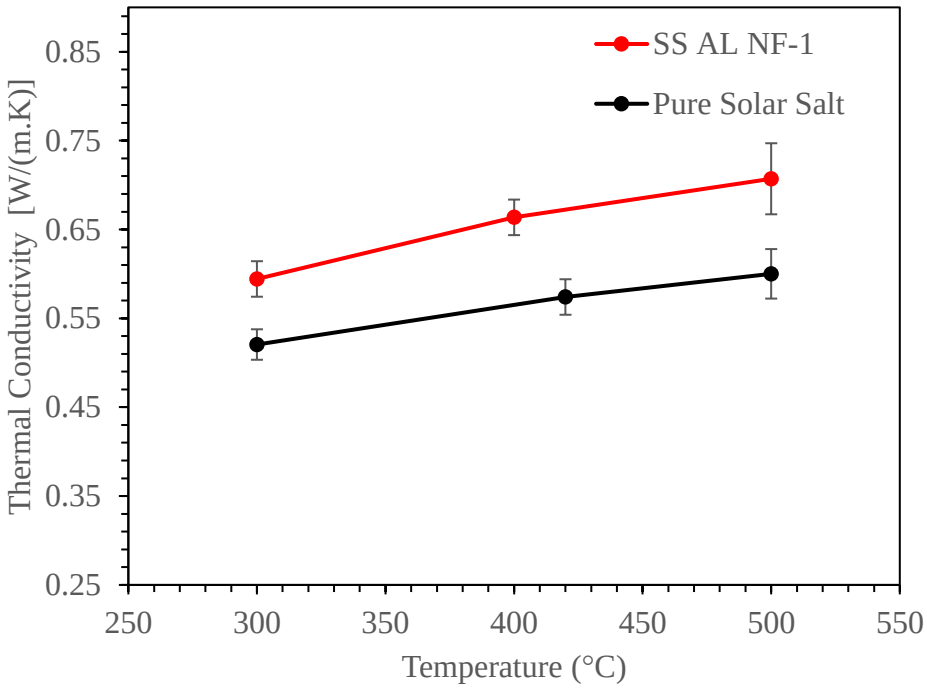

Figure 61. Plot of thermal conductivity a function of temperature for solar salt based alumina nanofluid synthesized through one-step synthesis protocol and pure solar salt sample.

[1] Solar Salt + 6.9% by mass fraction $Al(NO_3)_3.9H_2O$ nanofluid (targeting 1.0% Al_2O_3)

Table 24 summarizes the measurement result over the temperature range for solar salt nanofluid synthesized through a one-step thermal decomposition technique. As the results indicate, thermal conductivity of both pure solar salt and solar salt based nanomaterial increased with an increase in temperature (300°C to 500°C). The enhancement observed in thermal conductivity varied from ~13% to 18% over the tested temperature range for the solar salt nanomaterial. The measurement uncertainty ranged from 4% to 5%.

3.3.3 Ternary nitrate salt nanofluid (One-step synthesis)

The effect of the nanoparticle concentration on the thermal conductivity of the molten salt nanomaterial was examined for a ternary nitrate salt eutectic. The eutectic is $LiNO_3$-$NaNO_3$-KNO_3 (38:15:47 by molar ratio) and has a melting point of 120°C. The lower melting point is favorable in a CSP plant as the need for freeze protection in the form of auxiliary heaters is eliminated. Current commercially used binary eutectic, solar salt, melts at 220°C and needs special care in the form of freeze protection lowering the exegetic efficiency and increasing the cost of electricity. Hence, the ternary nitrate salt eutectic and its nanomaterials for different concentration of nanoparticles are investigated. The synthesis protocol for nanofluid preparation is detailed in section 2.1.2. Table 25 summarizes the components of each salt component along with the additive mass needed for 0.5%, 1.0% and 1.5% by mass fraction of Alumina (Al_2O_3) after complete thermal decomposition of the precursor. All the molten salt nanomaterials are tested for thermal conductivity enhancement through steady state 1-D concentric cylindrical device as detailed in section 2.4.2.1.

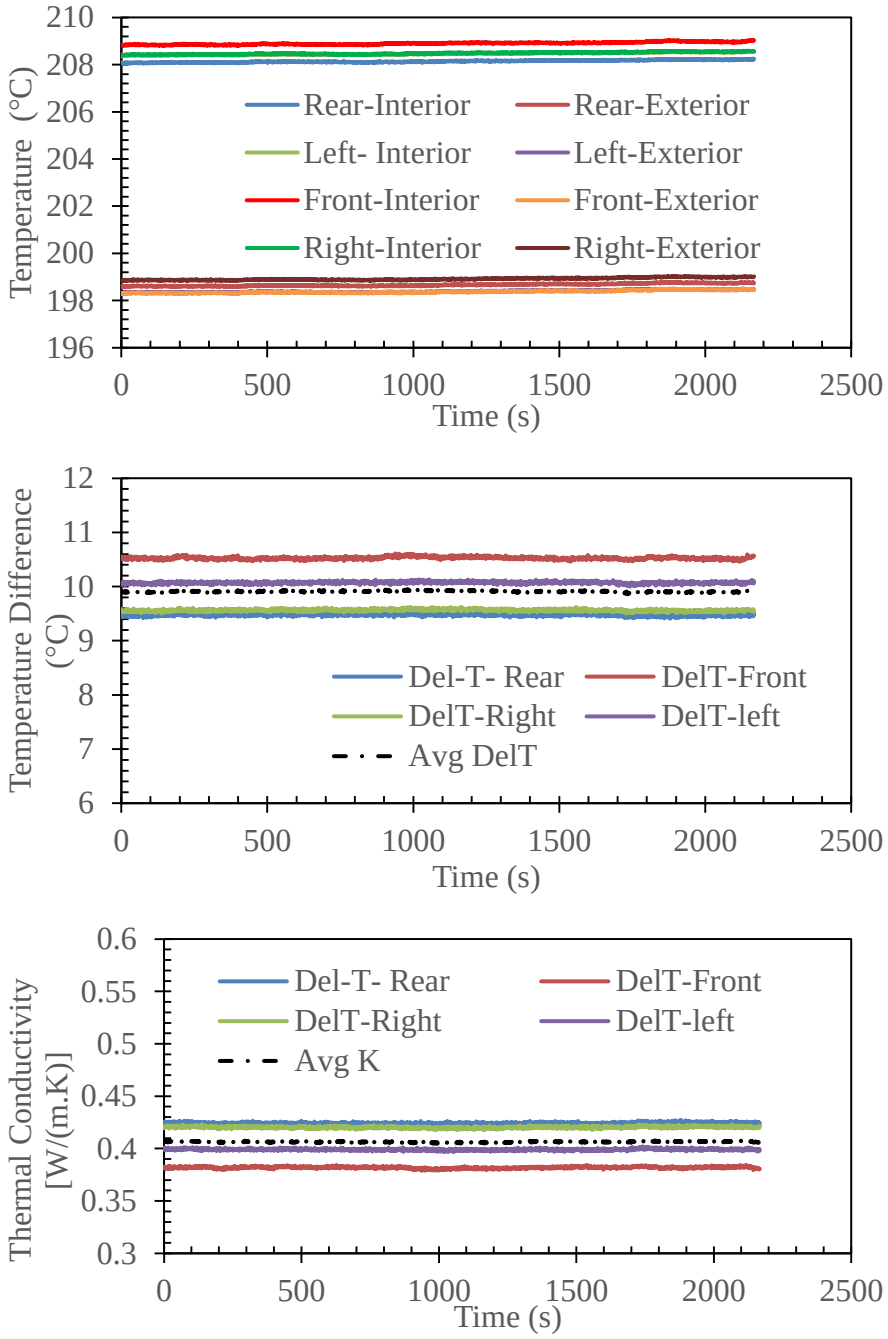

Figure 62. Plot of temperature obtained from thermal conductivity tests at 200°C (TOP). Plot of temperature drop between inner and outer thermocouples obtained from the temperature response curve (MIDDLE). Plot of thermal conductivity calculated for each pair of thermocouple (BOTTOM) for Ternary nitrate salt + 6.9% by mass fraction $Al(NO_3)_3 \cdot 9H_2O$ nanofluid (targeting 1% Al_2O_3).

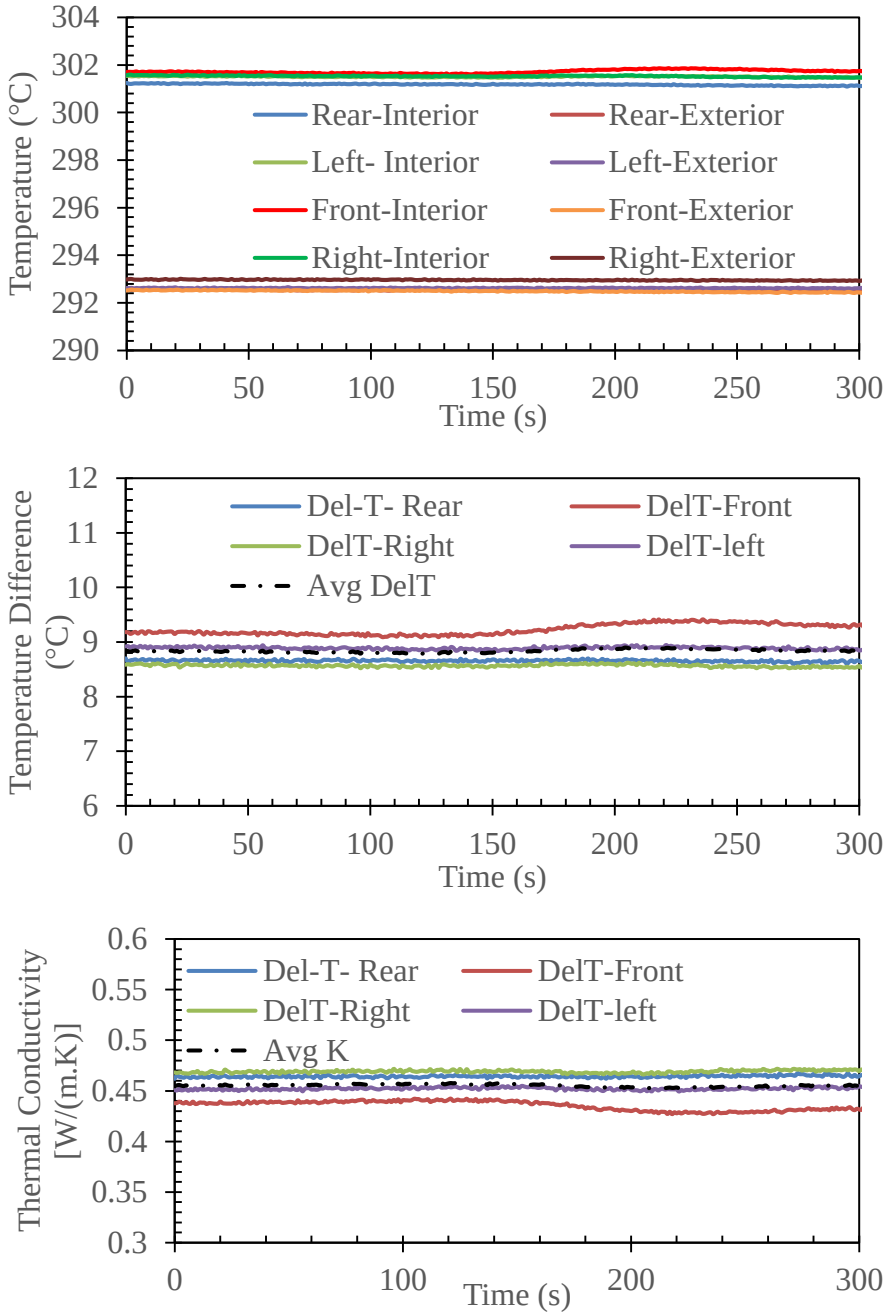

Figure 63. Plot of temperature obtained from thermal conductivity tests at 300°C (TOP). Plot of temperature drop between inner and outer thermocouples obtained from the temperature response curve (MIDDLE). Plot of thermal conductivity calculated for each pair of the thermocouple (BOTTOM) for Ternary nitrate salt + 6.9% by mass fraction $Al(NO_3)_3 \cdot 9H_2O$ nanofluid (targeting 1% Al_2O_3).

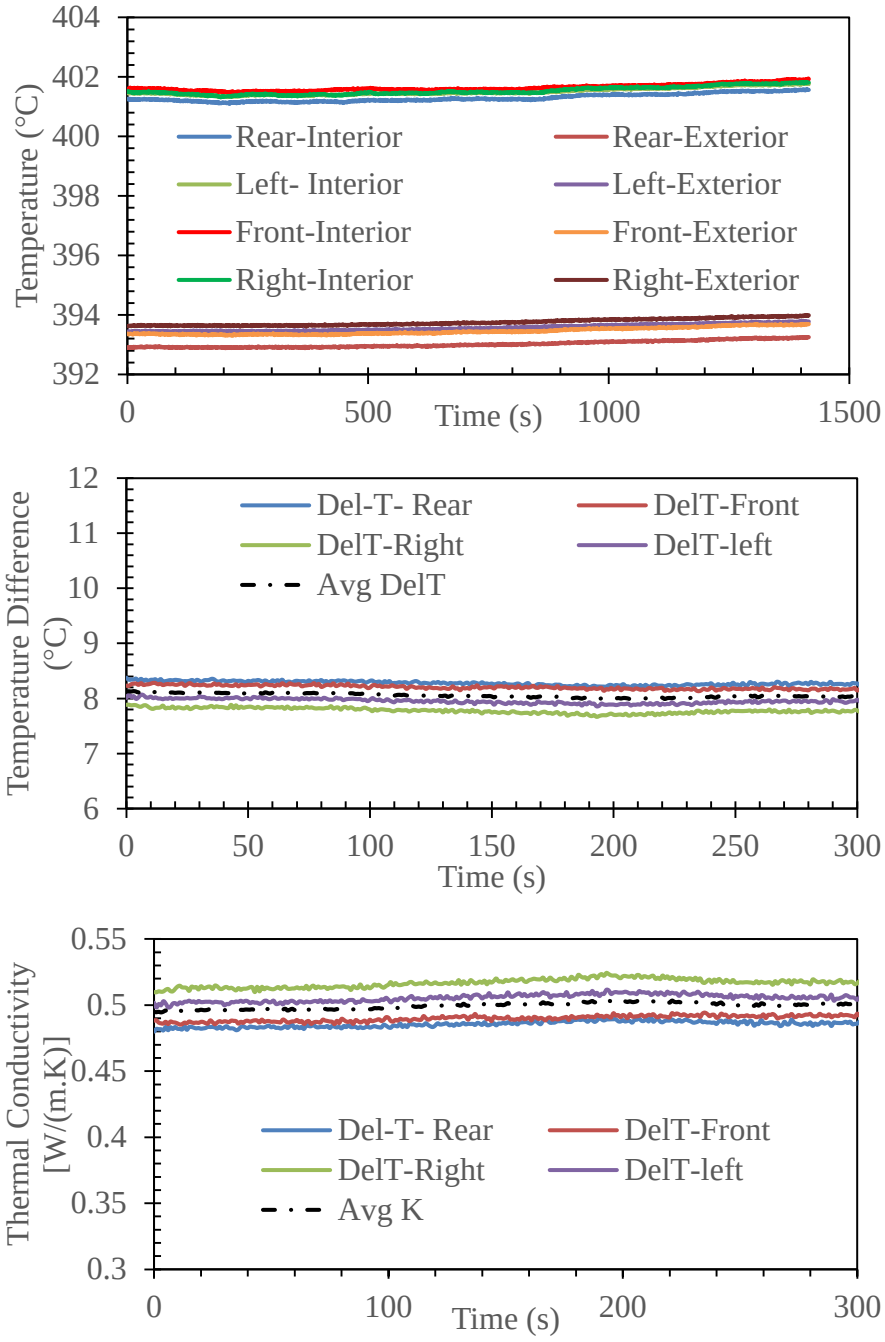

Figure 64. Plot of temperature obtained from thermal conductivity tests at 400°C (TOP). Plot of temperature drop between inner and outer thermocouples obtained from the temperature response curve (MIDDLE). Plot of thermal conductivity calculated for each pair of the thermocouple (BOTTOM) for Ternary nitrate salt + 6.9% by mass fraction $Al(NO_3)_3.9H_2O$ nanofluid (targeting 1% Al_2O_3).

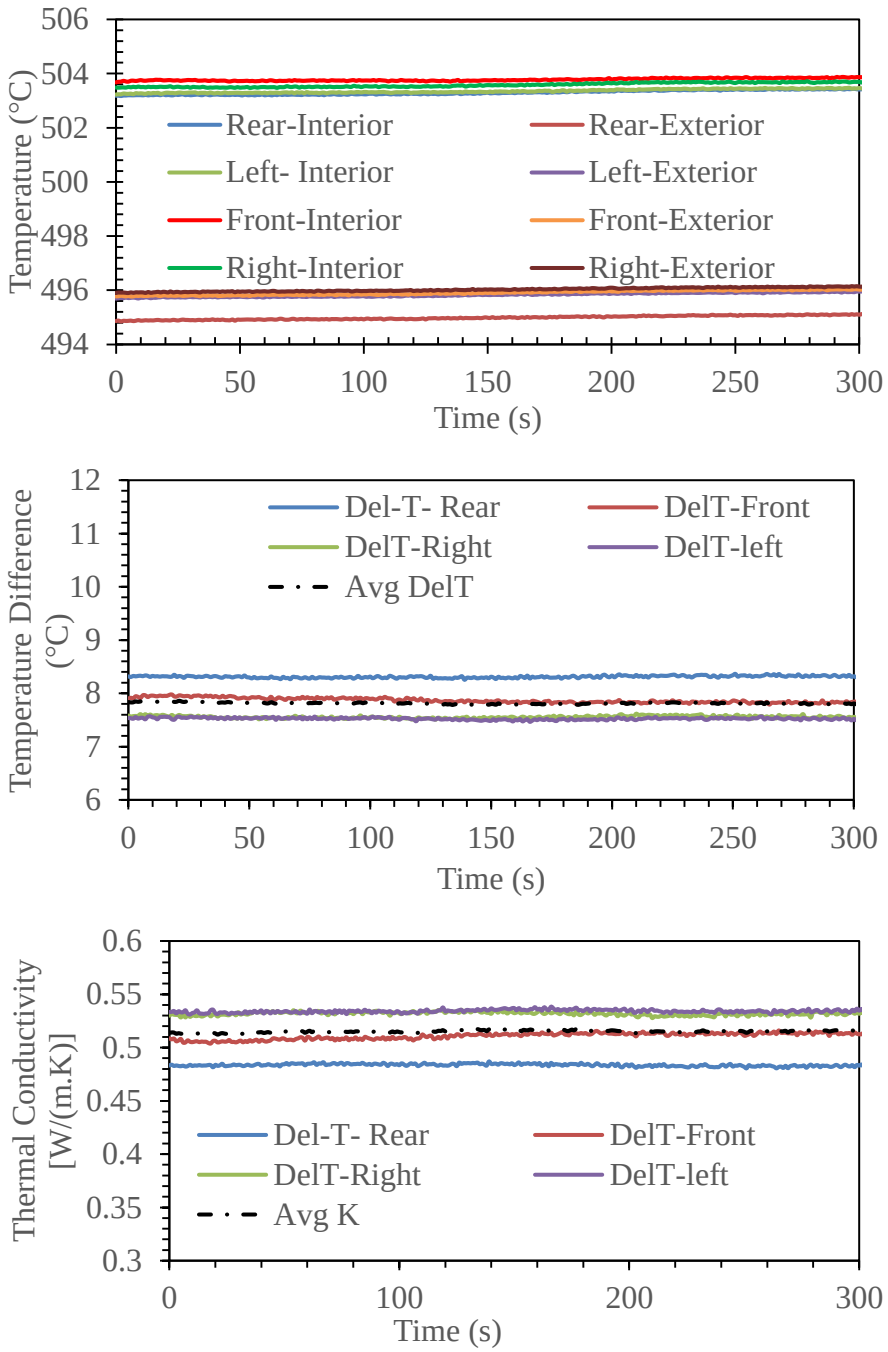

Figure 65. Plot of temperature obtained from thermal conductivity tests at 500°C (TOP). Plot of temperature drop between inner and outer thermocouples obtained from the temperature response curve (MIDDLE). Plot of thermal conductivity calculated for each pair of the thermocouple (BOTTOM) for Ternary nitrate salt + 6.9% by mass fraction $Al(NO_3)_3.9H_2O$ nanofluid (targeting 1% Al_2O_3).

Table 25. Thermal conductivity as a function of temperature for Ternary nitrate salt nanofluid samples prepared through one-step synthesis protocol from 6.9% by mass fraction of $Al(NO_3)_3.9H_2O$ nanofluid (targeting 1.0% Al_2O_3).

Temperature °C	*TS Al NF[2] [W/(m.K)]*	*Pure ternary salt [W/(m.K)]*	*% Enhancement*	*% Uncertainty*
200	0.48	0.40	20%	5%
300	0.54	0.44	21%	7%
400	0.59	0.48	23%	3%
500	0.60	0.52	17%	7%

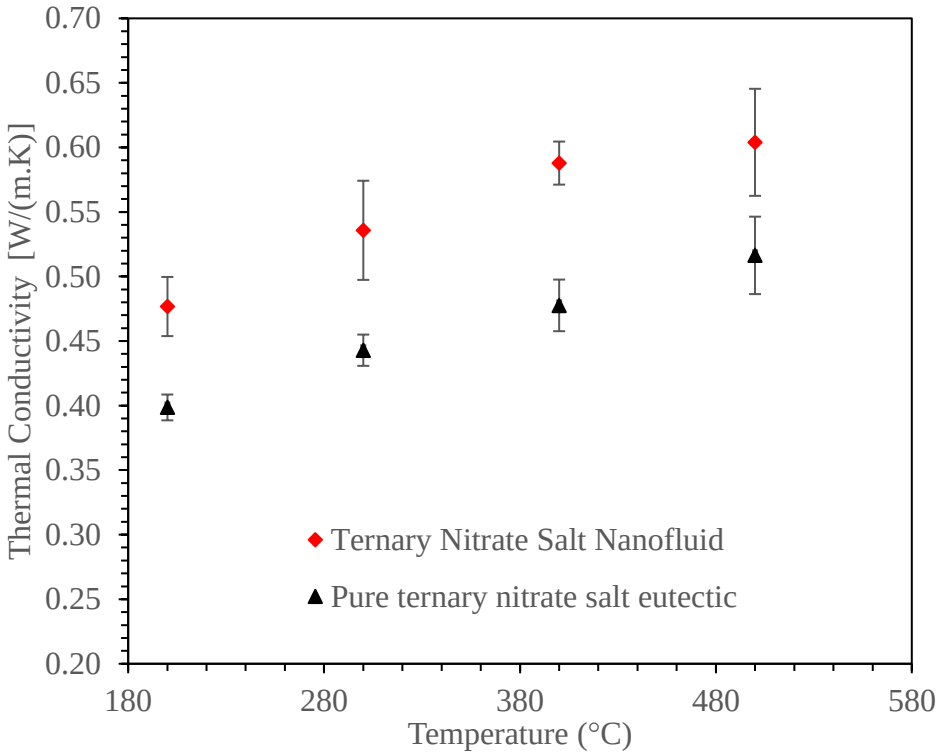

Figure 66. Plot of thermal conductivity a function of temperature for ternary nitrate salt based alumina nanofluid (6.9% by mass fraction $Al(NO_3)_3.9H_2O$ nanofluid targeting 1.0% Al_2O_3)synthesized through one-step synthesis protocol and pure ternary nitrate salt eutectic.

[2] Ternary nitrate salt + 6.9% by mass fraction $Al(NO_3)_3.9H_2O$ nanofluid (targeting 1.0% Al_2O_3)

Figure 62, Figure 63, Figure 64, Figure 65 indicate the experimental measurement result for thermal conductivity measurement at 200°C, 300°C, 400°C and 500°C respectively. As shown in the figures, the temperature drop across the four pairs of thermocouples in the radial direction is uniform under steady state conditions indicative of uniform radial heat conduction in the device. The nanofluid sample is synthesized through a thermal degradation 6.9% of $Al(NO_3)_3 \cdot 9H_2O$ additive (that served as precursor for target mass fraction of 1% of Al_2O_3 nanoparticles on thermal decomposition as discussed in the synthesis protocol outlined in Section 2.1.2). Figure 66 and Table 26 summarize the measurement results for the testing temperature range of 300°C to 500°C. As the results indicate the thermal conductivity of the ternary nitrate salt eutectic enhanced by an average of ~20% over the entire temperature range by target mass fraction of 1.0% of Alumina nanoparticles generated through an *in-situ* technique.

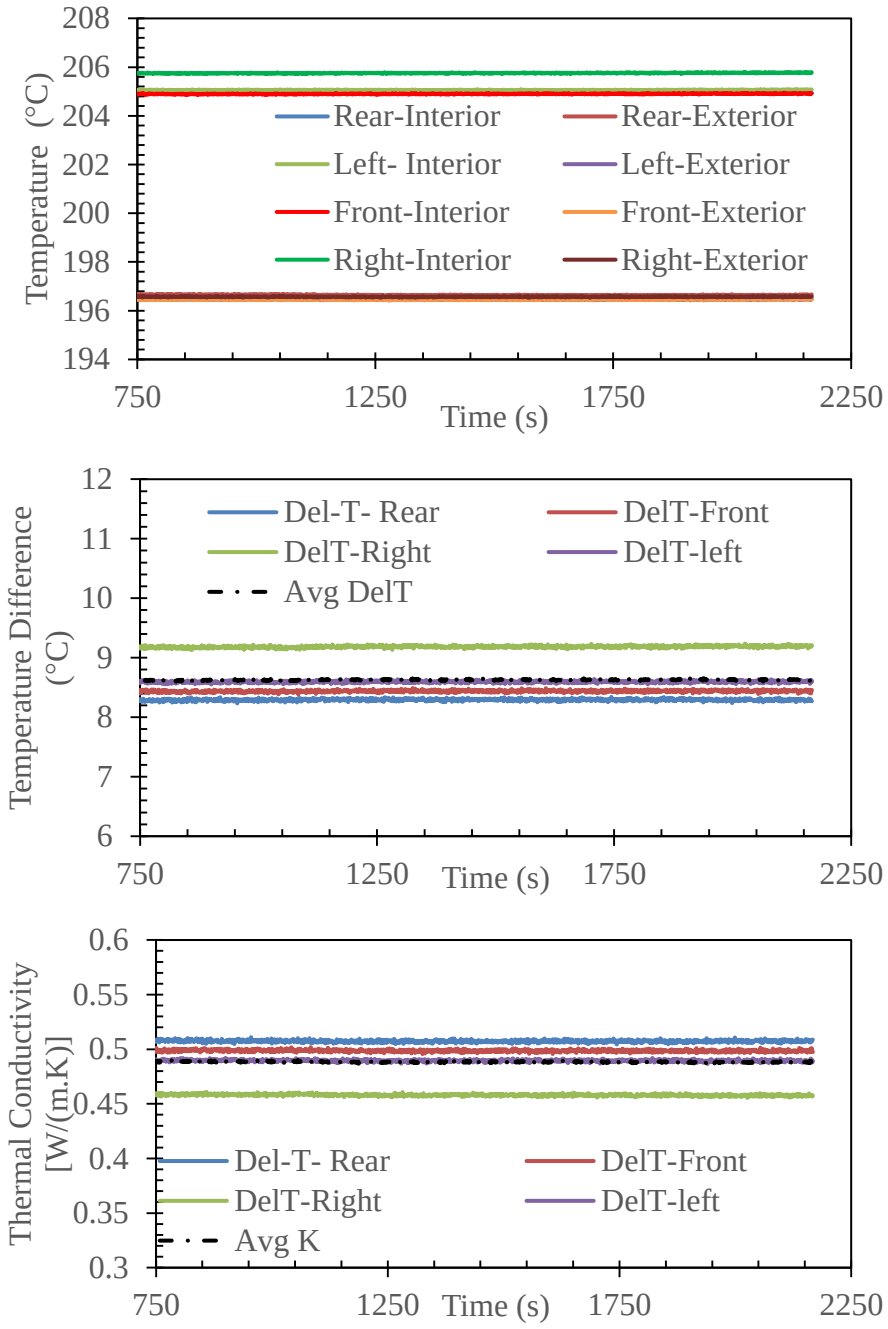

Figure 67. Plot of temperature obtained from thermal conductivity tests at 200°C (TOP). Plot of temperature drop between inner and outer thermocouples obtained from the temperature response curve (MIDDLE). Plot of thermal conductivity calculated for each pair of thermocouple (BOTTOM) for Ternary nitrate salt + 3.6% by mass fraction $Al(NO_3)_3.9H_2O$ nanofluid (targeting 0.5% Al_2O_3).

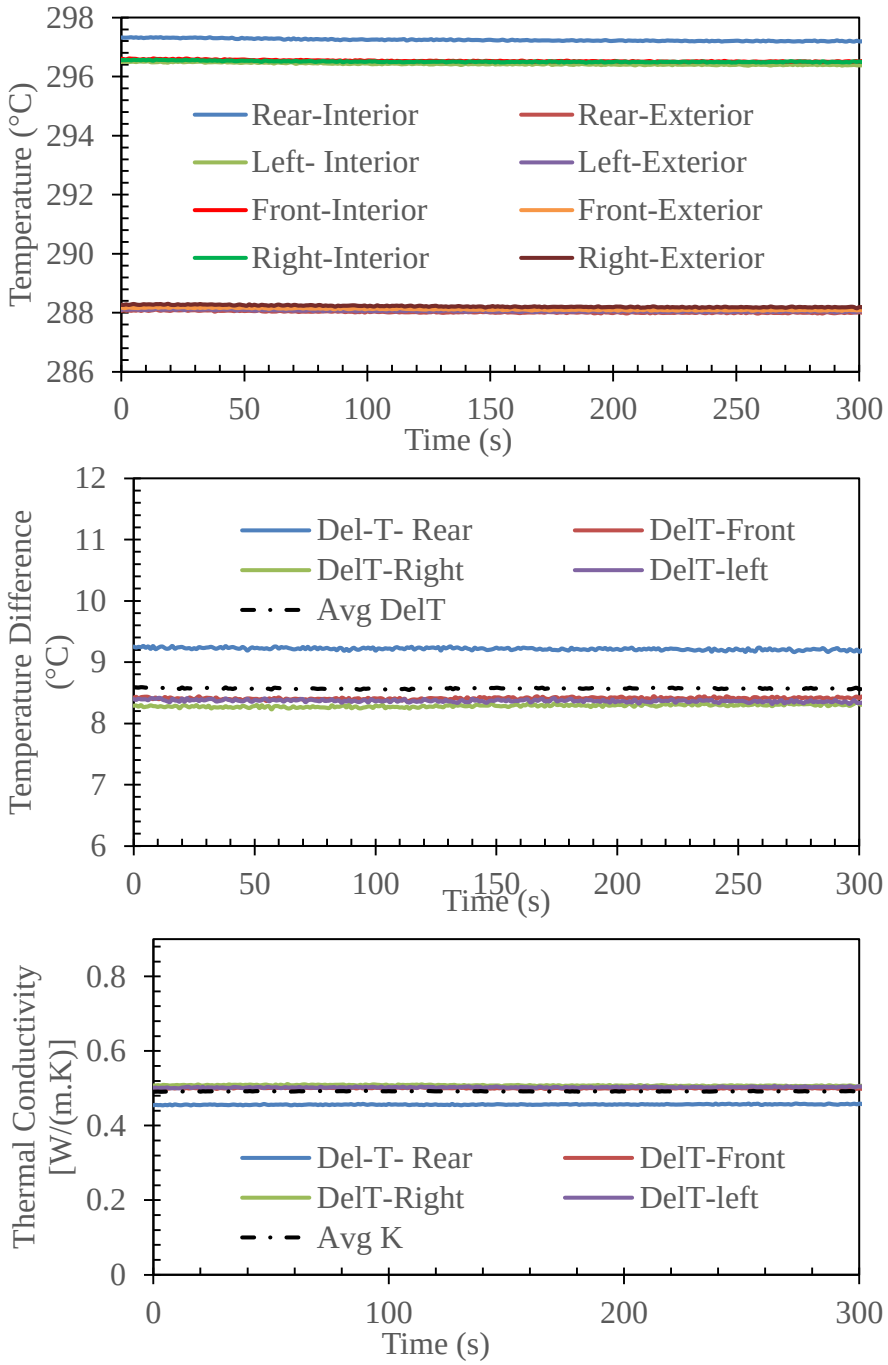

Figure 68. Plot of temperature obtained from thermal conductivity tests at 300°C (TOP). Plot of temperature drop between inner and outer thermocouples obtained from the temperature response curve (MIDDLE). Plot of thermal conductivity calculated for each pair of thermocouple (BOTTOM) for Ternary nitrate salt + 3.6% by mass fraction $Al(NO_3)_3.9H_2O$ nanofluid (targeting 0.5% Al_2O_3).

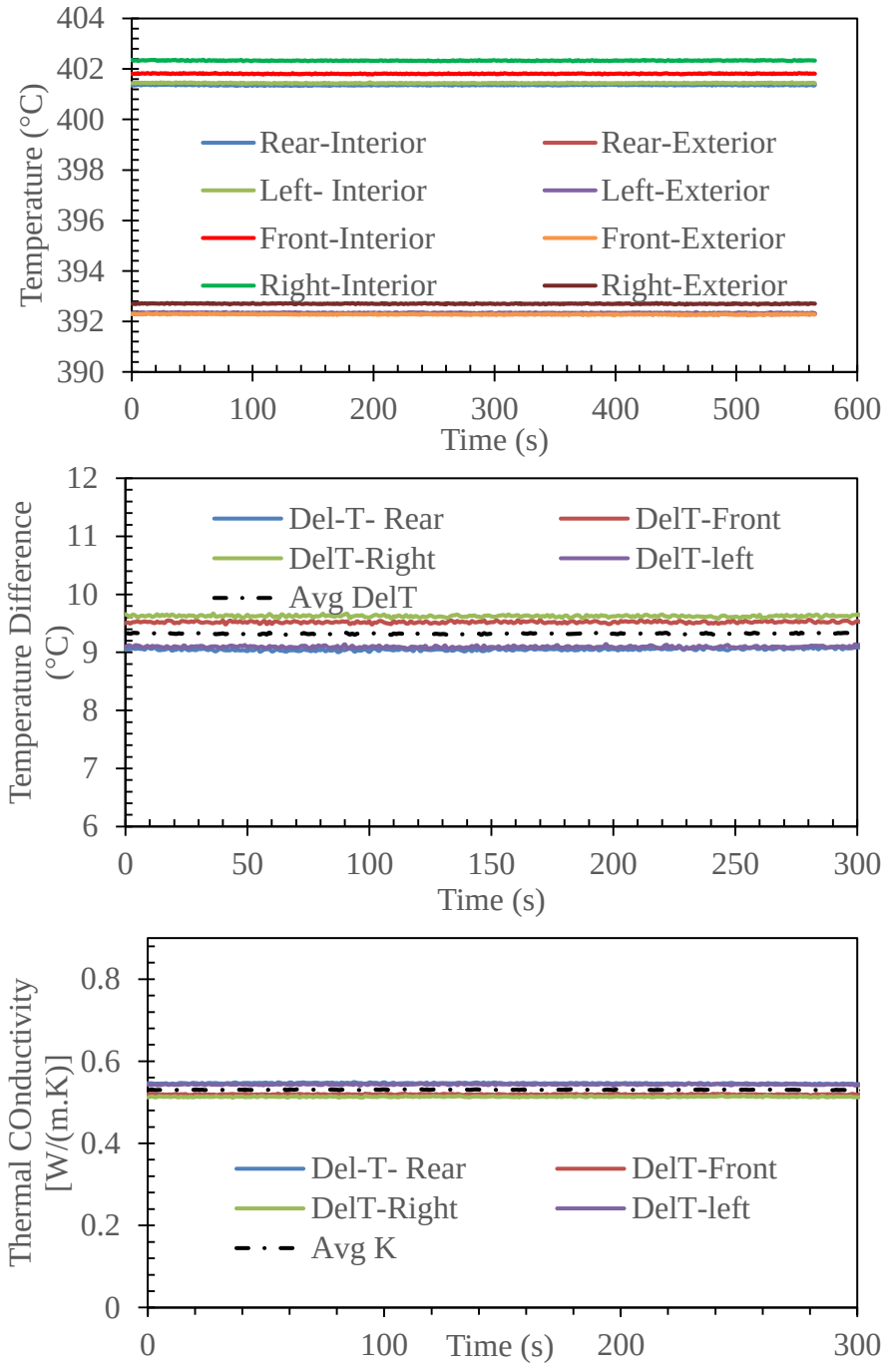

Figure 69. Plot of temperature obtained from thermal conductivity tests at 400°C (TOP). Plot of temperature drop between inner and outer thermocouples obtained from the temperature response curve (MIDDLE). Plot of thermal conductivity calculated for each pair of thermocouple (BOTTOM) for Ternary nitrate salt + 3.6% by mass fraction $Al(NO_3)_3.9H_2O$ nanofluid (targeting 0.5% Al_2O_3).

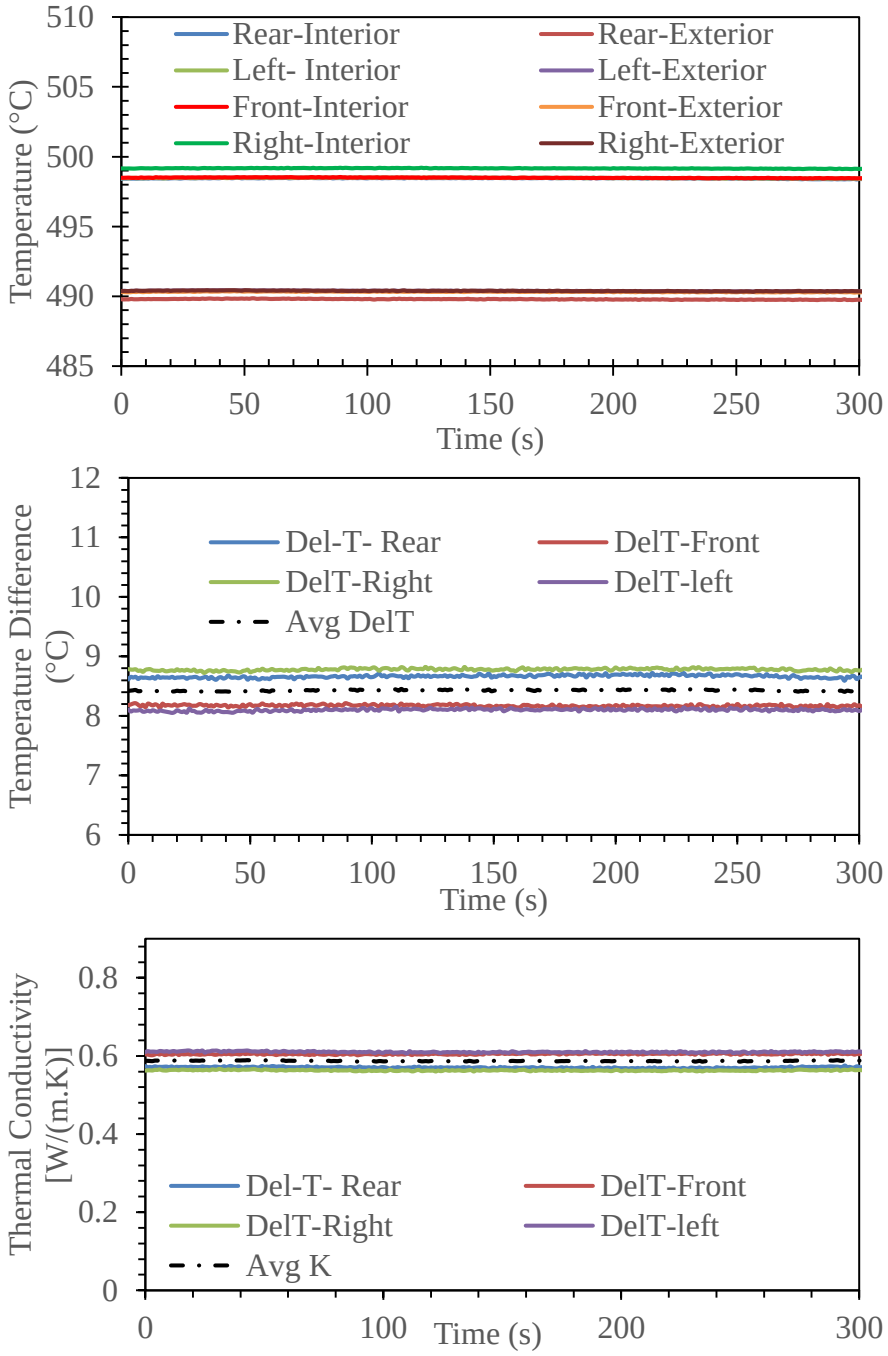

Figure 70. Plot of temperature obtained from thermal conductivity tests at 500°C (TOP). Plot of temperature drop between inner and outer thermocouples obtained from the temperature response curve (MIDDLE). Plot of thermal conductivity calculated for each pair of the thermocouple (BOTTOM) for Ternary nitrate salt + 3.6% by mass fraction $Al(NO_3)_3.9H_2O$ nanofluid (targeting 0.5% Al_2O_3).

Table 26. Thermal conductivity as a function of temperature for Ternary nitrate salt nanofluid samples prepared through one-step synthesis protocol from 3.6% by mass fraction of $Al(NO_3)_3.9H_2O$ nanofluid (targeting 0.5% Al_2O_3).

Temperature °C	*TS Al NF[3] [W/(m.K)]*	*Pure ternary salt [W/(m.K)]*	*% Enhancement*	*% Uncertainty*
200	0.49	0.40	22%	5%
300	0.49	0.44	11%	6%
400	0.53	0.48	11%	3%
500	0.69	0.52	14%	3%

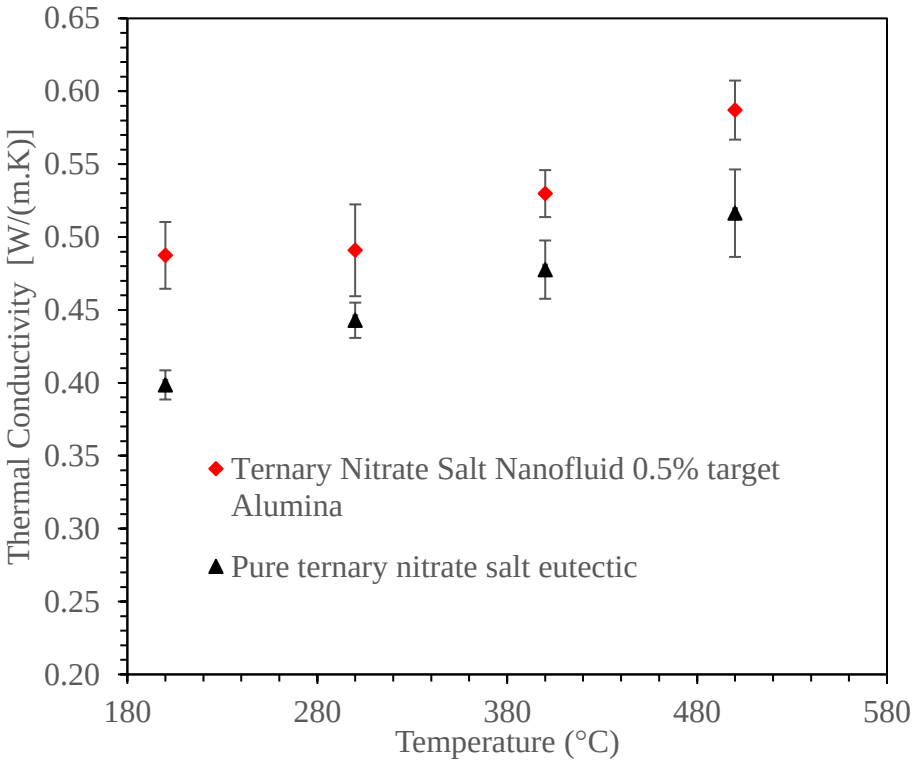

Figure 71. Plot of thermal conductivity a function of temperature for ternary nitrate salt based alumina nanofluid (3.6% by mass fraction $Al(NO_3)_3.9H_2O$ nanofluid targeting 0.5% Al_2O_3) synthesized through one-step synthesis protocol and pure ternary nitrate salt eutectic.

[3] Ternary nitrate salt + 3.6% by mass fraction $Al(NO_3)_3.9H_2O$ nanofluid (targeting 0.5% Al_2O_3)

Figure 67, Figure 68, Figure 69, Figure 70 indicate the experimental measurement result for thermal conductivity measurement at 200°C, 300°C, 400°C and 500°C respectively. The nanofluid sample is synthesized through a thermal degradation 3.6% of $Al(NO_3)_3 \cdot 9H_2O$ additive (that served as precursor for target mass fraction of 0.5% of Al_2O_3 nanoparticles on thermal decomposition as discussed in the synthesis protocol outlined in Section 2.1.2). As shown in the figures, the temperature drop across the four pairs of thermocouples in the radial direction is uniform under steady state conditions suggestive of uniform radial heat conduction in the apparatus. Table 27 and Figure 71 summarize the measurement results for the testing temperature range of 300°C to 500°C. As the results indicate the thermal conductivity of the ternary nitrate salt eutectic enhanced by an average of ~14% over the entire temperature range by target mass fraction of 0.5% of Alumina nanoparticles generated through an *in-situ* technique. The enhancement observed for target concentration of 0.5% Alumina is lower compared to that of 1.0% Alumina (target mass fraction).

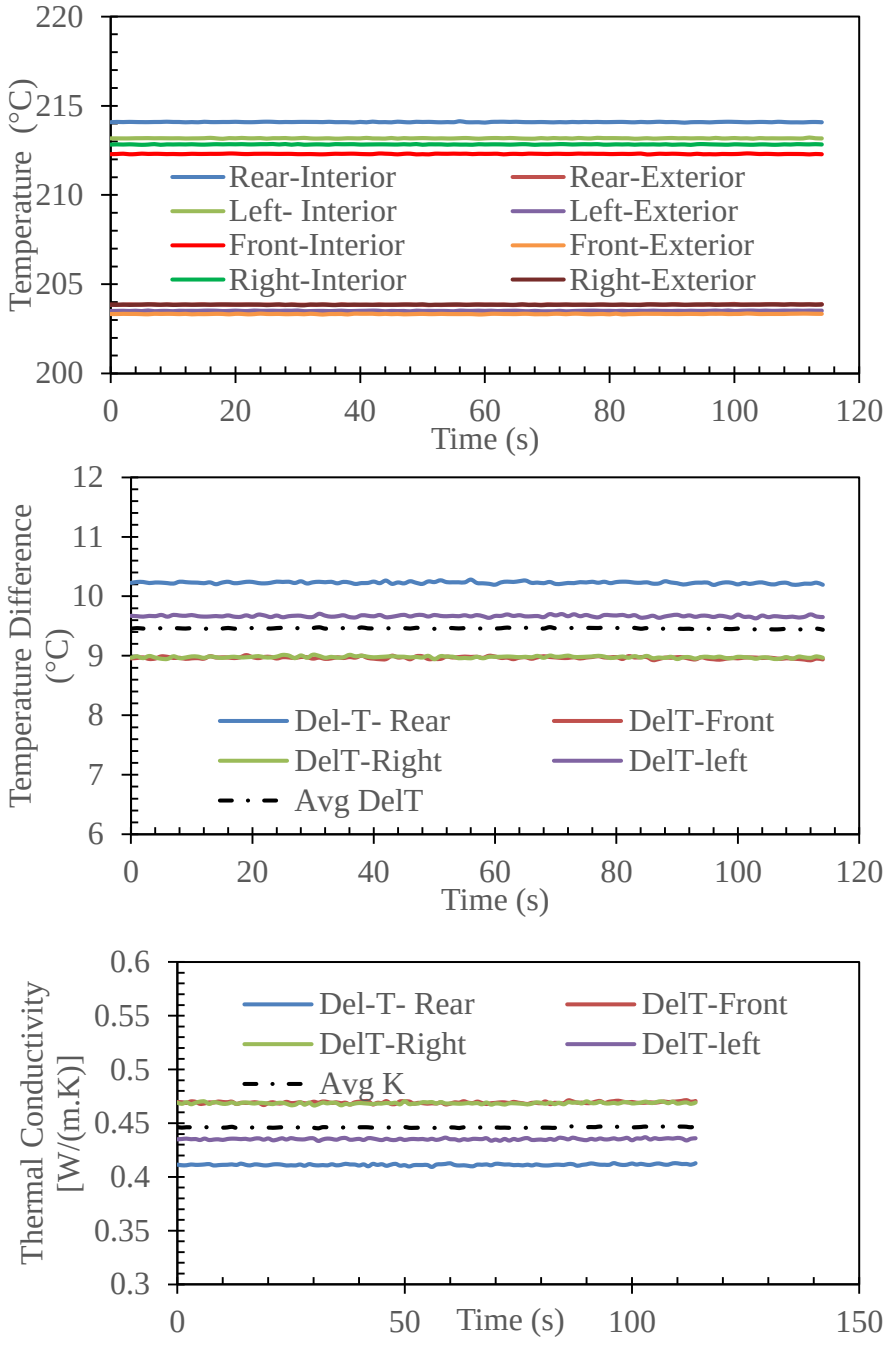

Figure 72. Plot of temperature obtained from thermal conductivity tests at 200°C (TOP). Plot of temperature drop between inner and outer thermocouples obtained from the temperature response curve (MIDDLE). Plot of thermal conductivity calculated for each pair of the of thermocouple (BOTTOM) for Ternary nitrate salt + 10.2% by mass fraction $Al(NO_3)_3.9H_2O$ nanofluid (targeting 1.5% Al_2O_3).

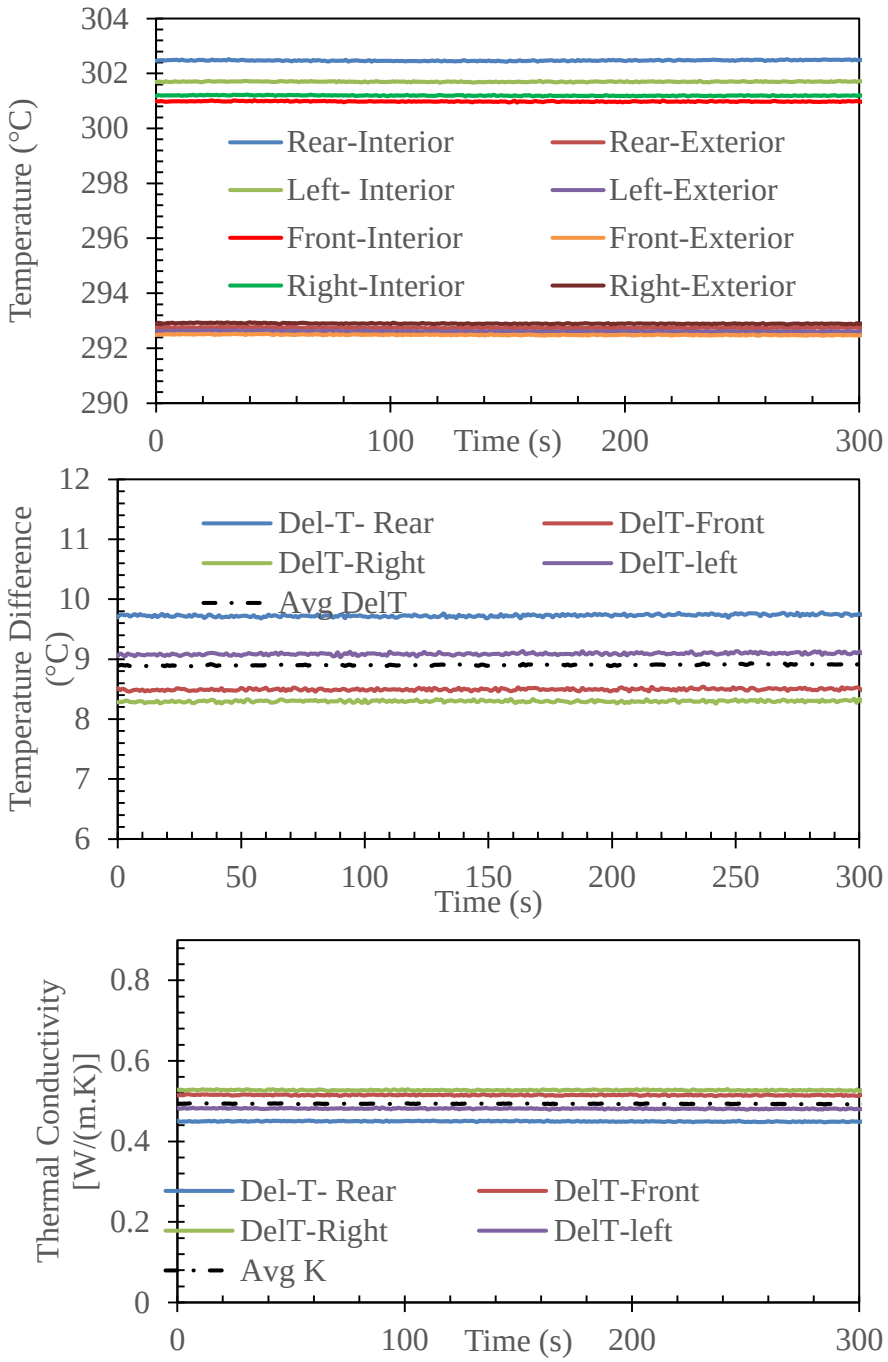

Figure 73. Plot of temperature obtained from thermal conductivity tests at 300°C (TOP). Plot of temperature drop between inner and outer thermocouples obtained from the temperature response curve (MIDDLE). Plot of thermal conductivity calculated for each pair of the of thermocouple (BOTTOM) for Ternary nitrate salt + 10.2% by mass fraction $Al(NO_3)_3.9H_2O$ nanofluid (targeting 1.5% Al_2O_3).

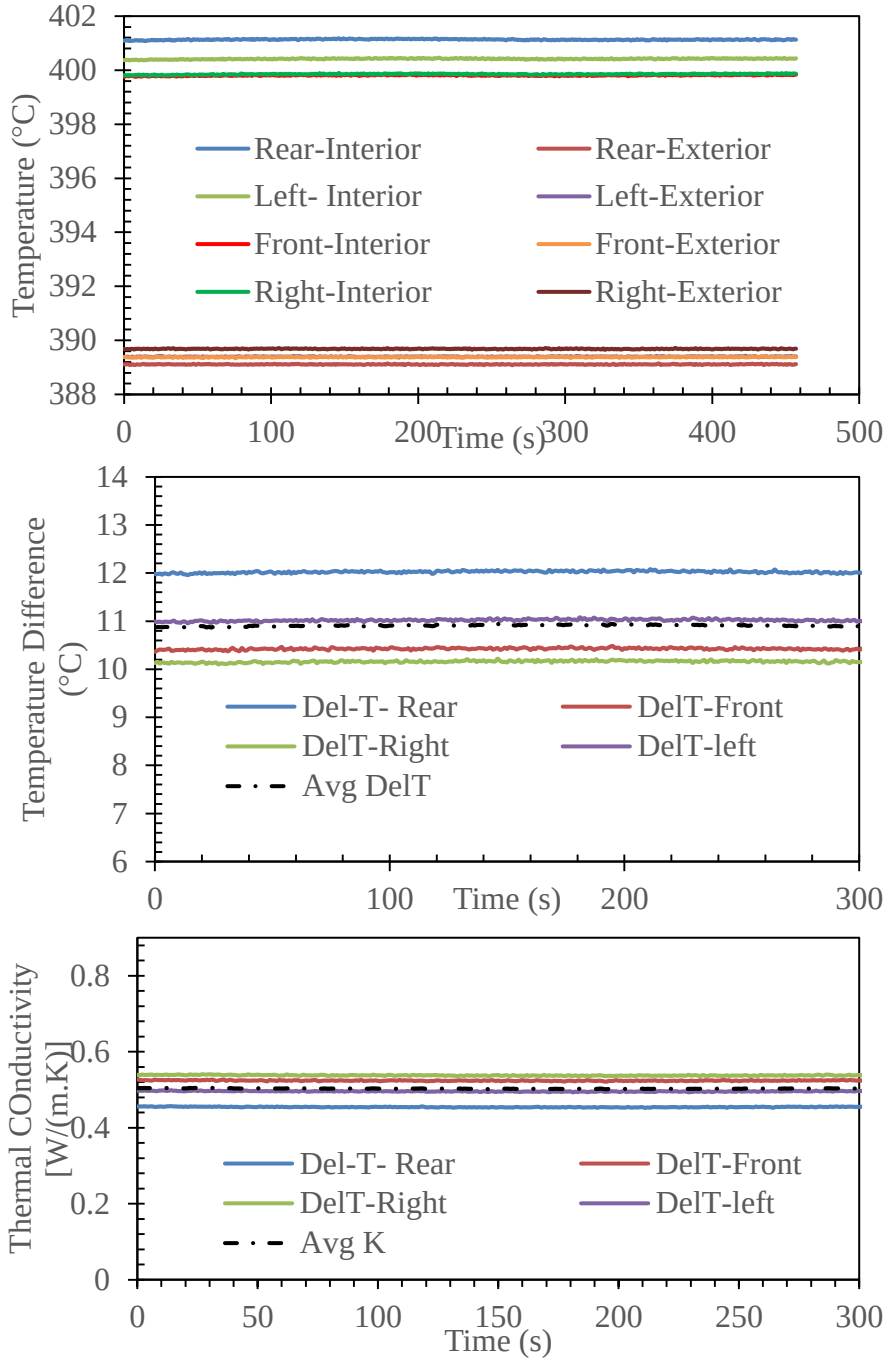

Figure 74. Plot of temperature obtained from thermal conductivity tests at 400°C (TOP). Plot of temperature drop between inner and outer thermocouples obtained from the temperature response curve (MIDDLE). Plot of thermal conductivity calculated for each pair of the thermocouple (BOTTOM) for Ternary nitrate salt + 10.2% by mass fraction $Al(NO_3)_3.9H_2O$ nanofluid (targeting 1.5% Al_2O_3).

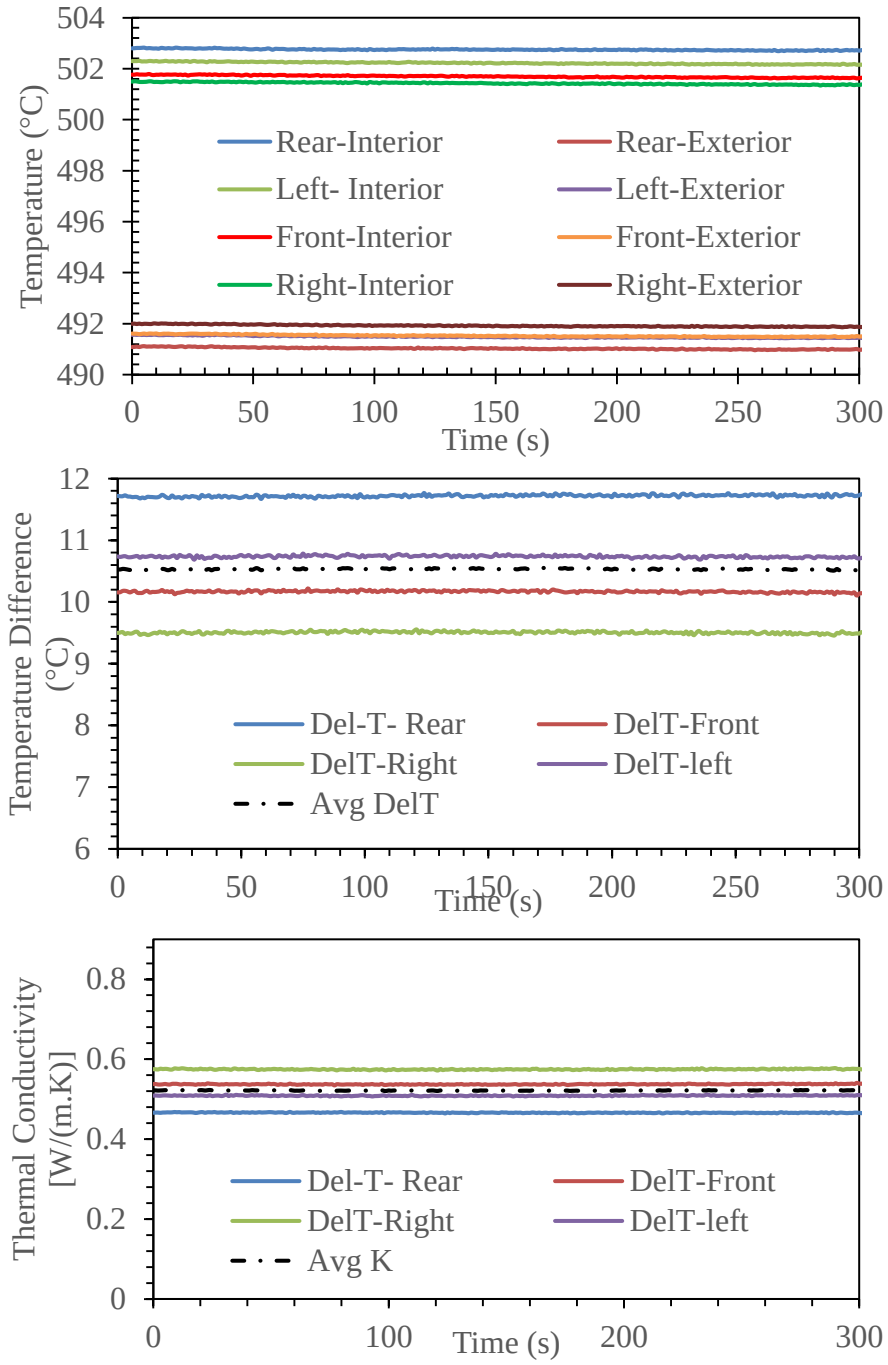

Figure 75. Plot of temperature obtained from thermal conductivity tests at 500°C (TOP). Plot of temperature drop between inner and outer thermocouples obtained from the temperature response curve (MIDDLE). Plot of thermal conductivity calculated for each pair of the thermocouple (BOTTOM) for Ternary nitrate salt + 10.2% by mass fraction $Al(NO_3)_3.9H_2O$ nanofluid (targeting 1.5% Al_2O_3).

Table 27. Thermal conductivity as a function of temperature for Ternary nitrate salt nanofluid samples prepared through one-step synthesis protocol from 10.2% by mass fraction of $Al(NO_3)_3.9H_2O$ nanofluid (targeting 1.5% Al_2O_3).

Temperature °C	*TS Al NF[4] [W/(m.K)]*	*Pure ternary salt [W/(m.K)]*	*% Enhancement*	*% Uncertainty*
200	0.44	0.40	12%	5%
300	0.49	0.44	11%	3%
400	0.50	0.48	5%	3%
500	0.52	0.52	1%	3%

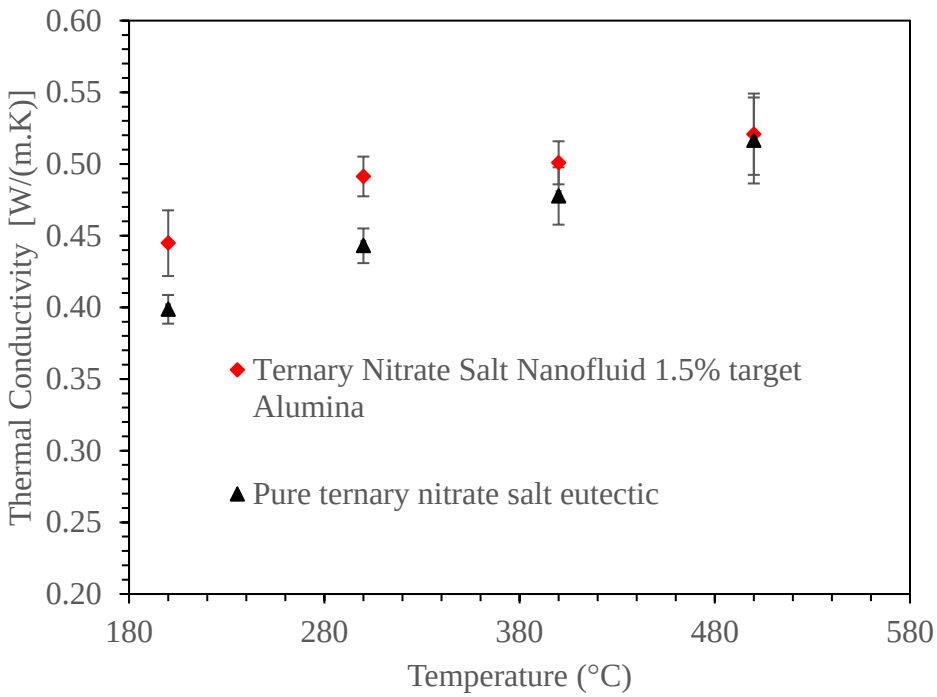

Figure 76. Plot of thermal conductivity a function of temperature for ternary nitrate salt based alumina nanofluid (10.2% by mass fraction $Al(NO_3)_3.9H_2O$ nanofluid targeting 1.5% Al_2O_3) synthesized through one-step synthesis protocol and pure ternary nitrate salt eutectic.

[4] Ternary nitrate salt + 10.2% by mass fraction $Al(NO_3)_3.9H_2O$ nanofluid (targeting 1.5% Al_2O_3)

Figure 72, Figure 73, Figure 74 and Figure 75 indicate the experimental measurement result for thermal conductivity measurement at 200°C, 300°C, 400°C and 500°C respectively. The nanofluid sample is synthesized through a thermal degradation 10.2% of $Al(NO_3)_3 \cdot 9H_2O$ additive (that served as precursor for target mass fraction of 1.5% of Al_2O_3 nanoparticles on thermal decomposition as discussed in the synthesis protocol outlined in Section 2.1.2). As shown in the figures, the temperature drop across the four pairs of thermocouples in the radial direction is uniform under steady state conditions suggestive of uniform radial heat conduction in the apparatus. Figure 76 and Table 27 summarize the measurement results for the testing temperature range of 300°C to 500°C. As the results indicate the thermal conductivity of the ternary nitrate salt eutectic enhanced by an average of ~7% over the entire temperature range by target mass fraction of 0.5% of Alumina nanoparticles generated through an *in-situ* technique. The enhancement observed for the target concentration of 1.5% Alumina is lower compared to 0.5% and 1.0%. This may be due to particle agglomeration and sedimentation of nanoparticles during the testing period.

3.4 Two Phase Heat Transfer

As discussed in section 1.5.2 data for nanofluid flow boiling are controversial and scarce. Subcooled flow boiling experiments were conducted in the flow boiling apparatus as shown in Figure 77, Figure 78 and Figure 79.

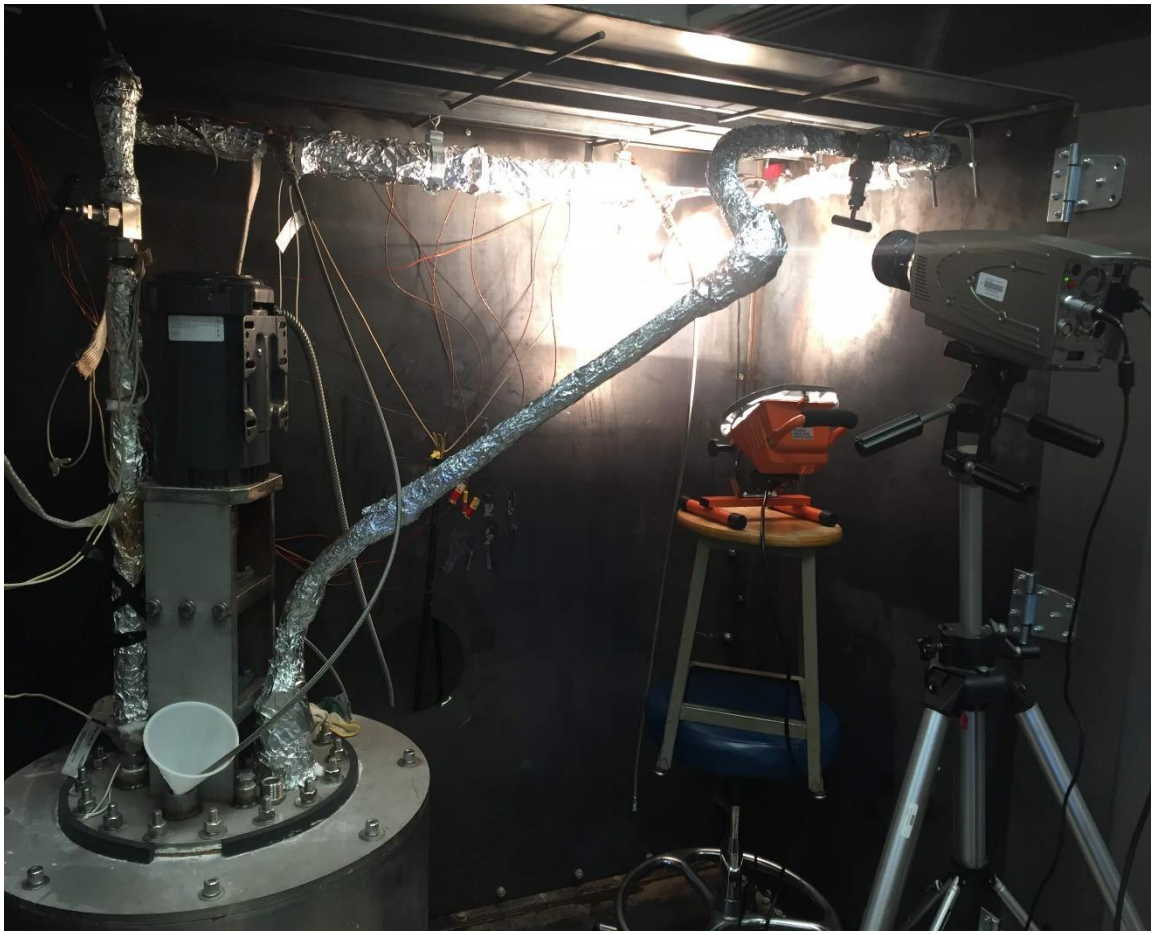

Figure 77. Overview of experimental apparatus for flow boiling of nanofluids

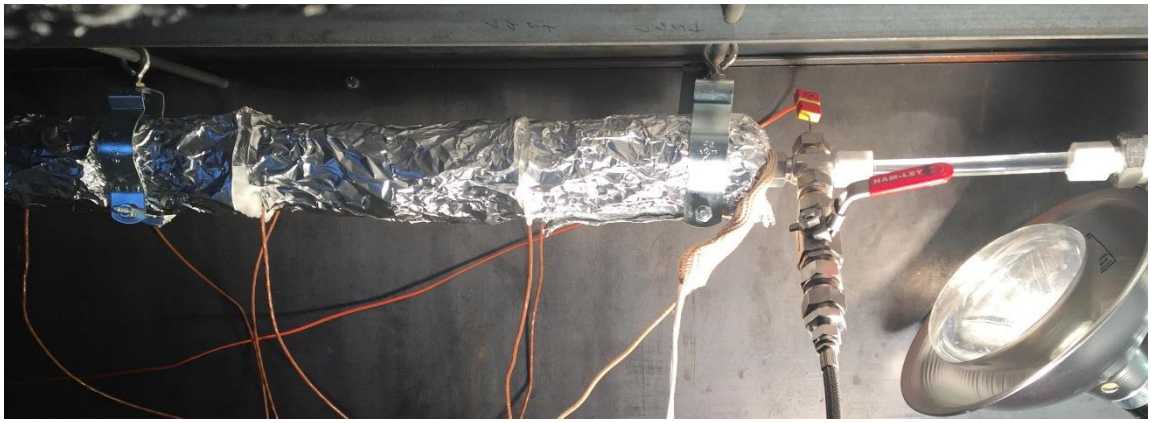

Figure 78 Test section and flow visualization setup at the end of test section

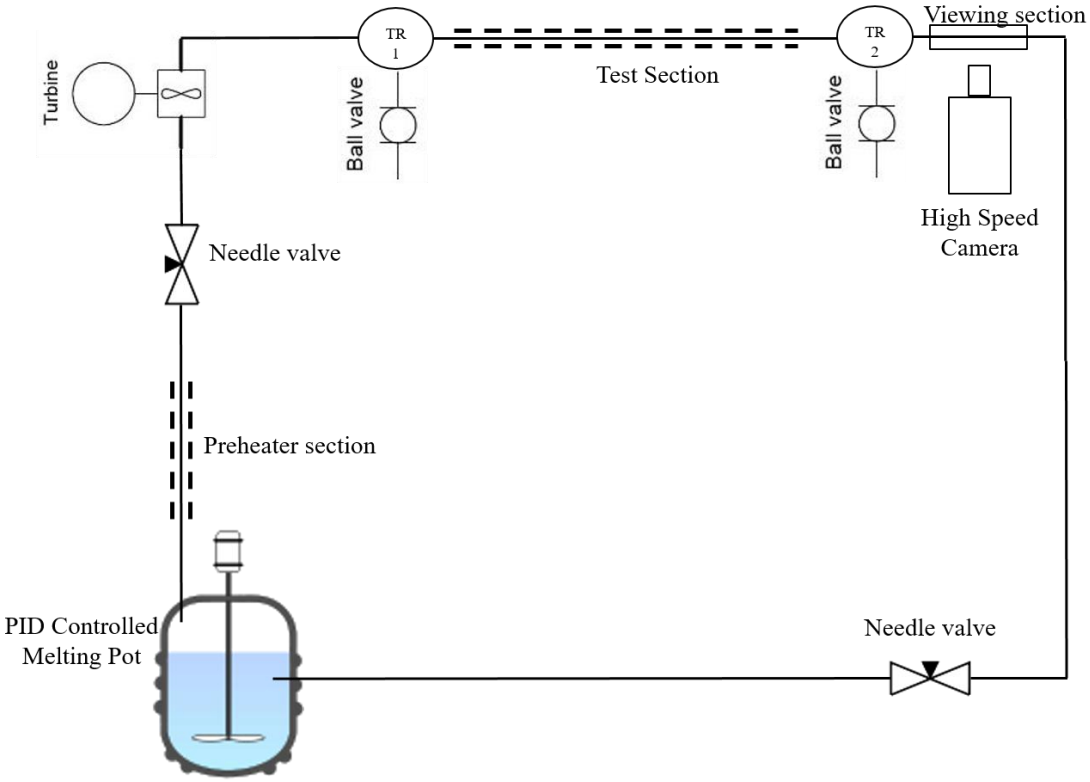

Figure 79 Schematic of the flow loop

3.4.1 Baseline experiments

A series of baseline experiments were performed with DI Water (at pH of 9) as the working fluid to verify the experimental measurements obtained. All tests were performed for a fixed inlet sub cooling of 2°C and at a fixed value of mass flux (G) at 165 [kg/(m^{2}s)]. To select the desired range of input heat flux, the onset of nucleate boiling (ONB) for the selected sub cooling and mass flux was estimated through different models available in literature as shown in Figure 80.

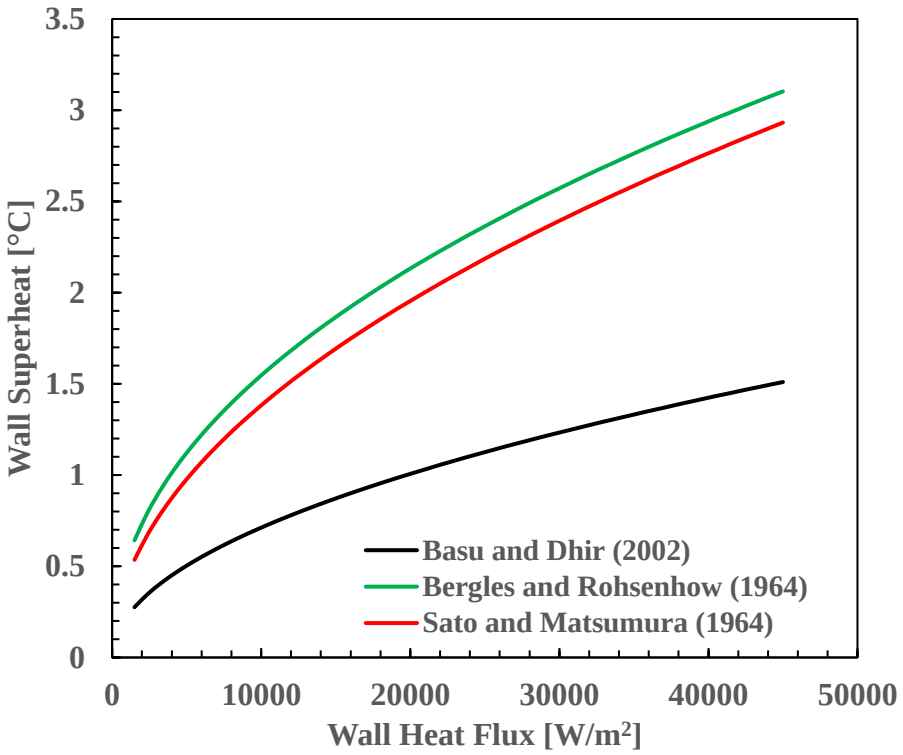

Figure 80. Onset of nucleate boiling predictions for water at atmospheric pressure

Based on the equipment available for heating the test section a maximum heat flux of 16.9 [kW/m^2]was fixed and as can be seen from Figure 80, a wall superheat of about ~1.8°C would favor nucleate boiling in the test section given the surface has nucleating cavities with a wide range of sizes. Figure 81 shows the wall superheat measured as a function of applied wall heat flux for an inlet mass flux of 165 [kg/(m^2s)] and an inlet sub cooling of 2 °C. The temperature measurement results along the axial direction of the test section indicate that the first two locations i.e., at an axial length of 7.25in. and 15.5 in. are consistency in single phase heat transfer regime. On the other hand, temperature measurement data indicate that there is partial boiling regime at axial location of 22.25in.from the entrance of the test section. Hence, coupled with the experimental results for single phase convection heat transfer experiment and the preliminary results for two-phase heat transfer coefficient the loop operation is verified. Flow boiling experiments with aqueous silica nanofluids were performed subsequently and the experimental results are provided in the next section.

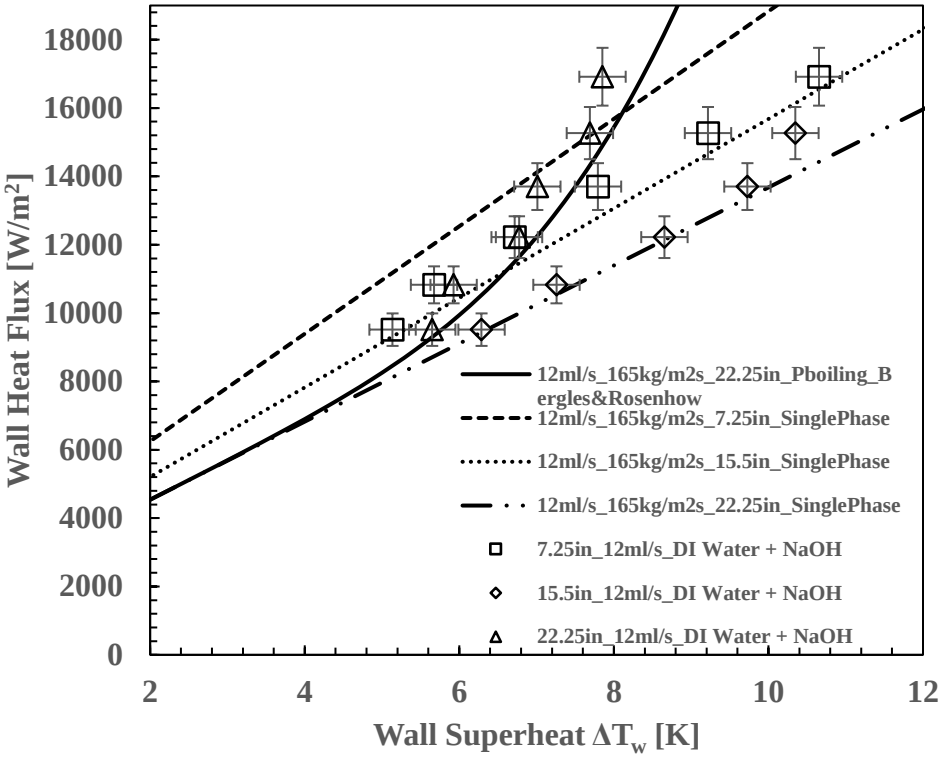

Figure 81. Wall superheat as a function of applied heat flux for DI Water as the working fluid for an inlet mass flux of 165 [kg/(m^{2}s)] and inlet sub cooling of 2 °C

3.4.2 Aqueous silica nanofluids

Experimental results from subcooled flow boiling heat transfer experiments of aqueous silica nanofluids are presented in this section. The mass fraction of the silica (SiO_2) nanoparticles in the system was varied to study the influence of nanoparticle concentration on the forced convective boiling heat transfer. The mass fraction of the silica nanoparticles explored in this study were 0.5%, 1.0% and 1.5%. Figure 82, Figure 83, and Figure 84 shows the wall temperature as a function of applied wall heat flux for the test section for SiO_2 nanofluids at mass fraction of 0.5%, 1.0%, and 1.5%, respectively. The results

indicate that the wall temperature increases as the wall heat flux increases linearly at axial distance of 7.25 [in.] and 15.5 [in.] from the inlet of the test section. However, as can be seen from the experimental results the increase in wall temperature with increase in wall heat flux at the third location i.e. at an axial distance of 22.25 [in.] from the inlet is nonlinear suggesting that there is nucleation between the second and third thermocouple locations. Furthermore, the surface temperature at an axial distance of 22.25 [in.] was consistently lower for SiO_2 nanofluids compared to that of DI Water. In other words, there is a clear improvement in heat transfer coefficient for nanofluids compared to that of DI Water for same wall heat flux resulting in a lower wall temperature. The experimental values of heat transfer coefficients and measured wall superheat values as a function of wall superheat are listed in Appendix E and Appendix B

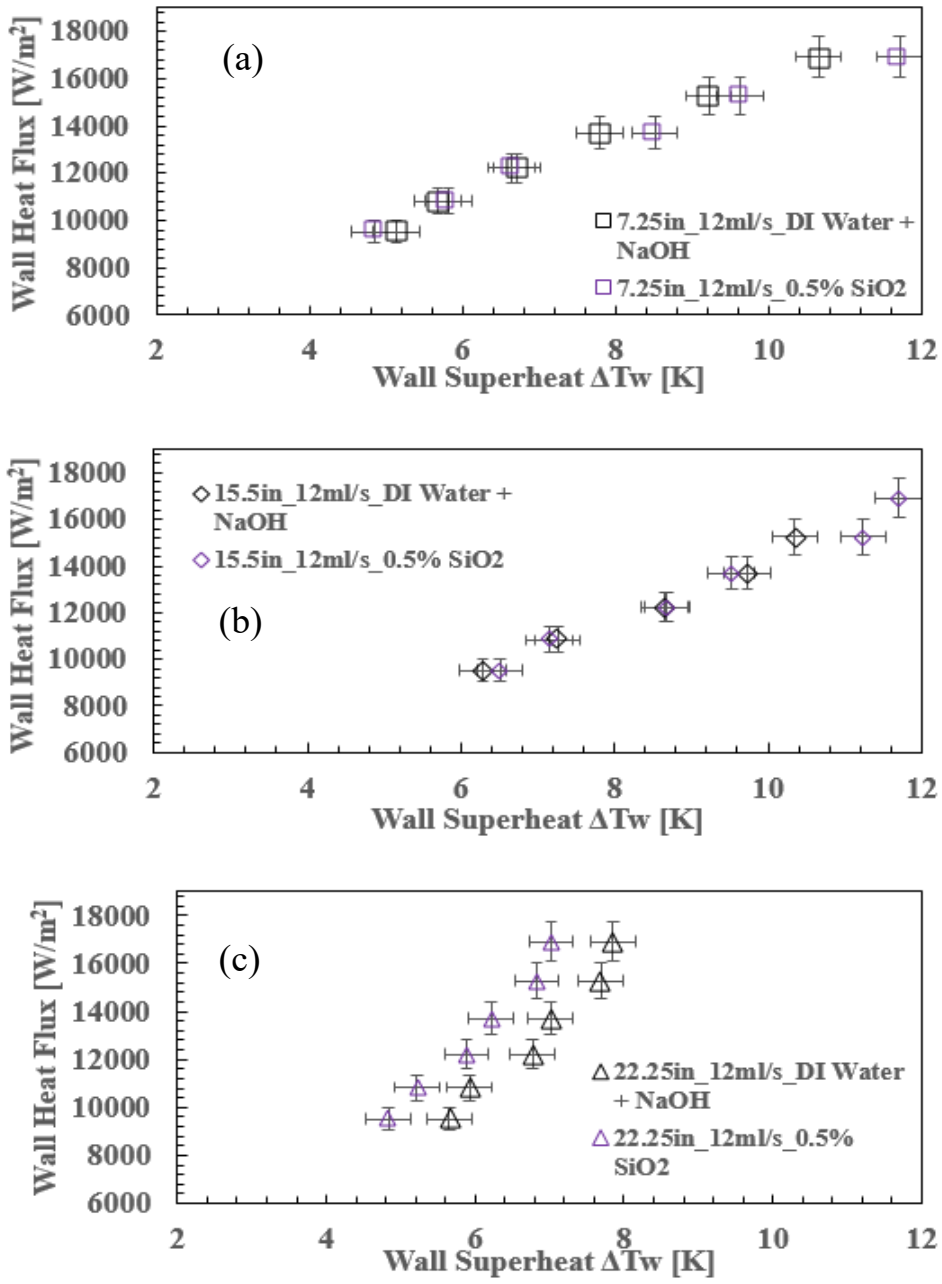

Figure 82 Wall superheat (ΔT_w) as a function of wall heat flux for experiments performed using SiO_2 nanofluids at a mass fraction of 0.5% for: (a) axial distance 7.25 [in.], (b) axial distance 15.5 [in.], and (c) axial distance 22.25 [in.] from inlet of test section

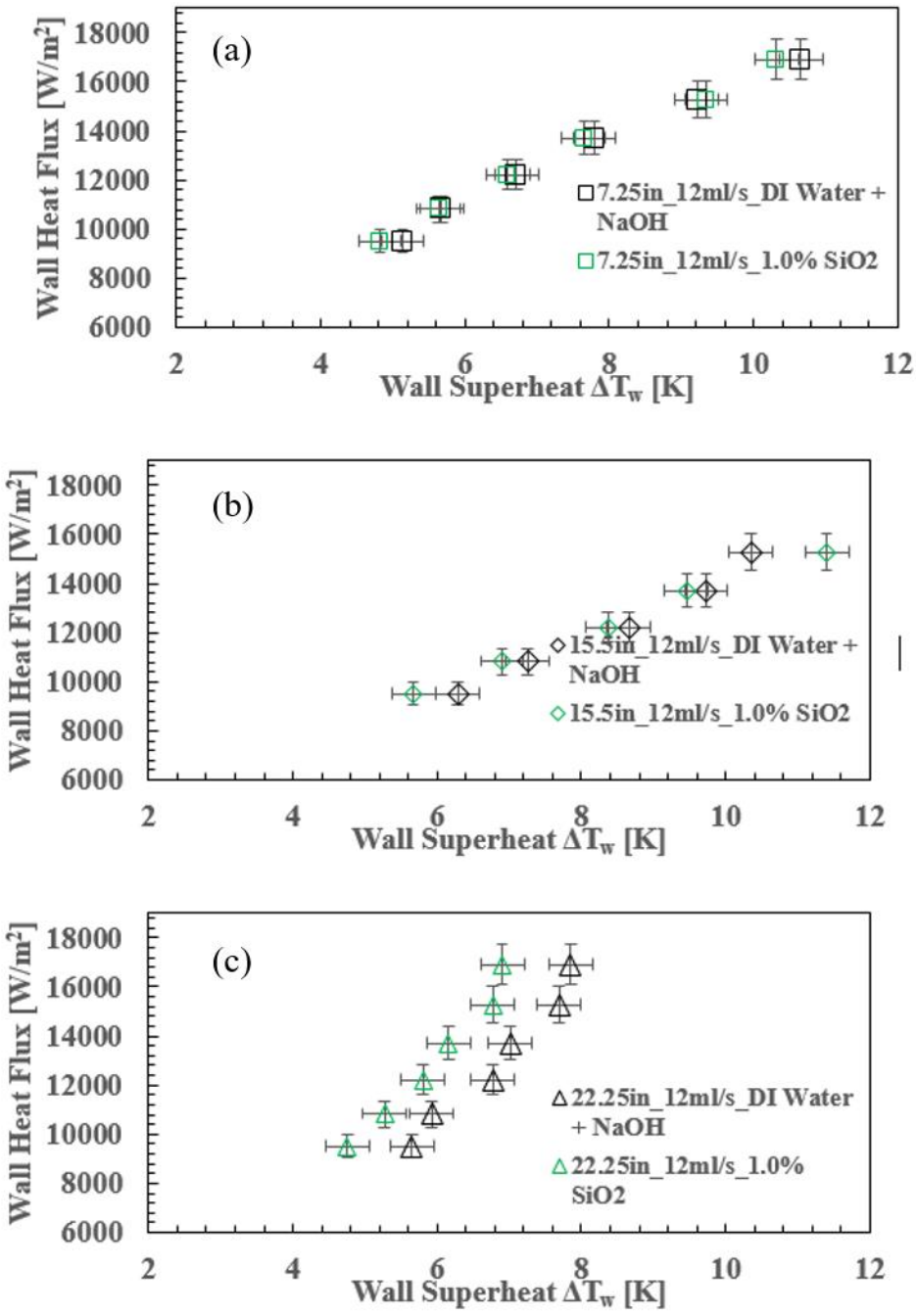

Figure 83.Wall temperature profile as a function of heat flux for experiments performed using SiO_2 nanofluids at a mass fraction of 1.0% for: (a) axial distance 7.25 [in.], (b) axial distance 15.5 [in.], and (c) axial distance 22.25 [in.] from inlet of test section

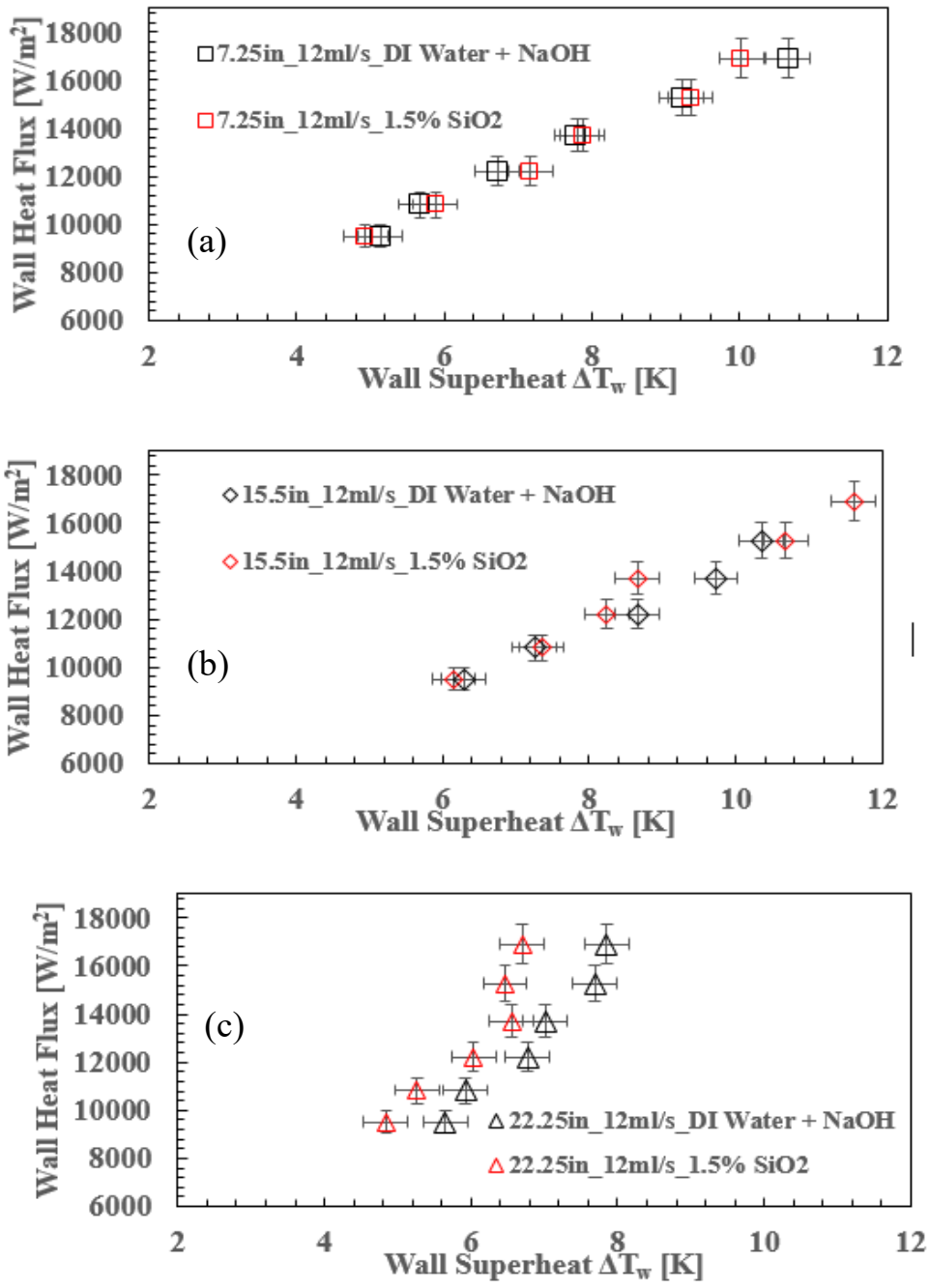

Figure 84. Wall temperature profile as a function of heat flux for experiments performed using SiO_2 nanofluids at a mass fraction of 1.5% for: (a) axial distance 7.25 [in.], (b) axial distance 15.5 [in.], and (c) axial distance 22.25 [in.] from inlet of test section

The convection heat transfer coefficient was computed according to equation (7) in section 2.5.8. Figure 85, Figure 86, and Figure 87 show the heat transfer coefficient as a function of axial distance along the test section for each wall heat flux. It is apparent from the experimental measurements from surface thermocouple that the bulk liquid temperature increased as the working fluid passed through the test section. Furthermore, the heat transfer coefficient significantly increased between the centrally located thermocouple and thermocouple at the end of the test section-indicating onset of nucleate boiling between 15.5 [in] and 22.25 [in.] from the inlet of test section. The measured single-phase convection heat transfer coefficient at the first and second thermocouple locations, from the inlet of the test section, is within ±10% of Gnielinksi correlation, listed in Table 4.

The heat transfer coefficient values are shown in Table 28 for applied wall heat flux of 16.9 [kW/m^2]. It is clear that the addition of SiO_2 nanoparticles to DI Water enhanced the two-phase heat transfer coefficient at an axial distance of 22.25 [in] from the inlet of the test section. A maximum enhancement of 17.3% was observed for the tested conditions. After performing nanofluid experiment at a given mass fraction of SiO_2 nanoparticles, the whole loop was flushed and DI Water experiments were repeated. As seen from the tabulated values in Table 28, the heat transfer coefficient values for the DI Water experiments immediately following a nanofluid experiment are marginally enhanced compared to that the value before performing nanofluid experiments. The experimental uncertainty for the heat transfer coefficient was computed as introduced in section 2.5.9.

The range of uncertainty for heat transfer coefficient ranged from 5% to 10% of the measured value for the tested heat flux values. The increase in heat transfer coefficient for DI Water experiments performed after nanofluids is attributed to the precipitation of nanoparticles form the nanofluid resulting in "nanofins" on the heater surface. As a result, the thermal energy is removed more efficiently from the heater surface for identical testing conditions. The presence of SiO_2 nanoparticle precipitation in confirmed my observing the surface of the heater under a Scanning Electron Microscope (SEM) and through Energy Dispersive X-ray Spectroscopy (EDS) as shown in Figure 89. This behavior is in excellent agreement with prior literature reports indicating that precipitation of nanoparticles effectively increasing the heat transfer.

Furthermore, the increase in heat transfer coefficient for lower wall heat fluxes was higher compared to that of higher wall heat flux. To elaborate, the level of enhancement in heat transfer coefficient for a heat flux of 16.9 [kW/m^2]. is 1% as opposed to 13.2% for 12.2 [kW/m^2] for DI Water experiments performed immediately after 0.5% SiO_2 nanofluid experiments This is possibly due to extended contact of nanofluids with the heater surface for higher heat flux values. The steady state conditions are achieved after about ~4 hours at high heat flux values as opposed to ~2 hours in case of lower heat flux. Hence, the excessive precipitation resulting during progression of steady state conditions effectively reduced the level of heat transfer enhancement. The experimental values of heat transfer coefficients for all other test conditions are listed in Appendix E and Appendix B

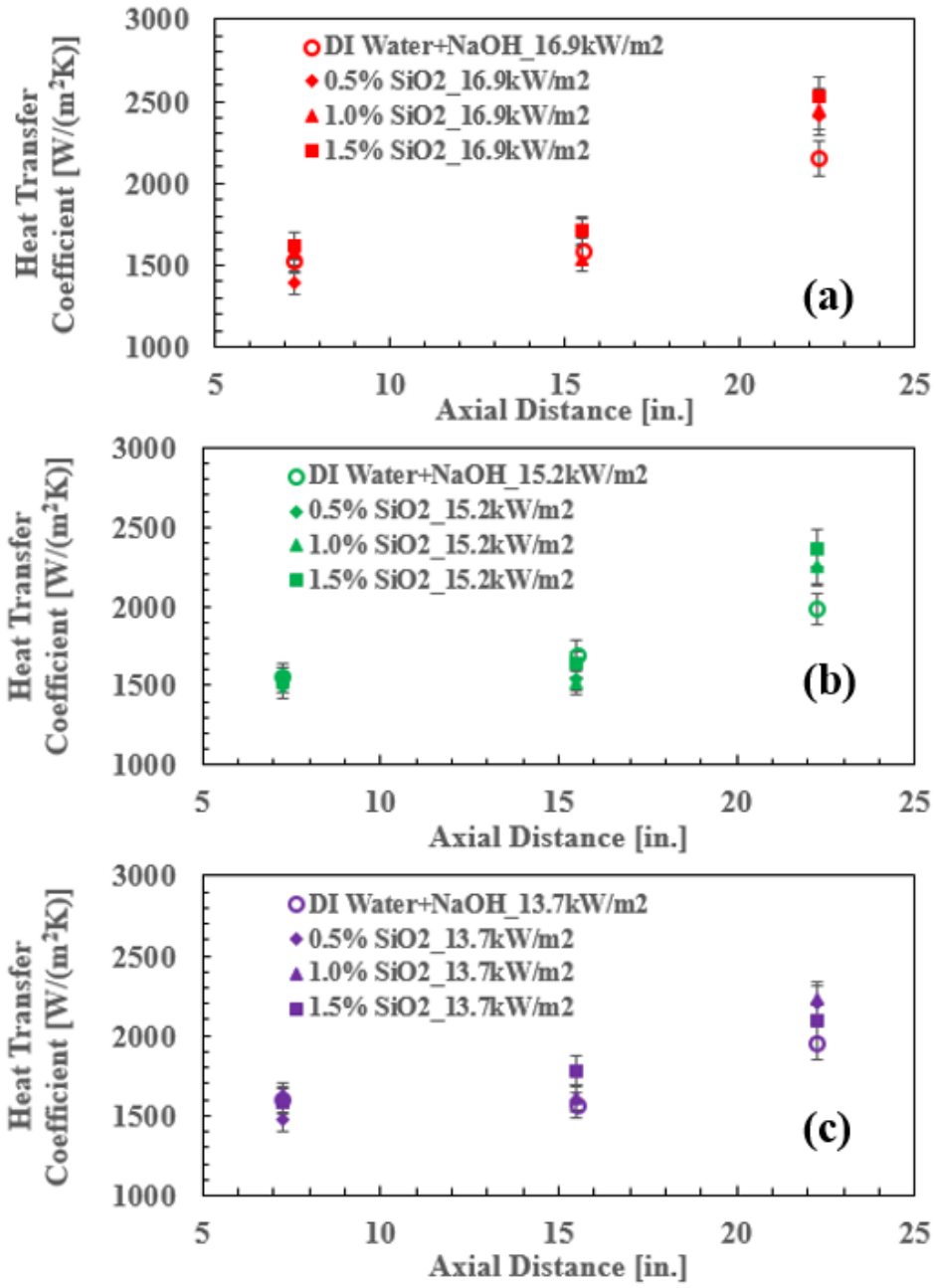

Figure 85. Heat transfer coefficient as a function of heat flux for axial distance from inlet of test section performed using DI Water and SiO_2 nanofluids at a mass fraction of 0.5%, 1.0%, and 1.5% for: (a) wall heat flux of 16.9 [kW/m^2], (b) 15.2 [kW/m^2], and (c) 13.7 [kW/m^2]

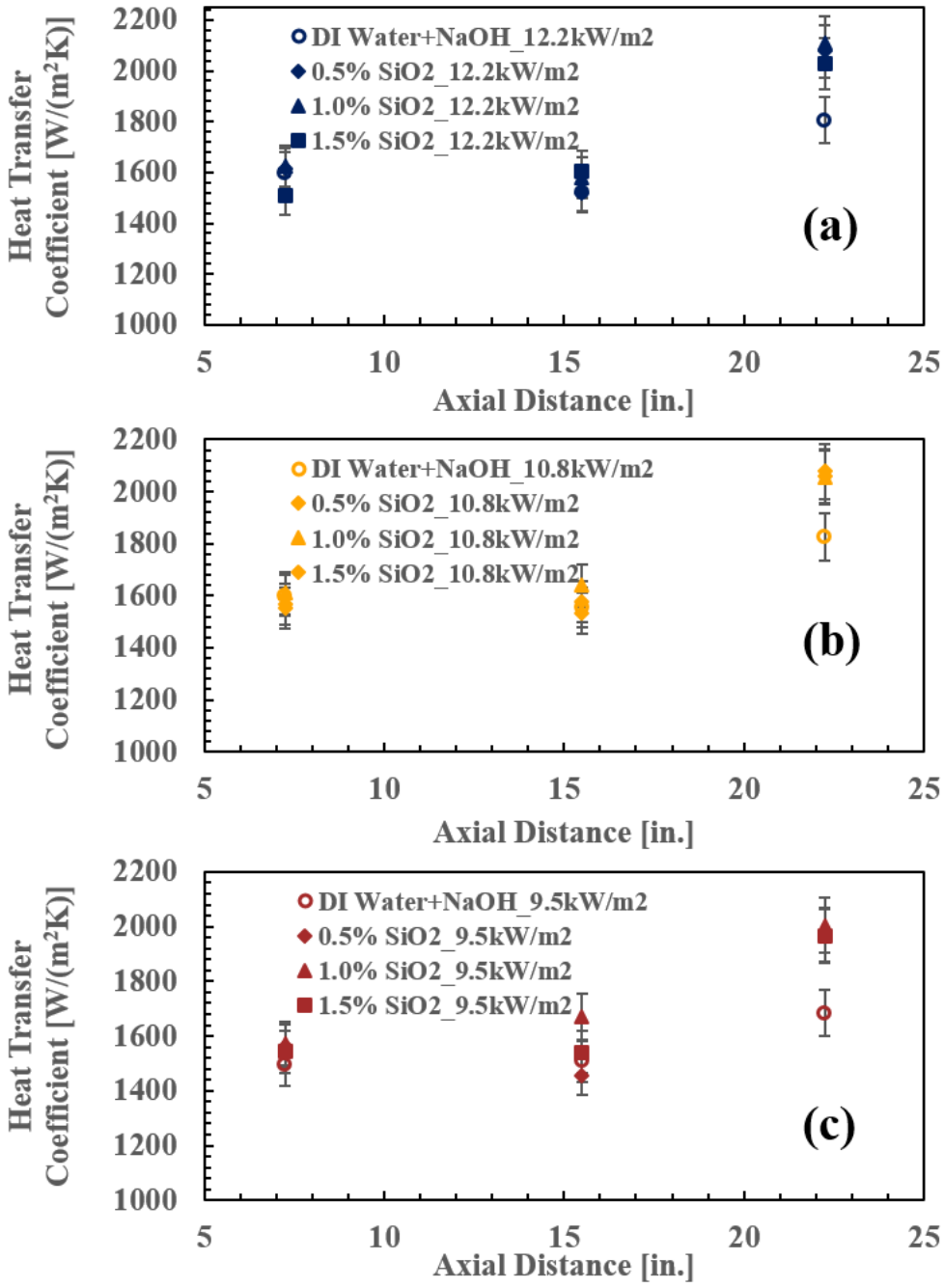

Figure 86. Heat transfer coefficient as a function of heat flux for axial distance from inlet of test section performed using DI Water and SiO_2 nanofluids at a mass fraction of 0.5%, 1.0%, and 1.5% for: (a) wall heat flux of 12.2 [kW/m^2], (b) 10.8 [kW/m^2], and (c) 9.5 [kW/m^2]

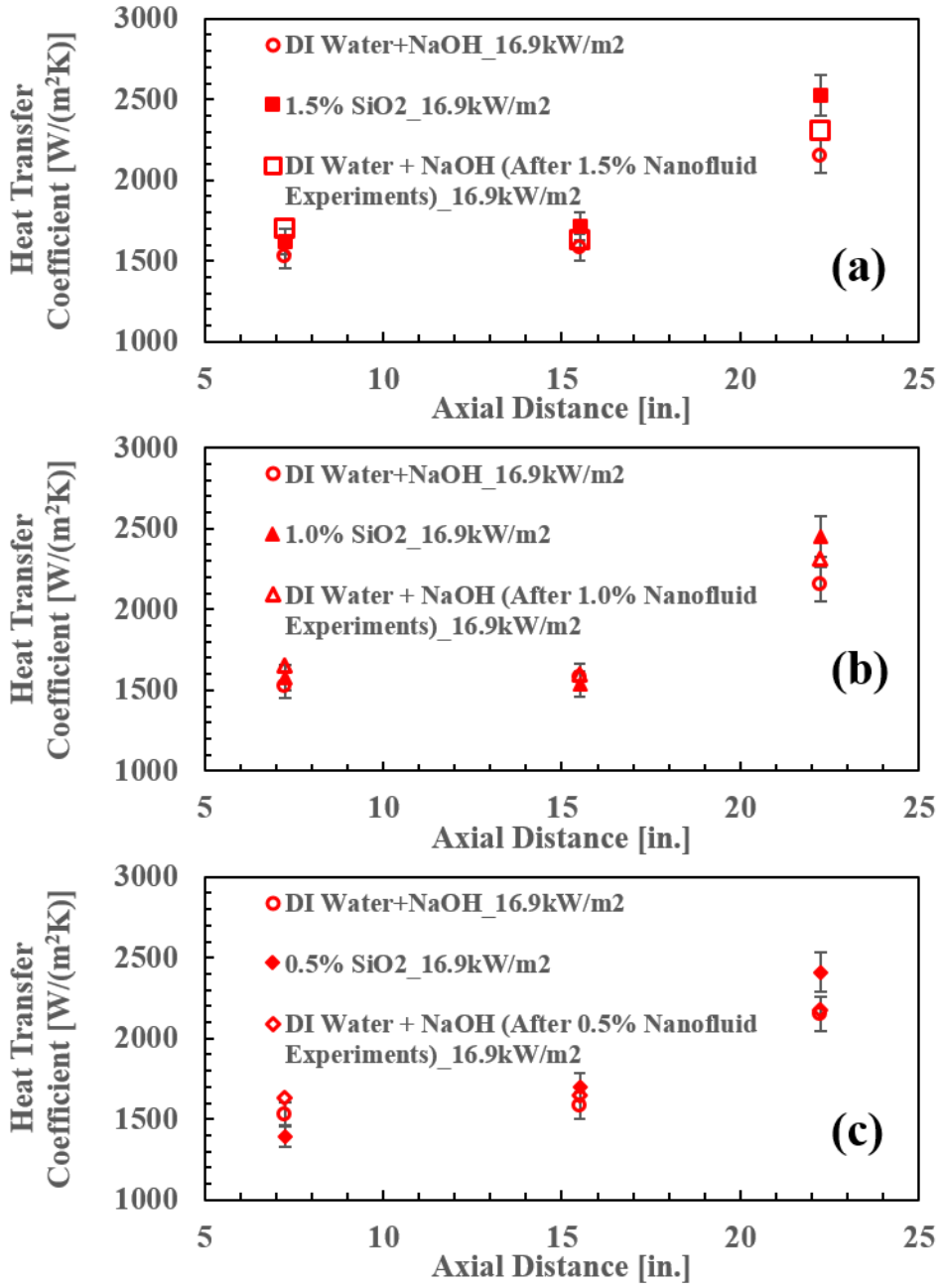

Figure 87. Heat transfer coefficient as a function of axial distance from inlet of test section performed using DI Water and SiO_2 nanofluids for a wall heat flux of 16.9 [kW/m^2] at a mass fraction of (a) 0.5% (b) 1.0%, and (c) 1.5%

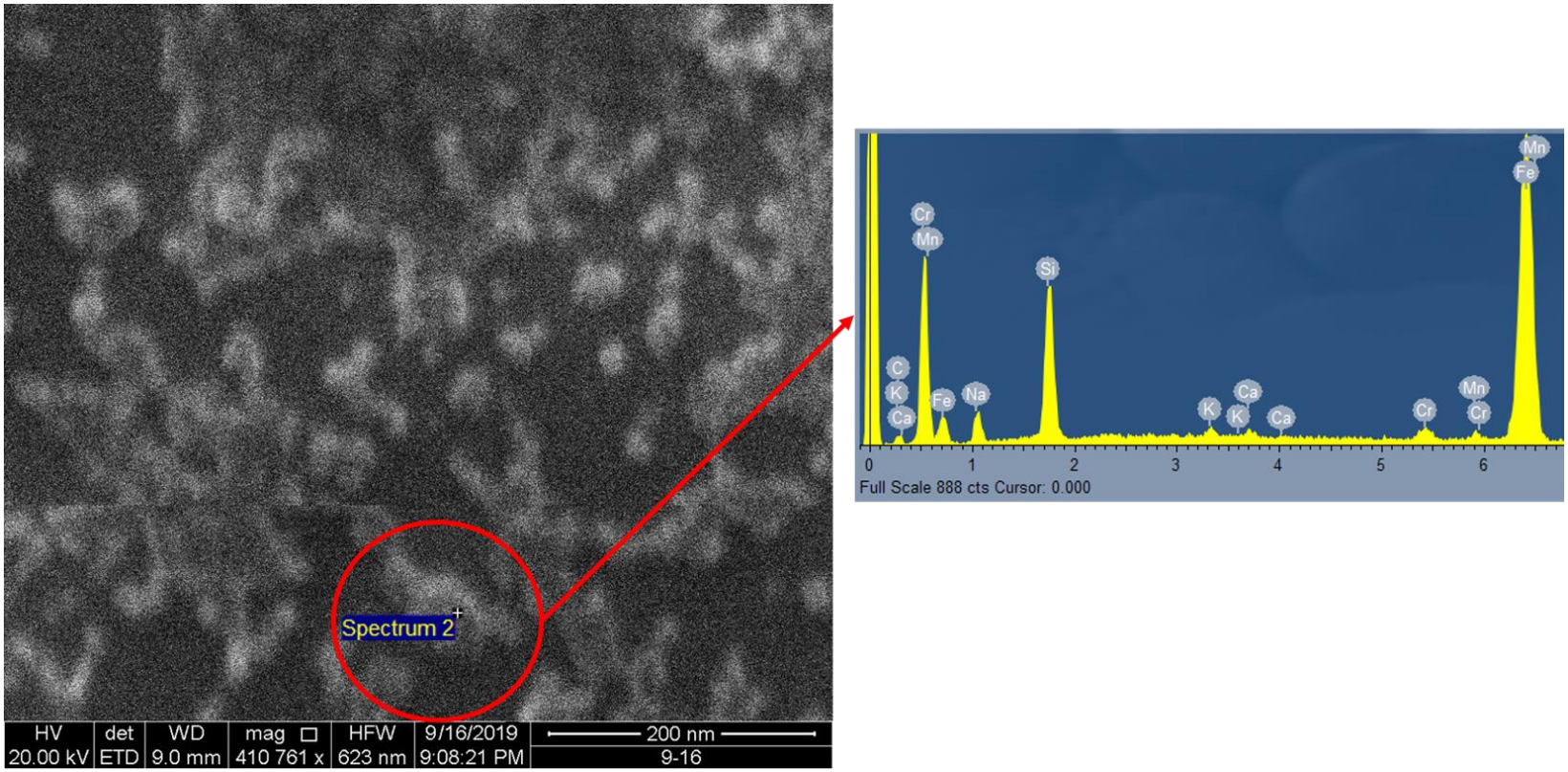

Figure 88. Scanning Electron Microscope (SEM) image of the surface of the pipe surface after performing nanofluid experiments alongside EDX elemental composition confirming the presence of SiO_2 nanoparticles

Table 28. Comparison of heat transfer coefficient for various nanofluids at an axial distance of 22.5 [in.] from the inlet of the test section for an applied wall heat flux of 16.9 [kW/(m^2)] at a mass flux of 165 [kg/(m^{2}s)]

Test Condition	Heat Transfer Coefficient [W/(m^{2}K)]	% enhancement
DI Water+NaOH	2154.03	-
0.5% SiO_2	2410.41	11.9%
1.0% SiO_2	2450.72	13.8%
1.5% SiO_2	2527.45	17.3%
DI Water + NaOH (After 0.5% Nanofluid Experiments)	2175.62	1.0%
DI Water + NaOH (After 1.0% Nanofluid Experiments)	2311.30	7.3%
DI Water + NaOH (After 1.5% Nanofluid Experiments)	2312.55	7.4%

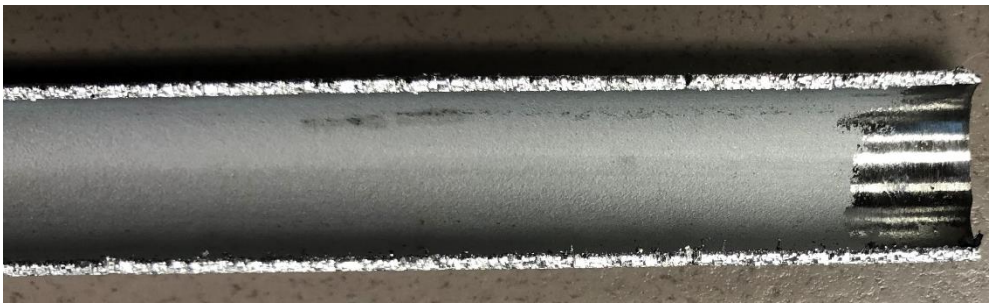

Figure 89. Image of the cross section of the interior surface of the test section after performing 1.0% mass fraction SiO_2 nanoparticles flow boiling experiments

Table 29. Comparison of heat transfer coefficient for various nanofluids at an axial distance of 22.5 [in.] from the inlet of the test section for an applied wall heat flux of 15.2 [kW/(m^2)] at a mass flux of 165 [kg/(m^{2}s)]

Test Condition	Heat Transfer Coefficient [W/(m^{2}K)]	% enhancement
DI Water+NaOH	1985.37	-
0.5% SiO_2	2238.11	12.7%
1.0% SiO_2	2254.26	13.5%
1.5% SiO_2	2364.81	19.1%
DI Water + NaOH (After 0.5% Nanofluid Experiments)	2097.30	5.6%
DI Water + NaOH (After 1.0% Nanofluid Experiments)	2131.55	7.4%
DI Water + NaOH (After 1.5% Nanofluid Experiments)	2075.55	4.5%

Table 30 Comparison of heat transfer coefficient for various nanofluids at an axial distance of 22.5 [in.] from the inlet of the test section for an applied wall heat flux of 13.7 [kW/(m^2)] at a mass flux of 165 [kg/(m^{2}s)]

Test Condition	Heat Transfer Coefficient [W/(m^{2}K)]	% enhancement
DI Water+NaOH	1954.82	-
0.5% SiO_2	2205.63	12.8%
1.0% SiO_2	2225.64	13.9%
1.5% SiO_2	2093.07	7.1%
DI Water + NaOH (After 0.5% Nanofluid Experiments)	2212.14	13.2%
DI Water + NaOH (After 1.0% Nanofluid Experiments)	2184.01	11.7%
DI Water + NaOH (After 1.5% Nanofluid Experiments)	2146.66	9.8%

To summarize, the series of experiments performed in this study validate that "moderate" precipitation of nanoparticles from the working fluid on the heater surface enhance the heat transfer coefficient while excessive precipitation can lead to agglomeration/scaling of the surface thereby impeding the net heat transfer rate. Furthermore, surface characterization of the heater surface was performed in this study to validate the surface modification of the heater surface using Scanning Electron Microscope (SEM).

3.5 Density

Before measuring the density of nanofluids, the experimental apparatus is calibrated by measuring the density of pure liquids whose densities are well known, namely mineral oil and DI water. The density measurements were performed for both liquids at a temperature of 24°C. Table 31 summarizes the results from the benchmark tests (calibration tests) that were performed with DI water and mineral oil. The results from the experimental measurements show that the percentage difference between the measured values and the values listed in the ASTM standard database are: 2.2% and 0.9%, for DI water and mineral oil, respectively (hence, for measurements involving oil based samples, the measurement uncertainty is expected to be less than 1%). Hence, the overall uncertainty for the density ratio between the test samples and reference samples ranged from 0.9% ~ 1% (based on a minimum of three repeats for each test). After performing the benchmark tests (calibration tests), the density measurement of the samples of oleo-nanofluids were performed. The results of the measurements are presented in Table 32**.**

Table 31. Benchmark test results for DI Water and Mineral Oil

Test Liquid	Mass in air [g]	Mass in liquid [g]	Density of liquid [kg/m^3]	Standard value [144] of density [kg/m^3]	Difference [%]
DI Water	20	17.3	1022.6	1000	2.2
Mineral Oil	20	17.8	842.1	850	0.9

Table 32. Experimental measurements for samples of oleo-nanofluids Casein based protein nanoparticles and SDS surfactant dispersed in PureTemp15X (Baseline Density for Neat Solvent, ρ_f = 860 [(kg/m^3)]; Measurement Uncertainty <1%)

$\alpha \pm \Delta\alpha$	12.375 ± 0.0625 [inches]	
$\beta \pm \Delta\beta$	14.125 ± 0.0625 [inches]	
m_α sinker mass in air	20 [grams]	
m_β for sinker completely immersed in sample (oleo-nanfluid)	17.52 [grams]	
ρ_{SS} Density of stainless steel	7700 [(kg/m^3)]	
ρ_{T2} Measured value of density for the sample (oleo-nanofluid)	953.9 [(kg/m^3)]	12.2 % (enhancement over ρ_f)
ρ_{T1} Predicted value using simple mixing rule	924.4 [(kg/m^3)]	8.8 % (enhancement over ρ_f)
$\rho_{T21} = \rho_{T2} - \rho_{T1}$ Surplus Density	29.4 [(kg/m^3)]	3.2 % (enhancement over ρ_{T1})

As the experimental results show, the traditional mixing rule under predicts the density of nanofluid by 3.2%. The value of density measured through Archimedean technique for the synthesized nanofluid is 953.9 kg/m^3 while the traditional mixing rule predicts the density of the nanofluid to be 924 kg/m^3. The density of the neat solvent is 860 [(kg/m^3)].

To ascertain the proportion of the contribution of the compressed phase to the total density of the nanofluid samples in these experimental results, the predictions from the analytical model were obtained by parametric variation of both the nanoparticle size and

the thickness of the compressed phase. The predictions from the analytical model are plotted in Figure 90. The specific gravity of the compressed phase was assumed to be the same as that of the solid phase of the solvent (ρ_c = 950 [(kg/m^3)]) while the specific gravity of the liquid phase of the solvent is assumed to be the same as that of the neat solvent at 24 °C (ρ_f = 860 [(kg/m^3)]). The plots are obtained by assuming ε = 5 Å (i.e., 0.5 nm). The plots are obtained for two different values of the compressed layer thickness (δ), i.e., δ = 1 nm and δ = 2 nm. The plots show that for nanoparticle radius of 2 nm the surplus density is 3% (for δ = 1 nm and x = 0.5%) while the value of surplus density is 6% (for δ = 2 nm and x = 0.5%). Hence, correlating the experimental measurements to the numerical predictions, it is expected that the thickness of the compressed phase engulfing the protein nanoparticles (casein) is approximately in the range of 1~2 nm.

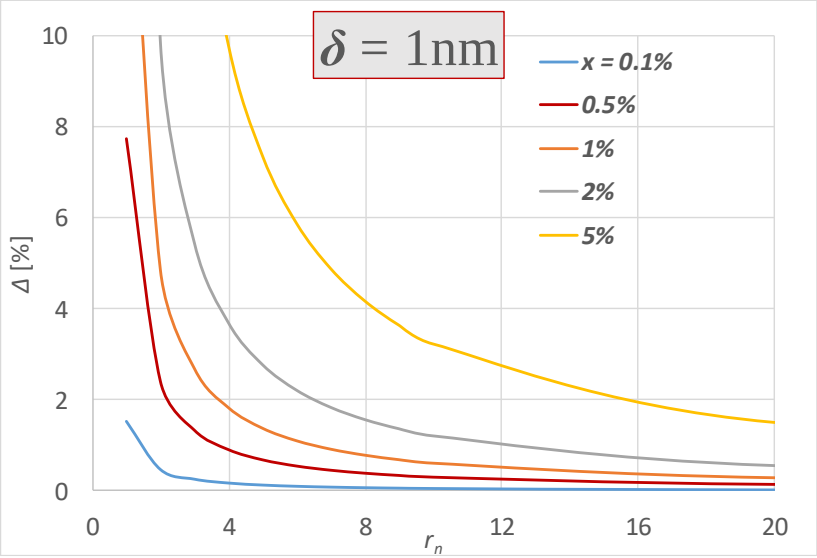

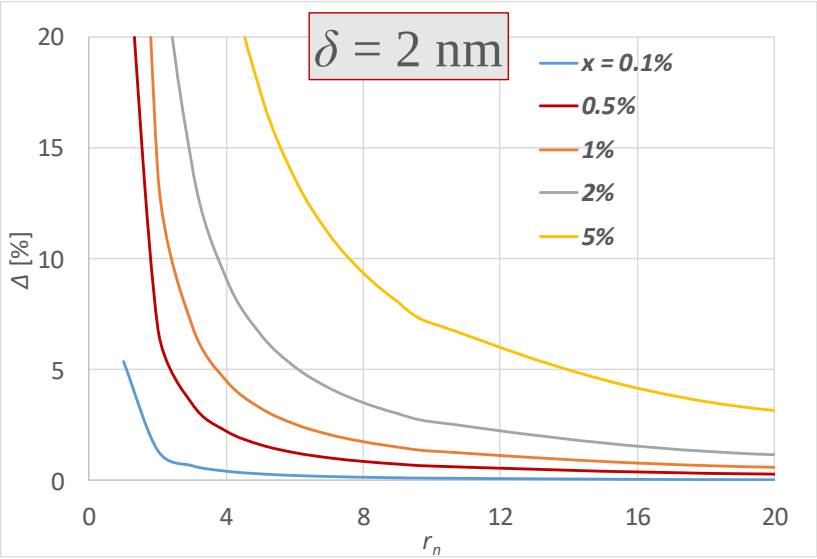

Figure 90. Plots for analytical predictions for estimating the magnitude of density surplus (Δ) in oleo-nanofluid suspension and as a function of the Stokes-radius of a nanoparticle (e.g., casein/ milk proteins dispersed in a PCM oil) at different mass fractions of the protein nanoparticles. The deviant density enhancement (i.e., surplus density) is hypothesized to occur due to the presence of a compressed phase that forms on the surface of a nanoparticle and in turn engulfs each casein nanoparticle within the bulk phase of the oil (PCM).

3.6 Material Characterization

Materials characterization was performed using electron microscopy techniques for the nanofluid samples prepared by one step synthesis protocol. Alumina nanoparticles are generated due to thermal decomposition of aluminum nitrate precursor that were mixed apriori with molten salt eutectic in powder form. The SEM images obtained from this study are shown in Figure 91 for the ternary nitrate nanofluid sample with a target alumina mass fraction of 1% (from alumina nitrate precursors mixed at a mass fraction of 6.9%). Section 2.2.1 details the sample preparation for SEM imaging.

Although individual nanoparticles are not easily discernible in these SEM images, clusters of secondary nano-structures (inter-connected structures) are observed in Figure 91. On higher magnification of a few locations within the samples, the SEM images show that the nominal diameter of these nano-needles is approximately 50 nm with lengths ranging from 2 ~ 3 microns. These nano-structures are observed to be located in the crevices of the bulk salt phase (amorphous phase). Figure 93 indicates the crystal structure of a pure ternary nitrate salt eutectic obtained through SEM imaging. The pure salt has a clear crystal boundary and has no secondary structures contributing to enhanced properties. As shown in Figure 92, EDS (Energy Dispersive X-Ray Spectroscopy) of the nanofluid samples was also performed using the SEM apparatus. The results from the EDS elemental composition indicate of fairly uniform distribution of Aluminum in the observed nanostructure, potentially due to generation of fine grained alumina nanoparticle generation during the thermal decomposition of precursor. Furthermore, the lack of clear SEM image can be attributed to shallow penetration of electrons into the sample, but the elemental composition perceived by EDS confirms the Alumina in the nano-structures (due to high energy of X-rays, deeper penetration of sample can be achieved, resulting in distinct peaks)

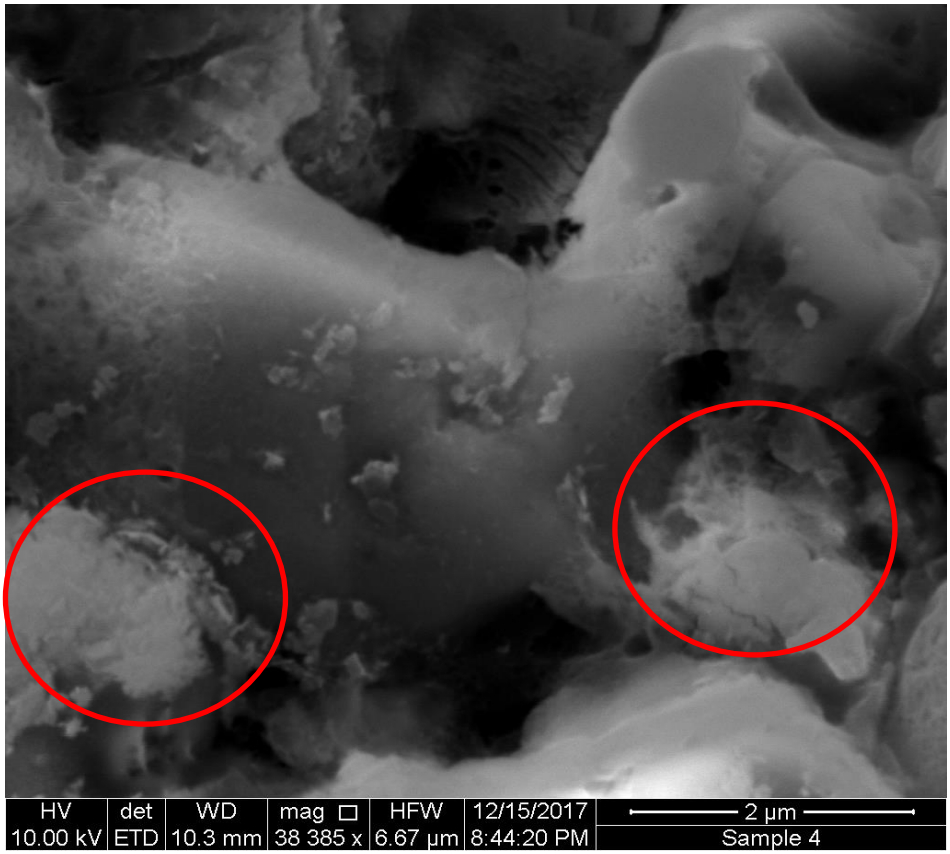

Figure 91. SEM image of ternary nitrate salt e nanofluid sample with 1% target concentration of Alumina generated from thermal decomposition of 6.9% mass fraction of Aluminum nitrate nonahydrate precursor.

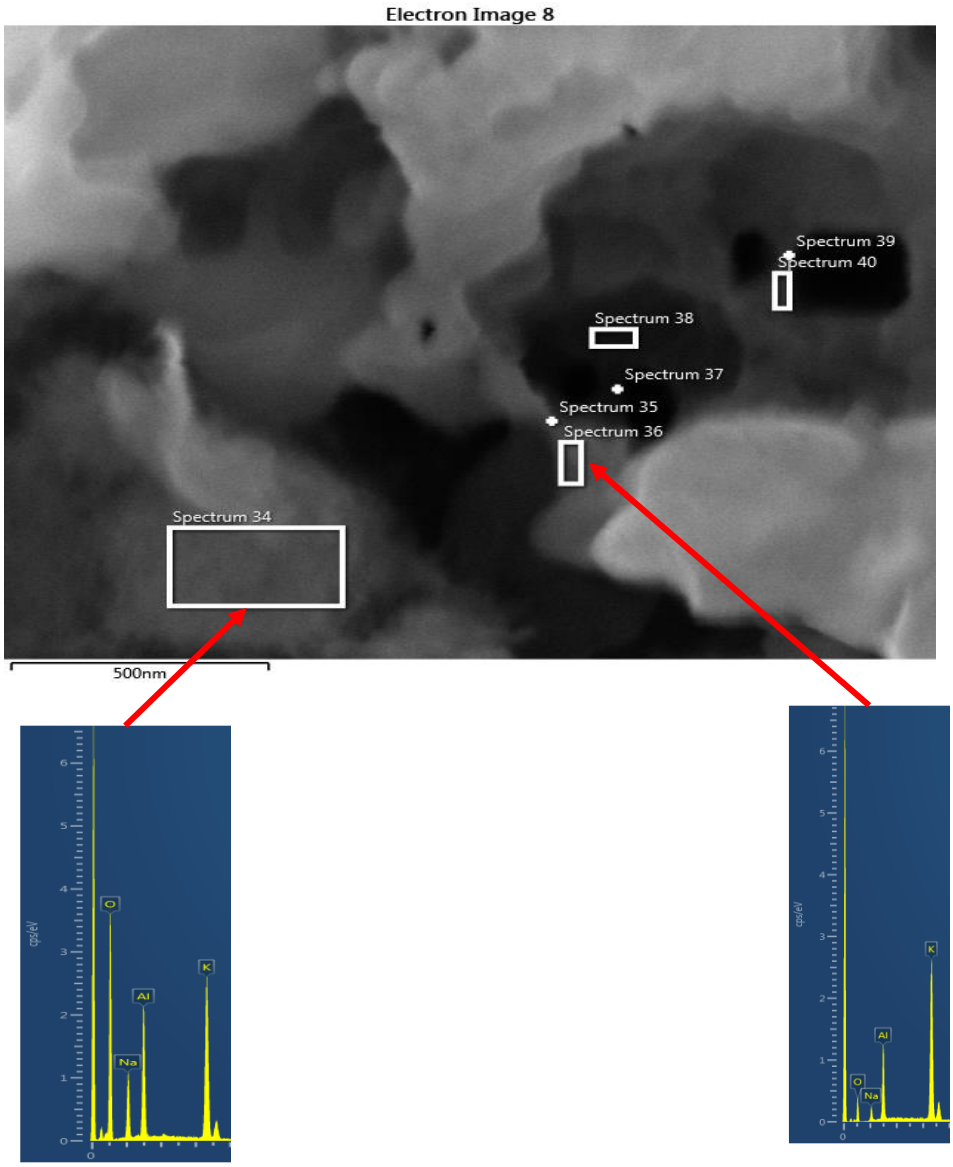

Figure 92. EDS analysis of elemental composition of ternary nitrate salt nanofluid (one-step thermal decomposition of Alumina through thermal pyrolysis).

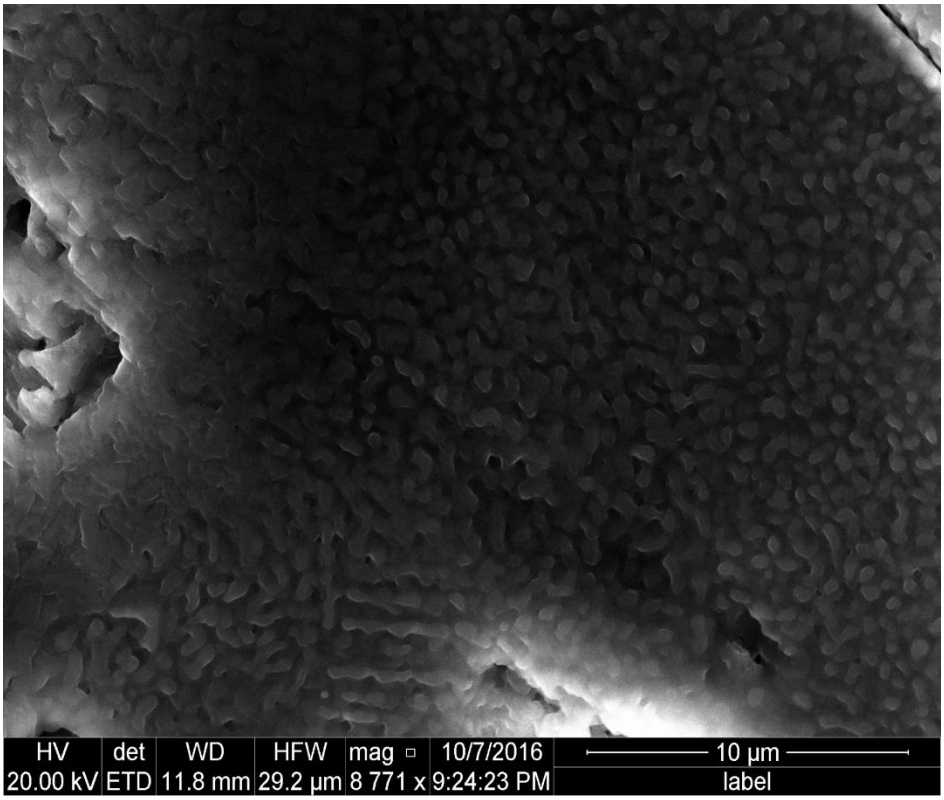

Figure 93. SEM image of pure ternary nitrate salt eutectic.

3.7 Stability Tests

3.7.1 Thermal Stability

The details of the thermal stability testing protocol are provided in section 2.3.1 for ternary nitrate eutectic with Alumina nanoparticles. The mass loss data for the samples with and without nanoparticles was recorded after soaking the samples in a muffle furnace at 550°C for 72 hours. Table 33 summarizes the values of mass loss data obtained from thermal stability tests. As discussed in Section 2.3.1, total mass loss of the samples due to the trapped/dissolved gas is denoted by M_0-M_1. In addition, M_2-M_3 indicates the actual mass loss resulting from limited thermal decomposition (not including trapped gas or from evaporation of the salt samples).

As the results indicate evaporative losses dominate the mass loss of molten salt nanofluid samples compared to mass loss due to thermal decomposition. Furthermore, no statistically significant difference was observed between mass loss data of molten salt samples and molten salt nanofluid samples. Hence, it can be considered from the study that the presence of nanoparticles had no significant effect on the thermal stability of pure salt samples.

Table 33. Experimental results from chemical stability tests (mass loss values) of Ternary nitrate salt (with and without nanoparticles) using one-step synthesis protocol from additives.

Samples	ternary salt	ternary salt + Al_2O_3	ternary salt	ternary salt + Al_2O_3
sample mass (g)	27.604	27.40133	27.384	27.227
M_0 (g)	60.751	62.619	60.531	62.445
M_1 (g)	60.51	62.41	60.18	61.96
M_2 (g)	49.51	50.725	48.78	49.84
M_3 (g)	49.489	50.69	48.55	49.68
(M_0-M_1) (% loss)	0.87%	0.76%	1.28%	1.78%
M_2-M_3 [g]	0.021	0.035	0.23	0.16
(M_2-M_3) (% loss)	0.12%	0.22%	0.47%	0.32%

3.7.2 Colloidal Stability

The ternary nitrate salt nanofluid samples are tested for colloidal stability through visual observation under quiescent conditions as discussed in section 2.3.2. The ternary nitrate salt nanofluid sample are synthesized through one-step thermal decomposition of 6.9% $Al(NO_3)_3.9H_2O$ precursor for a target mass fraction of 1% Al_2O_3 nanoparticles. Figure 94 demonstrates the colloidal stability of the nanofluid synthesized. The suspension was stable in the vial up to 14 days with no noticeable sedimentation of nanoparticles. However, as seen in Figure 94, the bottom row of images indicate the slow sedimentation of nanoparticles started after two-week period. This can be evidenced by formation of a transparent supernatant liquid on the top of the vial, potentially due to agglomeration of nanoparticles.

This simple test demonstrates that the nanofluid samples synthesized in this study through one-step thermal decomposition technique are stable up to 14 days with no visual sedimentation from agglomeration or coagulation of nanoparticles. However, another technique for determining the size of nanoparticles in the colloidal suspension such as Dynamic Light Scattering (DLS) through dissolution of solid nanofluid sample in a liquid or through Scanning Electron Microscopy (SEM) for determining the size of nanoparticles or nanostructures resulting in the liquid phase is necessary.

Figure 94. Photographs of a ternary nitarte salt nanofluid synthesized through one-step thermal decomposition technique. The molten salt nanomaterial is a $LiNO_3$-$NaNO_3$-KNO_3 (38:15:47 by moldar ratio) with 6.9% by mass fraction of $[Al(NO_3)_3.9H_2O]$ for target mass concentration of 1.0% Al_2O_3 nanoparticles. The nanofluid sample is synthesized and transferred to a vial and stored in a muffle furnace at 300°C and photographs were collected periodically using a digital camera.

3.8 Summary

In this section, forced convection heat transfer results performed using a flow loop are presented along with hydrodynamic performance curves for the range of flow conditions for water and aqueous nanofluids as the test fluids. The measured local Nusselt number was within 20% of widely accepted Gnielinski correlation over the range of experiments. The reason for higher uncertainty was attributed to uncertainty in the wall temperature measurement during the tests. The wall temperature measurement technique was subsequently improved. A confirmatory high temperature was performed and the experimental results were within 3% of the theoretical predictions.

A novel transient T-History technique was developed for the measurement of specific heat capacity of molten salt nanofluid samples. Furthermore, a concentric cylindrical apparatus based on steady-state 1D conduction was constructed for measuring thermal conductivity of molten salt nanofluids synthesized. The experimental results indicated that both thermal conductivity and specific heat capacity enhanced significantly for all nanofluids samples synthesized. Material characterization of the nanofluid samples revealed secondary nanostructures resulting in inter-connected and long range dendrites enhancing the specific area (specific energy) and also paving way for additional pathways for thermal phonon transport. As a result, both specific heat capacity and thermal conductivity are enhanced form the generation of nanoparticles *in-situ.* The thermal and colloidal stability results indicated that no significant mass loss was observed due to

addition of nanoparticles generated from thermal pyrolysis and the colloidal stability of the synthesized nanofluids was stable up to 2 weeks.

4. CONCLUSION

4.1 Summary

In this study, various molten salt nanomaterials are synthesized through a low-cost *in-situ* one-step synthesis protocol for realizing a cheap method that is amenable for industrial scale production of molten salt nanofluids. This technique involving one-step synthesis procedure of nanofluids can be employed for working fluids in various commercial applications, including:

(a) Power Generation (Solar thermal, nuclear, geothermal, coal fired power plants, etc.);

(b) Energy Storage (Water heaters, fuel cell, electrical batteries, etc.);

(c) Improving energy efficiency (e.g., refrigerators, HVAC, manufacturing, mining);

(d) Thermal management (e.g., Defense applications, cooling opto-electronics/ lasers);

(e) Heat Transfer Fluid for heating and cooling applications (chemical processing, metals);

(f) "Smart lubricants" and smart materials (stimuli responsive lubricants and materials).

Several advantages accrue from this one-step synthesis procedure, such as:

(a) Faster and cheaper manufacturing technique (1000 times cheaper material costs);

(b) Simple (compared with conventional approach of explicitly mixing nanoparticles);

(c) Less laborious; enables rapid scale-up and large scale industrial deployment;

(d) Uses conventional materials (exotic or expensive nanoparticles not required);

(e) Amenable for alternate manufacturing techniques, including – radiation treatment (electro-magnetic/ micro-wave, ultrasound, laser, nuclear and electrical stimuli);

(f) Energy storage capacity and power rating improved by 20~120%; and

(g) Corrosion reduced by 50 ~ 100% (i.e., increases equipment life by 25~50%).

The material characterization of the molten salt nanomaterials was conducted with SEM imaging and Dynamic Light Scattering (DLS). For SEM imaging, based on the sample several imaging techniques such as Pd/Pt coating to enhance the thermal conductivity of the sample or backscatter electron images were obtained. Energy Dispersive X-ray Spectroscopy (EDS) was employed to identify the elemental composition of the molten salt nanomaterials after the thermal decomposition synthesis step.

Thermo-physical properties such as specific heat capacity and thermal conductivity of the molten salts and their nanomaterials are experimentally determined. A transient T-History technique was developed for measurement of specific heat capacity instead of conventional Differential Scanning Calorimetry (DSC) technique. It is crucial to note that typical sample size in a DSC instrument is 5-15 mg, nanofluids inherently are non-homogeneous, and hence a characterization technique capable of measuring specific heat capacities of larger (~ 30 g) sample quantities is developed. The thermal conductivity of pure molten salts and molten salt nanomaterials is measured through a custom designed concentric cylindrical apparatus.

A high temperature flow-loop apparatus capable of handling high temperature molten salts up to (~600°C) was assembled and initial validation tests were performed. Water was the working fluid and thermal-hydraulic performance was experimentally characterized by differential pressure drop measurement, volumetric flow rate and heat

transfer measurement. Initial tests indicate good repeatability in local heat-transfer coefficient measurement. Instrument upgrades in flow meter and differential pressure transducer are required in future for molten salt testing.

Furthermore, subcooled flow boiling heat transfer using aqueous nanofluids in a macro channel is investigated in this study. Experimental results from this study indicate that the precipitation of nanoparticles is the most prevailing heat transfer mechanism of nanofluids. The precipitation of nanoparticles resulted in formation of nanofins resulting in significant enhancement of heat transfer coefficient. Nevertheless, excessive precipitation of nanoparticles can result in formation of fouling film and can cause the degradation of heat transfer coefficient. On the other hand, this approach of employing nanofluids for developing nanofins on the heater surface through selective precipitation is practical considering the high cost associated with fabrication of nanofins. Thus, from cost considerations it is suggested to employ the technique of flowing nanofluids for a short period to realize selective precipitation and thereby enhance the heat transfer coefficient.

4.2 Future direction

A natural logical extension for this study would be to evaluate the heat transfer performance of molten salts and molten salt nanofluids developed through one-step *in-situ* synthesis technique. Furthermore, there is a need for development of a compilation of thermo-physical properties of molten salt nanofluids measured appropriately to capture the bulk properties to help estimate the performance of these novel class of working fluids in a Concentrated Solar Power (CSP) plant. The use of advanced computing techniques such as machine learning algorithms to predict the thermo-physical properties of nanofluids is a potential future research direction for this topic. For example, Hassan [146] developed an artificial neural network model to predict the specific heat capacity of molten salt nanofluid. Such soft computing approaches aid in predicting the thermo-physical properties of nanofluids by taking the plethora of existing literature reports and obviating the need for extensive experimentation needed for determining the effective properties of these new class of working fluids.

From the flow boiling heat transfer experiments performed in this study, it can be concluded conclusively that the selective precipitation of the nanoparticles resulted in enhancement in heat transfer. However, this study did not explore the rate of precipitation or at what flow conditions could result in excessive precipitation (fouling) would cause in heat transfer degradation. Hence, further studies on investigating the rate of precipitation or removal of excessive precipitated nanoparticles from the heater surface are to be explored for controlling the enhancement of heat transfer resulting from nanofluids. To

examine the precipitation of nanoparticles on the heater surface, commercially available techniques such as Surface Plasmon Resonance (SPR) can be employed. For instance, the potential change in refractive index of a transparent heater surface due to precipitation of nanoparticles can provide a means for *in-situ* monitoring of nanoparticle precipitation. A Surface Plasmon Resonance (SPR) affinity sensor hence can be used to detect the surface binding of nanoparticles. Therefore, by coupling heat transfer experiments of nanofluids with techniques such as SPR (concurrent monitoring of heater surface modification) can aid in commercial deployment of nanofluids.

Furthermore, this study did not evaluate the bubble dynamics or bubble growth phenomena in flow boiling due to the limitations of the experimental apparatus. Hence, monitoring the formation of bubbles and bubble dynamics in a flow condition is suggested as a topic of future investigation. The flow regimes explored in this study for two-phase heat transfer coefficient measurements of aqueous nanofluids is limited to low heat fluxes due to equipment limitations. There is a need for investigating the behavior of nanofluids in enhancing the Critical Heat Flux (CHF) of conventional working fluids. The flow boiling experiments performed in this study demonstrated the feasibility of enhancing the heat transfer through nanofluids. A similar experimental campaign can be performed for evaluating the CHF behavior for various nanofluids.

In addition, more experiments on two-phase nanofluid flow boiling heat transfer should be performed to evaluate the potential benefits of nanofluids as working fluids. These studies should also include pressure drop measurements along with two-phase flow

patterns in various types of channels. In particular, correlating two-phase flow patterns with heat transfer characteristics is essential. So far, no systematic knowledge/theory exists in the literature on nanofluid two-phase heat transfer.

REFERENCES

[1] "World Key Energy Statistics," International Energy Agency, 2017.

[2] "Technology Roadmap - Solar Thermal Electricity," International Energy Agency, 2014.

[3] "Special report on Renewable Energy Sources and Climate Change Mitigation," International Panel on Climate Change, 2012.

[4] Mark Lausten, "Gen3 CSP Technology Development," in *Department of Energy (DOE) Gen3 CSP Systems Workshop*, Sacramento, California, 2017.

[5] A. O'Donnell and K.-A. Adamson, "Thermal Storage for HVAC in Commerical Bildings, District Cooling and Heating, Utility and Grid Support Applications, and High Temperature Storage at CSP Facilities," *Pike Research,* 2012.

[6] S. Kuravi, J. Trahan , D. Y. Goswami, M. M. Rahman and E. K. Stefanakos, "Thermal Energy Storage technologies and Systems for Concentrating Solar Power Plants," *Progress of Energy and Combustion Science,* Vols. 285-319, p. 39, 2013.

[7] J. Stekli, L. Irwin and R. Pitchumani, "technical Challanges and Opportunities for Concentrating Solar power with Thermal Energy Storage," *Journal of Thermal Science Engineering,* vol. 5, 2013.

[8] "Department of Energy," [Online]. Available: https://energy.gov/eere/solar/articles/concentrating-solar-power-thermal-storage-system-basics. [Accessed 30 12 2017].

[9] D. Kearney, U. herrmann, P. Nava, B. Kelly, R. Mahoney, P. J. R. Cable, N. Portrovitza, D. Blake and H. Price, "Assessment of a Molten Salt heat transfer Fluid in a Parabolic Trough Solar Field," *Journal of Solar Energy Engineering,* vol. 125, no. 2, pp. 170-176, 2003.

[10] R. Devaradjane and D. Shin, "Nanoparticle Dispersions on Ternary Nitrate Salts for Heat Transfer Fluid Applications in Solar Thermal Power," *Journal of Heat Transfer,* vol. 138, 2016.

[11] "Office of Energy Efficiency and Renewable Energy: Department of Energy," [Online]. Available: https://www.energy.gov/eere.

[12] "Oak Ridge National Laboratory: Molten Salt Reactor," [Online]. Available: https://www.ornl.gov/msr.

[13] "ISI Web of Knowledge," [Online]. Available: https://apps.webofknowledge.com.

[14] H. W. Hoffmann and J. Jones, "Fused Salt Heat Transfer, PartII: Forced Convection Heat Transfer in Circular tubes Containing NaF-KF-LiF," ORNL-1777, 1955.

[15] H. W. Hoffmann and S. I. Cohen, "Fused Salt Heat Transfer Part III: Forced Convection Heat Transfer in Circular Tubes Containing the Salt Mixture NaNO2-KNO3-NaNO3," ORNL-2433, 1960.

[16] A. P. Colburn, "A method of correlating forced convection heat transfer data and a comparison with fluid friction," *Trans Am Inst Chem Engrs,* vol. 29, pp. 174-210, 1993.

[17] T. L. Bergman and F. P. Incropera, Introduction to heat transfer, Hoboken, New jersey: John Wiley & Sons, 2011.

[18] J. W. Cooke and B. Cox, "Forced Convection Heat Trasnfer Measurements with a Molten Flouride Slat MIxture Flowing in a Smooth Tube," ORNL-4079, 1973.

[19] M. D. Silverman, W. R. Huntley and H. E. Robertson, "Heat Transfer Measurements in a Forced Convective Loop with Two Molten Flouride Salts: LiF-BeF2-ThF2-UF4 and eutectic NaBF4-NaF," ORNL 5335, 1976.

[20] H. Hausen, "Neue Gleichungen Fur die Warmeubertragung bei freier oder erzwungener Stromung(New equations for heat transfer in free or forced flow)," *Allgemeine Wärmetechnik,* vol. 9, pp. 75-79, 1959.

[21] E. N. Sieder and G. E. Tate, "Heat Transfer and Pressure Drop of Liquids in Tubes," *Ind Eng Chem,* vol. 28, pp. 1429-35, 1936.

[22] L. Bin, W. Yu-Ting, M. Chong-fang, Y. Meng and G. Hang, "Turbulent Convective Heat Transfer with Molten Salt in a Circular Pipe," *International Communications in Heat and Mass Transfer,* vol. 36, pp. 912-916, 2009.

[23] W. Yu-Ting, L. Bin, M. Chong-Fang and G. hang, "Convective Heat Transfer in the Laminar-Turbulent Transition Region with molten Salt in a Circular Tube," *Experimental Thermal and Fluid Science,* vol. 33, pp. 1128-1132, 2009.

[24] V. Gnielinski, "New equations for heat and mass transfer for turbulent pipe and channel flows," *International Chemical Engineering,* vol. 16, no. 2, 1976.

[25] Y.-T. Wu, C. Chen, B. Liu and C. F. Ma, "Investigation on Forced Convective Heat Transfer of Molten Salts in Circular Tubes," *International Communications in Heat and Mass Transfer,* vol. 39, pp. 1550-1555, 2012.

[26] M. Yang, X. Yang, X. Yang and J. Ding, "Heat Transfer Enhancement and Performance of the Molten Salt Receiver of a Solar Power Tower," *Applied Energy,* vol. 87, pp. 2808-2811, 2010.

[27] L. Jianfeng, S. Xiangyang, D. Jing and Y. Jianping, "Transition and Turbulent Convective Heat Transfer of Molten Salt in Spirally Grooved Tube," *Experimental Thermal and Fluid Science,* vol. 47, pp. 180-185, 2013.

[28] L. Jianfeng, S. Xiangyang, D. Jing, P. Qjang and W. Yuliang, "Convective Heat Transfer of High temperature Molten Salt in Transversely Grooved Tube," *Applied Thermal Engineering,* vol. 61, pp. 157-162, 2013.

[29] "Coastal Chemical Co," [Online]. Available: http://stoppingclimatechange.com.

[30] C. Chen, W. Yu-Ting, S.-T. Wang and M. Chong-Fang, "Experimental Investigation on enhacned heat transfer in transversally corrugated tube with molten salt," *Experimental Thermal and Fluid Science,* vol. 47, pp. 108-116, 2013.

[31] L. Jianfeng, h. Shiquan, L. Junming, D. Jing and Y. Jianping, "Convective Heat Transfer in the Laminar-Turbulent Transition Region of Molten Salt in annular Passage," *Experimental Thermal and Fluid Science,* vol. 51, pp. 71-76, 2013.

[32] Y. S. Chen, Y. Wang, J. H. Zhnag, X. F. Yuan, J. Tian, Z. F. Tang, H. H. Zhu, Y. Fu and N. X. Wang, "Convective heat transfer characteristics in the turbulent region of molten salt in concentric tube," *Applied Thermal Engineering,* vol. 98, pp. 213-219, 2016.

[33] Y. S. Chen, J. Tian, Z. F. Tang, H. H. Zhu and N. X. Wang, "Experimental study of heat transfer enhancement for molten salt with transversely grooved tube heat exchanger in laminar-transition-turbulent regimes," *Applied Thermal Engineering,* vol. 132, pp. 95-101, 2018.

[34] S. He, J. Lu, J. Ding, T. Yu and Y. Yuan, "Convective Heat Transfer of Molten Salt Outise the Tube Bundle of Heat Exchanger," *Experimental Thermal and Fluid Science,* vol. 59, pp. 9-14, 2014.

[35] B.-C. Du, Y.-L. He, K. Wang and H.-H. Zhu, "Convective heat transfer of molten salt in the shell-and-tube heat exchanger with segmental baffles," *International Journal of Heat and Mass Transfer,* vol. 113, pp. 456-465, 2017.

[36] G. F. Hewitt, G. L. Shires and T. R. Bott, in *Process Heat Trasnfer,* 1994, pp. 263-280.

[37] j. Qian, Q.-L. Kong, H. W. Zhang, Z.-H. Zhu, W.-G. Huang and W.-H. Li, "Experimental study of shell-and-tube molten salt heat exchangers," *Applied Thermal Engineering,* pp. 616-623, 2017.

[38] Y. Qiu, M.-J. Li, W.-Q. Wang, B.-C. Du and K. Wang, "An experimental study on the heat transfer performance of a prototype molten-salt rod baffle heat exchanger for concentrated solar power," *Energy,* vol. 156, pp. 63-72, 2018.

[39] C. C. Gentry, "Rod baffle heat exchanger technology," *Chem eng Prog,* vol. 86, pp. 48-57, 1990.

[40] Q. W. Dong, Y. Q. Wang and M. S. liu, "Numerical and expeirmental investigation of shell side characteristics for a rod baffle heat exchanger," *Applied Thermal Engineering,* vol. 28, pp. 651-660, 2008.

[41] Y.-T. Wu, S.-W. Liu, Y.-X. Xiong, C.-F. Ma and Y.-L. Ding, "Experimental study on the heat transfer characteristics of a low melting point salt in a parabolic trough solar collector system," *Applied Thermal Engineering,* vol. 89, pp. 748-754, 2015.

[42] C. Renault, E. Merle and V. V. Ignatiev, "Liquid Salt Applications and Molten Salr Reactors," in *Proceedings of ICAPP*, Nice, France, 2007.

[43] D. Kearney, B. kelly, U. Herrmann, R. Cable, J. Pacheco and R. Mahoney, "Engineering Aspects of a Molten Salt heat transfer Fluid in a Trough Solar Field," *Energy,* vol. 29, pp. 861-870, 2004.

[44] S. U. S. Choi and J. A. Eastman, "Enhancing thermal conductivity of fluids with nanoparticles," in *ASME International Mechanical Engineering Congress and Exposition*, San Francisco, 1995.

[45] J. C. Maxwell, "A Treatise on Electricity and Magnetism," Oxford: Clarendon Press, 1873.

[46] X. Wang, X. Xu and S. U. S. Choi, "Thermal Conductivity of Nanoparticle-Fluid Mixture," *Journal of Thermophysics and Heat Transfer,* vol. 13, pp. 474-480, 1999.

[47] S. Lee, S. Choi, S. Li, W. Yu and L. J. Thompson, "Measring Thermal Conductivity of Fluids Containing Oxide Nanoparticles," *Journal of Heat Transfer,* vol. 121, pp. 280-290, 1999.

[48] Y. Xuan and Q. Li, "Heat Transfer Enhancement of Nanofluids," *International Journal of Heat and Fluid Flow,* vol. 21, pp. 58-64, 2000.

[49] H. Xie, J. Wang, T. Xi and Y. Liu, "Thermal Conductivity of Suspensions Containing nanosized SiC particles," *International Journal of Thermophysics,* vol. 23, pp. 571-580, 2002.

[50] M.-S. Liu, M.-C. Lin, I.-T. Huang and C.-C. Wang, "Enhancement of Thermal Conductivity with Carbon Nanotube for Nanofluids," *Internal Communications of Heat and Mass Transfer,* vol. 32, pp. 1202-1210, 2005.

[51] S. M. S. Murshed, K. C. Leong and C. Yang, "Enhanced Thermal Conductivity of TiO2 water based Nanofluids," *International Journal of Thermal Science,* vol. 44, pp. 367-373, 2005.

[52] Y. Ding, H. Alias, D. Wen and R. A. Williams, "Heat Transfer of Aqueous Suspensions of Carbon Nanotubes (CNT Nanofluids)," *International Journal of Heat and Mass Transfer,* vol. 49, pp. 240-250, 2006.

[53] H. Xie, H. Lee, W. youn and M. Choi, "Nanofluids Containing Multiwalled Carbon Nanotubes and their Enhanced Thermal Conductivities," *Journal of Applied Physics,* vol. 94, pp. 4568-4572, 2003.

[54] Y. J. Hwang, Y. C. Ahn, H. S. Shin, C. G. Lee, G. T. Kim and H. S. Park, "Investigation on Characteristics of Thermal Conductivity Enhancement of Nanofluids," *Current Applied Physics,* vol. 6, pp. 1068-1071, 2006.

[55] B. C. Pak and Y. I. Y. Cho, "Hydrodyanmic and Heat Transfer Study of Dispersed Fluids with Submicron Metallic Oxide Particles," *Experminetal Heat Transfer,* vol. 11, pp. 151-170, 1998.

[56] X. Zhang, H. Gu and M. Fujii, "Effective Thermal Conductivity and Thermal Diffusivity of Nanofluids containing Spherical and Cylindrical Nanoparticles," *Experimental and Thermal and Fluid Science,* vol. 31, pp. 593-599, 2007.

[57] S. M. S. Murshed, K. C. Leong and C. Yang, "Investigations of thermal conductivity and viscosity of nanofluids," *Internation Journal of Thermal Sciences,* vol. 47, no. 5, pp. 560-568, 2008.

[58] S. K. Das, N. Putra, P. Thisen and W. roetzel, "temperature Dependence of Thermal Conductivity Enhancement of Nanofluids," *Journal of Heat Transfer,* vol. 2003, pp. 567-574, 2003.

[59] Y. Hwang, J. K. Lee, C. H. Lee, Y. Jung, S. I. Cheong and C. G. Lee, "Stability and Thermal Conductivity Characteristics of Nanofluids," *Thermochimca Acta,* vol. 455, 2007.

[60] M. P. Beck, Y. Yuan, P. Warrier and A. S. Teja, "The Thermal Conductivity of Alumina Nanofluids in Water, Ethylene Glycol, and Ethylene Glycol+Water Mixtures," *Journal of Nanoparticle Research,* vol. 12, pp. 1469-1477, 2010.

[61] I. C. Nelson and D. Banerjee, "Floe Loop Experiments Using Polyalphsolefin Nanofluids," *Journal of Thermophysicas and Heat Transfer,* vol. 23, no. 4, pp. 752-761, 2009.

[62] D. Shin and D. Banerjee, "Enhancement of Specific Heat Capacity of High-Temperature Silica-Nanofluids Synthesized in Alkali Chloride Salt Eutectics for Solar Thermal Energy Storage Applciations," *International Journal of Heat and Mass Transfer,* vol. 54, pp. 1064-70, 2011.

[63] B.-X. Wang, L.-P. Zhou and X.-F. Peng, "Surface adn Size Effects on the Specific Heat Capacity of Nanoparticles," *International Journal of Thermophysics,* vol. 27, pp. 139-51, 2006.

[64] L. Wang, Z. Tan, S. Meng, D. Liang and G. Li, "Enhancement of Molar Heat Capacity of Nanostructured Al2O3," *Journal of Nanoparticle Research,* vol. 3, pp. 483-487, 2001.

[65] S. Oh, Y. Kauffmann, C. Scheu, W. Kaplan and M. Ruhle, "Ordered Liquid Aluminum at the Interface with Sapphire," *Science,* vol. 310, pp. 661-663, 2005.

[66] K. Khanafer, F. Tavakkoli, K. Vafai and A. Al Amiri, "A critical Investigation of the Anomalous Behavior of Molten Salt-based Nanofluids," *International Communications of Heat and Mass Transfer,* vol. 69, pp. 51-58, 2015.

[67] N. Singh and D. Banerjee, Nanofins: Science and Applications, College Station: Springer, 2013.

[68] V. Sathyamurthi, H. S. Ahn, D. Banerjee and S. C. Lau, "Subcooled pool boiling experiments on horizontal heaters coated with carbon nanotubes," *Journal of Heat Transfer ,* vol. 131, 2009.

[69] H. S. Ahn, N. Sinha, M. Zhnag, D. banerjee, S. Fang and R. H. Baughman, "Pool boiling experiments on multiwalled carbon nanotube (mwcnt) forests," *Journal of Heat Transfer,* vol. 128, pp. 1335-1342, 2006.

[70] S. Ujereh, T. Fisher and I. Mudawar, "Effects of carbon nanotube arrays on nucleate pool boiling," *International Journal of Heat and Mass Transfer,* vol. 50, pp. 4023-4038, 2007.

[71] N. Singh, V. Sathyamurthy, W. Peterson, J. Arendt and BanerjeeD, "Flow boiling enhancement on a horizontal heater using carbon nanotube coatings," *International Journal of Fluid Flow,* vol. 31, pp. 201-207, 2010.

[72] S. R. Sriraman, "Pool boiling on nano-finned surfaces," Texas A&M University, College Station, 2007.

[73] H. Zhong and J. R. Lukes, "Interfacial thermal resistance between carbon nanotubes: Molecular dynamics simulations and analytical thermal modeling," *Physical Review B,* vol. 74, 2006.

[74] D. Estrada and E. Pop, "Imaging dissipation and hot spots in carbon nanotube network transistors," *Applied Physics Letters,* vol. 98, 2011.

[75] G. L. Pollack, "Kaptiza Resistance," *Reviews of Modern Physics,* vol. 41, no. 1, 1969.

[76] N. Singh, "Computational analysis of thermo-fluidic characteristics of a carbon nano-fin," Texas A&M University, College Stattion, 2010.

[77] V. U. Unnikrishnana, D. Banerjee and J. N. Reddy, "Atomistic-mesoscale interfacial resistance based thermal analysis of carbon nanotube systems," *International Journal of Thermal Science,* vol. 47, pp. 1602-1609, 2008.

[78] N. Singh, V. Unnikrishnana, D. Banerjee and J. Reddy, "Analysis of thermal interfacial resistance between nanofins and various coolants," *International Journal of Computational Methods,* vol. 12, pp. 254-260, 2011.

[79] B. Jo and D. Banerjee, "Interfacial thermal resistance between a carbon nanoparticle and molten salt eutectic: effect of material properties, particle shapes and sizes," in *ASME/JSME 8th thermal engineering joint conference*, Honolulu, 2011.

[80] H. Maune, H. Y. Chiu and M. Bockrath, "Thermal resistance of the nanoscale constrictions between carbon nanotubes and solid substrates," *Applied Physics Letters,* vol. 89, 2006.

[81] S. Murad and I. K. Puri, "Thermal transport across nanoscale solid-fluid interfaces," *Applied Physics Letters,* vol. 92, 2008.

[82] S. T. Huxtable, D. G. Cahill, S. Shenogin, L. Xue, R. Pzisik, P. Barone, M. Usrey, M. S. Strano, G. Siddons and M. Shim, "Interfacial heat flow in carbon nanotube suspensions," *Nature,* vol. 2, pp. 731-734, 2003.

[83] B. Jo, "Numerical and Experimental Investigation of Organic Nanomaterials for Thermal Energy Storage and for Concentrating Solar Power Applications," Texas A&M University, College Station, 2012.

[84] S. Jung, "Numerical and Experimental Investigation of Inorganic Nanomaterials for Thermal Energy Storage (TES) and Concentrated Solar Power (CSP) Applications," Texas A&M University, College Station, 2012.

[85] D. Shin, "Molten Salt Nanomaterials for Thermal Energy Storage and Concentrated Solar Power Applications," Texas A&M University, College Station, 2011.

[86] N. Singh and D. Banerjee, Nanofins: Science and Applications, Springer, 2013.

[87] H. Yang, "Experimental and Numerical Investigation of Pool Boiling Heat Transfer on," Texas A&M University, College Station, 2014.

[88] S. H. Oh, Y. Kauffmann, C. Scheu, W. D. Kaplan and M. Ruhle, "Ordered Liquid Aluminum at the Interface with Sapphire," *Science,* vol. 310, no. 5748, pp. 661-663, 2005.

[89] L. Li, Y. Zhnag, H. Ma and M. Yang , "Molecular Dynamics Simulation of Effect of Liquid Layering around the Nanoparticle on the Enhanced Thermal Conductivity of Nanofluids," *Journal of Nanoparticle Research,* vol. 12, no. 3, pp. 811-821, 2010.

[90] C. I. Chang, W. J. Lee, T. F. young, S. P. Ju, C. W. Chang, H. L. Chen and J. G. Chang, "Adsorption Mechanism of Water Molecules Surrounding Au Nanoparticles of Different Sizes," *Journal of Physical Chemistry,* vol. 128, no. 15, 2008.

[91] B. Jo and D. Banerjee, "Effect of solvent on specific heat capacity enhancement of binary molten salt-based carbon nanotube nanomaterials for thermal energy storage," *International Journal of Thermal Sciences,* 2015.

[92] B. Jo and D. Banerjee, "Thermal properties measurement of binary carbonate salt mixtures for concentrating solar power plants," *AIP Journal of Renewable and Sustainable Energy,* vol. 7, no. 3, 2015.

[93] D. Shin and D. Banerjee, "Enhanced thermal properties of SiO2 nanocomposite for solar thermal energy storage applications," *International Journal of Heat and Mass Transfer,* vol. 84, pp. 898-902, 2015.

[94] B. Jo and D. Banerjee, "Enhanced specific heat capacity of molten salt based nanomaterials: Effect of nanoparticle dispersion and solvent material," *Acta Materialia,* vol. 75, pp. 80-91, 2014.

[95] H. Tiznobaik, D. Banerjee and D. Shin, "Effect of formation of long range secondary dendritic nanostructures in molten salt nanofluids on the values of specific heat capacity," *International Journal of Heat and Mass Transfer,* vol. 91, pp. 342-346, 2015.

[96] R. S. Vajjh, D. K. Das and B. M. Mahagaonkar, "Density Measurement of Different Nanofluids and Their Comparison With Theory," *Petroleum Science and Technology,* vol. 27, no. 6, pp. 612-624, 2009.

[97] A. Mariano, M. J. Pastoriza-gallego, L. Lugo, A. camacho, S. Canzonieri and M. Pineiro, "Thermal conductivity, rheological behaviour and density of non-Newtonian ethylene glycol-based SnO2 nanofluids," *Fluid Phase Equilibria,* pp. 119-124, 2013.

[98] m. J. Pastoriza-Gallego, C. casanova, R. Paramo, B. Barbes, J. L. Legido and M. M. Pineiro, "study on stability and thermophysical properties (density and viscosity) of Al2O3 in water nanofluid," *Journal of Applied Physics,* 2009.

[99] M. M. Heyhat, F. kowsary, A. M. Rashidi, m. H. Momenour and A. Amrollahi, "Experimental Investigation of laminar convective heat transfer and pressure drop of water-based Al2O3 nanofluids in fully developed flow regime," *Experimental Thermal and Fluid Science,* vol. 44, pp. 483-489, 2013.

[100] D. R. Selvakumar and J. Wu, "A comprehensive model for effective density of nanofluids based on particle clustering and interfacial layer formation," *Journal of Molecular Liquids,* vol. 292, 2019.

[101] M. Sharifpur, S. Yousefi and P. J. Meyer, "A new model for density of nanofluids including nanolayer," *International Communications in Heat and Mass Transfer,* vol. 78, pp. 168-174, 2016.

[102] C. J. Yu, A. G. Richter, A. Datta, M. K. Durbin and P. Dutta, "Observation of molecular layering in thin liquid films using X ray reflectivity," *Physics Revision Letters,* pp. 2326-2329, 1999.

[103] C. J. Yu, A. G. Richter, J. Kmetko, S. W. Dugan, A. Datta and P. Dutta, "Structure of interfacila liquids:X-ray scattering studies," *Physics Revisions E,* p. 021205, 2001.

[104] M. M. Heyhat, F. Kowsary, A. M. Rashidi, M. H. Momenpour and A. Amrollahi, "Experimental investigation of laminar convective heat transfer and pressure drop of water-based Al2O3 nanofluids in fully developed flow regime," *Experimental Thermal and Fluid Science,* vol. 44, pp. 483-489, 2013.

[105] W. Yu, D. M. France, D. S. Smith, D. Singh, E. V. Timofeeva and J. L. Routbort, "Heat transfer to a silicon carbide/water nanofluid," *International Journal of Heat and Mass Transfer,* vol. 52, pp. 3606-3612, 2009.

[106] Y. He, Y. Jin, H. Chen, Y. Ding, D. Cang and H. Lu, "Heat transfer and flow behaviour of aqueous suspensions of TiO2 nanoparticles (nanofluids) flowing upward through a vertical pipe," *International Journal of Heat and Mass Transfer,* vol. 50, pp. 2272-2281, 2007.

[107] A. T. Utomo, E. B. Haghighi, A. I. T. Zavareh, M. Ghanbarpourgeravi, H. Poth, R. Khodabandeh, B. Palm and A. W. Pacek, "The effect of nanoparticles on

laminar heat transfer in a horizontal tube," *International Journal of Heat and Mass Transfer,* vol. 69, pp. 77-91, 2014.

[108] K. S. Hwang, S. P. Jang and S. U. Choi, "Flow and convective heat transfer characteristics of water-based Al2O3 nanofluids in fully developed laminar flow regime," *International Journal of Heat and Mass Transfer,* vol. 52, pp. 193-199, 2009.

[109] E. B. Haghighi, M. Saleemi, N. Nikkam, R. Khodabandeh, M. S. Toprak, M. Muhammed and B. Palm, "Accurate basis of comparison for convective heat transfer in nanofluids," *International Communications in Heat and Mass Transfer,* vol. 52, pp. 1-7, 2014.

[110] S. Ferrouillat, A. Bontemps, J.-P. Ribeiro, J.-A. Gruss and O. Soriano, "Hydraulic and heat transfer study of SiO2/water nanofluids in horizontal tubes with imposed wall temperature boundary conditions," *International Journal of Heat and Fluid Flow,* vol. 32, pp. 424-439, 2011.

[111] H. Chen, W. Yang, Y. He, Y. Ding, L. Zhnag, C. Tan, A. A. Lapkin and D. V. Bavykin, "Heat transfer and flow behaviour of aqueous suspensions of titanate nanotubes (nanofluids)," *Powder Technology,* vol. 183, pp. 63-72, 2008.

[112] Y. Li, J. Fernandez-Seara, K. Du, A. A. Pardinas, L. L. Latas and W. Jiang, "Experimental investigation on heat transfer and pressure drop of ZnO/ethylene glycol-water nanofluids in transition flow," *Applied Thermal Engineering,* vol. 93, pp. 537-548, 2016.

[113] D. Huang, Z. Wu and B. Sunden, "Pressure drop and convective heat transfer of Al2O3/water and MWCNT/water nanofluids in a chevron plate heat exchanger," *International Journal of Heat and Mass Transfer,* vol. 89, pp. 620-626, 2015.

[114] D. K. Agarwal, A. Vaidyanathan and S. S. Kumar, "Investigation on convective heat transfer behaviour of kerosene-Al2O3 nanofluid," *Applied Thermal Engineering,* vol. 84, pp. 64-73, 2015.

[115] H. Yarmand, S. Gharehkhani, S. F. S. Shirazi, A. Amiri, M. S. Alehashem, M. Dahari and S. N. Kazi, "Experimental investigation of thermo-physical properties, convective heat transfer and pressure drop of functionalized graphene nanoplatelets aqueous nanofluid in a square heated pipe," *Energy Conversion and Management,* vol. 114, pp. 38-49, 2016.

[116] J. Yu, S.-W. Kang, S. Jeon and D. Banerjee, "Heat Transfer Measurements for Flow of Nanofluids in Microchannels using Temperature Nano-Sensors," *Frontiers in Heat and Mass Transfer,* 2012.

[117] S. Khandekar, Y. M. Joshi and B. Mehta, "Thermal Performance of Closed Tw-Phase Thermosyphon Using Nanofluids," *International Journal of Thermal Sciences,* vol. 47, no. 6, pp. 659-667, 2008.

[118] K. Henderson, Y. G. Park and L. P. Liu, "Flow Boiling Heat Transfer of R-134a-based Nanofluids in a Horizontal Tube," *International Journal of Heat Mass Transfer,* vol. 53, no. 6, pp. 944-951, 2010.

[119] H. S. Xue, J. R. Fan, Y. C. Hu, R. H. Hong and K. F. Cen, "The interface effect of carbon nanotube suspension on thermal performance of a two-phase closed thermosyphon," *Journal of Applied Physics,* vol. 100, no. 10, 2006.

[120] Y. Park, "Nanoparticles to enhance evaporative heat trabsfer," in *The 22nd International Congress of Refrigeration*, Beijing, 2007.

[121] M. A. Akhavan-Behabadi, M. Nasr and S. Baqeri, "Experimental Investigation of Flow Boiling Heat Transfer of R-600a/Oil/CuO ina plain horizontal tube," *Experimental Thermal Fluid Science,* vol. 58, pp. 105-111, 2014.

[122] H. Setoodeh, A. Keshavarz, A. Ghasemian and A. Nasouhi, "Subcooled Flow Boiling of Alumina/Water Nanofluid in a Channel with a Hot Spot: An Experimental Study," *Applied Thermal Engineering,* vol. 90, pp. 384-394, 2015.

[123] V. Nikkhah, M. M. Sarafraz, F. Hormozi and S. M. Peyghambarzadeh, "Particulate fouling of CuO-water nanofluid at isothermal diffusive condition inside the conventional heat exchnager-experimental and modeling," *Experimental Thermal and fluid Science,* vol. 60, pp. 83-95, 2015.

[124] M. M. Sarafraz, F. hormozi, S. M. Peyghambarzadeh and N. Vaeli, "upward flow boiling to Di-Water and CuO nanofluids inside the concentric annulu," *Journal of Applied Fluid Mechanics,* vol. 8, no. 4, pp. 651-659, 2015.

[125] H. B. Ma, "An experimental investigation of heat transport capability in a nanofluid oscillating heat pipe," *Journal of Heat Transfer,* vol. 128, no. 11, pp. 1213-1216, 2006.

[126] Z. h. Liu and Y. H. Qiu, "Boiling heat transfer charcteristics of nanofluids jet impingement on a plate surface," *Heat Mass Transfer,* vol. 43, no. 7, pp. 699-706, 2007.

[127] Z. h. Liu, J. G. Xiong and R. Bao, "Boiling heat transfer characteristics of nanolfuids in a flat heat pipe evaporator with micro-grooved heating surface," *International Journal of Multiphase Flow,* vol. 33, no. 12, pp. 1284-1295, 2007.

[128] Y. Park, "Nanoparticles to enhance evaporative heat transfer," in *The 22nd International Congress of Refrigeration*, Beijing, 2007.

[129] G. Paul, P. K. Das and I. Manna, "Assessment of the process of boiling heat transfer during rewetting of a vertical tube bottom flooded by alumina nanofluid," *International Journal of Heat and Mass Transfer,* vol. 94, pp. 390-402, 2016.

[130] Y. Wang and G. H. Su, "Experimental Investigation on nanofluid flow boiling heat transfer in a vertical tube under different pressure conditions," *Experimental Thermal Fluid Science,* vol. 77, pp. 116-123, 2016.

[131] B. Ma, "EXPERIMENTAL AND NUMERICAL INVESTIGATION OF MOLTEN SALT NANOMATERIALS FOR ENHANCED THERMAL ENERGY STORAGE (TES) AND HEAT TRANSFER FLUID (HTF)," Texas A&M University, College Station, 2017.

[132] R. Shaw, "Dynamic Light Scattering Training: Achieving Reliable Nano Particle Sizing," 2013.

[133] Nanocomposix, "Zeta Potential Analysis of Nanoparticles," Nanocomposix Publication.

[134] S. J. Kline and F. A. McClintok, "Describing Uncertainties in Single-Sample Experiments," *Mechanical Engineering,* vol. 75, no. 1, pp. 3-8, 1953.

[135] P. J. Feibelman, "the first wetting layer on a solid," *Physics Today,* vol. 63, no. 2, 2010.

[136] W. J. Huisman, J. F. Peters, J. W. Derks, D. L. Abernathy and J. F. van der Veen, "A new X-ray diffraction method for structural investigation of solid-liquid interfaces," *Science Instruments,* vol. 11, p. 4169, 1997.

[137] [Online]. Available: https://www.azonano.com/article.aspx?ArticleID=3398.

[138] A. Pugliese, G. Cabassi, E. Chiavaro, M. Paciulli, E. Carini and G. Mucchetti, "Physical Characterization of Whole and Skim Dried Powders".

[139] F. Saporito, G. Sandri, C. M. Bonferoni, S. Rossi, C. Boselli, I. A. Cornaglia, B. Mannucci, P. Grisoli, B. Vigani and F. Ferrari, "Essential oil-loaded lipid nanoparticles for wound healing," *International Journal of Nanomedicine,* pp. 175-186, 2018.

[140] M. Guo and G. Wang, "Milk Protein Polymer and Its Application in Environmentally Safe Adhesives," *POlymers,* 2016.

[141] L. Zhnag, D. Hayes, G. Chen and Q. Zhong, "Transparent Dispersions of Milk-Fat-Based Nanostructured Lipid Carriers for Delivery of Carotene," *Journal of Agriculture and Food Chemistry,* vol. 61, pp. 9435-9443, 2013.

[142] G. Duplatre, m. F. Ferreira marques and M. M. Graca , "Size of Sodium Dodecyl Sulfate Micelles in Aqueous Solutions as Studied by Positron Annihilation Lifetime Spectroscopy," *Journal of Physical Chemistry,* vol. 100, 1996.

[143] j. A. Reynolds and C. Tanford, "The Gross Conformation of Protein-Sodium Dodecyl Sulfate Complexes," *The Journal of Biological Chemistry,* vol. 245, no. 19, pp. 5161-5165, 1970.

[144] "NIST Reference Tables," [Online]. Available: https://www.nist.gov/ncnr/sample-environment/sample-mounting/reference-tables.

[145] "Thermo-Kinetics," [Online]. Available: http://www.thermo-kinetics.com/documents/Thermowells.pdf. [Accessed 07 05 2018].

[146] M. Hassan and D. Banerjee, "A soft computing approach for estimating the specific heat capacity of molten salt based nanofluids," *Journal of Molecular Liquids,* vol. 281, pp. 365-375, 2019.

[147] L. Wojtan, T. Ursenbacher and J. R. Thome, "INvestigation of flow boiling in horizontal tubes : Part I - a new diabatic two-phase flow pattern map," *International Journal of Heat and Mass Transfer,* pp. 2955-2960, 48.

[148] A. Layek, G. Mishra, A. Sharma, M. Spasova, S. Dhar, A. Chowdhury and R. Bandyopadhyaya, "A Generalized Three-Stage Mechanism of ZnO Nanoparticle Formation in Homogeneous Liquid Medium," *The Journal of Physical Chemistry C,* vol. 116, no. 46, pp. 24757-24769, 2012.

[149] y.-T. Wu, C. Chen, B. Liu and C. F. Ma, "Investigation on Forced Convective Heat Transfer of Molten Salts in Circular Tubes," *International Communications in Heat and Mass Transfer,* vol. 39, pp. 1550-1555, 2012.

[150] M. yang, X. Yang, X. Yang and J. Ding, "Heat Transfer Enhancement and Performance of the Molten Salt Receiver of a Solar Power Tower," *Applied Energy,* vol. 87, pp. 2808-2811, 2010.

[151] L. Jiangfeng, S. He, J. Ding, J. Yang and J. Liang, "Convective Heat Transfer of High Temperature Molten Salt in a vertical annular duct with cooled wall," *Applied Thermal Engineering,* vol. 73, pp. 1519-1524, 2014.

[152] t. Satoh, K. Yuki, S.-Y. Chiba, H. Hashizume and A. Sagara, "Heat Transfer Performance for High Prnadtl and High Temperature Molten Salt Flow in SPhere-Packed Pipes," *Fusion Science and Technology,* vol. 52, no. 3, pp. 618-624, 2007.

[153] H. Badenhorst and L. F. Cabeza, "Critical Analysis of the T-History Method: A Fundamental Approach," *Thermochimica Acta,* vol. 27, no. 4, pp. 360-366, 2017.

[154] B. Sun, C. Peng, R. Zuo, D. Yang and H. Li, "Investigation on the flow and convective heat transfer characteristics of nanofluids in the plate heat exchanger," *Experimental Thermal and Fluid Science,* vol. 76, pp. 75-86, 2016.

[155] L. Megatif, A. Ghozatloo, A. Arimi and M. Shariati-Niasar, "Investigation of Laminar Convective Heat Transfer of a Novel Tio2–Carbon Nanotube Hybrid Water-Based Nanofluid," *Experimental Heat Transfer,* vol. 29, no. 1, pp. 124-138, 2016.

[156] A. Shahsavar, M. Saghafian, M. R. Salimpour and M. B. Shafii, "Experimental investigation on laminar forced convective heat transfer of ferrofluid loaded with carbon nanotubes under constant and alternating magnetic fields," *Experimental Thermal and Fluid Science,* Vols. 1-11, p. 76, 2016.

[157] M. Goharkhah, M. Ashjaee and M. Shahabadi, "Experimental investigation on convective heat transfer and hydrodynamic characteristics of magnetite nanofluid

under the influence of an alternating magnetic field," *International Journal of Thermal Sciences,* vol. 99, pp. 113-124, 2016.

[158] M. H. Aghabozorg, A. Rashidi and S. Mohammadi, "Experimental investigation of heat transfer enhancement of Fe2O3-CNT/water magnetic nanofluids under laminar, transient and turbulent flow inside a horizontal shell and tube heat exchanger," *Experimental Thermal and Fluid Science,* vol. 72, pp. 182-189, 2016.

[159] A. Noghrehabadi and R. Pourrajab, "Experimental investigation of forced convective heat transfer enhancement of AL2O3/water nanofluid in a tube," *Journal of mechanical science and tenchnology,* vol. 30, pp. 943-952, 2016.

[160] M. H. Esfe and S. Saedodin, "Turbulent forced convection heat transfer and thermophysical properties of Mgo–water nanofluid with consideration of different nanoparticles diameter, an empirical study," *Journal of Thermal Analysis and Calorimetry,* vol. 119, no. 2, pp. 1205-1213, 2015.

[161] L. Colla, L. Fedele and M. H. Buschmann, "Laminar mixed convection of TiO2ewater nanofluid in horizontal uniformly heated pipe flow," *International Journal of Thermal Sciences,* vol. 97, pp. 26-40, 2015.

[162] E. Nourafkan, G. Karimi and J. Moradgholi, "Experimental Study of Laminar Convective Heat Transfer and Pressure Drop of Cuprous Oxide/ Water Nanofluid Inside a Circular Tube," *Experimental Heat Transfer,* vol. 28, no. 1, pp. 58-68, 2015.

[163] B. Mehrjou, Z. S. Heris and K. Mohamadifard, "Experimental Study of CuO/Water Nanofluid Turbulent Convective Heat Transfer in Square Cross-section Duct," *Experimental Heat Transfer,* vol. 28, no. 3, pp. 282-297, 2015.

[164] H. M. Ali, H. Ali, H. Liaquat, H. T. B. Maqsood and M. A. Nadir, "Experimental investigation of convective heat transfer augmentation for car radiator using ZnOewater nanofluids," *Energy,* vol. 84, pp. 317-324, 2015.

[165] S. L. Sundar, V. E. Ramana, M. K. Singh and A. C. Sousa, "Thermal conductivity and viscosity of stabilized ethylene glycol and water mixture Al2O3 nanofluids for heat transfer applications: An experimental study," *International Communications in Heat and Mass Transfer,* vol. 56, pp. 86-95, 2014.

[166] E. B. Haghighi, N. Nikkam, M. Saleemi, M. Behi, S. A. Mirmohammadi, H. Poth, R. Khodabandeh, M. S. Toprak, M. Muhammed and B. Palm, "Shelf stability of nanofluids and its effect on thermal conductivity and viscosity," *Measurement Science and Technology,* vol. 24, p. 105301, 2013.

[167] C. Depcik, T. Jacobs, J. Hagena and D. Assanis, "Instructional Use of a Single-Zone, Premixed Charge, Spark-Ignition Engine Heat Release Simulation," *International Journal of Mechanical Engineering Education,* vol. 35, no. 1, pp. 1-31, 12 November 2012.

[168] B. Aladag, S. Halelfad, N. Doner, T. Mare, S. Duret and P. Estelle, "Experimental investigations of the viscosity of nanofluids at low temperatures," *Applied Energy,* vol. 97, pp. 876-880, 2012.

[169] Y. Wei and X. Huaqing, "A review on nanofluids: preparation, stability mechanisms, and applications," *Journal of Nanomater,* vol. 2012, pp. 1-17, 2012.

[170] A. R. Sajadi and M. H. Kazemi, "Investigation of turbulent convective heat transfer and pressure drop of TiO2/water nanofluid in circular tube," *International Communications in Heat and Mass Transfer,* vol. 38, pp. 1474-1478, 2011.

[171] S. Suresh, M. Chandrasekar and S. Chandra Sekhar, "Experimental studies on heat transfer and friction factor characteristics of CuO/water nanofluid under turbulent flow in a helically dimpled tube," *Experimental Thermal and Fluid Science,* vol. 35, pp. 542-549, 2011.

[172] M. Hojjat, S. G. Etemad, R. Bagheri and J. Thibault, "Convective heat transfer of non-Newtonian nanofluids through a uniformly heated circular tube," *International Journal of Thermal Sciences,* vol. 50, pp. 525-531, 2011.

[173] S. M. Fotukian and N. M. Esfahany, "Experimental study of turbulent convective heat transfer and pressure drop of dilute CuO/water nanofluid inside a circular tube," *International Communications in Heat and Mass Transfer,* vol. 37, pp. 214-219, 2010.

[174] M. Chandrasekar, S. Suresh and A. Chandra Bose, "Experimental studies on heat transfer and friction factor characteristics of Al2O3/water nanofluid in a circular pipe under laminar flow with wire coil inserts," *Experimental Thermal and Fluid Science,* vol. 34, pp. 122-130, 2010.

[175] A. D. Sommers and K. L. Yerkes, "Experimental investigation into the convective heat transfer and system-level effects of Al2O3-propanol nanofluid," *Journal of Nanoparticle Research,* vol. 12, no. 3, pp. 1003-1014, 2010.

[176] R. S. Vajjha, D. K. Das and D. P. Kulkarni, "Development of new correlations for convective heat transfer and friction factor in turbulent regime for nanofluids," *International Journal of Heat and Mass Transfer,* vol. 53, no. 21-22, pp. 4607-4618, 2010.

[177] H. E. Patel, T. Sundararajan and S. K. Das, "An experimental investigation into the thermal conductivity enhancement in oxide and metallic nanofluids," *Journal of Nanoparticle Research,* vol. 12, pp. 1015-1031, 2010.

[178] H. A. Mintsa, G. Roy, C. T. Nguyen and D. Doucet, "New temperature dependent thermal conductivity data for water-based nanofluids," *International Journal of Thermal Sciences,* vol. 48, no. 2, pp. 363-371, 2009.

[179] U. Rea, T. McKrell, L.-w. Hu and J. Buongiorno, "Laminar convective heat transfer and viscous pressure loss of alumina–water and zirconia–water

nanofluids," *International Journal of Heat and Mass Transfer,* vol. 52, pp. 2042-2048, 2009.

[180] L. Liao and Z.-H. Liu, "Forced convective flow drag and heat transfer characteristics of carbon nanotube suspensions in a horizontal small tube," *Heat and Mass Transfer,* vol. 45, no. 8, pp. 1129-1136, 2009.

[181] R. S. Vajjha and D. K. Das, "Experimental determination of thermal conductivity of three nanofluids and development of new correlations," *International Journal of Heat and Mass Transfer,* vol. 52, pp. 4675-4682, 2009.

[182] K. B. Anoop, T. Sundararajan and S. K. Das, "Effect of particle size on the convective heat transfer in nanofluid in the developing region," *International Journal of Heat and Mass Transfer,* vol. 52, pp. 2189-2195, 2009.

[183] H. Mehling and L. F. Cabeza, Heat and Cold Storage with PCM, Springer, 2008.

[184] D. P. Kulkarni, P. K. Namburu, H. E. Bargar and D. K. Das, "Convective Heat Transfer and Fluid Dynamic Characteristics of SiO2 Ethylene Glycol/Water Nanofluid," *Heat Transfer Engineering,* vol. 29, no. 12, pp. 1027-2035, 2008.

[185] C. T. Nguyen, F. Desgranges, G. Roy, N. Galanis, T. Mare, S. Boucher and A. H. Mintsa, "Temperature and particle-size dependent viscosity data for water-based nanofluids-hysteresis phenomenon," *International Journal of Heat Fluid Flow,* vol. 28, pp. 1492-1506, 2007.

[186] Z. S. Heris, N. M. Esfahany and S. G. Etemad, "Experimental investigation of convective heat transfer of Al2O3/water nanofluid in circular tube," *International Journal of Heat and Fluid Flow,* vol. 28, pp. 203-210, 2007.

[187] G. H. Ko, K. Heo, K. Lee, D. S. Kim, C. Kim, Y. Sohn and M. Choi, "An experimental study on the pressure drop of nanofluids containing carbon nanotubes in a horizontal tube," *International Journal of Heat and Mass Transfer,* vol. 50, pp. 4749-4753, 2007.

[188] Z. S. Heris, S. G. Etemad and M. N. Esfahany, "Experimental investigation of oxide nanofluids laminar flow convective heat transfer," *International Communications in Heat and Mass Transfer,* vol. 33, pp. 529-535, 2006.

[189] R. Prasher , P. Bhattacharya and P. Phelan, "Thermal Conductivity of Nanoscale Colloidal Solutions (Nanofluids)," *Physics Review Letters,* vol. 94, p. 025901, 2005.

[190] C. H. Chon, K. D. Kihm, S. P. Lee and S. U. S. Choi, "Empirical correlation finding the role of temperature and particle size for nanofluid (Al2O3) thermal conductivity enhancement," *Applied Physics Letters,* vol. 87, no. 15, p. 153107, 2005.

[191] D. Wen and Y. Ding, "Experimental investigation into convective heat transfer of nanofluids at the entrance region under laminar flow conditions," *International Journal of Heat and Mass Transfer,* vol. 47, pp. 5181-5188, 2004.

[192] H. Hong, S. K. Kim and Y. S. Kim, "Accuracy Improvement of T-History Method for measuring heat of fusion of various materials," *International Journal of Refrigeration,* vol. 27, no. 4, pp. 360-366, 2004.

[193] Y. M. Xuan and Q. Li, "Investigation on convective heat transfer and flow features of nanofluids," *Journal of heat transfer,* vol. 125, no. 1, pp. 151-155, 2003.

[194] J. M. Marin, "Determination of enthalpy-temperature curves of phase change materials with the temperature-history method: Improvement to Temperature dependent Properties," *Measurement Science and Technology,* vol. 14, no. 2, p. 184, 2003.

[195] Z. YInping and J. Yi, "A simple method, the-history method of determining the heat of fusion, specific heat and thermal conductivity of phase-change materials," *Materials Science and Technology,* vol. 10, no. 3, p. 201, 1999.

[196] B. C. Pak and Y. I. Cho, "Hydrodynamic and heat transfer study of dispersed fluids with submicron metallic oxide particles," *Experimental Heat Transfer,* vol. 11, no. 2, pp. 151-170, 1998.

[197] M. Chieruzzi, A. Miliozzi, T. Crescenzi, J. M. Kenny and L. Torre, "Synthesis and characterization of nanofluids useful in concentrated solar power plants produced by new mixing methodologies for large-scale production," *Journal of Heat Transfer,* 2017.

[198] D. Ercole, O. Manca and K. Vafai, "An investigation of thermal characteristics of eutectic molten salt-based nanofluids," *International Communications in Heat and Mass Transfer,* vol. 87, pp. 98-104, 2017.

[199] Y. Hu, Y. He, Z. Zhnag and D. Wen, "Effect of Al2O3 nanoparticle dispersion on the specific heat capacity of a eutectic binary nitrate salt for solar power applications," *Energy Conversion and Management,* vol. 142, pp. 366-373, 2017.

[200] X. Chen, Y.-T. Wu, L.-D. Zhnag, X. Wang and C.-F. Ma, "Experimental study on the specific heat and stability of molten salt nanofluids prepared by high-temperature melting," *Solar Energy Materials and Solar Cells,* vol. 176, pp. 42-48, 2018.

[201] M.-C. Lu and C.-H. Huang, "Specific heat capacity of molten salt-based alumina nanofluid," *Nanoscale Research Letters,* vol. 292, 2013.

[202] B. Jo and D. Banerjee, "Enhanced specific heat capacity of molten salt-based nanomaterials: Effects of nanoparticle dispersion and solvent material," *Acta Materialia,* vol. 75, pp. 80-91, 2014.

[203] M. X. Ho and C. Pan, "Optimal concentration of alumina nanoparticles in molten Hitec salt to maximize its specific heat capacity," *International Journal of Heat and Mass Transfer,* vol. 70, pp. 174-184, 2014.

[204] M. Chieruzzi, A. Miliozzi, T. Crescenzi, L. Torre and J. M. Kenny, "A New Phase Change Material Based on Potassium Nitrate with Silica and Alumina Nanoparticles for Thermal Energy Storage," *Nanoscale Research Letters,* vol. 10, 2015.

[205] H. Tiznobaik and D. Shin, "Enhanced specific heat capacity of high-temperature molten salt-based nanofluids," *International Journal of Heat and Mass Transfer,* vol. 57, pp. 542-548, 2013.

[206] M. Schuller, Q. Shao and T. Lalk, "Experimental investigation of the specific heat of a nitrate-alumina nanofluid for solar thermal energy storage systems," *International Journal of Thermal Sciences,* vol. 91, pp. 142-145, 2015.

[207] H. Tiznobaik and D. Shin, "Experimental validation of enhanced heat capacity of ionic liquid-based nanomaterial," *Applied Phsyics Letters,* vol. 102, 2013.

[208] B. Dudda and D. Shin, "Effect of nanoparticle dispersion on specific heat capacity of a binary nitrate salt eutectic for concentrated solar power applications," *International Journal of Thermal Sciences,* vol. 69, pp. 37-42, 2013.

[209] M. Lasfargues, A. Bell and Y. Ding, "In situ production of titanium dioxide nanoparticles in molten salt phase for thermal energy storage and heat transfer fluid applications," *Journal of Nanoparticle Research,* vol. 18, 2016.

[210] M. Lasfargues, Q. Geng, H. Cao and Y. Ding, "Mechanical Dispersion of Nanoparticles and Its Effect on the Specific Heat Capacity of Impure Binary Nitrate Salt Mixtures," *Nanomaterials,* vol. 5, pp. 1136-1146, 2015.

[211] P. Andreu-Cabedo, R. Mondragon, L. Hernandez, R. Martinez-Cuenca, L. Cabedo and J. E. Julia, "Increment of specific heat capacity of solar salt with SiO2 nanoparticles," *Nanoscale Research Letters,* vol. 9, p. 582, 2014.

[212] A. Sadegh, J. Kourosh, J. Amin and A. Hossein, "A complete experimental investigation on the rheological behavior of silver nanofluid," *Heat Transfer Research,* pp. 1-16, 2016.

[213] R. S. Khedkar, N. Shrivastava, S. S. Sonwane and K. L. Wasewar, "Experimental investigations and theoretical determination of thermal conductivity and viscosity of TiO2–ethylene glycol nanofluid," *International Communications of Heat and Mass Transfer,* vol. 73, pp. 54-61, 2016.

[214] S. Aberoumand, A. Jafarimoghaddam, M. Moravej, H. Aberoumand and K. Javaherdeh, "Experimental study on the rheological behavior of silver-heat transfer oil nanofluid and suggesting two empirical based correlations for thermal conductivity and viscosity of oil based nanofluids," *Applied Thermal Engineering,* 2016.

[215] R. Agarwal, K. Verma, N. K. Agarwal, R. K. Duchaniya and R. Singh, "Synthesis, characterization,thermal conductivity and sensitivity of CuO nanofluids," *Applied Thermal Engineering,* vol. 102, pp. 1024-36, 2016.

[216] H. Li, L. Wang, Y. He, Y. Hu, K. Zhu and B. Jiang, "Experimental investigation of thermal conductivity and viscosity of ethylene glycol based ZnO nanofluids," *Applied Thermal Engineering,* vol. 88, pp. 363-8, 2015.

[217] X. Li, C. Zou, L. Zhou and A. Qi, "Experimental study on the thermo-physical properties of diathermic oil based SiC nanofluids for high temperature applications," *International of Journal of Heat and Mass Transfer,* vol. 97, pp. 631-7, 2016.

[218] E. M. Hemmat, M. Afrand, A. Karimipour, W.-M. Yan and N. Sina, "An experimental study on thermal conductivity of MgO nanoparticles suspended in a binary mixture of water and ethylene glycol," *International Communications of Heat and Mass Transfer,* vol. 67, pp. 173-5, 2015.

[219] A. Karimi, M. A. A. Sadatlu, B. Saberi, H. Shariatmadar and M. Ashjaee, "Experimental investigation on thermal conductivity of water based nickel ferrite nanofluids," *Advanced Powder Technology,* vol. 26, pp. 1529-36, 2015.

[220] T. Parametthanuwat, N. Bhuwakietkumjohn, S. Rittidech and Y. Ding, "Experimental investigation on thermal properties of silver nanofluids," *International Journal of Heat and Fluid Flow,* vol. 56, pp. 80-90, 2015.

[221] N. A. Usri, W. H. Azmi, R. Mamat, K. A. Hamid and G. Najafi, "Thermal conductivity enhancement of Al2O3 nanofluid in ethylene glycol and water mixture," *Energy Procedia,* vol. 79, pp. 397-402, 2015.

[222] E. M. Hemmat, W.-M. Yan, M. Akbari, A. Karimipour and M. Hassani, "Experimental study on thermal conductivity of DWCNT-ZnO/water-EG nanofluids," *International Communications of Heat and Mass Transfer,* vol. 68, pp. 248-51, 2015.

[223] B. Buonomo, O. Manca, L. Marinelli and S. Nardini, "Effect of temperature and sonication time on nanofluid thermal conductivity measurements by nano-flash method," *Applied Thermal Engineering,* vol. 91, pp. 181-90, 2015.

[224] S. Cingarapu, D. Singh, E. V. Timifeeva and M. R. Moravek, "Nanofluids with encapsulated tin nanoparticles for advanced heat transfer and thermal energy storage," *International Journal of Energy Research,* vol. 2014, pp. 51-9, 2014.

[225] S. A. Angayarkanni and J. Philip, "Effect of Nanoparticle Aggregation on Thermal and Electrical Conductivites of Nanofluids," *Journal of Nanofluids,* vol. 3, pp. 17-25, 2014.

[226] L. S. Sundar, M. H. Farooky, S. N. Sarada and M. K. Singh, "Experimental thermal conductivity of ethylene glycol and water mixture based low volume

concentration of Al2O3 and CuO nanofluids," *International Communications of Heat and Mass Transfer,* vol. 41, pp. 41-46, 2013.

[227] C. Sun, B. Bai, W.-Q. Lu and J. Liu, "Shear-rate dependent effective thermal conductivity of H2O+SiO2 nanofluids," *Physics of Fluids,* vol. 25, 2013.

[228] F. M. Pakdaman, M. A. Akhavan-Behabadi and P. Razi, "An experimental investigation on thermo-physical properties and overall performance of MWCNT/heat transfer oil nanofluid flow inside vertical helically coiled tubes," *Experimental Thermal and Fluid Science,* vol. 40, pp. 103-111, 2012.

[229] R. S. Khedkar, S. S. Sonawane and K. L. Wasewar, "Influence of CuO nanoparticles in enhancing the thermal conductivity of water and monoethylene glycol based nanofluids," *International Communications of Heat and Mass Transfer,* vol. 39, pp. 665-9, 2012.

[230] S. Harish, K. Ishikawa, E. Einarsson, S. Aikawa, S. Chiashi and J. Shiomi, "Enhanced Thermal Conductivity of ethylene glycol with single-walled carbon nanotube inclusions," *International Journal of Heat and Mass Transfer,* vol. 55, 2012.

[231] A. Bonk, S. Sau, N. Urnaga, M. Hernaiz and T. Bauer, "Advanced heat transfer fluids for direct molten salt line-focusing CSP plants," *Progress in Energy and Combustion Science,* vol. 67, pp. 69-87, 2018.

[232] V. Gnielinski, "New Equations for heat and mass transfer in turbulent pipe and channel flow," *International journal of Chemical Engineering,* vol. 16, pp. 359-367, 1976.

[233] E. N. Sider and G. E. Tate, "Heat Transfer and pressure drop of liquids in tubes," *Industrial and Engineering Chemistry,* vol. 28, pp. 1429-1435, 1936.

[234] J. P. Holman, "Heat Transfer," New York, 2002, pp. 261-270.

[235] B. S. Petukhov, "Heat transfer and friction in turbulent pipe flow with variable physical properties," *Advances in Heat Transfer,* vol. 6, pp. 503-564, 1970.

[236] J. Lu, S. He, J. Ding, J. Yang and J. Liang, "Convective heat transfer of high temperature molten salt in a vertical annular duct with cooled wall," *Applied Thermal Engineering,* vol. 73, pp. 1519-1524, 2014.

[237] P. Xiao, L. Guo and X. Zhang, "Investigations on heat transfer characteristic of molten salt flow in a helical annular duct," *Applied Thermal Engineering,* vol. 88, pp. 22-32, 2015.

[238] T. Satoh, K. Yuki, S.-y. Chiba, H. Hashizume and A. Sagara, "Heat Transfer performance for High prnadtl and high temperature Molten Slat Flow in Sphere-Packed Pipes," *Fusion Science and Technology,* vol. 52, no. 3, pp. 618-624, 2017.

APPENDIX A

(Forced convection heat transfer plots for various heater power are presented in this section.)

320W Heat Input

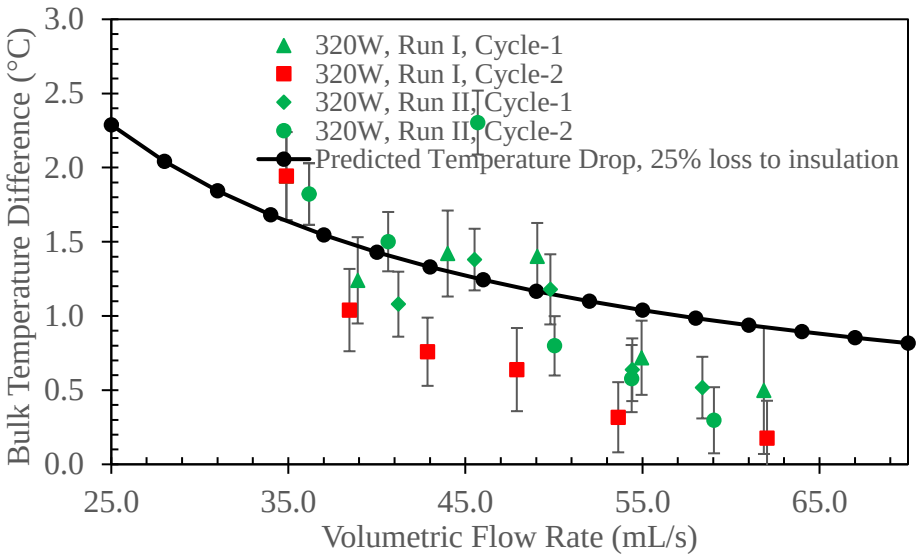

Figure 95. Fluid bulk temperature drop across the test section as a function of flow rate for 320W heat input

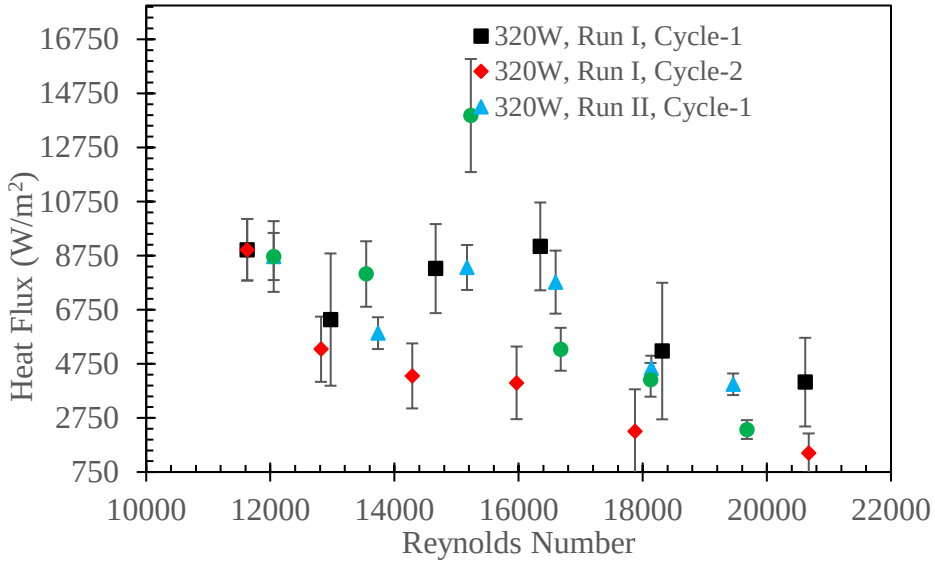

Figure 96. Applied heat flux computed from the energy balance across the test section for heater input setting of 320W

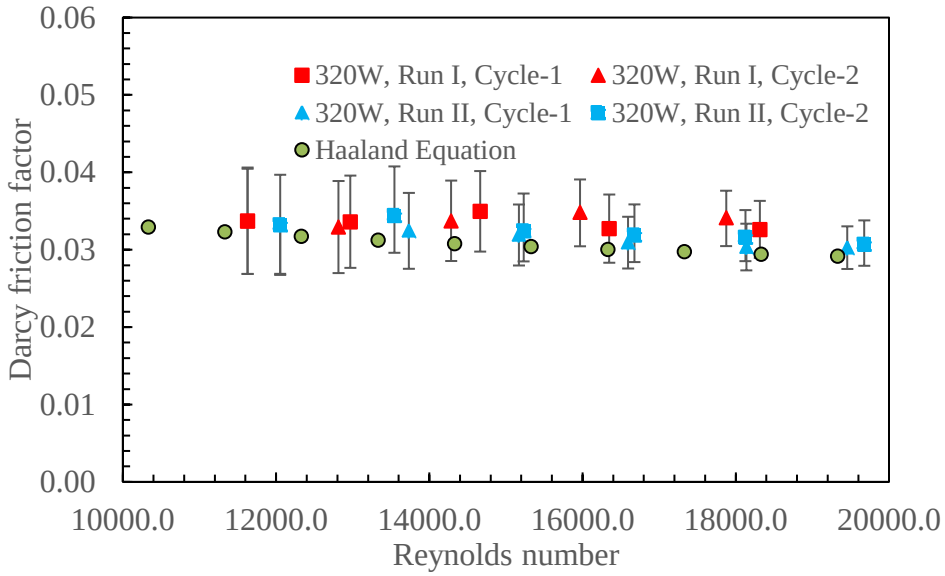

Figure 97. Experimental friction factor computed from measured pressure drop across the test section plotted as a function of Reynolds number compared with theoretical friction factor computed from Haaland equation for 320W heat transfer test

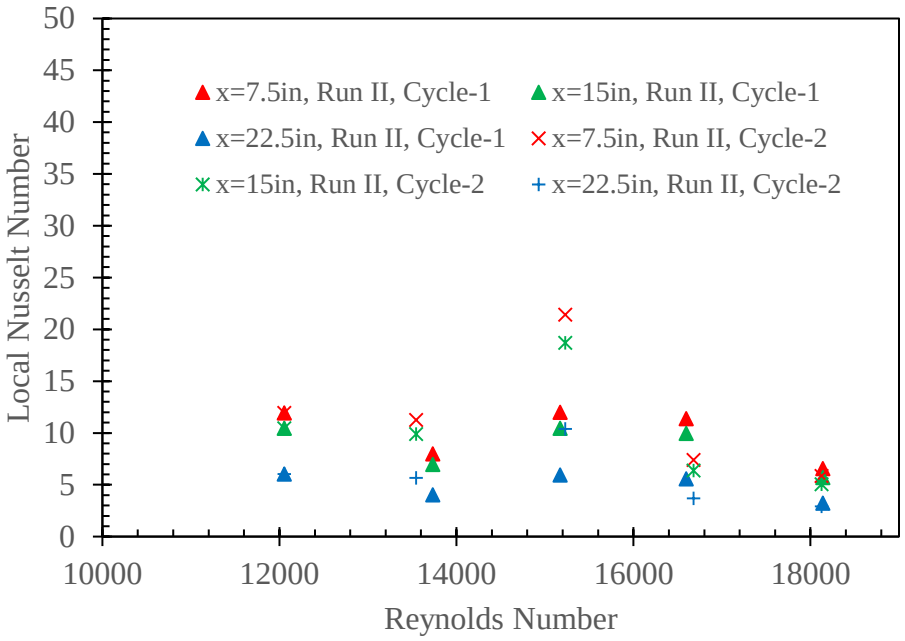

Figure 98. Local Nusselt number (axial distance) as a function of Reynolds number for a circular test section for a heater input of 320W

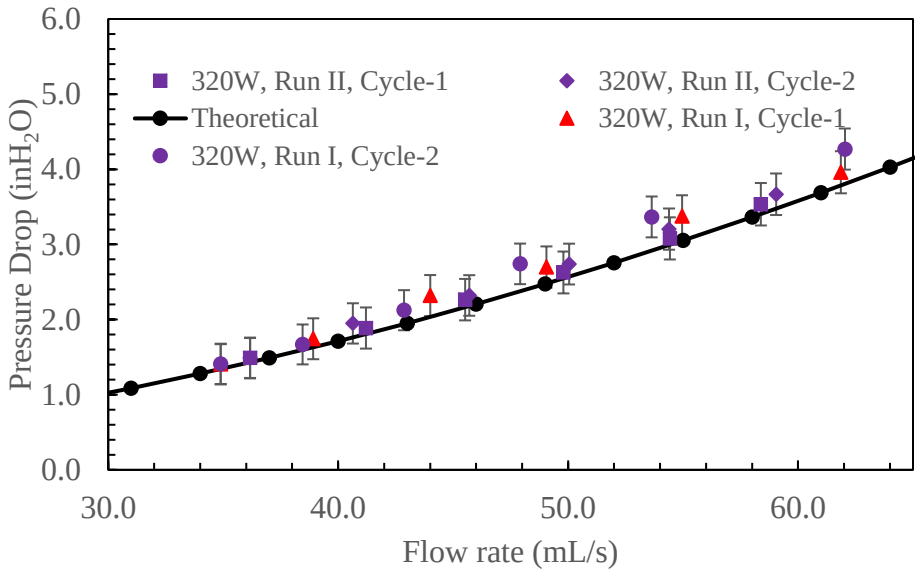

Figure 99. Experimental pressure drop across the test section plotted as a function of volumetric flow rate compared with theoretical pressure drop for heat input of 320W to the stainless steel circular test section

405W Heat Input

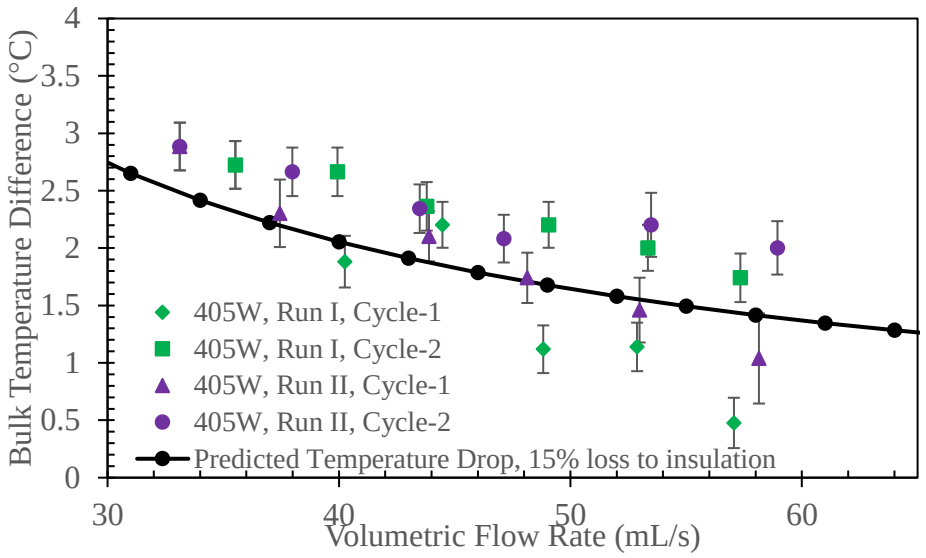

Figure 100. Fluid bulk temperature drop across the test section as a function of flow rate for 405W heat input

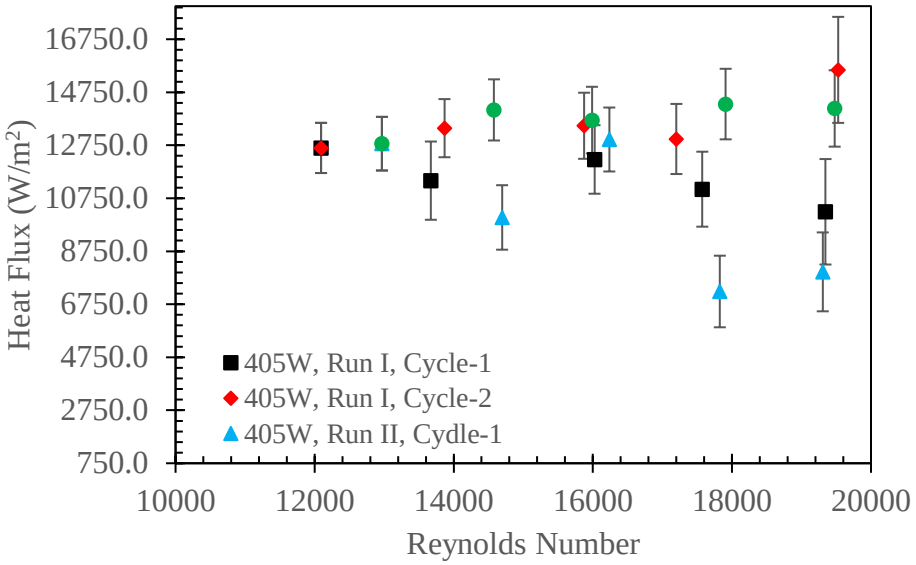

Figure 101. Applied heat flux computed from the energy balance across the test section for heater input setting of 405W

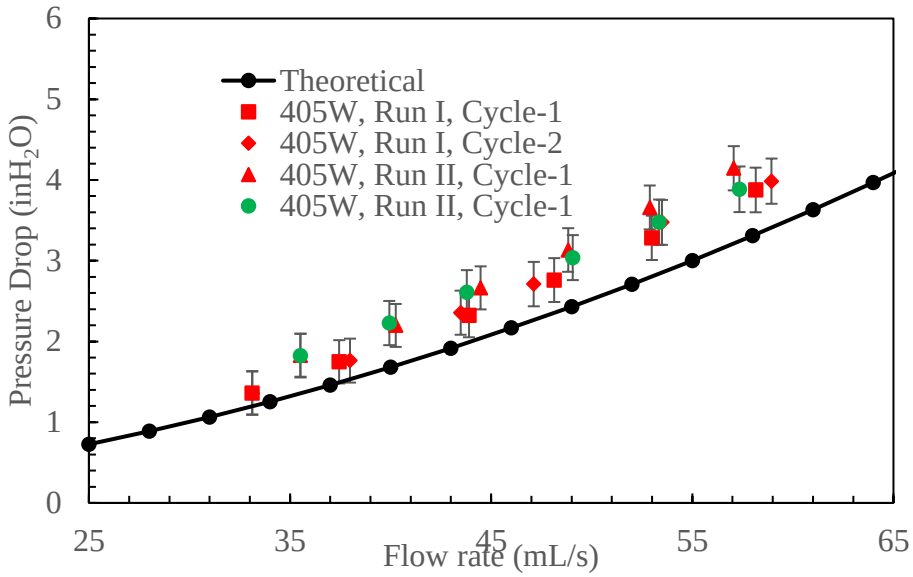

Figure 102. Experimental pressure drop across the test section plotted as a function of volumetric flow rate compared with theoretical pressure drop for heat input of 405W to the stainless steel circular test section

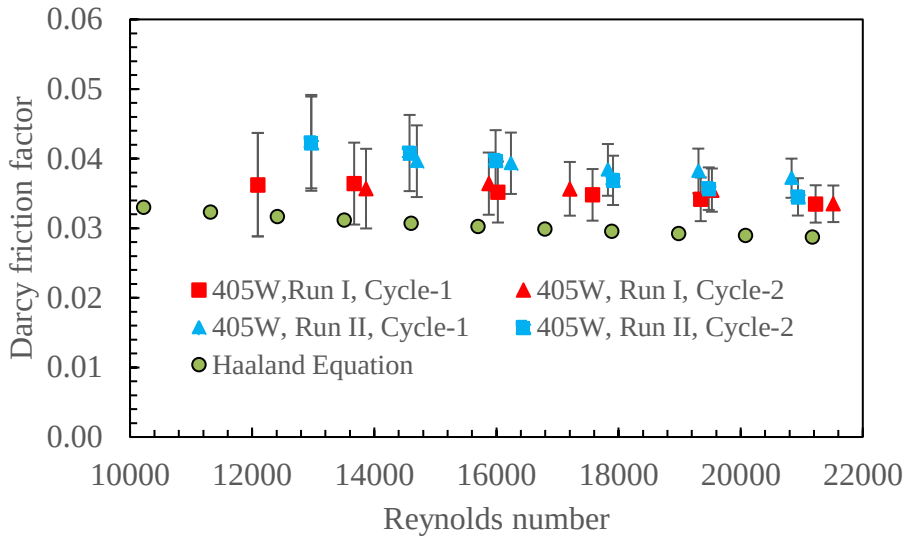

Figure 103. Experimental friction factor computed from measured pressure drop across the test section plotted as a function of Reynolds number compared with theoretical friction factor computed from Haaland equation for 405W heat transfer test

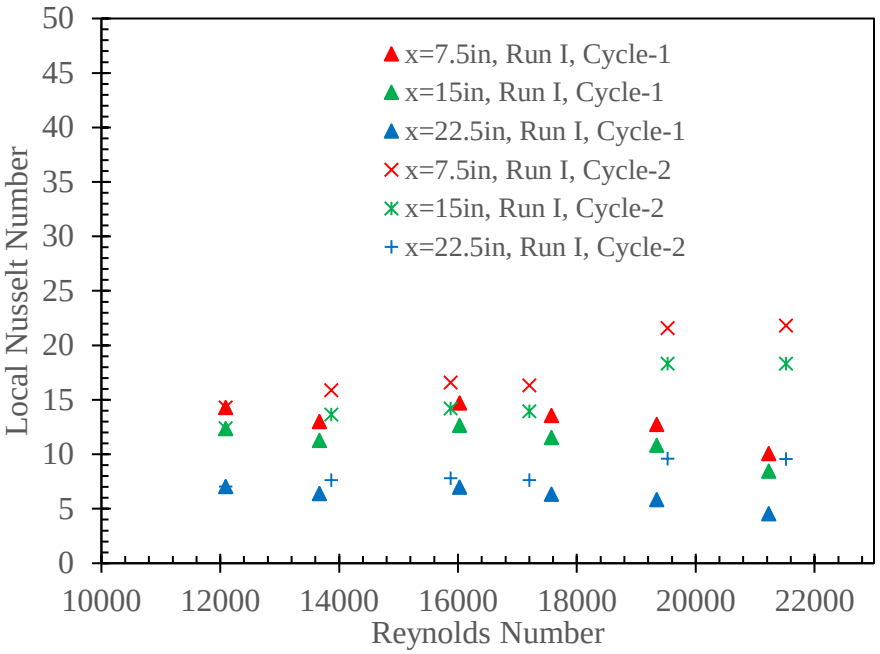

Figure 104. Local Nusselt number (axial distance) as a function of Reynolds number for a circular test section for a heater input of 405W

475W Heat Input

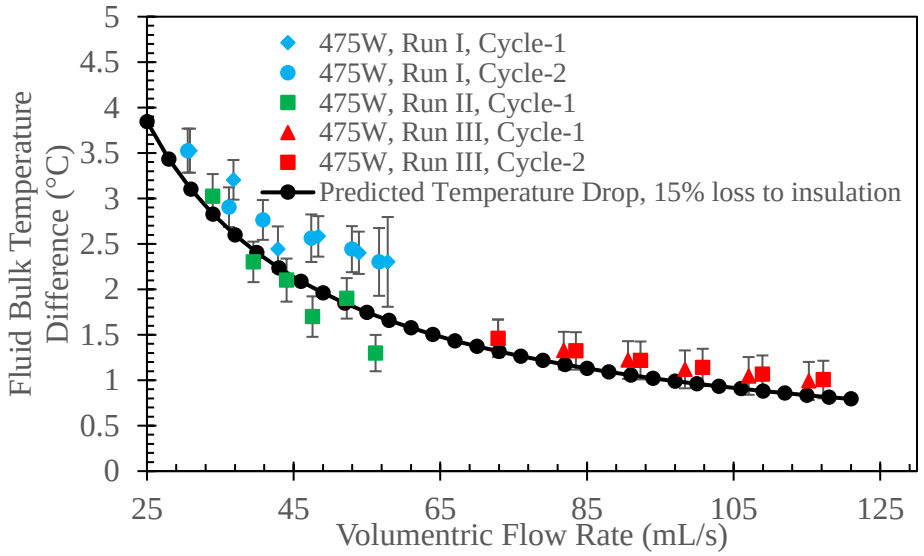

Figure 105. Fluid bulk temperature drop across the test section as a function of flow rate for 475W heat input

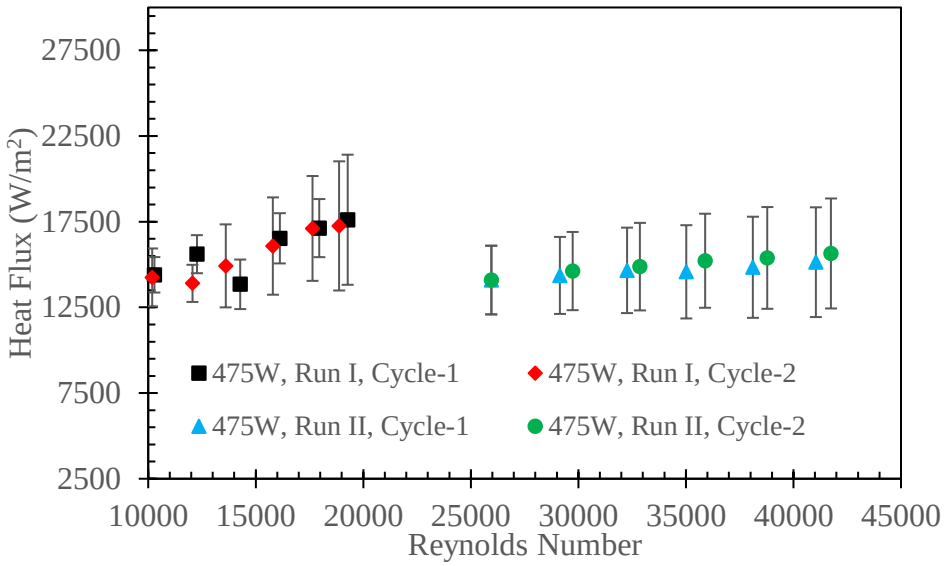

Figure 106. Applied heat flux computed from the energy balance across the test section for heater input setting of 405W

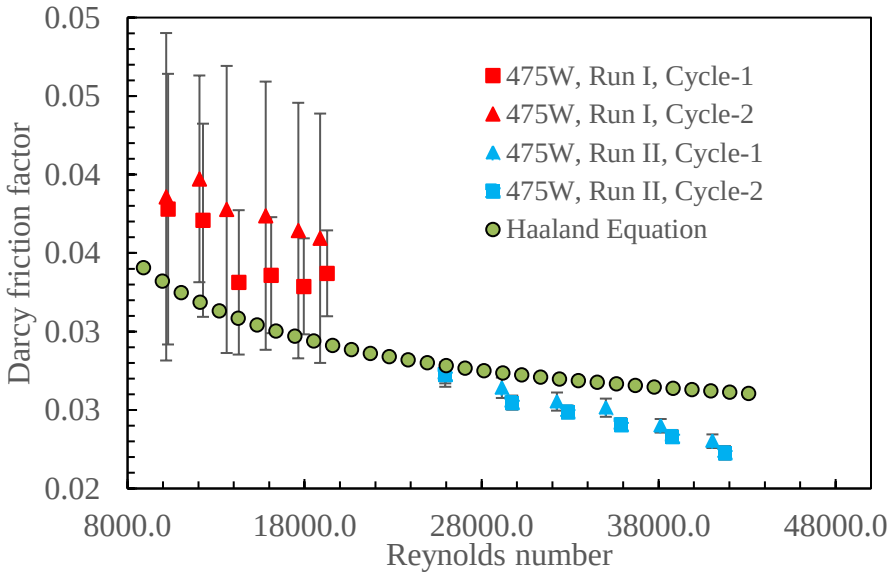

Figure 107. Experimental friction factor computed from measured pressure drop across the test section plotted as a function of Reynolds number compared with theoretical friction factor computed from Haaland equation for 475W heat transfer test

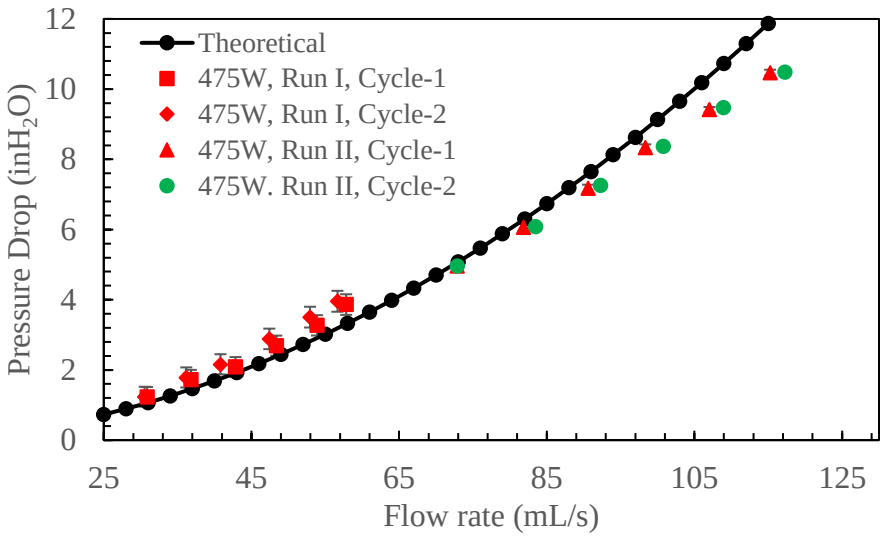

Figure 108. Experimental pressure drop across the test section plotted as a function of volumetric flow rate compared with theoretical pressure drop for heat input of 475W to the stainless steel circular test section

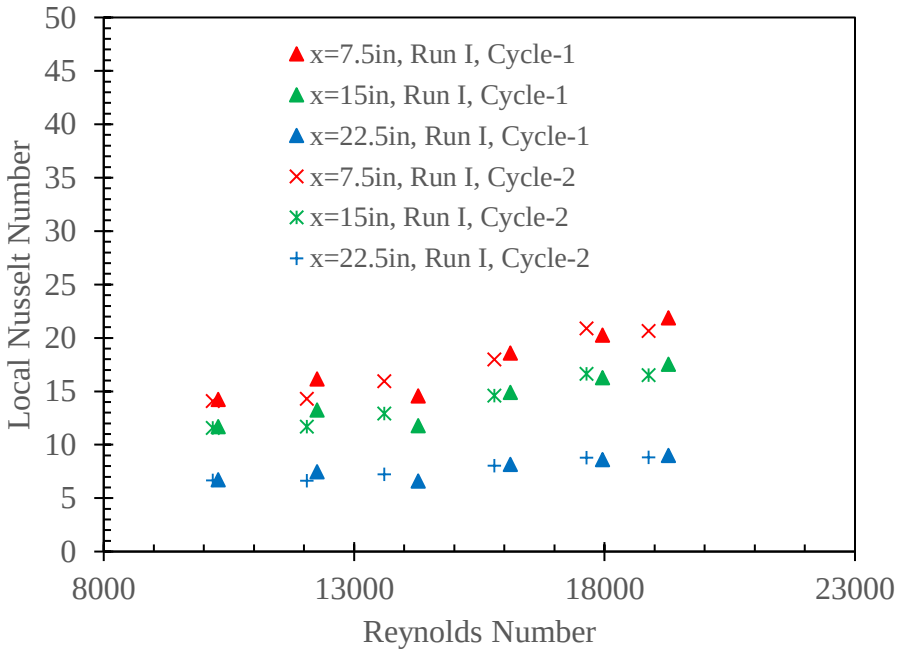

Figure 109. Local Nusselt number (axial distance) as a function of Reynolds number for a circular test section for a heater input of 475W

APPENDIX B

The experimental results for subcooled flow boiling heat transfer results are presented in this section

B1: Surface Wall Temperature

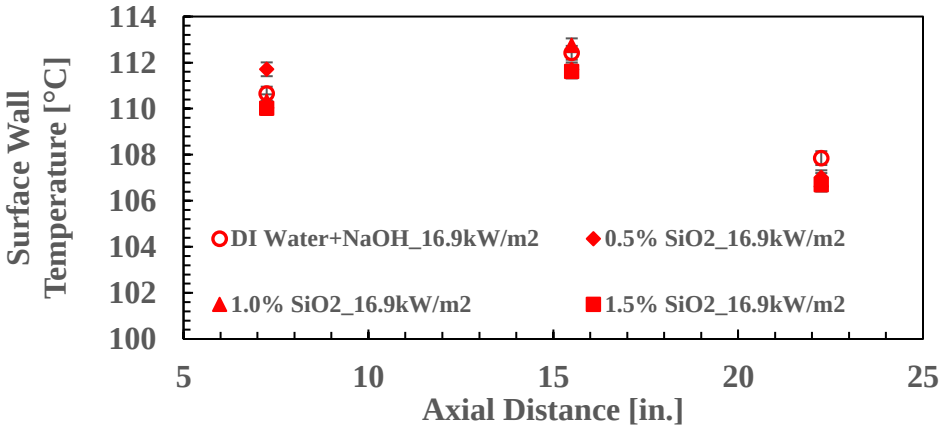

Figure 110. Surface wall temperature as a function of axial distance for tested working fluids at a wall heat flux of 16.9 [kW/m^2]

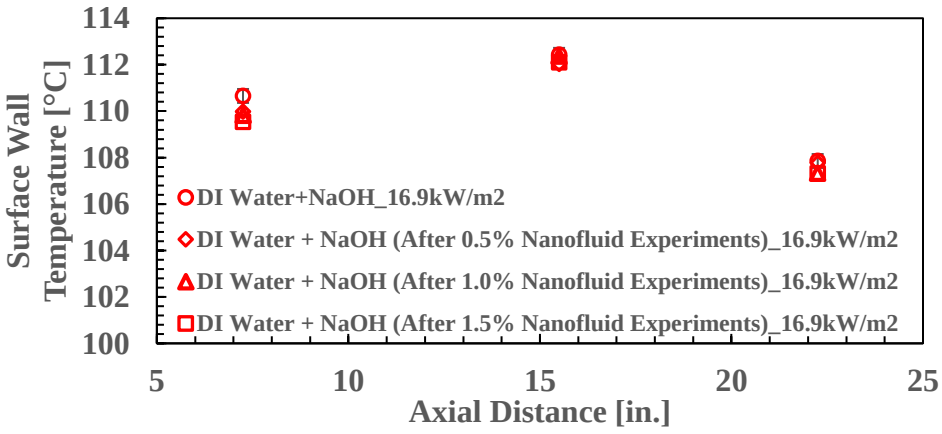

Figure 111. Surface wall temperature as a function of axial distance for tested DI Water after performing nanofluid experiments at a wall heat flux of 16.9 [kW/m^2]

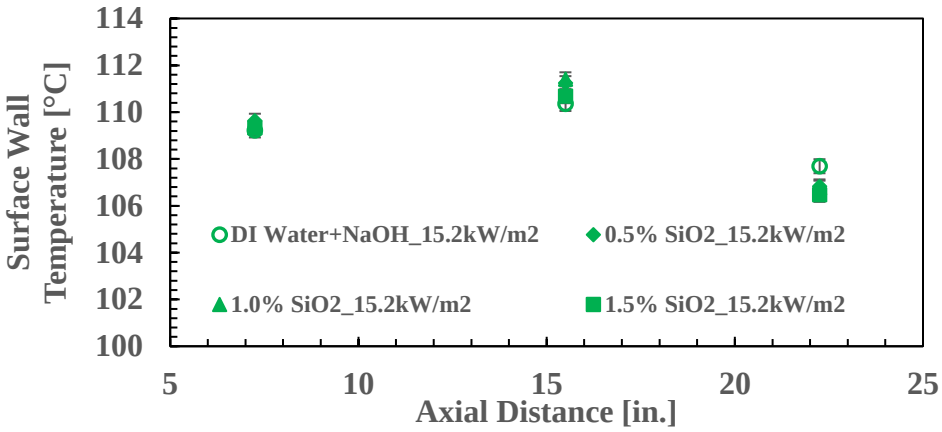

Figure 112. Surface wall temperature as a function of axial distance for tested working fluids at a wall heat flux of 15.2 [kW/m^2]

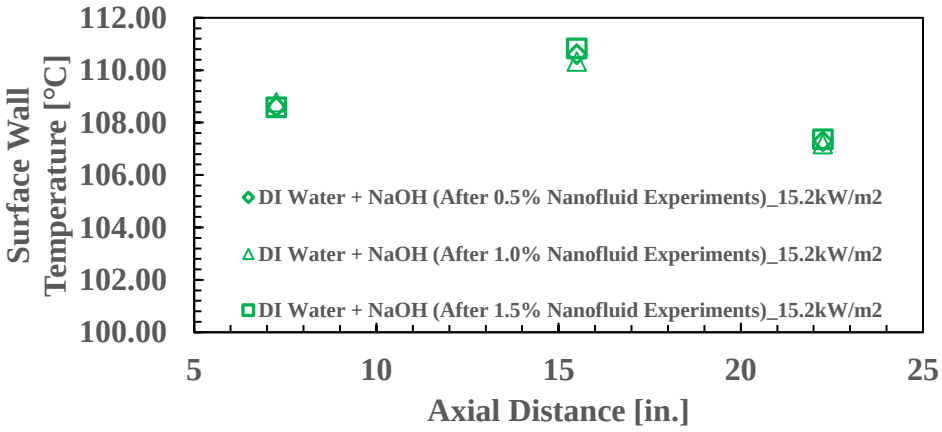

Figure 113. Surface wall temperature as a function of axial distance for tested working fluids at a wall heat flux of 15.2 [kW/m^2]

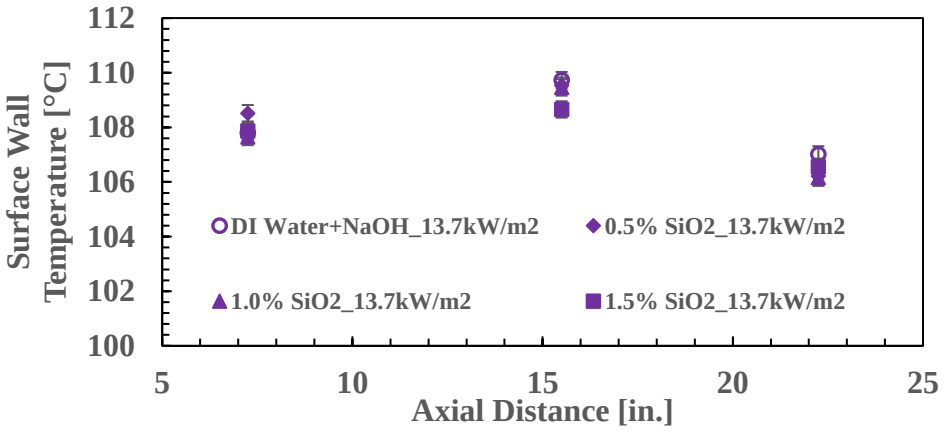

Figure 114. Surface wall temperature as a function of axial distance for tested working fluids at a wall heat flux of 13.7 [kW/m^2]

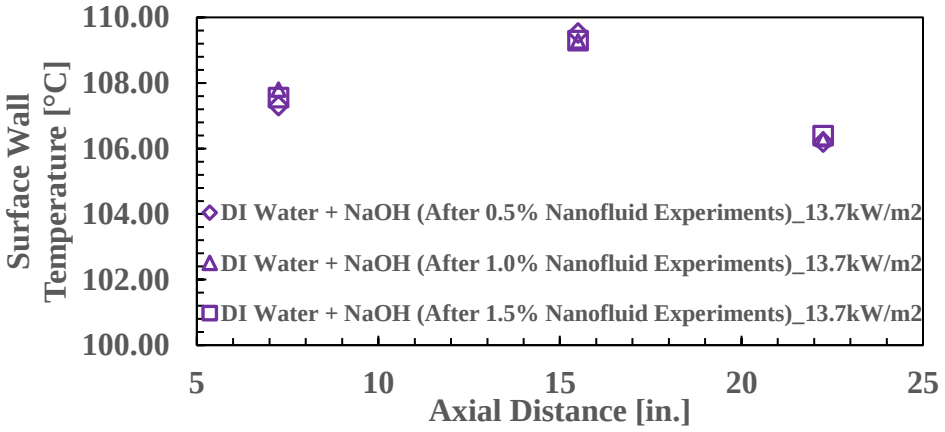

Figure 115. Surface wall temperature as a function of axial distance for tested working fluids at a wall heat flux of 13.7 [kW/m^2]

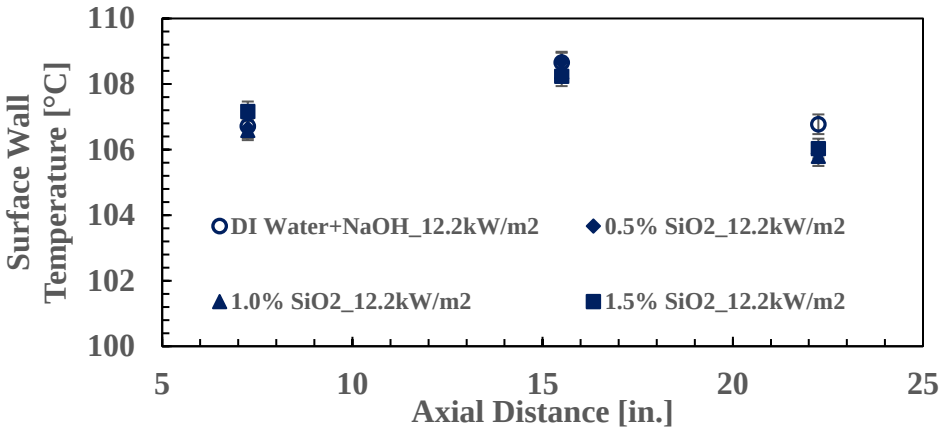

Figure 116. Surface wall temperature as a function of axial distance for tested working fluids at a wall heat flux of 12.2 [kW/m^2]

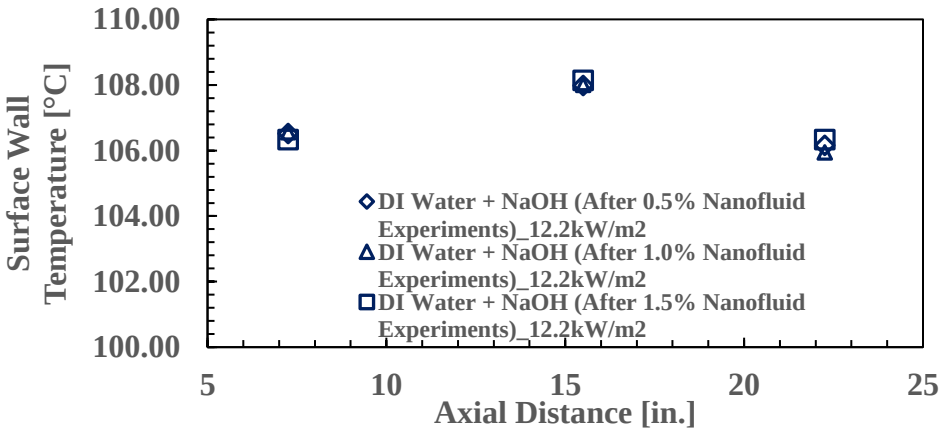

Figure 117. Surface wall temperature as a function of axial distance for tested DI Water after performing nanofluid experiments at a wall heat flux of 12.2 [kW/m^2]

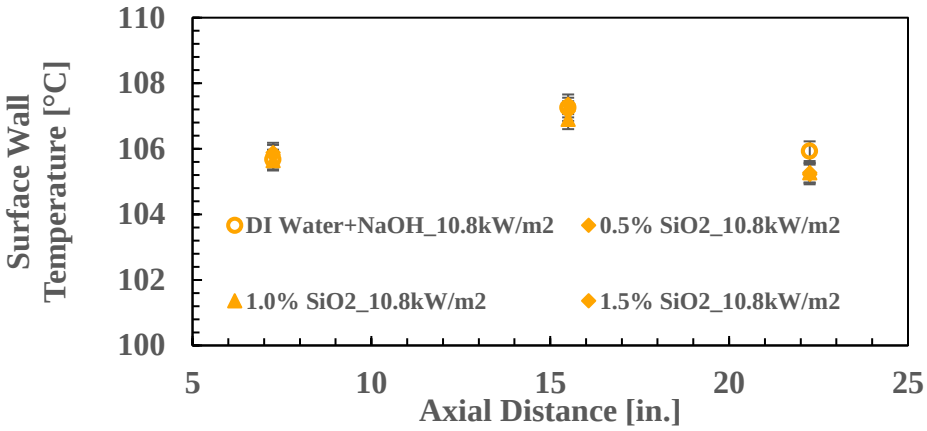

Figure 118. Surface wall temperature as a function of axial distance for tested working fluids at a wall heat flux of 10.8 [kW/m^2]

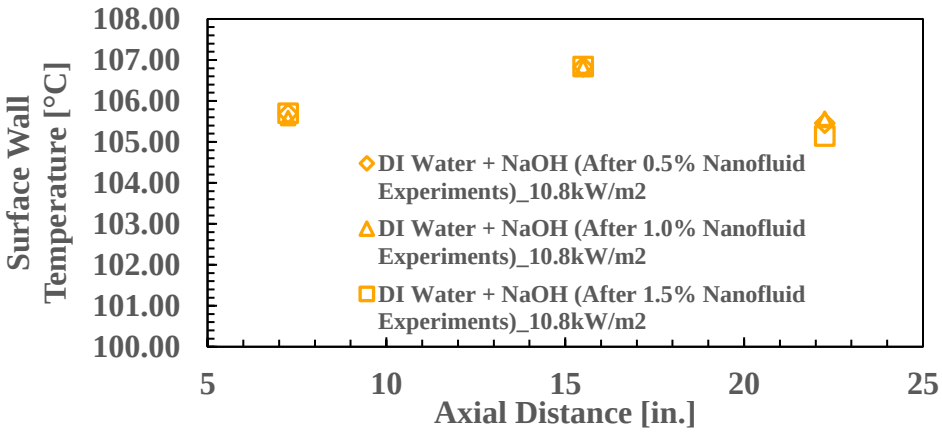

Figure 119. Surface wall temperature as a function of axial distance for tested DI Water after performing nanofluid experiments at a wall heat flux of 10.8 [kW/m^2]

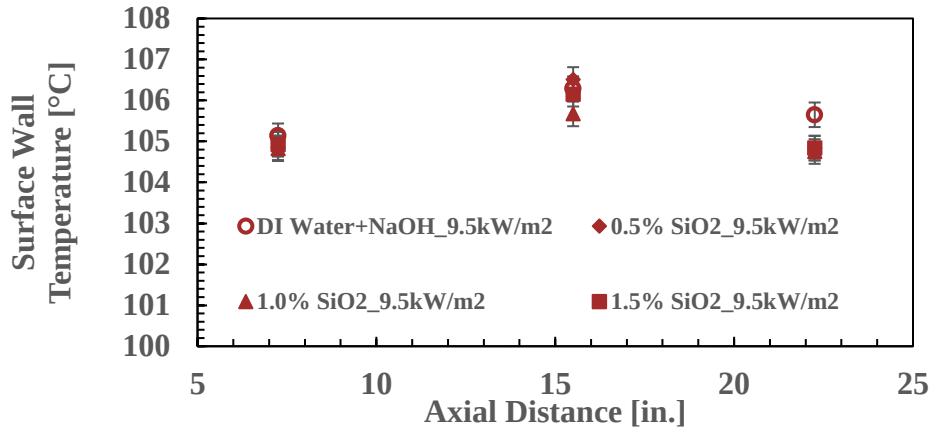

Figure 120Surface wall temperature as a function of axial distance for tested working fluids at a wall heat flux of 9.5 [kW/m^2]

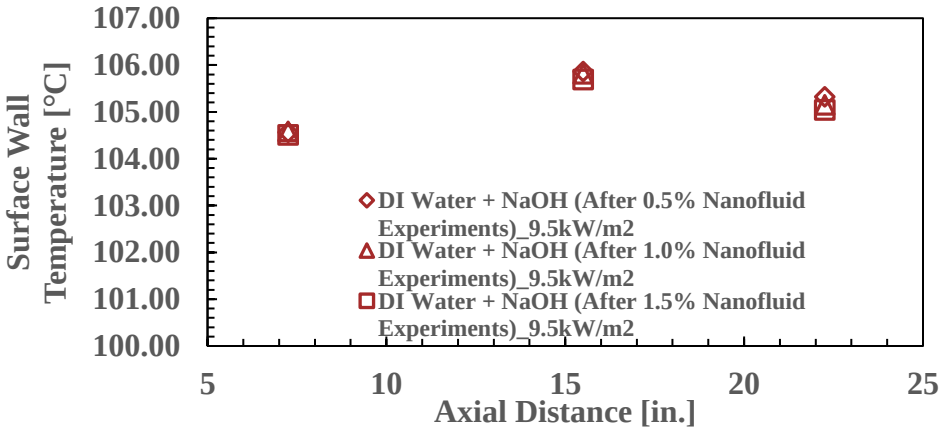

Figure 121Surface wall temperature as a function of axial distance for tested DI Water after performing nanofluid experiments at a wall heat flux of 9.5 [kW/m2]

Table 34. Measured surface wall temperature at different axial distances from the inlet of the test section for DI Water experiments for various mass fraction of SiO_2 nanoparticles

Axial Distance [in.]	16.9kW/m^2				15.2kW/m^2				13.7kW/m^2			
	DIW+ NaOH	0.5% SiO_2	1.0% SiO_2	1.5% SiO_2	DIW+ NaOH	0.5% SiO_2	1.0% SiO_2	1.5% SiO_2	DIW+ NaOH	0.5% SiO_2	1.0% SiO_2	1.5% SiO_2
7.25	110.7	111.7	110.3	110.0	109.2	109.6	109.3	109.3	107.8	108.5	107.6	107.9
15.5	112.4	111.7	112.8	111.6	110.3	111.2	111.4	110.7	109.7	109.5	109.5	108.7
22.25	107.9	107.0	106.9	106.7	107.7	106.8	106.8	106.5	107.0	106.2	106.2	106.6

Axial Distance [in.]	12.2kW/m^2				10.8kW/m^2				9.5kW/m^2			
	DIW+ NaOH	0.5% SiO_2	1.0% SiO_2	1.5% SiO_2	DIW+ NaOH	0.5% SiO_2	1.0% SiO_2	1.5% SiO_2	DIW+ NaOH	0.5% SiO_2	1.0% SiO_2	1.5% SiO_2
7.25	106.7	106.6	106.6	107.2	105.7	105.8	105.6	105.9	105.1	104.8	104.8	104.9
15.5	108.7	108.7	108.4	108.2	107.3	107.2	106.9	107.4	106.3	106.5	105.7	106.2
22.25	106.8	105.9	105.8	106.0	105.9	105.2	105.3	105.3	105.7	104.8	104.8	104.8

Table 35. Measured surface wall temperature at different axial distances from the inlet of the test seciton for DI Water experiments after performing nanofluid experiments

Axial Distance [in.]	16.9kW/m^2			15.2kW/m^2			13.7kW/m^2		
	DIW + NaOH (After 0.5% SiO_2)	DIW + NaOH (After 1.0% SiO_2)	DIW + NaOH (After 1.5% SiO_2)	DIW + NaOH (After 0.5% SiO_2)	DIW + NaOH (After 1.0% SiO_2)	DIW + NaOH (After 1.5% SiO_2)	DIW + NaOH (After 0.5% SiO_2)	DIW + NaOH (After 1.0% SiO_2)	DIW + NaOH (After 1.5% SiO_2)
7.25	109.97	109.82	109.54	108.60	108.78	108.58	107.30	107.79	107.54
15.5	112.04	112.37	112.09	110.61	110.33	110.83	109.52	109.26	109.29
22.25	107.78	107.33	107.32	107.28	107.17	107.36	106.19	106.28	106.39

Axial Distance [in.]	12.2kW/m^2			10.8kW/m^2			9.5kW/m^2		
	DIW + NaOH (After 0.5% SiO_2)	DIW + NaOH (After 1.0% SiO_2)	DIW + NaOH (After 1.5% SiO_2)	DIW + NaOH (After 0.5% SiO_2)	DIW + NaOH (After 1.0% SiO_2)	DIW + NaOH (After 1.5% SiO_2)	DIW + NaOH (After 0.5% SiO_2)	DIW + NaOH (After 1.0% SiO_2)	DIW + NaOH (After 1.5% SiO_2)
7.25	106.51	106.55	106.33	105.68	105.58	105.70	104.56	104.58	104.50
15.5	107.97	108.00	108.14	106.83	106.83	106.84	105.86	105.81	105.68
22.25	106.15	105.94	106.33	105.45	105.56	105.14	105.32	105.15	105.04

Table 36. Measured convective heat transfer coefficient [W/(m^{2}K)] at different axial distances from the inlet of the test section for DI Water and various mass concentration of SiO_2 nanoparticles

Axial Distance [in.]	16.9kW/m^2				15.2kW/m^2				13.7kW/m^2			
	DIW+ NaOH	0.5% SiO_2	1.0% SiO_2	1.5% SiO_2	DIW+ NaOH	0.5% SiO_2	1.0% SiO_2	1.5% SiO_2	DIW+ NaOH	0.5% SiO_2	1.0% SiO_2	1.5% SiO_2
7.25	1529.6	1396.5	1577.2	1622.0	1556.7	1493.5	1537.1	1538.2	1600.8	1476.3	1628.8	1586.7
15.5	1585.1	1699.6	1538.0	1715.6	1697.9	1545.2	1519.9	1637.3	1566.7	1603.8	1616.3	1785.7
22.25	2154.0	2410.4	2450.7	2527.4	1985.4	2238.1	2254.3	2364.8	1954.8	2205.6	2225.6	2093.1
Axial Distance [in.]	**12.2kW/m^2**				**10.8kW/m^2**				**9.5kW/m^2**			
	DIW+ NaOH	0.5% SiO_2	1.0% SiO_2	1.5% SiO_2	DIW+ NaOH	0.5% SiO_2	1.0% SiO_2	1.5% SiO_2	DIW+ NaOH	0.5% SiO_2	1.0% SiO_2	1.5% SiO_2
7.25	1598.3	1613.0	1625.4	1509.4	1601.5	1567.9	1610.0	1553.4	1493.7	1565.3	1571.5	1544.0
15.5	1522.8	1517.0	1578.9	1606.2	1554.7	1579.0	1638.9	1532.7	1508.3	1456.7	1671.8	1541.6
22.25	1804.7	2077.5	2108.5	2026.7	1827.1	2076.9	2056.4	2059.4	1684.4	1972.2	2005.1	1967.5

Table 37 Measured convective heat transfer coefficient [W/(m^{2}K)] at different axial distances from the inlet of the test section for DI Water after performing nanofluid experiments

Axial Distance [in.]	16.9kW/m^2			15.2kW/m^2			13.7kW/m^2		
	DIW + NaOH (After 0.5% SiO_2)	DIW + NaOH (After 1.0% SiO_2)	DIW + NaOH (After 1.5% SiO_2)	DIW + NaOH (After 0.5% SiO_2)	DIW + NaOH (After 1.0% SiO_2)	DIW + NaOH (After 1.5% SiO_2)	DIW + NaOH (After 0.5% SiO_2)	DIW + NaOH (After 1.0% SiO_2)	DIW + NaOH (After 1.5% SiO_2)
7.25	1630.0	1654.0	1701.8	1661.5	1630.2	1665.5	1698.5	1602.0	1649.0
15.5	1644.8	1593.6	1635.8	1650.1	1702.0	1611.3	1604.4	1654.5	1649.2
22.25	2175.6	2311.3	2312.6	2097.3	2131.6	2075.5	2212.1	2184.0	2146.7

Axial Distance [in.]	12.2kW/m^2			10.8kW/m^2			9.5kW/m^2		
	DIW + NaOH (After 0.5% SiO_2)	DIW + NaOH (After 1.0% SiO_2)	DIW + NaOH (After 1.5% SiO_2)	DIW + NaOH (After 0.5% SiO_2)	DIW + NaOH (After 1.0% SiO_2)	DIW + NaOH (After 1.5% SiO_2)	DIW + NaOH (After 0.5% SiO_2)	DIW + NaOH (After 1.0% SiO_2)	DIW + NaOH (After 1.5% SiO_2)
7.25	1641.8	1633.9	1684.5	1598.8	1624.1	1595.7	1642.9	1636.0	1658.6
15.5	1663.8	1657.5	1627.8	1657.0	1656.0	1654.7	1617.8	1632.4	1668.1
22.25	1989.4	2057.5	1937.2	1991.5	1947.7	2107.6	1788.9	1852.6	1890.9

APPENDIX C

This section contains the system level analysis performed for estimating the cost savings that could result from employing solar salt nanofluid in an actual Concentrated Solar Power (CSP) plant. National Renewable Energy laboratory's (NREL) open source System Advisor Model (SAM) was employed for estimating the cost benefits from deploying solar salt-based nanofluid

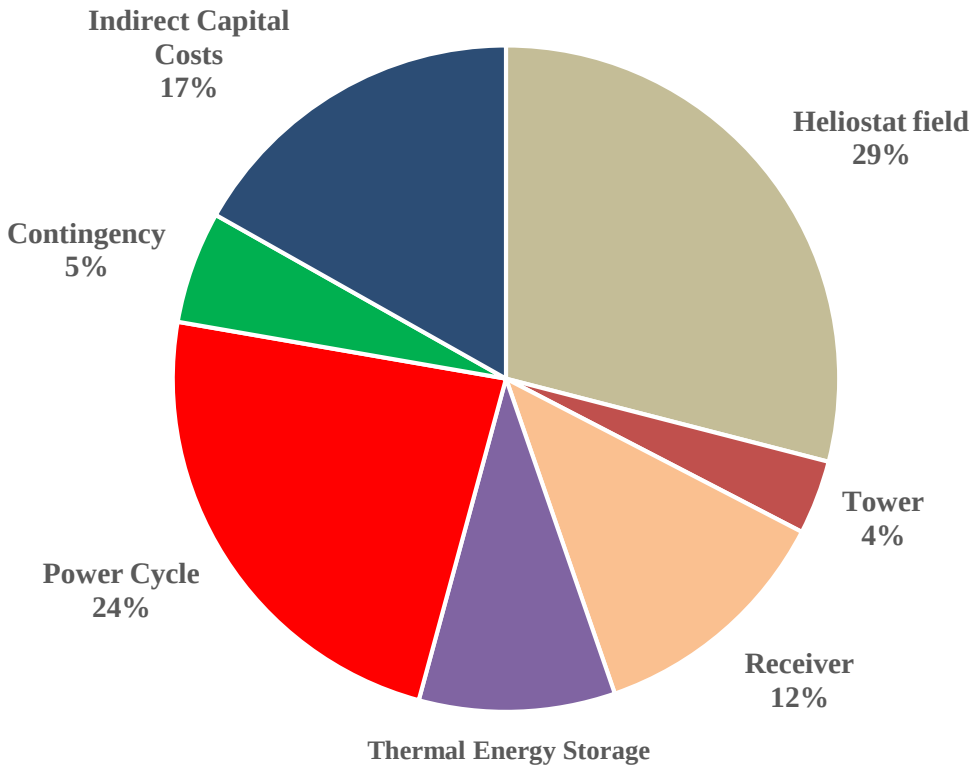

Figure C122. The cost distribution of various components of a Concentrated Solar Power (CSP) plant

Table C1. The design parameters employed for the Concentrated Solar Power (CSP) plant in SAM analysis

System	Variable	Default Value
Climate	Location	CA Dagget
Heliostat Field	Heliostat width	12.2 m
	Heliostat height	12.2 m
	Heliostat distance to tower height ratio	9.5
Tower and Receiver	Receiver height	20.41 m
	Receiver diameter	17.67 m
	Number of panels	20
	Required HTF outlet temperature	574 °C
	Tower height	203 m
Power Cycle	Design turbine gross output	115MW
	Estimated gross to net conversion	0.87
	Designed HTF inlet temperature	574 °C
	Condenser type	Air cooled
	Ambient temperature at design	43 °C
Thermal Storage	Full load hours of TES	10 hours
	Initial hot HTF temperature	574 °C
Parasitic	Piping loss coefficient	10,200 Wt./m

The thermo-physical properties of solar salt nanofluid measured in this study i.e., specific heat capacity and thermal conductivity are directly fed to the SAM model. Density and Viscosity are estimated from available literature models. Table C2 lists the data input for thermo-physical properties for SAM model. Table C3 lists the simulation results indicating that by employing solar salt nanofluid with 1 % mass fraction of alumina nanoparticle can result in about 25% reduction of material for same thermal energy storage.

Table C2. Thermo-physical properties used for Solar Salt nanofluid at 1.0% mass fraction of Alumina nanoparticles used for data input to the SAM model

T	Specific Heat Capacity	Density	Viscosity	Kinematic Viscosity	Thermal Conductivity	Enthalpy
[°C]	[kJ/kg-K]	[kg/m^3]	[Pa-s]	[m^2-s]	[W/m-K]	[J/kg]
260	1.488	1925	0.004343	2.26E-06	0.4924	380994
277.9	1.491	1913	0.003818	2E-06	0.4958	407643
295.8	1.494	1902	0.003361	1.77E-06	0.4992	434348
313.7	1.497	1890	0.002967	1.57E-06	0.5026	461109
331.6	1.5	1879	0.002629	1.4E-06	0.506	487924
349.5	1.503	1868	0.002344	1.26E-06	0.5094	514794
367.4	1.506	1856	0.002106	1.13E-06	0.5128	541719
385.3	1.509	1845	0.00191	1.04E-06	0.5162	568700
403.2	1.512	1834	0.001751	9.55E-07	0.5196	595735
421.1	1.515	1822	0.001624	8.91E-07	0.523	622825
438.9	1.518	1811	0.001523	8.41E-07	0.5264	649971
456.8	1.522	1799	0.001445	8.03E-07	0.5298	677172
474.7	1.525	1788	0.001383	7.73E-07	0.5332	704428
492.6	1.528	1777	0.001332	7.50E-07	0.5366	731738
510.5	1.531	1765	0.001289	7.30E-07	0.54	759104
528.4	1.534	1754	0.001247	7.11E-07	0.5434	786525
546.3	1.537	1743	0.001201	6.89E-07	0.5468	814001
564.2	1.54	1731	0.001147	6.62E-07	0.5502	841532
582.1	1.543	1720	0.001078	6.27E-07	0.5536	869119

Table C3. Summary of simulation results from SAM model for Thermal Energy Storage (TES) system for 10-hour storage for Solar Salt and Solar Salt nanofluid with 1.0% mass fraction of alumina nanoparticles

Thermal Energy Storage Hours	10	10
Total HTF Volume	9679	12986
Medium	Solar Salt Alumina NF	Solar Salt
Tank Diameter	25.5	29.5
Tank Height	20	20

APPENDIX D

This section contains the copy of EES code employed for predicting the heat transfer coefficient for subcooled partial flow boiling

```
"q_w= 13000 [W/m^2]"
"Temperature and Pressure"
P=1.01325 [bar]
P_int=P*100 [KPa]
T_int =t_sat(Water,P=P_int)
T_sat = T_int + 273.15 [K]
"Saturated Properties: Density, Viscosity, Thermal conductivity, and Enthalpy of vaporization"
sigma = surfacetension(Water,T=T_int)
DELTAh_vap=enthalpy_vaporization(Water,T=T_int)
 k_f=conductivity(Water,T=T_int,x=0)
rho_f=density(Water,T=T_int,x=0)
rho_g=density(Water,T=T_int,x=1)
v_f=volume(Water,T=T_int,x=0)
v_g=volume(Water,T=T_int,x=1)
"Calculation of Onset of Nucleate Boiling: Bergles and Rosenhow"
n=(0.463)*(P^0.0234)
DELTAT_w_ONB_B&R = (0.556)*((q_w/(1082*(P^1.156)))^n)
"Calculation of Onset of Nucleate Boiling: Sato and Matsumura"
DELTAT_w_ONB_S&M = ((8*sigma*q_w*T_sat)/(DELTAh_vap* k_f*rho_g*1000))^0.5
R_c = ((2*sigma*T_sat*k_f)/(1000*DELTAh_vap*q_w*rho_g))^0.5
"Calculation of Onset of Nucleate Boiling: Basu and Dhir"
Theta_w_SS=81 [Deg]
F=1- exp(-(((pi*Theta_w_SS)/180)^3)- (0.5*((pi*Theta_w_SS)/180)))
DELTAT_w_ONB_B&D = ((2*sigma*T_sat)/(R_c*F*rho_g*DELTAh_vap*1000))
"Heat Transfer Correlations"
"Test Section Dimensions"
d_in = 0.009398 [m]
d_out = 0.0127 [m]
```

l = 0.762 [m]

e= 0.00001524 [m]

"Inlet Flow Conditions"

V_dot = (12*0.000001) [m^3/s]

T_inlet = 98 [C]

rho_inlet = **density**(***Water***,***T***=T_inlet,***x***=0)

m_ddot = (((V_dot)*rho_inlet)/(0.25*pi*((d_in^2))))

mu_inlet=**viscosity**(***Water***,***T***=T_inlet,***x***=0)

cp_inlet=**specheat**(***Water***,***T***=T_inlet,***x***=0)

k_inlet=**conductivity**(***Water***,***T***=T_inlet,***x***=0)

Re_D = ((m_ddot*d_in)/mu_inlet)

Pr = (mu_inlet*cp_inlet*1000)/k_inlet

"Single Phase : Gnielinski"

f_l = (1.58***ln**(Re_D) - 3.28)^(-2)

Nusselt_l_D_Gnielinski = ((Re_D-1000)*Pr*0.5*f_l)/(1+((12.7*((Pr^(2/3))-1)*((0.5*f_l)^0.5))))

h_l_D_Gnielinski = (Nusselt_l_D_Gnielinski)*(k_inlet/d_in)

DELTAT_w_SPhase_Gnielinski_z1 = ((q_w/h_l_D_Gnielinski)*(1+(4*(h_l_D_Gnielinski/(m_ddot*cp_inlet*1000))*(0.18415/d_in))))-(T_int-T_inlet)

DELTAT_w_SPhase_Gnielinski_z2 = ((q_w/h_l_D_Gnielinski)*(1+(4*(h_l_D_Gnielinski/(m_ddot*cp_inlet*1000))*(0.3937/d_in))))-(T_int-T_inlet)

DELTAT_w_SPhase_Gnielinski_z3 = ((q_w/h_l_D_Gnielinski)*(1+(4*(h_l_D_Gnielinski/(m_ddot*cp_inlet*1000))*(0.57785/d_in))))-(T_int-T_inlet)

"Fully Developed Flow Boiling : Sub Cooled Boiling Correlations"

"McAdams (1949)"

DELTAT_w_superheat_McAdams = ((q_w/2.26)^(1/3.86))

"Jens & Lottes (1951)"

DELTAT_w_superheat_Jens&Lottes = (25*((q_w/1000000)^0.25)***exp**(P/62))

"Thom et. al. (1965)"

DELTAT_w_superheat_Thom = (22.65*((q_w/1000000)^0.25)***exp**(P/87))

"Shah (1977)"

h_l_Dittus_Boelter = (0.023*(Re_D^(4/5))*(Pr^0.4))*(k_inlet/d_in)

q_w = (230*((m_ddot*DELTAh_vap*1000)^(-0.5))*h_l_D_Gnielinski*DELTAT_w_superheat_Shah)^2

"Kandlikar (1998)"

q_w=(1058*((m_ddot*DELTAh_vap*1000)^(-0.7))*h_l_D_Gnielinski*DELTAT_w_superheat_Kandlikar)^3.33

"Onset of Fully Developed Boiling

(1058*q_f*((m_ddot*DELTAh_vap*1000)^(-0.7)))-((q_f)^(0.3))-(1058*h_l_D_Gnielinski*(T_int-T_inlet)*((m_ddot*DELTAh_vap*1000)^(-0.7)))=0

q_E = 1.4*q_f

q_E = (1058*((m_ddot*DELTAh_vap*1000)^(-0.7))*h_l_D_Gnielinski*DELTAT_E_superheat_Kandlikar)^3.33

Partial Boiling Line: Kandlikar

DELTAT_ONB = (4*sigma*T_int*(v_g-v_f)*h_l_D_Gnielinski)/(k_f*DELTAh_vap*1000)*(1+((1+((k_f*DELTAh_vap*1000*(T_int-T_inlet))/(2*sigma*T_int*(v_g-v_f)*h_l_D_Gnielinski)))^0.5))

q_ONB = ((k_f*DELTAh_vap*1000)/(8*sigma*(v_g-v_f)*T_int))*(DELTAT_ONB^2)

ps = 2.33/(q_E-q_ONB)

ns=1-(ps*q_ONB)

m = ns + (ps*q_w)

b = (q_E-q_ONB)/((DELTAT_E_superheat_Kandlikar^m)-(DELTAT_ONB^m))

a = q_ONB - (b*(DELTAT_ONB^m))

q_w= a + (b*((DELTAT_w_Partial_Boiling)^m))

APPENDIX E

This section contains the measured values of two-phase heat transfer coefficient values at an axial distance of 22.25 [in.] from the inlet of test section for a inlet mass flux of 165 [kg/(m^2s)]

Table 38. Comparison of heat transfer coefficient for various nanofluids at an axial distance of 22.5 [in.] from the inlet of the test section for an applied wall heat flux of 12.2 [kW/(m^2)] at a mass flux of 165 [kg/(m^2s)]

Test Condition	Heat Transfer Coefficient [W/(m^2K)]	% enhancement
DI Water+NaOH	1804.75(±3.8%)	-
0.5% SiO_2	2077.53(±4.1%)	15.1%
1.0% SiO_2	2108.49(±5.1%)	16.8%
1.5% SiO_2	2026.68(±4.6%)	12.3%
DI Water + NaOH (After 0.5% Nanofluid Experiments)	1989.39(±4.7%)	10.2%
DI Water + NaOH (After 1.0% Nanofluid Experiments)	2057.46(±5.3%)	14.0%
DI Water + NaOH (After 1.5% Nanofluid Experiments)	1937.23(±5.5%)	7.3%

Table 39. Comparison of heat transfer coefficient for various nanofluids at an axial distance of 22.5 [in.] from the inlet of the test section for an applied wall heat flux of 10.8 [kW/(m^2)] at a mass flux of 165 [kg/(m^{2}s)]

Test Condition	Heat Transfer Coefficient [W/(m^{2}K)]	% enhancement
DI Water NaOH	1827.13(±3.6%)	-
0.5% SiO_2	2076.87(±5.3%)	13.7%
1.0% SiO_2	2056.43(±4.6%)	12.6%
1.5% SiO_2	2059.42(±4.4%)	12.7%
DI Water + NaOH (After 0.5% Nanofluid Experiments)	1991.52(±4.2%)	9.0%
DI Water + NaOH (After 1.0% Nanofluid Experiments)	1947.70(±5.5%)	6.6%
DI Water + NaOH (After 1.5% Nanofluid Experiments)	2107.62(±5.9%)	15.4%

Table 40. Comparison of heat transfer coefficient for various nanofluids at an axial distance of 22.5 [in.] from the inlet of the test section for an applied wall heat flux of 9.5 [kW/(m^2)] at an mass flux of 165 [kg/(m^{2}s)]

Test Condition	Heat Transfer Coefficient [W/(m^{2}K)]	% enhancement
DI Water NaOH	1684.38(±6.2%)	-
0.5% SiO_2	1972.20(±6.5%)	17.1%
1.0% SiO_2	2005.07(±6.6%)	19.0%
1.5% SiO_2	1967.51(±7%)	16.8%
DI Water + NaOH (After 0.5% Nanofluid Experiments)	1788.89(±5.5%)	6.2%
DI Water + NaOH (After 1.0% Nanofluid Experiments)	1852.55(±6.2%)	10.0%
DI Water + NaOH (After 1.5% Nanofluid Experiments)	1890.92(±6.9%)	12.3%

APPENDIX F

This section contains image analysis performed for determining the void fraction at the exit of the test section for different tested working fluids.

The void fraction for all the experiments was estimated at the exit of the test section through visual inspection. The image acquisition system consisting of a high-speed camera (Manufacturer: Olympus, Model: i-Speed 3) was employed in this study. In this study, the images were acquired at a frame rate of 1500 frames/s and at a resolution of 1280 × 1024 pixels. A set of halogen lamps provided the required lighting for the viewing port during high-speed image acquisition. Void fraction measurements in this study were performed based on prior methods employed by Wojtan et al. [147].

Table 41. Computed void fractions for different working fluids obtained from image analysis

Wall Heat Flux [kW/m^2]	DI Water	SiO_2 nanofluid (1.0% mass fraction)	SiO_2 nanofluid (0.5% mass fraction)	SiO_2 nanofluid (1.5% mass fraction)
16.9	0.4 (±10.1%)	0.47(±9.5%)	0.51(±9.2%)	0.55(±9.2%)
15.2	0.3(±8.8%)	0.4(±9.5%)	0.42(±9.2%)	0.31(±9.3%)
13.7	0.09 (±13.5%)	0.16(±13.5%)	0.1(±11.5%)	0.1(±12.1%)

Figure 123. Image of bubble in the flow for DI Water at the end of the test section for a mass flux of 165 [kg/(m^{2}s)] at a wall heat flux of 16.9 [kW/(m^2)]

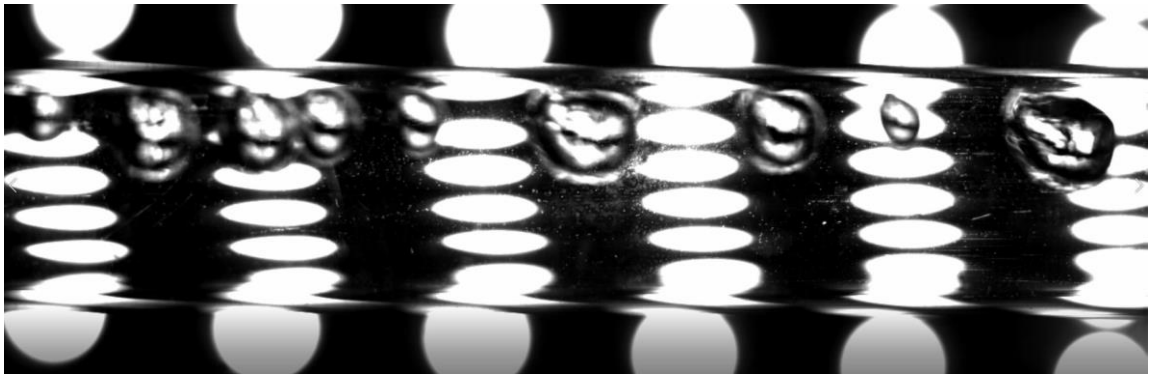

Figure 124. Image of bubble in the flow for DI Water at the end of the test section for a mass flux of 165 [kg/(m^{2}s)] at a wall heat flux of 15.2 [kW/(m^2)]

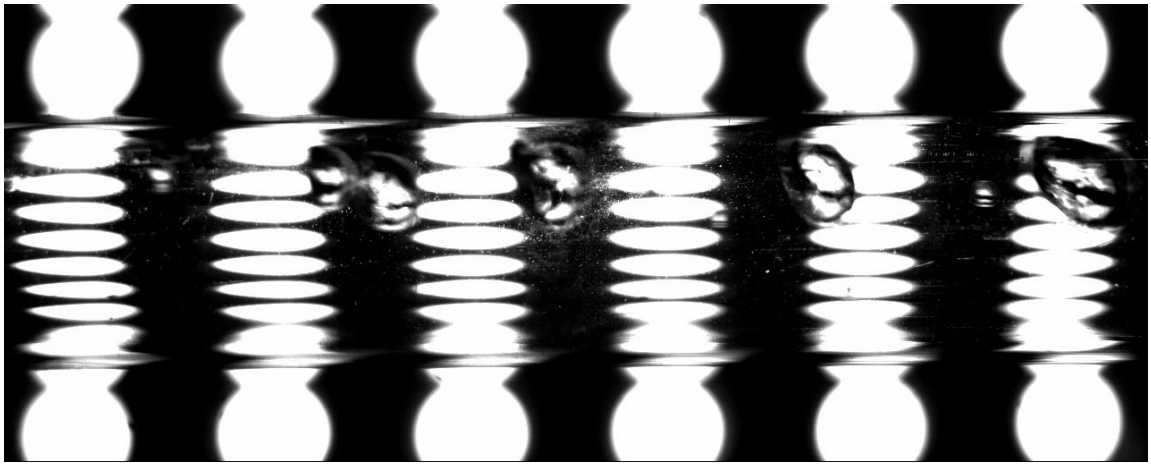

Figure 125. Image of bubble in the flow for DI Water at the end of the test section for a mass flux of 165 [kg/(m^{2}s)] at a wall heat flux of 13.7 [kW/(m^2)]

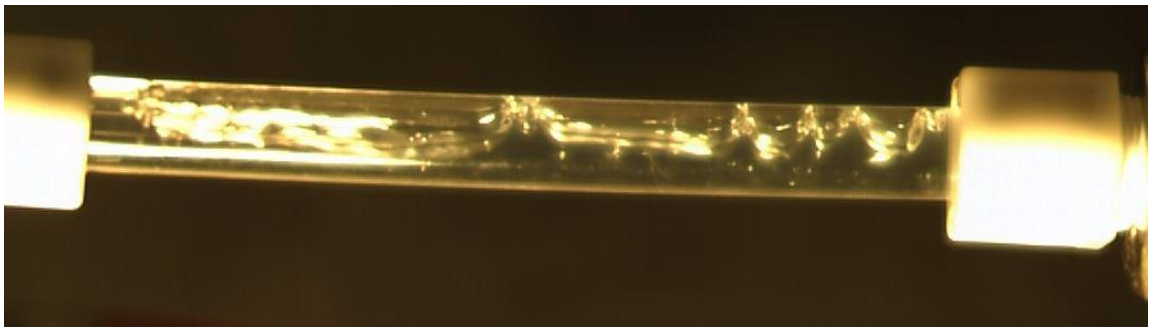

Figure 126. Image of bubble in the flow for aqueous silica nanofluid at a mass fraction of 1.0% at the end of the test section for a mass flux of 165 [kg/(m^{2}s)] at a wall heat flux of 16.9 [kW/(m^2)]

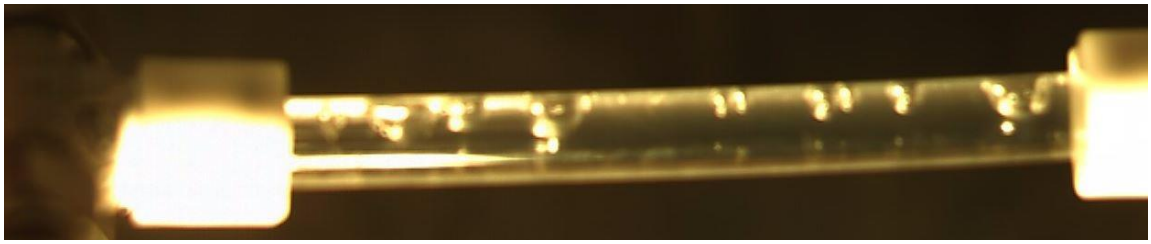

Figure 127. Image of bubble in the flow for aqueous silica nanofluid at a mass fraction of 1.0% at the end of the test section for a mass flux of 165 [kg/(m^{2}s)] at a wall heat flux of 15.2 [kW/(m^2)]

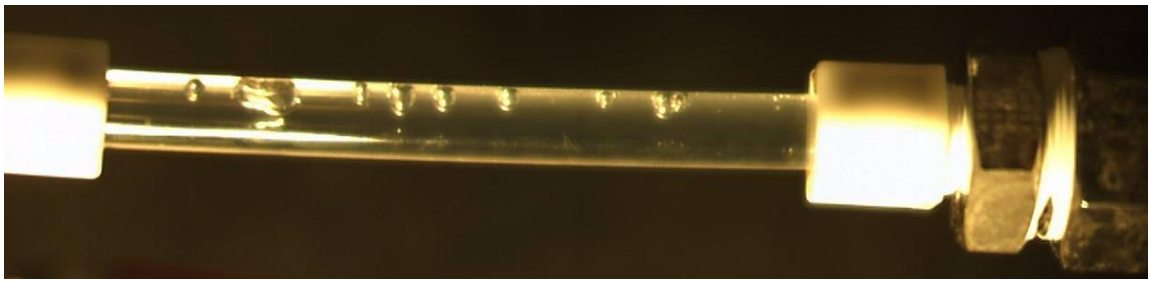

Figure 128. Image of bubble in the flow for aqueous silica nanofluid at a mass fraction of 1.0% at the end of the test section for a mass flux of 165 [kg/(m^{2}s)] at a wall heat flux of 13.7 [kW/(m^2)]

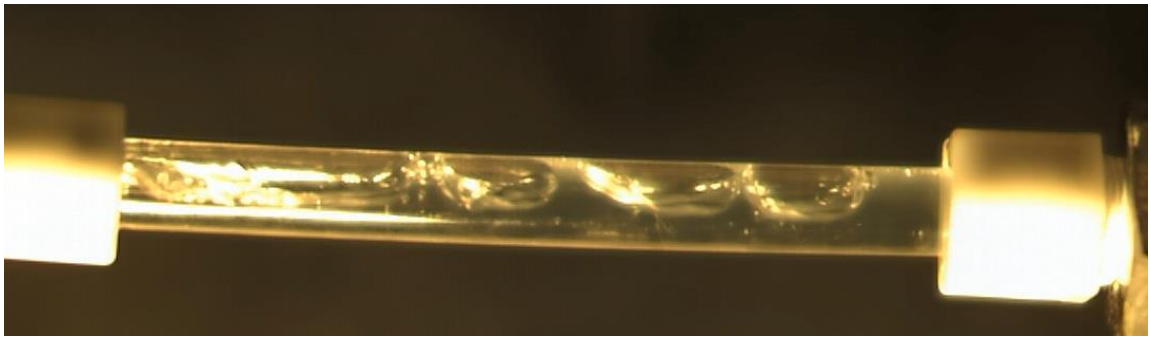

Figure 129. Image of bubble in the flow for aqueous silica nanofluid at a mass fraction of 0.5% at the end of the test section for a mass flux of 165 [kg/(m^{2}s)] at a wall heat flux of 16.9 [kW/(m^2)]

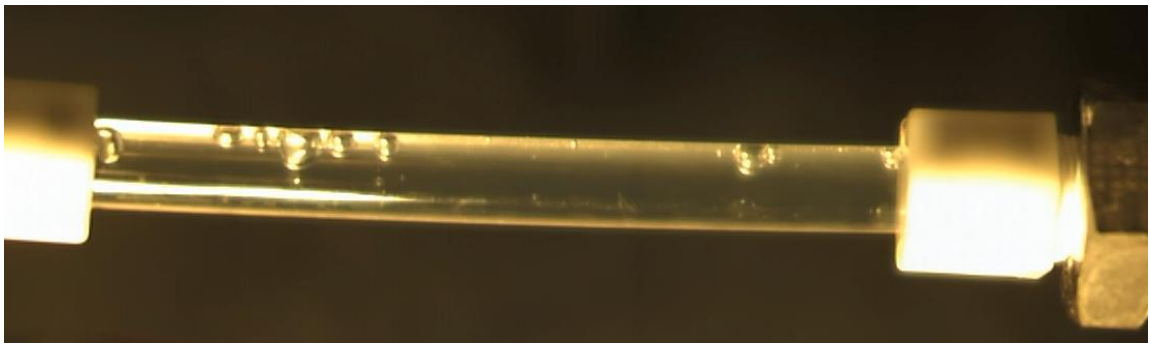

Figure 130. Image of bubble in the flow for aqueous silica nanofluid at a mass fraction of 0.5% at the end of the test section for a mass flux of 165 [kg/(m^{2}s)] at a wall heat flux of 15.2 [kW/(m^2)]

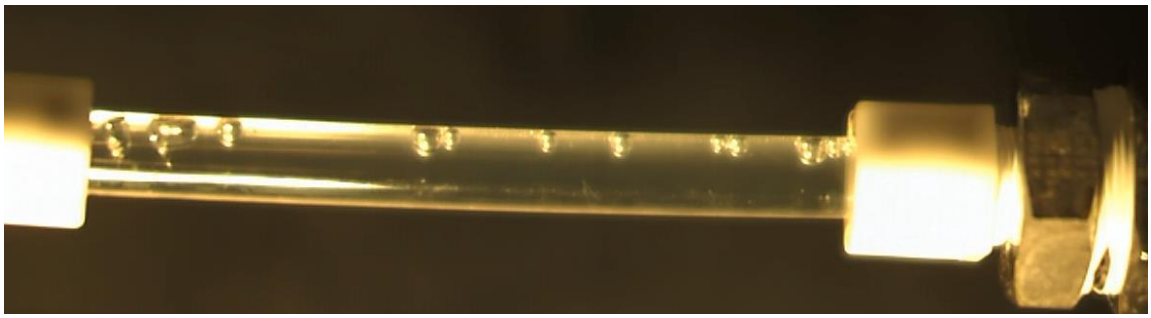

Figure 131. Image of bubble in the flow for aqueous silica nanofluid at a mass fraction of 0.5% at the end of the test section for a mass flux of 165 [kg/(m^{2}s)] at a wall heat flux of 13.7 [kW/(m^2)]

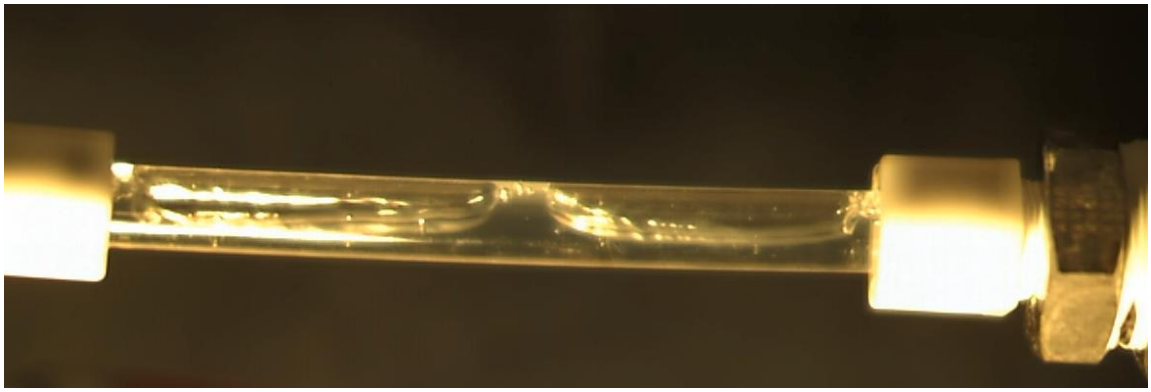

Figure 132. Image of bubble in the flow for aqueous silica nanofluid at a mass fraction of 1.5% at the end of the test section for a mass flux of 165 [kg/(m^{2}s)] at a wall heat flux of 16.9 [kW/(m^2)]

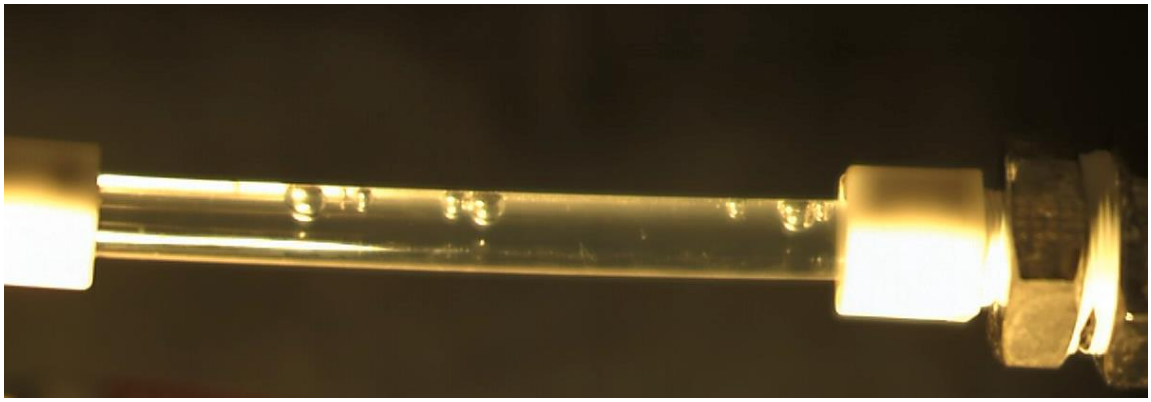

Figure 133. Image of bubble in the flow for aqueous silica nanofluid at a mass fraction of 1.5% at the end of the test section for a mass flux of 165 [kg/(m^{2}s)] at a wall heat flux of 15.2 [kW/(m^2)]

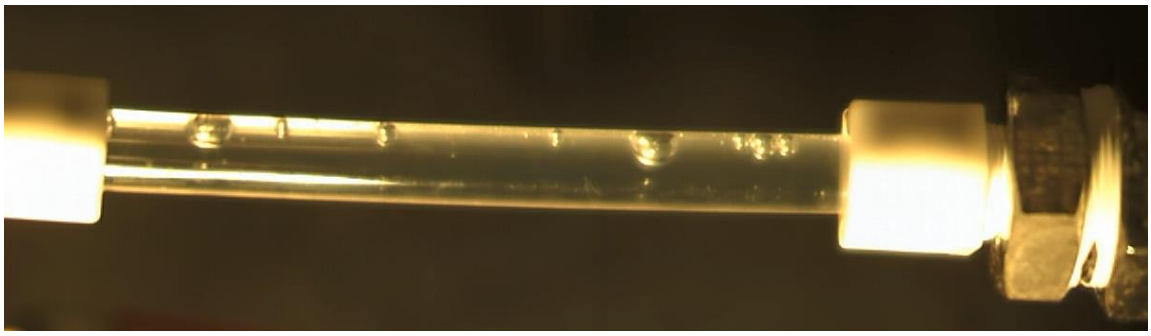

Figure 134. Image of bubble in the flow for aqueous silica nanofluid at a mass fraction of 1.5% at the end of the test section for a mass flux of 165 [kg/(m^{2}s)] at a wall heat flux of 13.7 [kW/(m^2)]

APPENDIX G

This section contains the flow boiling experimental results performed for aqueous nanofluid with SiO_2 nanoparticles (at 1.0% mass fraction) for various input wall heat flux. The series of experiments started with running pure DI Water (solvent) in the flow loop followed by 1.0% (mass fraction) of SiO_2 – DI Water aqueous nanofluid, followed by control experiment i.e. pure DI Water as the working fluid. Experiments were performed in this sequence to obviate the effect of NaOH on formed "nanofins" on the heater surface (formed due to isolated precipitation of nanoparticles from the nanofluid).

Test Condition	Heat Transfer Coefficient [W/(m^{2}K)]	% enhancement
DI Water__16.9kW/m^2	2029.03	-
1.0% SiO2_16.9 kW/m^2	2244.41	10.6%
DI Water (After 1.0% nanofluid experiments)_16.9 kW/m^2	2207.72	8.8%
DI Water__15.2 kW/m^2	1976.45	-
1.0% SiO2_15.2 kW/m^2	2175.62	10.1%
DI Water (After 1.0% nanofluid experiments)_15.2 kW/m^2	2067.76	4.6%
DI Water__13.7 kW/m^2	1890.65	-
1.0% SiO2_13.7 kW/m^2	2092.94955	10.7%
DI Water (After 1.0% nanofluid experiments)_13.7 kW/m^2	2013.54225	6.5%
DI Water__12.2 kW/m^2	1815.65	-
1.0% SiO2_12.2 kW/m^2	2048.0532	12.80%
DI Water (After 1.0% nanofluid experiments)_12.2 kW/m^2	1985.23171	9.34%
DI Water__10.8 kW/m^2	1789.54	-
1.0% SiO2_10.8 kW/m^2	1997.12664	11.6%
DI Water (After 1.0% nanofluid experiments)_10.8 kW/m^2	1937.17705	8.25%
DI Water__9.5 kW/m^2	1705.12	-
1.0% SiO2_9.5 kW/m^2	1971.97128	15.65%
DI Water (After 1.0% nanofluid experiments)_ kW/m^2	1873.841624	9.90%

Table 42. Measured surface wall temperature at different axial distances from the inlet of the test section for DI Water experiments for various mass fraction of SiO_2 nanoparticles

Axial Distance [in.]	16.9kW/m^2			15.2kW/m^2			13.7kW/m^2		
	DIW (Before Nanofluid Experiment)	DIW (Before Nanofluid Experiment)	DI Water + 1.0% SiO_2	DIW (Before Nanofluid Experiment)	DIW (Before Nanofluid Experiment)	DI Water + 1.0% SiO_2	DIW (Before Nanofluid Experiment)	DIW (Before Nanofluid Experiment)	DI Water + 1.0% SiO_2
7.25	110.7	109.78	110.2	109.2	108.65	109.6	107.8	107.55	107.1
15.5	112.4	112.17	112.1	110.3	110.59	110.8	109.7	109.36	109.0
22.25	107.9	107.48	106.8	107.7	107.27	106.2	107.0	106.29	106.1

Axial Distance [in.]	12.2kW/m^2			10.8kW/m^2			9.5kW/m^2		
	DIW (Before Nanofluid Experiment)	DIW (Before Nanofluid Experiment)	DI Water + 1.0% SiO_2	DIW (Before Nanofluid Experiment)	DIW (Before Nanofluid Experiment)	DI Water + 1.0% SiO_2	DIW (Before Nanofluid Experiment)	DIW (Before Nanofluid Experiment)	DI Water + 1.0% SiO_2
7.25	106.7	106.46	106.2	105.7	105.65	105.1	105.1	104.55	104.1
15.5	108.7	108.04	108.6	107.3	106.83	106.5	106.3	105.78	105.6
22.25	106.8	106.14	105.4	105.9	105.38	104.6	105.7	105.17	104.0

APPENDIX H

This section of the appendix contains the following

- Experimental results for the thermal conductivity of aqueous nanofluids
- Theoretical predictions of viscosity and specific heat capacity for aqueous SiO_2 nanofluids.

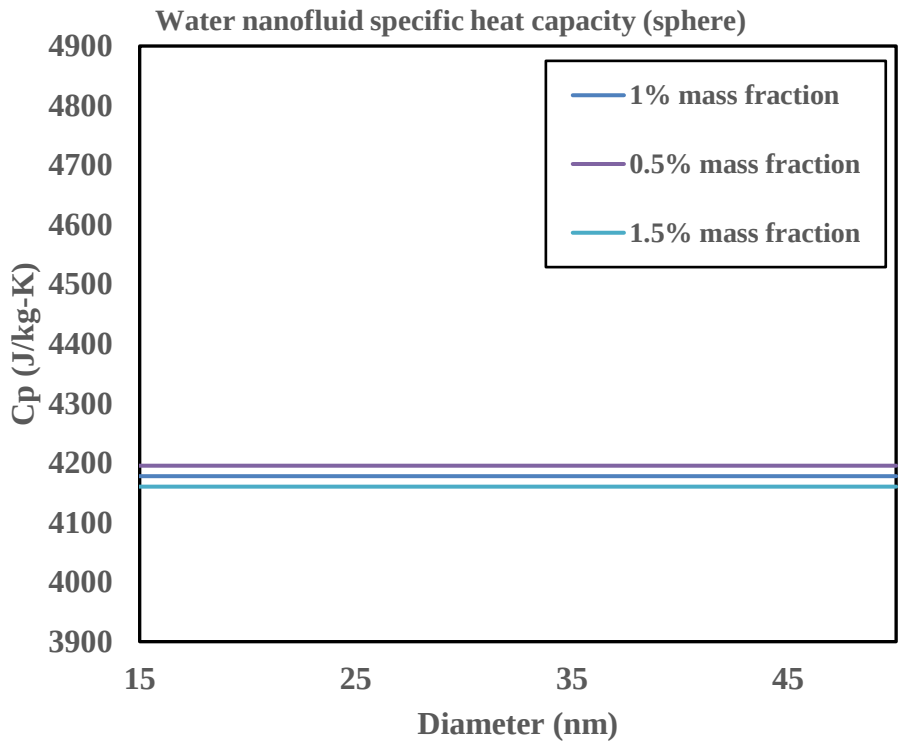

Figure 135. Theoretical prediction of specific heat capacity of aqueous silica nanofluid at various mass fraction computed from compressed layer model

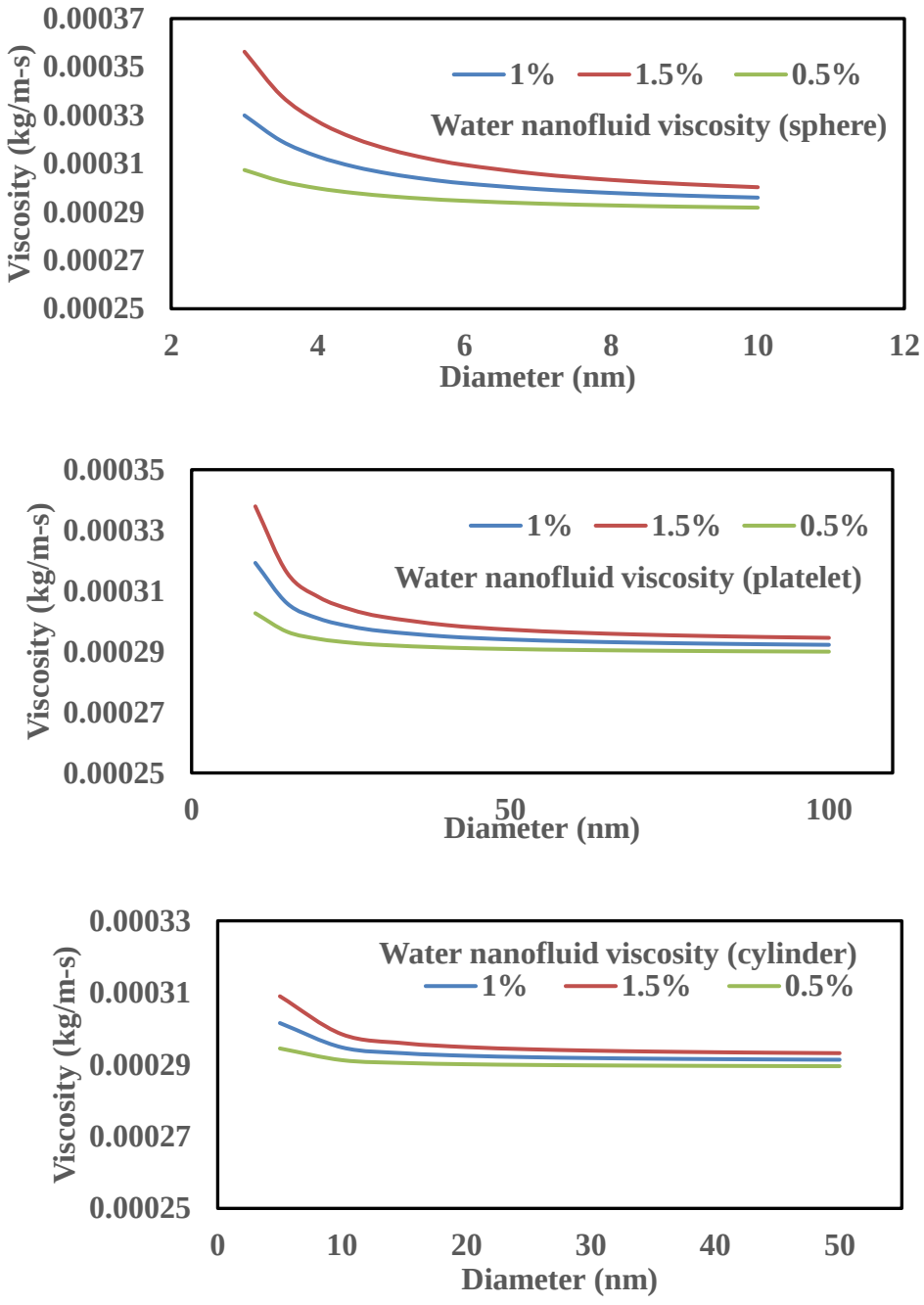

Figure 136. Theoretical prediction of viscosity for aqueous nanofluids for various mass concentration of silica nanoparticles computed from renewed ward model [130]

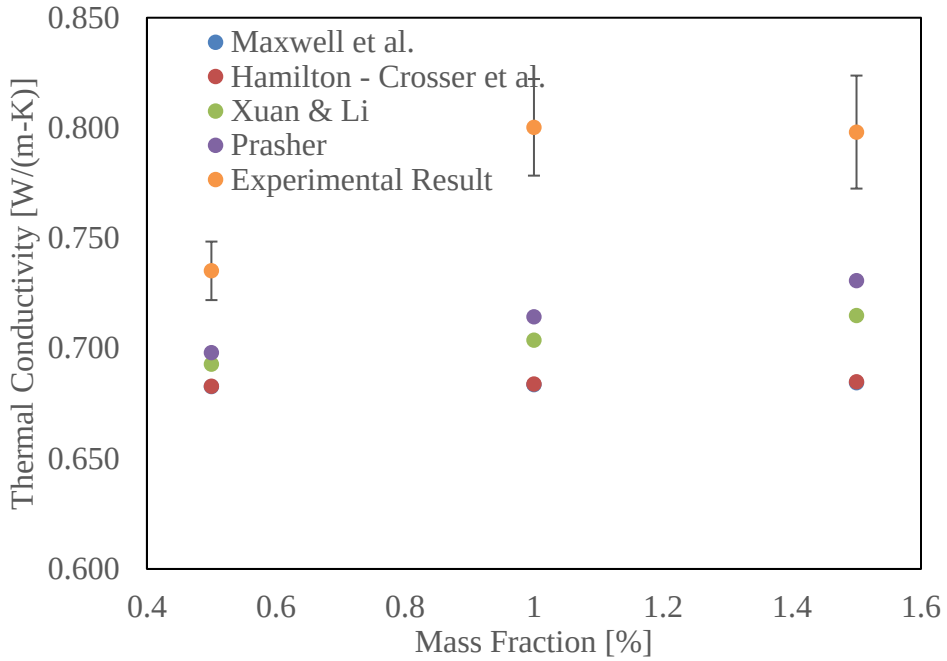

Figure 137. Thermal conductivity of aqueous silica nanofluid at different mass fraction compared to theoretical models

Table 43. Prandtl number computed for DI Water and SiO_2 nanofluids at different mass concentration based on the theoretical value of specific heat capacity and viscosity, and experimental measurement of thermal conductivity

Property	0.5% SiO_2	1% SiO_2	1.5% SiO_2	DI Water
k [W/(m-K)]	0.735	0.800	0.798	0.680
Cp [J/(kg-K)]	4195.43	4177.87	4160.31	4213
Mu [Pa-s]	0.00032	0.00036	0.00038	0.000288
Pr	1.826	1.879	1.980	1.783

Table 44. Summary of experimental results for thermal conductivity of aqueous silica nanofluids

	0.5% SiO_2			1.0% SiO_2			1.5% SiO_2		
	Sample 1	Sample 2	Sample 3	Sample 1	Sample 2	Sample 3	Sample 1	Sample 2	Sample 3
Run-1	0.7411 W/mK	0.7363 W/mK	0.7582 W/mK	0.7633 W/mK	0.7894 W/mK	0.7939 W/mK	0.7477 W/mK	0.7785 W/mK	0.8214 W/mK
Run-2	0.7459 W/mK	0.7295 W/mK	0.7353 W/mK	0.7915 W/mK	0.8047 W/mK	0.7954 W/mK	0.7756 W/mK	0.8205 W/mK	0.8279 W/mK
Run-3	0.7125 W/mK	0.7172 W/mK	0.7408 W/mK	0.8323 W/mK	0.7920 W/mK	0.8400 W/mK	0.7869 W/mK	0.8095 W/mK	0.8152 W/mK
Average	0.7332 W/mK	0.7277 W/mK	0.7448 W/mK	0.7957 W/mK	0.7954 W/mK	0.8098 W/mK	0.7701 W/mK	0.8028 W/mK	0.8215 W/mK

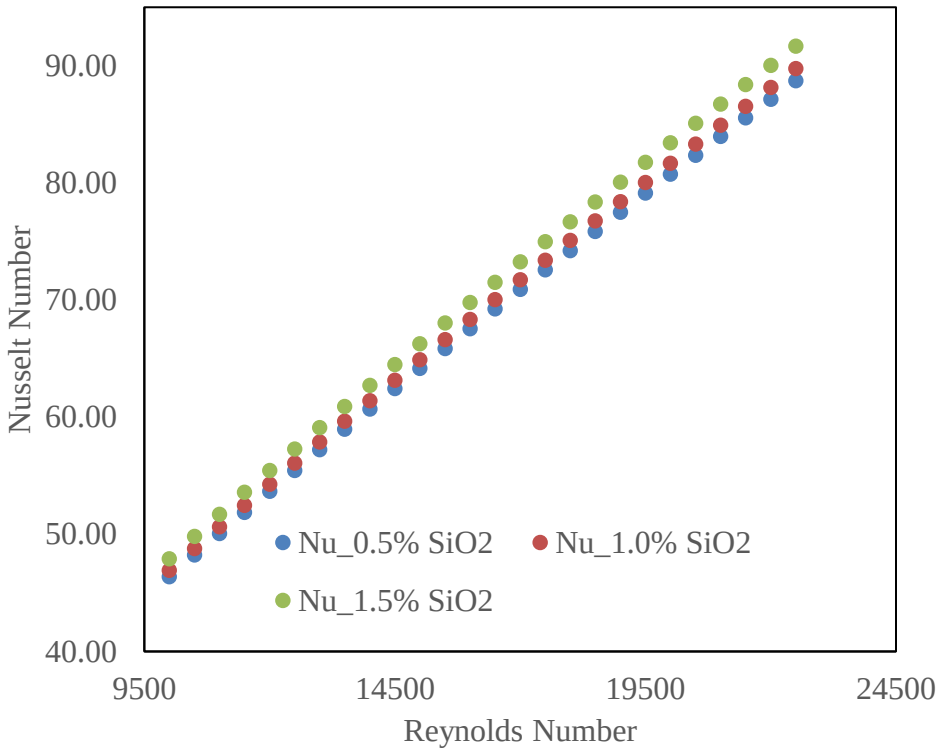

Figure 138. Comparison of Nusselt number computed form Dittus Boelter correlation for different aqueous silica nanofluids based on the properties computed from theoretical models